

DIAGNOSING THUNDERSTORM INDUCED POWER OUTAGES WITH THE
RAPID REFRESH MODEL (RAP)

by

Rachel Cucinotta

A thesis submitted to the faculty of
The University of North Carolina at Charlotte
in partial fulfillment of the requirements
for the degree of Master of Science in
Earth Science

Charlotte

2019

Approved by:

Dr. Matthew Eastin

Dr. Brian Magi

Terry Shirley

Stanton Lanham

©2019
Rachel Cucinotta
ALL RIGHTS RESERVED

ABSTRACT

RACHEL CUCINOTTA. Diagnosing Thunderstorm Induced Power Outages with the Rapid Refresh Model (RAP). (Under the direction of DR. MATTHEW EASTIN)

Duke Energy customers frequently experience electrical power outages caused by thunderstorms that produce strong surface winds and subsequently damage power distribution infrastructure. To better anticipate such outages, forecasters would benefit from outage-focused guidance regarding storm strength and timing so proper outage-mitigation can be initiated prior to each event. This study identified meteorological parameters that could best predict total daytime and nighttime power outages across each Duke Energy service area using generalized linear models (GLMs). A total of 392 event dates were stratified with regard to five service areas, two seasons, six convective modes, and three dominant severe weather types. Daytime and nighttime GLMs were attempted for each stratification with more than 10 event dates and the resulting GLMs were deemed “operational” if predictors remained statistically significant (p -values < 0.05) for ten trials using a randomly-selected portion of the training dataset. In total, 58 operational GLMs were developed using 24 unique parameters as predictors. The most common predictors were low-level vertical velocity and composite parameter used to predict large hail. The resulting operational GLMs can be implemented within an ensemble framework to provide Duke Energy with a total outage estimate for each service area.

DEDICATION

I would like to dedicate this thesis to my parents, Michael and Kelly Cucinotta. Their loving support has always encouraged me to chase my dreams and the value of a higher education. Thank you for always being there for me, I am so very fortunate to have parents like you!

ACKNOWLEDGEMENTS

I would like to acknowledge Duke Energy Corporation for project funding. I would also like to express great appreciation to my graduate advisor, Dr. Matthew Eastin, whom provided ample constructive feedback and helped immensely with project development. My sincerest gratitude for his patience, encouragement, and well-articulated dissemination of knowledge. A special thank you to my committee, Stanton Lanham, Terry Shirley, and Dr. Brian Magi and to Dr. Casey Davenport for serving on my committee during the proposal stages. Lastly, I would like to acknowledge my fellow officemates for advice with project management and specifically, Matt Gropp and Alex Schaefer for helping me with my python scripts.

TABLE OF CONTENTS

LIST OF TABLES	viii
LIST OF FIGURES	ix
CHAPTER 1: INTRODUCTION	1
a. Duke Energy Forecasting Process	2
CHAPTER 2: LITERATURE REVIEW	5
a. Microburst Generation	5
b. Microburst Forecasting	6
c. Past Power Outage Studies	8
CHAPTER 3: DATA	13
a. Duke Energy Service Areas	13
b. Storm Prediction Centers Convective Outlooks	13
c. Power Outages	14
d. Environmental Data	14
e. Radar Data	15
CHAPTER 4: METHODS	16
a. Case Data Selection	16
b. Quality Control of Outage Data	17
c. Creation of the Spatial Analysis Grid	18
d. Acquisition and Processing of Environmental Observations	19
e. Stratification of Dates	32
f. Summary Statistics	34
g. GLM Development for Total Number of Power Outage Estimation	36
h. GLM Validation	37
CHAPTER 5: RESULTS AND DISCUSSION	39
a. Midwest Cincinnati (MWC)	39

i. MWC Model Discussion	40
ii. MWC Error Analysis	45
b. Midwest Indiana (MWI)	47
i. MWI Model Discussion	48
ii. MWI Error Analysis	56
c. Florida (FLA)	58
i. FLA Model Discussion	59
ii. FLA Error Analysis	64
d. Carolina West (DEC)	66
i. DEC Model Discussion	67
ii. DEC Error Analysis	70
e. Carolina East (DEP)	72
i. DEP Model Discussion	72
ii. DEP Error Analysis	75
CHAPTER 6: CASE STUDIES	77
a. Midwest (MWC, MWI)	78
b. Florida (FLA)	79
c. Carolinas (DEC, DEP)	80
CHAPTER 7: CONCLUSION	82
CHAPTER 8: FUTURE WORK	86
TABLES	87
FIGURES	103
REFERENCES	174

LIST OF TABLES

TABLE 1:	Number of Event Dates per Service Area	87
TABLE 2:	Metrics	88
TABLE 3:	Number of Severe Weather Type Events per Service Area	90
TABLE 4:	Metric Categories for Multi-collinearity	91
TABLE 5:	Operational GLMs	92
TABLE 6a:	Event Date Stratification for MWC Hot Season	98
TABLE 6b:	Event Date Stratification for MWC Warm Season	98
TABLE 7a:	Event Date Stratification for MWI Hot Season	99
TABLE 7b:	Event Date Stratification for MWI Warm Season	99
TABLE 8a:	Event Date Stratification for FLA Hot Season	100
TABLE 8b:	Event Date Stratification for FLA Warm Season	100
TABLE 9a:	Event Date Stratification for DEC Hot Season	101
TABLE 9b:	Event Date Stratification for DEC Warm Season	101
TABLE 10a:	Event Date Stratification for DEP Hot Season	102
TABLE 10b:	Event Date Stratification for DEP Warm Season	102

LIST OF FIGURES

FIGURE 1:	Duke Energy Service Areas	103
FIGURE 2:	Stratification Method	104
FIGURE 3:	MWC-HOT-SCAT-WIND-NIGHT (1) Outage Count Histogram	105
FIGURE 4:	MWC-HOT-SQLL-WIND-DAY (2) Outage Count Histogram	105
FIGURE 5:	MWC-WARM-SQLL-DAY (3) Outage Count Histogram	106
FIGURE 6:	MWC-WARM-SQLL-NIGHT (4) Outage Count Histogram	106
FIGURE 7:	MWC-WARM-DAYS (5) Outage Count Histogram	107
FIGURE 8:	MWC-WARM-NIGHT (6) Outage Count Histogram	107
FIGURE 9a:	Mean Absolute Error Distributions (Models 1-6)	108
FIGURE 9b:	Root Mean Square Error Distributions (Models 1-6)	109
FIGURE 9c:	Percent Error Distributions (Models 1-6)	110
FIGURE 9d:	Bias Distributions (Models 1-6)	111
FIGURE 10:	MWI-HOT-SCAT-WIND-NIGHT (8) Outage Count Histogram	112
FIGURE 11:	MWI-HOT-SQLL-WIND-NIGHT (10) Outage Count Histogram	112
FIGURE 12:	MWI-HOT-SQLL-NIGHT (12) Outage Count Histogram	113
FIGURE 13:	MWI-WARM-SCAT-HAIL-TOR-NIGHT (16) Outage Count Histogram	113
FIGURE 14:	MWI-WARM-SQLL-WIND-DAY (17) Outage Count Histogram	114
FIGURE 15:	MWI-WARM-SQLL-WIND-NIGHT (18) Outage Count Histogram	114
FIGURE 16:	MWI-WARM-SCAT-NIGHT (20) Outage Count Histogram	115
FIGURE 17:	MWI-WARM-SQLL-NIGHT (22) Outage Count Histogram	115
FIGURE 18a:	Mean Absolute Error Distributions (Models 7-12)	116

FIGURE 18b: Root Mean Square Error Distributions (Models 7-12)	117
FIGURE 18c: Percent Error Distributions (Models 7-12)	118
FIGURE 18d: Bias Distributions (Models 7-12)	119
FIGURE 19a: Mean Absolute Error Distributions (Models 13-18)	120
FIGURE 19b: Root Mean Square Error Distributions (Models 13-18)	121
FIGURE 19c: Percent Error Distributions (Models 13-18)	122
FIGURE 19d: Bias Distributions (Models 13-18)	123
FIGURE 20a: Mean Absolute Error Distributions (Models 19-24)	124
FIGURE 20b: Root Mean Square Error Distributions (Models 19-24)	125
FIGURE 20c: Percent Error Distributions (Models 19-24)	126
FIGURE 20d: Bias Distributions (Models 19-24)	127
FIGURE 21: FLA-HOT-SCAT-WIND-NIGHT (26) Outage Histogram	128
FIGURE 22: FLA-HOT-SCAT-DAY (27) Outage Histogram	128
FIGURE 23: FLA-HOT-SCAT-NIGHT (28) Outage Histogram	129
FIGURE 24: FLA-HOT-DAY (29) Outage Histogram	129
FIGURE 25: FLA-WARM-SCAT-WIND-DAY (30) Outage Histogram	130
FIGURE 26: FLA-WARM-SCAT-WIND-NIGHT (31) Outage Histogram	130
FIGURE 27: FLA-WARM-SQLL-WIND-DAY (32) Outage Histogram	131
FIGURE 28: FLA-WARM-SQLL-WIND-NIGHT (33) Outage Histogram	131
FIGURE 29: FLA-WARM-PULSE-DAY (34) Outage Histogram	132
FIGURE 30: FLA-WARM-SCAT-NIGHT (36) Outage Histogram	132
FIGURE 31: FLA-WARM-SQLL-DAY (37) Outage Histogram	133
FIGURE 32: FLA-WARM-DAY (39) Outage Histogram	133

FIGURE 33a: Mean Absolute Error Distributions (Models 25-30)	134
FIGURE 33b: Root Mean Square Error Distributions (Models 25-30)	135
FIGURE 33c: Percent Error Distributions (Models 25-30)	136
FIGURE 33d: Bias Distributions (Models 25-30)	137
FIGURE 34a: Mean Absolute Error Distributions (Models 31-36)	138
FIGURE 34b: Root Mean Square Error Distributions (Models 31-36)	139
FIGURE 34c: Percent Error Distributions (Models 31-36)	140
FIGURE 34d: Bias Distributions (Models 31-36)	141
FIGURE 35a: Mean Absolute Error Distributions (Models 37-40)	142
FIGURE 35b: Root Mean Square Error Distributions (Models 37-40)	143
FIGURE 35c: Percent Error Distributions (Models 37-40)	144
FIGURE 35d: Bias Distributions (Models 37-40)	145
FIGURE 36: DEC-HOT-SCAT-WIND-DAY (41) Outage Histogram	146
FIGURE 37: DEC-HOT-SQLL-WIND-NIGHT (42) Outage Histogram	146
FIGURE 38: DEC-HOT-SQLL-NIGHT (43) Outage Histogram	147
FIGURE 39: DEC-HOT-DAY (44) Outage Histogram	147
FIGURE 40: DEC-WARM-SQLL-WIND-DAY (46) Outage Histogram	148
FIGURE 41: DEC-WARM-SCAT-DAY (47) Outage Histogram	148
FIGURE 42: DEC-WARM-SQLL-DAY (48) Outage Histogram	149
FIGURE 43: DEC-WARM-NIGHT (49) Outage Histogram	149
FIGURE 44a: Mean Absolute Error Distributions (Models 41-46)	150
FIGURE 44b: Root Mean Square Error Distributions (Models 41-46)	151
FIGURE 44c: Percent Error Distributions (Models 41-46)	152

FIGURE 44d: Bias Distributions (Models 41-46)	153
FIGURE 45a: Mean Absolute Error Distributions (Models 47-49)	154
FIGURE 45b: Root Mean Square Error Distributions (Models 47-49)	155
FIGURE 45c: Percent Error Distributions (Models 47-49)	156
FIGURE 45d: Bias Distributions (Models 47-49)	157
FIGURE 46: DEP-HOT-SCAT-WIND-DAY (50) Outage Histogram	158
FIGURE 47: DEP-HOT-SCAT-WIND-NIGHT (51) Outage Histogram	158
FIGURE 48: DEP-HOT-SQLL-WIND-DAY (52) Outage Histogram	159
FIGURE 49: DEP-HOT-SQLL-DAY (53) Outage Histogram	159
FIGURE 50: DEP-HOT- DAY (54) Outage Histogram	160
FIGURE 51: DEP-HOT-NIGHT (55) Outage Histogram	160
FIGURE 52: DEP-WARM-SQLL-WIND-DAY (56) Outage Histogram	161
FIGURE 53: DEP-WARM-SQLL-NIGHT (57) Outage Histogram	161
FIGURE 54: DEP-WARM-NIGHT (58) Outage Histogram	162
FIGURE 55a: Mean Absolute Error Distributions (Models 50-56)	163
FIGURE 55b: Root Mean Square Error Distributions (Models 50-56)	164
FIGURE 55c: Percent Error Distributions (Models 50-56)	165
FIGURE 55d: Bias Distributions (Models 50-56)	166
FIGURE 56a: Mean Absolute Error Distributions (Models 57-59)	167
FIGURE 56b: Root Mean Square Error Distributions (Models 57-59)	168
FIGURE 56c: Percent Error Distributions (Models 57-59)	169
FIGURE 56d: Bias Distributions (Models 57-59)	170
FIGURE 57: Midwest Service Area Case Date Ensemble Prediction	171

FIGURE 58: Florida Service Area Case Date Ensemble Prediction	172
FIGURE 59: Carolina Service Area Case Date Ensemble Prediction	173

CHAPTER 1: INTRODUCTION

Power outages caused by strong and severe thunderstorms frequently affect the Midwest and Southeast, especially during the warm season (March 1– October 31 for this study). These thunderstorms engender lightning and strong winds that cause whole trees or tree limbs to collapse, which consequently disturb power distribution lines. The severity of power interruption amplifies with time, as long restoration periods become costly to service providers and hinders customers' ability to return to normalcy after the storm has passed. Extreme power outages can even disrupt essential city infrastructure like water, transportation, or communication services provoking the city into a temporary fiscal stress.

Forecasting such events is challenging because the accurate representation of deep convection by existing numerical weather models is limited. Currently, even the most sophisticated models limit forecasters to producing broad regional outlooks that leave the outage mitigation decision makers with insufficient knowledge on storm severity and storm type at the desired spatiotemporal scale. Ideally, the decision makers need to know the rough timing, location, and severity of the storms in order to request and pre-position repair crews and reduce customer outage times.

The broad one-day Convective Outlooks provided by the Storm Prediction Center (SPC), when applied by weather forecasters at energy companies, often result in two undesired scenarios regarding power outage mitigation. The first scenario, referred to as “short-fuse events” entails poorly-forecasted storms, yet numerous storms and/or outages occur with insufficient repair crews on standby, leaving dissatisfied customers without power for an extended period. In the second scenario, referred to as “non-events”, storms

are forecast and repair crews are held in standby, but the storms do not produce the anticipated number of outages. Neither scenario is cost-effective for the service provider since repair crews are paid overtime during both. It has become clear that traditional *severe weather* forecast tools lack the ability to distinguish *outage-producing* thunderstorms from ordinary thunderstorms, often leaving power companies with dissatisfied customers and/or expensive repair costs.

This thesis addresses the following research questions. How can we improve our forecasting knowledge to better distinguish outage-producing and non-outage-producing thunderstorm events? What severe weather types are most likely responsible for power outages and what environmental conditions spawn such outage-producing severe weather? How can we provide better lead-time of outage location and density to pre-position repair crews?

a. Duke Energy's Forecasting Process

Duke Energy weather forecasters have several objectives, but the primary objective relevant to this study is to anticipate the number of power outages 0-3 days in advance (for each service area – Midwest, Florida, and Carolinas) so adequate repair crews can be requested or dismissed (particularly for weekend storms). Duke forecasters begin their process in the early morning (generally 5 am – varies based on service area) and develop daily outage forecasts based on current weather observations and numerical guidance. Outage forecasts for weekdays are finalized no later than 2 pm. Outage forecasts for the weekends are communicated during an 11 am conference call on Thursdays. The outage forecast is portrayed as one of four threat levels: (1) Green (isolated) < 10,000 customers affected; (2) Yellow (scattered) < 50,000 customers affected; (3) Orange (significant) <

100,000 customers affected; and (4) Red (widespread) > 100,000 customers affected. Once a threat level is determined, a set of procedures specific to that threat level are applied by call centers and followed by repair crews. For reasons of long-term economics, the operational mindset at Duke is that it is better to forecast more outages and to experience less (e.g., non-events) than to forecast few outages and experience more (e.g., short-fuse events).

Each service area has an experienced lead forecaster that have identified important indicators specialized to their individual service territory. For example, the Florida forecaster relies heavily on instability parameters such as the Lifted Index (LI) and 700-mb temperature to first identify dates with synoptic-mesoscale environments favorable for outage-producing storms. Then, precipitable water, low-level convergence (assuming an active sea breeze), and convective temperature is used to predict when and where, during a given date, any shallow cumulus and deep convection will develop. Finally, the 925-mb wind speed, anticipated storm speed, and microburst parameter are used to forecast convective outflow strength (i.e. the strong surface winds that damage trees and produce the power outage).

In the Midwest, the forecaster primarily focuses on shear-based parameters, such as helicity and directional shear. Instability parameters, such as LI and CAPE, have also proven to be good predictors when identifying outage prone days. In the Carolinas, unless there is frontal forcing, the strength of the air mass thunderstorms will vary greatly by the amount of daytime heating prior to onset of convection. Often, warm-season summertime, thunderstorms will develop in the western Appalachian Mountains and move eastward toward the more populated I-85 and I-40 corridors. Thus the Carolina forecaster will focus

on storm speed, not only to identify storms with stronger gust fronts, but also to identify storms capable of reaching the more populated regions of the state before the daytime heating source is eliminated.

While each service area is unique in regard to common convective modes and useful forecast parameters, the forecasters share a reliance on the SPC Convective Outlooks. For example, if the SPC forecasts a slight (SLGT) risk or greater, Duke forecasters instinctively place their service territory into a higher threat level (i.e. yellow, orange, or red), leaving more repair crews and call center staff in place to mitigate any reported outages.

CHAPTER 2: LITERTURE REVIEW

Fujita (1978) described a downburst as “a strong downdraft inducing an outward burst of damaging winds on or near the ground.” A microburst is a type of downburst and is specified by a horizontal dimension of less than 4 km and are of particular interest due to their high destruction rate. Their damage can be compared to that of a F3 tornado with winds ranging between 71-92 m s⁻¹, which is capable of removing roofs, tearing the walls off well-constructed houses and uprooting or snapping most trees in its path (Fujita and Wakimoto 1981; Forbes and Wakimoto 1983). Considering that fallen trees and/or tree limbs are major catalysts to power outages, a thorough investigation of microbursts is vital to establishing a basis for the types of thunderstorms capable of producing microburst strength destruction. Lastly, in addition to investigating the generation and forecast techniques of microbursts it will be important to investigate past power outage studies. The past power outage studies will bring forward knowledge about what types of models are most applicable to power outage prediction and potential predictors to use within said models.

a. Microbursts Generation

Thermodynamically speaking, there are multiple processes that work in concert to generate a microburst. However, microbursts can be categorized into either wet or dry microbursts based on the observational sounding. The study area brings attention to the wet microburst because they are more common in humid regions such as the Midwest and Southeast. Wet microburst characteristics include shallow sub-cloud layers, high radar reflectivity, warm (low) cloud bases and an environmental sounding that is more statically

stable (Atkins and Wakimoto 1991). Despite the fact that multiple processes are occurring at once, there are a few generalizations that can be made for the physical development of a wet microburst.

The updraft is forced by the total water mass accumulation from all hydrometeor types (cloud water, cloud ice, raindrops, snow, graupel and hail). As the hydrometeors grow, gravity will prompt the hydrometeor to fall and accelerate the downdraft (Tuttle et al. 1989). If the updraft is tilted the precipitation will exit adjacent to the updraft and the precipitation core will begin to mix with drier air. If the updraft is not tilted the downdraft generated by the precipitation will suppress the updraft and therefore the storm as a whole. As the parcel begins to descend adiabatic compressional warming will ensue, combined with the mixing of drier environmental air, causing the parcel to become unsaturated and induce a combination evaporation, sublimation, and melting that will then dominate the parcel (Knupp 1988; Mahoney et al. 2009). The latent heat of absorption associated with the evaporation, sublimation, and melting processes causes the air parcel to cool and be accelerated downward via the negative buoyancy generated by the temperature difference between the relatively cool air parcel and the surrounding warmer environment. The temperature of the parcel during this stage can be estimated through the equivalent potential temperature (Knupp 1987), which will be important to parameters designed for forecasting the strength of the downdraft.

b. Microburst Forecasting

In 1991, Atkins and Wakimoto conducted a study that analyzed environmental conditions favorable for wet microbursts to help develop criteria that forecasters could use to potentially predict such severe wind events. The most novel findings were associated

with the height of the minimum equivalent potential temperature and the precipitation core. The thought was that the minimum equivalent potential temperature would be a good proxy to estimate the likelihood of a downdraft because it ultimately measures the maximum negative buoyancy possible in a given environment. It was found that wet-microburst environments had a difference between the minimum equivalent potential temperature and surface equivalent potential temperature of 20K or more, whereas that difference was 13K or less on non-microburst days, demonstrating that downdrafts can occur for a range of values for equivalent potential temperatures. However, the maximum downdraft would only be achieved if the precipitation core coexisted at the same level as the minimum equivalent potential temperature (since that is where the potential greatest cooling and the greatest amount of negative buoyancy could be generated). Most of the microburst days analyzed had at least the upper portions of the main precipitation cores reaching the same level as the minimum equivalent potential temperature but non-microburst days had precipitation cores much lower in the atmosphere.

Evans and Doswell (2001) describe another parameter that has been developed to specifically estimate the strength of the downdraft, called downdraft convective available potential energy (DCAPE). It was developed to estimate downdraft intensity prior to downdraft development. Gilmore and Wicker (1998, p. 944) define DCAPE as “the maximum increase in kinetic energy (per unit mass) that could result from evaporative cooling of the air within hypothetical parcel as it descends from some source height to the ground”. This parameter uses equivalent potential temperature to estimate the maximum possible downdraft for the given environment via a more comprehensive measure of

available potential energy. A DCAPE value of 500 J kg^{-1} or greater is sufficient to produce a strong downdraft (Gilmore and Wicker 1998).

Johns and Hirt (1987) conducted a similar study in deciphering common microburst environments. They found that 88 percent of microbursts occur three hours after convection has been initiated and 57 percent of microbursts develop six hours after the convection initiation. In almost every case, warm air advection was occurring at the 850 mb level within 320 km of the microburst location. On average, the convective instability, measured by the difference between the parcel lifted to 500 mb and the environment at 500 mb (also called the Lifted Index) was -6 K. Cold cloud tops found in bulging squall lines are associated with microburst and can be found using satellite imagery. The forecasting techniques discussed in this section will be utilized to develop spatiotemporal relationships between microbursts and power outages.

c. Past Power Outage Studies

A power system's susceptibility to damage during warm season convection varies as geographic and climatic factors change. Many studies have found that the severity of weather-related impacts is dependent on (but are not limited to) the following: the number of customers being served by the utility company; the number of poles, switches and transformers; the geography, topography and climate of the region of interest; and finally wind characteristics like speed and the duration of exposure to the maximum wind gusts (Reed 2008; McRoberts et al. 2016). Most power outage studies have addressed various related objectives, such as predicting the number of outages (Guikema et al. 2014), modeling power outage duration (Nateghi et al. 2011, 2014) and predicting the number of customers affected by each outage (Guikema et al. 2008, 2014; Han et. al 2009; McRoberts

et al. 2016). Collectively, these studies address the complexity of the variable and methods used to enhance predictive accuracy.

Past power outage studies have suggested numerous important potential predictors and methods to consider when it comes to diagnosing power outages. Unfortunately, many of these studies are geared toward power outages caused by *hurricanes* (Liu et al. 2005, 2008; Han et al. 2009; Guikema et al. 2010; Nateghi et al. 2014; Quiring et al. 2014; McRoberts et al. 2016; Tonn et al. 2016) where obtaining a realistic estimate of local winds is possible due to hurricanes slow evolution and predictable synoptic-scale wind field associated with each hurricane. Although never a main focal point, a few studies consider *warm-season convection* (Cerruti and Decker 2012; Wanik et al. 2015) where strong winds capable of producing power outages are much less predictable due to their rapid evolution and smaller scale. With that in mind, the remainder of this section focuses on the warm-season convection outage models (methods and most important predictors) without neglecting the influential groundwork provided by the tropical-cyclone outage studies.

Cerruti and Decker (2012) adopted a “perfect-prognosis” (PP) approach which uses predictors derived from observations and/or initial model analyses to develop their statistical models. Such an approach minimizes any dependence on model resolution and/or physics from influencing the statistical relationships, and thus, minimizes any skill degradation to the statistical prediction as a result of regular numerical model updates (Wilks 2006). Cerruti and Decker (2012) develop 144 generalized-linear model (GLM; also known as a multiple-linear regression model) to predict various infrastructure damage events for a large New Jersey utility using predictors derived from surface weather observations. The event stratification was based on weather mode (*thunderstorm*, warm,

mix, cold, heat, wind), the region (four sub-regions within the service area), and infrastructure-type (transformers, poles, trees, service wires, primary wires, and secondary wires). A backwards-elimination method was employed, whereby an initial regression equation using all predictors was trimmed by repeatedly removing the predictor with the highest p-value (i.e. the least skillful predictor) until all remaining predictors exhibited p-values below 0.05. Overall, the models were used to predict total outage numbers across the service area (with no regard to where within the service area the outages might occur).

Regarding predictors, the study identified several custom composite parameters (referred to as SF_x terms) as the most common optimal predictors (found in 66% of their equations). For example, SF_1 (the product of the maximum wind gust and daily precipitation) was used to gauge overall weather severity, while SF_2 (the product of the maximum wind gust and 10-day accumulated precipitation) was used to anticipate tree damage. Indeed, many studies have agreed that wetter soils increase the chances of trees being uprooted (Liu et al. 2008; Han et al. 2009; Nateghi et al. 2014; McRoberts et al 2016). Finally, SF_3 (the product of the maximum wind gust and maximum temperature) proved influential in the thunderstorm mode equations. While high temperatures do not directly damage power infrastructure, they are indicative of unstable environments, containing steep low-level lapse rates that are favorable for microburst-producing thunderstorms. Moreover, note that gust speed was a common component in each SF_x in a manner consistent with most tropical-cyclone focused outage studies (Guikema et al. 2010; Nateghi et al. 2014; McRoberts et al. 2016; Tonn et al. 2016).

Wanik et al. (2015) developed multiple models to forecast where an outage would occur within a Connecticut service area. The Weather and Research Forecast (WRF) model

was used to simulate 89 storms and then relate outage numbers within numerous 2×2 grid cells to a multitude of explanatory predictors. Four different statistical model types were tested, decision tree (DT), random forest (RF), boosted gradient tree (BT), and an ensemble tree (ENS) - using full (weather variables, infrastructure, and land cover) and reduced (weather variables only) predictor pools, resulting in eight total models. The DT model follows a series of logical “if-then” declarations to relate outages to the explanatory variables by partitioning the variables into bins until the sum of squares error is minimized. The RF model expands upon the DF by boot-strapping (50% in their case) the data, to produce multiple DFs that are later averaged to make a final prediction. The BT model is an additive tree, building upon smaller tree residuals to increase the overall model outcome. Finally, the ENS model is a simple average of the DF, RF, and BT outage predictions. The ENS model using the full dataset proved to be most skillful. Since, their study’s main focus was to determine which statistical model type would perform best, the most influential explanatory predictors were not discussed in detail; however, the predictor pool included the maximum 10-m wind speed, maximum 10-m wind gust, wind duration above 9, 13, and 18 m s⁻¹, wind gust duration above 18, 27, 36, and 45 m s⁻¹, surface wind stress, maximum precipitation rate, total accumulated precipitation, and soil moisture.

Our study differs from previous power outage studies in two ways: (1) hourly three-dimensional environmental data before and during each power outage was represented through the Rapid Refresh Model (RAP) analyses; and (2) focused on warm season, non-tropical-cyclone-related convection. The following sections explain data and methodology, including the full pool of considered environmental predictors and how they were used to

build a series of GLMs that predict daily power-outage count for each Duke Energy service area.

CHAPTER 3: DATA

a. Duke Energy Service Areas

Figure 1 shows Duke Energy's five service areas, (1) Duke Energy Ohio-Kentucky/Cincinnati (MWC); (2) Duke Energy Indiana (MWI); (3) Duke Energy Florida (FLA); (4) Duke Energy Carolinas (DEC); and (5) Duke Energy Progress (DEP). The service areas encompass 24 million customers within 7.5 million households and/or business. Severe weather type and frequency allows the service areas to be grouped into three climatological territories: (1) Midwest; (2) Florida; and (3) Carolinas.

b. Storm Prediction Center Convective Outlooks

The Storm Prediction Center (SPC), issues broad, multi-day, Convective Outlooks (five times each day at 0100, 1200, 1300, 1630, and 2000 UTC) consisting of graphical forecasts of categorical severe weather risk. The NWS defines a *severe* thunderstorm as any convective storm that produces measured wind gusts greater than 58 mph, hail of at least one inch in diameter, or a tornado. Note that lightning and flooding threats exist with all thunderstorms. The utilized risk categories are as follows: (1) Thunderstorms (TSTM) no severe thunderstorms expected; (2) Marginal (MRGL) isolated severe thunderstorms possible but- limited in duration, coverage and/or intensity; (3) Enhanced (ENH) numerous severe storms possible that will be- more persistent and/or widespread with a few intense; (4) Moderate (MDT) widespread severe storms likely and will be- long-lived, widespread, and intense; and (5) High (HIGH) widespread severe storms expected and will be- long-lived, very-widespread, and particularly intense. The SPC maintains an online archive (<http://www.spc.noaa.gov/>) of these convective outlooks. Duke Energy relies heavily on

the one-day convective outlooks. As such, the archived convective outlooks were used to identify warm season case dates when outage-producing short-fuse thunderstorms were anticipated by Duke Energy forecasters (details provided below).

c. Power Outages

Power outage data was provided by Duke Energy for the case dates (also referred to as event dates) selected within the warm seasons of 2013-2017. The outage data are geolocated points with the following information associated: (1) date; (2) time; (3) latitude/longitude; (4) total customers affected; (5) weather at the time of the repair; (6) diagnosed reason of outage; and (7) any equipment failure.

d. Environmental Data:

The Rapid Refresh Model (RAP) is an hourly assimilated short-range forecasting system designed to help mitigation decision makers in now-casting situations. The RAP model replaced the original hourly assimilated now casting model, the Rapid Update Cycle (RUC) in 2012 and differs in the model component, assimilation component, and horizontal domain (Benjamin et al. 2004, 2016). Updated versions of the RAP became operational in 2014 and 2016. The RAP ingests observations made by surface weather stations, buoy/ships, aircrafts, rawinsondes, radars and satellites and then produces four-dimensional forecast fields of 129 parameters (wind, pressure, temperature, moisture, hydrometeor type/concentration, soil moisture, etc.) with 13-km horizontal resolution, 25 mb vertical resolution and 1 hour temporal resolution forecasted out to 18 hours. Our study period (2013-2017) encompasses three versions of the RAP; however, the horizontal,

vertical, and temporal resolutions of the model remain consistent throughout all three versions.

For all case dates, the analysis fields (i.e. forecast hour 00 for each hour initialization) falling between 1200 UTC of the event date through 1200 UTC of the following day were downloaded. These analysis fields represented the environmental conditions “observed” throughout the 24-hour period encompassing an outage event.

e. Radar Data:

The National Centers for Environmental Information has a radar archive of every Next Generation Radar System (NEXRAD) and Terminal Doppler Weather Radar (TDRW). The NEXRAD system consists of 160 pulse radars that obtain real time radar reflectivity and Doppler velocity observations in five-minute intervals at a 240-km radius from the radar. The radar scans at 14 different elevations scans ranging from 0.5°- 19.5° above the horizontal. The Duke Energy service area is covered by 18 different NEXRAD. The NEXRAD offers a multitude of products at two different data levels: Level-II data consists of raw volumetric reflectivity, Doppler velocity, and spectral width observations; while Level-III data consists of over 50 quality-controlled parameters calculated from the raw volumetric data. The Level III Products used for this project are as follows: (1) the base-level radar reflectivity [product code “DHR”]; (2) the base-level radial velocity [product code “NOV”]; (3) enhanced echo tops [product code “EET”]; (4) the vertically-integrated liquid [product code “DVL”]. The base-level velocity data comes in a high resolution native polar grid (with azimuthal and radial resolutions of 1 degree and 0.25 km, respectively) while the remaining three products come on lower-resolution polar grids (with azimuthal and radial resolutions of 1 degree and 1.0-km, respectively).

CHAPTER 4: METHODS

a. Case Date Selection:

As a reminder, Duke Energy forecasters struggle predicting “short-fuse events” (whereby strong storms are not forecast, yet storms and numerous power outages occur), and “non-events” (whereby strong storms are forecast and occur, but outages are minimal). To identify these cases, the SPC archive of one-day convective outlooks were used to identify warm season (March-October) dates during a recent 5-year period (2013-2017) when storms of various severity (via risk categories discussed above) were forecast, along with NWS severe weather storm reports as verification of whether or not severe storms transpired that day. This information was tabulated for each service area using classic 2×2 contingency tables that showed how often (1) an event was forecast and the event occurred (a “hit”), (2) an event was forecast but the event did not occur - (a “false alarm”), (3) an event was not forecast but the event occurred (a “miss”), and (4) an event was not forecast and the event did not occur (a “correct negative”). Within this context, short fuse-events are equivalent to “misses” and the non-events are equivalent to a “false alarms”.

This study examines dates that fall within three of the four contingency table quadrants. First, “false alarms” (or non-events) consist of dates when the SPC one-day convective outlook forecast SLGT, ENH, MDT or HIGH convection across a Midwest/Carolina (Florida) service area, yet less than 10 (less than 5) severe storm reports were made across the area. The lower threshold for Florida is due to climatological differences in convection and a desire to keep the total number of false alarm dates across the five service areas roughly equivalent. Second, the “misses” (or short fuse-events) consist of dates when SPC one-day convective outlook forecast NONE, TSTM or MRGL convection across a

Midwest/Carolina (Florida) service area, and 10 or more (5 or more) severe storm reports were made across the area. Finally, the third category, known as “hits” (or hit-events), consists of dates when the SPC one-day convective outlook forecast SLGT, ENH, MOD or HIGH convection across Midwest/Carolina (Florida) service area, and 10 or more (5 or more) storm reports were made. These hit-events are often well anticipated by Duke Energy forecasters and therefore were used as the “control” to which “misses” and “false alarms” were compared. Using the above criteria, ~10-15% of all warm-season dates (1225 total of the 5-year period) were classified as either “hits”, “misses” or “false alarms” in each service area. The number of dates per event type can be found in (Table 1). This subset of dates provides a sufficiently large sample size for statistical analysis and model development within a manageable time frame.

b. Quality Control of Outage Data:

The outage data provided by Duke Energy contains all power outages that occurred on that event date, not just outages caused by weather. To achieve the end goal of determining a statistical relationship between storm/-environmental parameters and total weather-related power outages, it is imperative to remove all non-weather-related outages. First, the cause attributed to each outage was screened. All outages directly caused by weather (such as lightning or tree limbs collapsing) and outages indirectly caused by weather (such as cars running into utility poles) were retained. Outages with no documented causation (most likely due to response crews not having time to report the causation of the outage because of the high volume of outage repairs to attend to) were also retained. Second, the remaining outages were compared to animated radar observations to ensure strong storms were present. As a result, a two additional criteria were enforced: (1) the outage had to be

reported within four hours of deep convection (maximum radar reflectivity > 20 dBZ and maximum echo tops > 15 kft) passing within 10 km of the location; and (2) there must have been at least five total reported outages during that hour. The first criterion ensured that the reported outage occurred in a region that had recently experienced deep convection, and the second criterion reduced the requested radar data to a manageable size (< 20 TB).

c. Creation of the Spatial Analysis Grid:

At the request of Duke Energy forecasters and outage repair crews, a 10 × 10 km grid was used for the spatial analysis across the three climatological territories. Duke Energy has found that 10 km is a safe distance by which repair crews can be pre-positioned near active thunderstorms. Moreover a 10 × 10 km grid is a conservative spatial compromise among the various data being analyzed in this study. For example, the spatial resolutions of potential environmental and radar predictors range from 30-m (for land cover classifications) to 13-km (for the hourly model analyses), while other vary (the local population was extracted from census blocks with scale of 1-20 km). Finally, the 10 × 10 km grid reduced the total observational database to less than 20 TB. The grid was generated via the ArcMap Fishnet Spatial Analysis Tool.

d. Acquisition and Processing of Environmental Observations:

The environmental data was obtained through the National Center for Environmental Information's (NCEI) online data portal. A total of 392 case dates during the 2013-2017 period were identified among the combined five service areas, for a total of 9,408 hours of RAP model analyses. The RAP's native grid was also downloaded for each case date, specifically for the extraction of soil moisture. Roughly ~10-15% of the dates were

removed for each service area due to missing files. Next, the model analyses grids were converted from their original form as a “.grib2” file to a “netCDF” to more easily access the data and develop a predictor database for each service area. There were 33 different atmospheric parameters chosen to be investigated in this study (Table 2). Custom software was developed to extract the meteorological parameters directly from the RAP analyses and native grids. Kinematic and thermodynamic variables not readily available through the RAP model output were computed using the python library “SHARPy”- (a sounding and hodograph analysis package; Blumberg et al. 2017). All environmental metrics (Table 2) were assigned to a 10 km spatial analysis point based on the closest RAP model grid point (13-km resolution). As such, metrics computed via SHARPy used the vertical sounding (37 vertical layers) from the closest RAP model grid point.

A brief description of each parameter (also referred to as metrics) can be found in Table 2. Below is a detailed description of each parameter/metric, the typical thresholds used in the operational settings, and the relevance of each parameter to this study.

Divergence at 500mb [DIV500] (s^{-1}) - is a measure of declining mass of air aloft that leads to rising motion at the surface to replace the absent mass. The rising motion at the surface can promote convection as well as cyclogenesis (Lackmann 2012). For example, Watson and Blanchard (1984) concluded that a steady decrease in divergence of 25×10^{-6} over the total area ($>1500 \text{ km}^2$) often produces sufficient surface convergence to initiate deep convection. Divergence is hard to implement in now-casting situations, but its potential during 3-12 h forecast scenarios lead it to be included a possible predictor in this study.

Height of 0°C Isotherm [HGTFRZ] (m) – the height of the freezing level can inform a forecaster about the hail/graupel development layer as well as the depth of the warm layer in which the hail/graupel can melt before reaching the surface. If the freezing level is closer than 650mb then large hail is likely to reach the surface. Moreover, Atkins and Wakimoto (1991) showed that wet microburst-producing storms tended to have higher freezing levels, and thus downdrafts could experience greater negative buoyancy from melting hail and achieve larger magnitudes before reaching the surface. Given that wet microbursts are believed to be a significant cause of power outages, the freezing level was included as potential predictor in this study.

Helicity 3 km [HEL03] ($\text{m}^2 \text{s}^{-2}$) - is storm relative helicity computed between 0-3km AGL via $SRH = \int_0^h k * (V - c) \times \frac{\delta V}{\delta z} dz$ (Davies-Jones et al. 1990), where V is the horizontal velocity, c is the storm motion vector, and h is the uppermost layer height. This parameter is used to measure the potential for a rotating updraft (Thompson et al. 2007). Environments supportive of non-severe (supercell) thunderstorm, rarely (often) exhibited HEL03 less than (greater than) $100 \text{ m}^2 \text{ s}^{-2}$ (Rasmussen and Blanchard 1998). Given that large HEL03 is associated with storms that could produce conditions responsible for power outages, the parameter was included in this study.

Helicity 1 km [HEL01] ($\text{m}^2 \text{s}^{-2}$) – is used to measure the potential for updraft rotation computed in the lowest 1km AGL (Thompson et al. 2007). Rotating updrafts are defining characteristics of supercells that often produce severe straight-line winds, large hail, and strong tornadoes. When HEL01 is greater than $75 \text{ m}^2 \text{ s}^{-2}$ the chance that a supercell will spawn a strong tornado increases drastically (Thompson et al. 2003). Given that large

HEL01 are associated with storms that could produce conditions responsible for power outages, the parameter was selected for investigation in this study.

Lifted Index [LI] (K) - is the temperature difference between a lifted parcel at 500mb and the environmental temperature at 500 mb. As the lifted index becomes more negative the atmosphere is considered to be more unstable. In contrast, if the lifted index is positive the atmosphere is considered to be stable (Galway 1956). One limitation to this parameter is that it only considers buoyancy at one level, which is why this parameter with other buoyancy parameters should be used collectively to get a greater understanding of the buoyancy and updraft potential within that column of the atmosphere. Given that it does provide some indication that convection is possible (i.e. buoyancy exists) the parameter was selected for examination in this study.

Precipitable Water of the Troposphere [PW] (kg m^{-2}) - is a measure of the total water vapor within an atmospheric column. PW is used to estimate water-loading and maximum precipitation amounts if convection were to develop. High PW can lead to greater precipitation intensities that have been connected to stronger microbursts because of the increase in precipitation particles to cool the atmosphere and generate more negative buoyancy (Proctor 1989). The range 1.0" – 1.5" is typically used for hail forecasting, primarily because the water-loading generated with those values does not immediately suppress the updraft, allowing for hail to form. Hail has also been tied to microbursts because of the rapid sublimative cooling that takes place as the hailstones begin to fall, accelerating the downdraft via negative buoyancy (Proctor 1989). In hopes to identify environments conducive for microburst development, this parameter was included in this study.

Relative Humidity Difference [RHBLML] (%) - represents the difference in mean relative humidity between the boundary layer and the 850-500mb layer. Proctor (1989) shows through a series of idealized numerical simulations of microbursts, that the strongest microbursts were those occurring from environments composed of a deep dry-adiabatic layer in the mid-levels and a relatively moist lower level from the surface to mid-levels and relatively moist lower levels. Therefore, large positive (RHBLML) differences (i.e. low-levels are much moister than mid-levels) would be supportive of strong microburst, while small positive or even negative RHBLML difference (i.e. low-levels are drier than mid-levels) would be less supportive. In hopes to identify environments conducive for microburst development, this parameter was included in this study.

700 mb Temperature [TMP700] (K) – is often used as an indicator of whether a strong capping inversion is present and thus will prevent convective development. Forecaster's generally use the rule of thumb that if TMP700 exceeds 10-12°C then the environment is unfavorable for convective development (Bunkers et al. 2010). This is a parameter used to decipher whether or not convective initiation will take place and therefore seemed to be good fit for this study.

700 mb Theta-e [THE700] (K) - is the equivalent potential temperature for a 700 mb environmental parcel. Atkins and Wakimoto (1991) showed that wet microburst-producing storms tended to have lower THE700, and thus entrainment of environmental air into a downdraft could experience greater negative buoyancy from evaporation and achieve larger magnitudes before reaching the surface. Given that wet microburst are believed to be a significant cause of power outages, the THE700 was included as potential predictor in this study.

850 mb Theta-e [THE850] (K) - is the equivalent potential temperature for an 850 mb environmental parcel. Atkins and Wakimoto (1991) showed that wet microburst-producing storms tended to have lower THE850, and thus entrainment of environmental air into a downdraft could experience greater negative buoyancy from evaporation and achieve larger magnitudes before reaching the surface. Given that wet microbursts are believed to be a significant cause of power outages, the THE850 was included as potential predictor in this study.

Vertical Velocity [LLVVEL] (Pa s^{-1}) - is the mean vertical velocity in the 850-500mb layer, whereby positive (negative) values indicate a mean sinking (rising) motion. If the rising motion is great enough, the parcel may become saturated and potentially tap into any available CAPE. Thus, large LLVVEL should provide forecasters with insight as to where deep convection would most likely develop and/or where deep convection would be supported by the synoptic mesoscale environment. Knowing that vertical velocity can indicate area of possible convection it became a parameter of interest for this study.

Surface Winds [WSPSFC] (m s^{-1}) – is the surface wind speed computed by adjusting the wind speed at the lowest model level to 10m AGL. Stronger winds increase the likelihood of falling trees and limbs negatively affecting power lines. Moreover, stronger pre-existing surface winds will be an added effect when storms produce strong straight-line winds (via downdrafts). Including surface wind speed a potential predictor seems like a wise choice.

700 mb Winds [WSP700] (m s^{-1}) – is the environmental wind speed at 700mb. Given that strong convective downdrafts (or microbursts) can descend from mid-levels and

transport low- and mid-level momentum down to the surface, stronger 700 mb wind speeds may result in greater power outage numbers.

850 mb Winds [WSP850] (m s^{-1}) – is the environmental wind speed at 850mb. Given that strong convective downdrafts (or microbursts) can descend from mid-levels and transport low- and mid-level momentum down to the surface, stronger 850 mb wind speeds may result in greater power outage numbers.

Mean Soil Moisture [SOILMS] (fraction) - is the mean moisture through the 0-300 cm layer below the surface. SOILMS is controlled by a one-dimensional planetary boundary layer scheme implemented in the Rapid Refresh Model that measures heat and moisture fluxes between the surface and the atmosphere (Smirnova et al. 1997). Soil moisture is important to power outage forecasting because wetter soils increase the chances of trees and/or utility poles being uprooted (Han et al. 2009; Nateghi et al. 2014).

Bulk Richardson Number [BRN] - is a non-dimensional parameter that incorporates both buoyancy and shear represented by the equation $BRN = \frac{CAPE}{\frac{1}{2}u^2}$. The numerator is used to represent the potential maximum updraft and the denominator represents the potential for an updraft to gain rotational characteristics via the tilting of horizontal vorticity induced by the ambient vertical shear in the lowest 6km. This parameter is used for the prediction of storm type as different combinations of buoyancy and shear have been proven to result in a variety of storm types (Weisman and Klemp 1982). The parameter does have limitations (such as only considering speed shear and not directional; and neglecting the vertical moisture distribution). BRN values between 10 and 45 have been associated with supercells, while smaller (larger) BRN values are symbolic of single cell (multi-cells).

Since storm type is an important piece of this study as more intense supercell and multi-cell storms often yield a larger number of power outages, BRN seemed like a parameter of interest for examination.

Downdraft Convective Available Potential Energy [DCAPE] (J kg^{-1}) - is a measure of the maximum negative buoyancy generated from evaporative cooling that can accelerate a descending parcel to surface. Maximum values of DCAPE are generally located between 2-7 km AGL and will be greater when the mid-levels are extremely dry (Gilmore and Wicker 1998). Evans and Doswell (2001) discuss the significant role of large DCAPE in convective wind storms occurring in weakly forced environments, whereby 0-6 km mean winds are weak and convection is initiated by daytime heating. In these types of events DCAPE often exceeds 1000 J kg^{-1} . Due to DCAPE's direct relation to downdraft strength, the parameter was selected for this study.

Effective Inflow Depth [EFFDEPTH] (m) – is the lowest contiguous layer of parcels that satisfies the criteria of $\text{CAPE} > 100 \text{ J kg}^{-1}$ and $\text{CIN} > -250 \text{ J kg}^{-1}$. The first criteria is to identify a parcel that contains enough buoyancy to preserve the updraft, while the second criteria ensures a parcel that will not endure excessive convective inhibition resulting in eradication the updraft (Thompson et al. 2007). Despite EFFDEPTH not varying amongst storm type (i.e. significantly tornadic, weakly tornadic and non-tornadic) the parameter was chosen for this study because they have not been tested against different event types.

Effective Inflow Base Height [EFFBASE] (m) – is the first parcel moving upward from the surface to satisfy the requirement of $\text{CAPE} > 100 \text{ J kg}^{-1}$ and $\text{CIN} > -250 \text{ J kg}^{-1}$ (Thompson et al. 2007). Despite EFFBASE not varying amongst storm type (i.e.

significantly tornadic, weakly tornadic and non-tornadic) the parameter was chosen for this study because they have not been tested against different event types.

Effective Inflow Top Height [EFFTOP] (m) – is the last parcel that contiguously from EFFBASE that meets the requirements of $CAPE > 100 \text{ J kg}^{-1}$ and $CIN > -250 \text{ J kg}^{-1}$ from EFFBASE (Thompson et al. 2007). Despite EFFTOP not varying amongst storm type (i.e. significantly tornadic, weakly tornadic and non-tornadic) the parameter was chosen for this study because they have not been tested against different event types.

Microburst Parameter [MBURST] - is a non-dimensional parameter developed at the SPC to predict the likelihood of a microburst. It is derived from the weighted sum of the SBCAPE, SBLI, 0-3 km lapse rates, vertical totals (850-500 mb temperature difference), DCAPE and PW. SBCAPE is used to identify the possibility of strong convection and SBLI is used to infer mid-level instability where downdrafts often development. The 0-3 km lapse rates and vertical totals help identify low-level environments that can support both strong updraft and downdrafts (i.e. a downdraft will accelerate faster if it descends into warmer air). DCAPE is used to identify environments supportive of strong evaporatively-driven downdrafts; and PW is used to infer the potential water-loading contribution to any microbursts. Environments resulting in a MBURST value between 3 and 4 are considered to host a “slight chance” for microburst development. If the MBURST value is between 5 and 8 there is a “chance” for microburst development and anything greater than 9, microbursts are “likely”. Details about MBURST can be found at (https://www.spc.noaa.gov/exper/mesoanalysis/help/help_mbcpl.html).

Mixed Layer Convective Available Potential Energy [MLCAPE] (J kg^{-1}) - is the total area between an environmental temperature and the temperature of parcel being lifted

moist adiabatically from the level of free convection to the equilibrium level. The parcel in this case is lifted using the average temperature and average dew point temperature measurements in the lowest 100 mb. The positive area shows where the parcel is warmer than the surrounding environment, thus identifying positively buoyant air capable of accelerating an updraft parcel. Evans and Doswell (2001) found that during weakly forced thunderstorm events (i.e. daytime heating thunderstorms) that MLCAPE often exceeded 1500 J kg^{-1} . Given that MLCAPE is a traditional parameter to determine whether convection will initiate, the parameter was chosen for investigation in this study.

Mixed Layer Convective Inhibition [MLCIN] (J kg^{-1}) – is the total area between the environmental temperature and parcel temperature that is being lifted dry adiabatically until the lifting condensation level and then moist adiabatically until the level of free convection is reached. The parcel in this case is lifted using the average temperature and average dew point temperature measurements in the lowest 100 mb. The negative area given shows where the parcel is cooler than the surrounding environment, thus identifying negatively buoyant air capable of decelerating an updraft parcel. This is a parameter used to decipher whether or not convective initiation will take place and therefore seemed to be good fit for this study.

Most Unstable Convective Available Potential Energy [MUCAPE] (J kg^{-1}) – is the total area between an environmental temperature and the temperature of parcel being lifted moist adiabatically from the level of free convection to the equilibrium level. The parcel in this case is lifted from the temperature and dew point temperature measurements in the lowest 300 mb that result in the greatest instability (greatest area). The positive area shows where the parcel is warmer than the surrounding environment, thus identifying positively

buoyant air capable of accelerating an updraft parcel. Evans and Doswell (2001) found that during weakly forced thunderstorm events (i.e. daytime heating thunderstorms) that MUCAPE often exceeded 2600 J kg^{-1} . Given that MUCAPE is a traditional parameter to determine whether convection will initiate, the parameter was chosen for investigation in this study.

Most Unstable Convective Inhibition [MUCIN] - is the total area between the environmental temperature and parcel temperature that is being lifted dry adiabatically until the lifting condensation level and then moist adiabatically until the level of free convection is reached. The parcel in this case is lifted from the temperature and dew point temperature measurements in the lowest 300 mb that result in the greatest instability (greatest area) for MUCAPE. The negative area given shows where the parcel is cooler than the surrounding environment, thus identifying negatively buoyant air capable of decelerating an updraft parcel. This is a parameter used to decipher whether or not convective initiation will take place and therefore seemed to be good fit for this study.

Supercell Composite Parameter [SCP] - is a non-dimensional metric designed to distinguish between supercell and non-supercell environments. The parameter was derived from soundings near supercells exhibited one or more radar reflectivity structures common in supercells (i.e. hook echoes, inflow notches, etc.), azimuthal shear of 20 m s^{-1} or greater in the $0.5^\circ - 1.5^\circ$ elevation angles with a horizontal dimension less than 10 km, and finally showed cyclonic shear for greater than 30 minutes. The SCP is a product of $(\text{MUCAPE}/1000 \text{ J kg}^{-1}) \times (0 - 3 \text{ km SRH}/100 \text{ m}^2 \text{ s}^{-2}) \times (\text{BRN shear}/40 \text{ m}^2 \text{ s}^{-2})$. The component thresholds were determined by the distributions of significantly tornadic, weakly tornadic and non-tornadic events in the dataset. Thompson et al. (2003) found that when the SCP

value was greater than 1, the environment was extremely conducive for supercell development, while SCP values less than 1 were common among non-supercell days (Thompson et al 2003). Supercells can cause a significant destruction to infrastructure through the rear-flank downdraft and potentially a tornado, therefore this parameter of interest for this study.

SHERBE [SHERBE] - is a non-dimensional metric used to discriminate between severe and non-severe thunderstorms in high shear, low CAPE (HSLC) environments. SHERBE is the product of $(EBWD / 27 \text{ m s}^{-1}) \times (LLLR / 5.2 \text{ K km}^{-1}) \times (LR75 / 5.6 \text{ K km}^{-1})$, where EBWD is the effective bulk wind difference, LLLR is the lapse rate 0-3 km, and LR75 is the lapse rate from 700-500mb (Sherburn and Parker 2014). One reason as to why this parameter is successful in HSLC environments is because the composite is not based on CAPE, unlike many other composite parameters designed to predict severe weather. By not including CAPE into its calculation it's able to identify severe potential in low CAPE environments. Instead, to identify instability it uses lapse rates. Steeper lapse rates have been associated with stronger downdrafts and then damaging winds (Johns and Hirt 1987) if combined with stronger winds aloft (represented by EBWD in this case) via downward momentum transfer. SHERBE values greater than 1 indicate a chance of severe weather. Given that this parameter is particularly helpful discriminating between severe and non-severe thunderstorms in HSLC environments, which are common across the Carolinas (i.e. two of Duke Energy's service area), it was selected as a parameter of interest for this study.

Significant Hail Parameter [SHP] - SHP is a non-dimensional parameter used to predict the probability hail sizes considered to be significant hail which is characterized by a diameter greater than 2 inches (Hales 1993). The parameter uses the product of

MUCAPE, Mixing Ratio of MU-Parcel, the 700-500 mb lapse rate, 500 mb temperature and SHR06, all divided by 42,000,000 to predict if there is a chance of hail sizes exceeding 2 inch in diameter. The product of CAPE and shear have been used as a proxy to estimate updraft duration and hail production (Brimelow et al 2002). SHP values greater than 1.0 indicate locations that are favorable for hail development greater than 2 inches in diameter (https://www.spc.noaa.gov/sfctest/help/help_sigh.html). Considering the significant hail is indicative of a strong updraft (i.e. strong convection), this parameter becomes of interest for this study.

Significant Tornado Parameter [STP] - The significant tornado parameter is designed to distinguish between significantly tornadic and non-tornadic supercell environments (Thompson et al. 2003). The metric is the product of $(MLCAPE/ 1000 \text{ J kg}^{-1}) \times (SHR06 / 20 \text{ m s}^{-1}) \times (HEL01/ 100 \text{ m}^2 \text{ s}^{-2}) \times [(2000 - MLLCL)/1500 \text{ m}]$ and values of ≥ 1 are a good guideline in identifying an environment conducive for significant tornadic supercell development (Thompson et al. 2003). Given that tornadoes are capable of causing power outages this parameter was selected for examination in this study.

Shear 0-1 km [SHR01] (kts) – the difference between the surface winds and the winds at 1 km AGL. Stronger low-level shear tends to be associated with strong convective wind storms (Johns and Hirt 1987). Stronger shear also results in a heightened chance of new cell development. Given that greater SHR01 can lead to convective wind storms and new cell development, it seemed to be a good fit for this study.

Shear 0-3 km [SHR03] (kts) – the difference between the surface and the winds at 3 km AGL. Evans and Doswell (2001) found that SHR03 often ranged between 4-8 kts for

derechos events. Given that derecho events are a catalyst for power outages (since, by definition, they produce widespread microbursts), SHR03 was selected for this study.

Shear 0-6 km [SHR06] (kts) – the difference between the surface and the winds at 6 km AGL. This term can help in the prediction of storm type and strength as shear is a major mechanism in storm generation. Low shear environments often result in ordinary cell convection, low-to-moderate shear environments generally result in multicellular development, and moderate-to-high shear environments typically produce supercells (Weisman and Klemp 1982). SHR06 has also been evaluated for derecho events and found that values generally range from 5-10 kts (Evans and Doswell 2001). Given that derecho events are more than capable of producing power outages, this parameter was selected for this study.

Wind Damage Parameter [WNDG] - is a non-dimensional composite parameter used to identify regions with heightened chances for wind damage outflow from thunderstorms (Blumberg et al. 2017). The parameter was designed to address warm season convection caused by daytime heating with minimum forcing. The parameter is a product of $(MLCAPE / 2000 \text{ J kg}^{-1}) \times (LR_{0-3\text{km}} / 9^\circ\text{C km}^{-1}) \times (\bar{U}_{1.0-3.5\text{km}} / 15 \text{ m s}^{-1}) \times (50 \text{ J kg}^{-1} + MLCINH / 40 \text{ J kg}^{-1})$. Values greater than one highlight a region of increased wind damage potential and values less than one are associated with environments with less wind damage potential. Given that strong winds are major cause of power outages, this parameter was selected for this study.

e. Stratification of Dates:

A useful guidance tool for Duke Energy forecasters, who are tasked each day with estimating the total number of weather-induced outages within a given service area, would be multiple-linear regression model (or equations) developed from prior events when particular storm types (i.e. pulse thunderstorms, squall lines, supercell, etc.) or severe weather (strong winds, large hail, tornadoes) occurred. To develop such event-specific models, the event dates must be stratified accordingly for each of the five service areas. The first stratification divided the dates into two seasons, “warm” and “hot”, to account for the seasonal difference in this study’s definition of the meteorological warm season (March 1st – October 31st). The “hot” season is considered to be the traditional meteorological summer months, June, July and August. The warm season is comprised of the remaining months, March, April, May, September, and October, except in the Carolina service areas where August dates are analyzed in both the “hot” and the “warm” seasons. These seasons were adopted to ensure each season contained enough (usually greater than 10) case dates to permit meaningful statistical analysis.

Next, a second stratification by convective mode was performed since, the storm type is largely a function of the atmospheric conditions present. Based on a survey of the observed convection in all service areas, six different convective modes were considered: pulse thunderstorms (PULSE), front driven thunderstorms (FRNT), scattered multicells (SCAT), squall lines (SQLL), supercells (SUPR) and none (NONE). The dominant convective mode for a given case date / service area was determined from the animated radar reflectivity fields during the 3-h period leading up to and encompassing the hour with

the maximum number of outages were reported outages for that area. The criteria to distinguish between the six convective modes are as follows.

Pulse Convection (PULSE): Deep convection consisting of multiple distinct convective cells with reflectivity maxima $> 30\text{-}50$ dBZ but no clear mesoscale organization. This pattern was most common on hot summer dates when no synoptic-scale front passed through/near the service area.

Frontal (FRNT): Deep convection oriented parallel/along an advancing synoptic-scale front with nearly contiguous reflectivity > 30 dBZ but few embedded convective cells exhibiting maximum reflectivity > 50 dBZ. This pattern was most common in the warm months (spring and fall) along cold fronts that (a) were moving northwest to southeast across the service area; (b) were accompanied by a moderate to strong pre-frontal low-level jet.

Scattered Multicells (SCAT): Deep convection consisting of multiple distinct cells with reflectivity maximum $> 40\text{-}50$ dBZ, but the cells were either (a) not aligned in a quasi-linear pattern with contiguous reflectivity > 40 dBZ or (b) did not exhibit a major axis greater than 100 km in length. This pattern often occurred when the convection passing through the service area was either: (a) in the early organizational stages before upscale growth into a squall line; or (b) on the warm side of a synoptic front (that was also located in service area).

Squall Line (SQLL): Deep convection consisting of nearly contiguous reflectivity > 40 dBZ oriented in a quasi-linear pattern with a major axis > 100 km in length. Individual cells embedded within the line often exhibited maximum reflectivities > 50 dBZ. Most

squall lines exhibited a trailing stratiform (TS) or parallel stratiform (PS) structure with embedded bowing segments and moved northwest to southeast either ahead of a cold front or along a warm/ stationary front.

Supercell (SUPER): Deep convection consists of multiple distinct (isolated) supercells with reflectivity maxima > 50 dBZ and clear hook echoes (or inflow notches).

No Deep Convection (NONE): No deep convection passing through the service area was observed by radar. Any reported outages were most likely a result of planned repairs or accidents and were unrelated to deep convection.

Finally, a third stratification was made with regard to the dominant (or most numerous) severe weather type (“wind”, “hail”, or “tornado” categories) reported on that event date based on the “filtered” storm report archive available from the Storm Prediction Center. If no dominant severe weather type occurred on a given day (i.e. no severe weather was reported or similar number of reports were made for two or more types), then that date was placed in a ‘no dominant severe weather type’ category. Table 3 summarizes the dates categorized by dominant severe weather type for each service area. The hail and tornado categories were combined into one category to provide a large enough sample of case dates to maintain the integrity of the statistical analysis. Overall, this stratification process (2 seasons \times 6 convective modes \times 3 severe weather type categories, Figure 2) resulted in 36 different possible classifications for each event date.

f. Summary Statistics

For each metric and case date, a file was created containing the metric’s value at each spatial analysis grid point for each hour of the day (from 12 UTC on the case date through

12 UTC on the next date). The Midwest service area (MWC and MWI) has 890 grid points, the Florida service area (FLA) has 703 grid points and the Carolina service area (DEC and DEP) was covered by 1590 spatial analysis grid points. Each Midwest case date file contained 21,360 data points (i.e. 890 spatial analysis grid points \times 24 hours), while each Florida case date files contained 16,872 data points, and each Carolina case date file contained 38,160 data points. The large magnitude of data for event date necessitated summary statistics for each of Duke's service area to represent the entire service area on a given event date.

In order to consolidate the number of data points and simultaneously identify diurnal differences across an area, four summary statistics were computed for each the day (12 - 24 UTC) and night (00-12 UTC) periods: (1) the day/night maximum of the hourly maximum (MAX-MAX); (2) the day/night average of the hourly maximum (AVG-MAX); (3) the day/night maximum of the hourly average (MAX-AVG); and (4) the day/night average of the hourly average (AVG-AVG). The events were broken into day and night for two reasons. First, atmospheric instability exhibits a strong diurnal cycle driven by low-level daytime solar heating and nocturnal cooling. For example, Gropp and Davenport (2018) analyzed changes in thermodynamic and kinematic forecast parameters during the nocturnal transition (1-2 hours after sunset), and the most impacted parameter was MUCIN (which experienced an increase, reflecting a stabilization of the atmosphere after sunset). Second, the day and night separation aligns well with Duke Energy's forecasters decisions as to whether or not to keep repair crews on call through the evening and into the overnight hours.

g. GLM Development for Total Number of Power Outage Estimation

If our stratified database of event dates were infinitely large, 360 unique, optimized, multiple linear regression prediction models could be developed for the five service areas in each of the seasons (“warm” and “hot”), each dominant convective mode (PULSE, FRNT, SCAT, SPLL, SUPER, and NONE), each dominant severe weather type category (wind, hail / tornado, and no dominant type) and each time (day/night) using the following general form:

$$(1) \quad y = \beta_0 + \beta_1x_1 + \beta_2x_2 + \cdots + \beta_kx_k + \epsilon$$

- where, y is the number of outages for a given event; x_k are the optimal predictor metrics (see Table 2); β_k are the estimators for each optimal metric; β_0 is the intercept; and ϵ represent average residual errors (which under the assumption of normality are assumed to be zero; Montgomery et al. 2013).

However, our finite database combined with multiple stratifications results in some categories containing few (or no) event dates. To address this limitation while maintaining statistical integrity with regard to sample size, prediction models were only developed for those categories with a sample size of 10 or more. For such categories, a unique model was optimized via the backward elimination method outlined in Cerruti and Decker (2012) using the JMP statistical software. The process began by randomly removing 20 percent of event dates (to be able to repeat the process later to compute average estimator values) and then relating the ten predictors most- correlated with outages into one regression equation. Then, the least-skillful predictor with the largest p-value was removed, and a new regression equation was developed. This process continued until all estimator p-values

were below 0.05 (or a confidence level above 95%). Next, the remaining predictors were tested for multi-collinearity, which is undesired because it will wrongfully influence the coefficient of determination (r-square) and makes it difficult to separate the influence of predictors on the response (Wilks 2006). However, because it is common for the metrics used in this study to be elevated on severe weather days, the metrics were categorized by what they predict (Table 4). If any two or more predictors within the same category (or as an element in a composite parameter) were highly correlated ($r > 0.30$), only the predictor with the highest correlation to the area's outage count was retained. This process was performed for each summary statistic for all categories that qualified for regression development (i.e. sample size > 10). The summary statistic that produced a model with the greatest r-square for that specific category was chosen as the optimal model. Lastly, a final set of mean estimators, p-values, and adjusted r-squares were determined for each optimal model by retraining the model a total of ten times (after randomly removing 20% of the data). The mean estimators (among the 10 iterations) were adopted for the final "operational model" since they should provide a more stable prediction (analogous to an ensemble prediction outperforming the prediction of single ensemble member).

h. GLM Validation

The operational models were validated using a technique referred to as reservoir sampling where a subset of k samples (approximately 80% of the dataset) is randomly selected from n samples (the whole dataset). The random sample, k , was then used to test the linear regression equation by calculating the Mean Absolute Error (MAE) (Equation 2), Root Mean Square Error (RMSE) (Equation 3), Percent Error (Equation 4), and the Bias (Equation 5):

$$(2) MAE = \frac{1}{n} \sum_{i=1}^n |y_i - \hat{y}_i|$$

$$(3) RMSE = \sqrt{\frac{1}{n} \sum_{i=1}^n (y_i - \hat{y}_i)^2}$$

$$(4) Percent Error = \frac{1}{n} \sum_{i=1}^n \left(\frac{|\hat{y}_i - y_i|}{y_i} \times 100 \right)$$

$$(5) Bias = \frac{1}{n} \sum_{i=1}^n \hat{y}_i - y$$

-where, y is the observed outages on the event date, \hat{y} is the predicted outages for the event date and n is the number of times the reservoir sampling was repeated, which in this case was 500 times to construct an array of error statistics for that category's regression equation. The error statistics array was visualized via box-whiskers plots showing the mean error statistics and 95% confidence interval about the mean.

CHAPTER 5: RESULTS AND DISCUSSION

It is envisioned that the multiple-linear regression equations developed here will become a tool for the forecasters at Duke Energy to estimate the total number of power outages likely to take place across each of their five service areas. The forecaster will be able to choose which equation(s) to use based on the service area, season, anticipated dominant convective mode, primary severe weather threat, and diurnal period. All optimal operational equations (whereby estimator p-values consistently remained below 0.05 during repeated trials with different training sets) are displayed in Table 5 along with the stratification category, time (D = day or N = night), summary statistic used, mean estimators from the ten trials, and the corresponding mean adjusted r-square. Below, all optimal models will be discussed within the context of the optimal predictors included in each equation, the relative importance among the predictors for a given equation, and the physical connection(s) through which each predictor would logically increase/decrease the total number of power outages for the given scenario.

a. Midwest Cincinnati (MWC)

The full database for the MWC service area consisted of 104 event dates that, when stratified by the process discussed in the methods section, led to eight categories (MWC-HOT-SCAT-WIND, MWC-HOT-SQLL-WIND, MWC-HOT-SCAT, MWC-HOT-SQLL, MWC-HOT, MWC-WARM-SCAT, MWC-WARM-SQLL and MWC-WARM) with sufficient dates (≥ 10) to build both day and night multiple-linear regression equation – for a total of *sixteen* possible regression equations. The number of dates for each category are listed in Table 6a and 6b. While four of these categories (MWC-HOT-SCAT, MWC-HOT-

SQLL, MWC-WARM-SCAT, and MWC-HOT) had sufficient sample sizes for model development, no statistically significant estimators (i.e. the p-values were not consistently below 0.05) could be identified among any of the daytime or nighttime summary statistics – reducing the pool of potential regression equations by eight. Also, despite some initial success with the MWC-HOT-SCAT-WIND-DAY category using the AVG-MAX, and MAX-AVG summary statistics, repeated trials with different training sets could not produce statistically significant estimators. The same failure was encountered for the MWC-HOT-SQLL-WIND-NIGHT category.

As a result, the following discussion focuses on the *six* remaining categories for which statistically significant estimators could be consistently identified. The models discussed below used summary statistic that exhibited the largest adjusted r-square in the original trial. Often, the disregarded summary statistics identified similar estimators but with lower adjusted r-squares. Thus, the reoccurrence of estimators in multiple summary statistics increases confidence that a relationship exists between the estimator and power outages.

i. MWC Model Discussion

Before attempting to develop an equation for the **MWC-HOT-SCAT-WIND-NIGHT** events, a log transformation was applied to the power outage counts to reduce skewness in the distribution (Figure 3). The nocturnal outages could then be significantly estimated using the summary statistics MAX-AVG of WSP850 (Table 5, Index 1) with a resulting mean adjusted r-square of 0.510 (indicating that the model approximately explains a little more than one-half of the total variability in nocturnal outages). Surprisingly, the WSP850 estimator was negative, implying that weaker 850 mb wind

speeds, produce more power outages. Given that most power outages are caused by strong surface winds, such relationship implies that simple downward advection of strong ambient winds from low- to mid-level was not the source of strong surface winds on dates when scattered storms were the dominant convective mode. Rather, numerous observational studies of wet microbursts (Caracena and Maier 1987; Wakimoto and Bringi 1988; Tuttle et al. 1989; Kingsmill and Wakimoto 1991; Atkins and Wakimoto 1991, Straka and Anderson 1993) have noted weak vertical shear magnitudes (i.e. weak 850 mb winds) in the local environment. Likewise, numerical simulations of wet microbursts (Srivastava 1987; Proctor 1988, 1989; Straka and Anderson 1993) suggest that weaker vertical shear will reduce the net entrainment allowing downdrafts to achieve greater velocities (via hydrometeor waterloading, melting, and evaporation cooling) before reaching the surface. Moreover, the weaker vertical shear is consistent with the dominant convective mode of these dates – scattered storms (consisting of single cells and disorganized multicells).

An optimal model for the **MWC-HOT-SQLL-WIND-DAY** category was identified using the MAX-MAX summary statistics of WNDG, SOILMS, and SHR01 (Table 5, Index 2) to predict the log-transform of power outages (Figure 4) with a mean adjusted r-square of 0.709. Interestingly, the WNDG estimator was negative, suggesting that more power outages were observed when the WNDG was small (even though larger WNDG are supposed to indicate an increased chance for wind damage). Unfortunately, no plausible explanation can be identified for the negative relationship between WNDG and power outages. The physical linkages could be explained through a series of carefully-designed experiments using mesoscale numerical models but that is outside the scope of the current project. In contrast, the estimators for SOILMS and SHR01 were both positive,

implying that more outages were observed when the soil was moister and low-level wind shear was greater. Larger SOILMS positively influences power outages because trees are more likely to be uprooted and fall onto power-lines (McRoberts et al. 2016). The presence of larger SHR01 magnitudes promotes initiation and maintenance of intense long-lived squall lines. In a manner consistent with RKW theory (Rotunno et al. 1988) larger magnitudes of low-level shear (i.e. SHR01) promote greater balance between the horizontal vorticity generated by the ambient low-level shear and the horizontal vorticity generated by the storm's cold pool, leading to the regular production of upright updrafts and convective line maintenance. Moreover, long-lived squall lines often produce an intense mid-level rear inflow jet (RIJ) that collides with the updraft. Upon collision, the RIJ is forced downward, creating surface winds strong enough to uproot trees and damage power lines (Markowski and Richardson 2010).

Additionally, a larger SHR01 implies strong low-level winds whereby simple downward momentum transport by weak/moderate downdrafts can significantly increase surface wind speeds (i.e. increasing the likelihood of power outages). Indeed, numerous studies of intense squall lines (Duke and Rogash 1992, Johns 1993; Wakimoto et al. 2006) have documented strong low-level shear in the local environments. Finally, it should be noted that the magnitude of the SOILMS and SHR01 estimators are one tenth and one third, respectively, of the WNDG estimator indicating that their contribution to total power outages are less than the WNDG parameter.

The power outages for the **MWC-WARM-SQLL-DAY** scenario can best be estimated using the AVG-MAX statistics of WNDG and SHR06 (Table 5, Index 3) with an adjusted r-square of 0.701. A log transformation was performed on the outage count

dataset for this category (Figure 5). In this case, both estimators were positively correlated to power outages with WNDG exhibiting the stronger correlation. Given that the WNDG parameter is computed from MLCAPE, MLCIN, the 0-3 km lapse rates, and the average wind speed in the 1.0 – 3.5 km AGL layer, one would expect larger WNDG values (which indicate a greater chance of strong surface winds) during the warm months (i.e. spring and autumn) when low-level lapse rates and vertical shear are climatologically larger (Sherburn and Parker 2014). Likewise, larger SHR06 magnitudes support squall line growth and maintenance by providing sufficient updraft tilt such that cold-pool-producing downdrafts will reach the surface well away from the updraft initiation region (Markowski and Richardson 2010). As noted above, such long-lived squall lines often produce a strong midlevel RIJ and numerous RIJ-driven downdrafts that can significantly increase surface winds and power outages.

Power outages for the **MWC-WARM-SQLL-NIGHT** events are best estimated using the MAX-MAX statistics for PW and HGTFRZ with a mean adjusted r-square of 0.425 (Table 5, Index 4). In this case, a log transformation was applied to the outage count data to reduce skewness (Figure 6). Of the two predictors, PW exhibited the larger estimator with a positive correlation to power outages. Numerous observational studies (Caracena and Maier 1987; Johns 1993; Atkins and Wakimoto 1991) and numerical studies (Srivastiva 1987; Coniglio et al. 2011) have shown the larger PW environments support both longer-lived squall lines (due to fewer negative impacts upon increased entrainment of dry environmental air) and more intense downdrafts (due to increased hydrometeor production and downdraft acceleration via waterloading), thereby increasing the likelihood that a given squall line will produce strong surface winds and multiple power outages over

a large area. In contrast to PW, the HGTFRZ was negatively correlated with power outages meaning more outages occurred when the freezing/melting level was at a lower altitude. First given that downdraft accelerations are forced (in part) by the melting and evaporation of hydrometeors, Srivastava (1987) demonstrated that lower HGTFRZs in moist environments (such as the MWC area) would support stronger/colder downdrafts reaching the surface due to complete hydrometeor melting but incomplete evaporation (i.e. the downdrafts experience moist-adiabatic descent down to the surface). In contrast, drier environments with higher HGTFRZs would support weaker/warmer downdrafts due to complete hydrometeor melting and evaporation followed by some dry-adiabatic descent before reaching the surface. Second, warm-season squall lines are often initiated and maintained by prominent cold or stationary fronts, such that the smaller MAX-MAX magnitudes for HGTFRZ may simply serve as an analog for frontal strength (with lower HGTFRZ on the cold side).

For the broader category of **MWC-WARM-DAY**, an optimal regression equation was identified using the AVG-MAX statistics for WSP700 (Table 5, Index 5) after a log transformation was applied to the outage count data (Figure 7). However, with a mean adjusted r-square of 0.264, this relationship is less robust than those found for more specific convective modes. Nevertheless, WSP700 was positively correlated to power outages, meaning more power outages occurred when the mid-level winds were stronger. As discussed above, such relationship is consistent with simple downward momentum transport by convective downdrafts.

Finally, for the broad **MWC-WARM-NIGHT** category, a statistically-significant equation was found using the MAX-MAX summary statistic for DIV500 (Table 5, Index

6) after a log transformation was applied to reduce skewness in the outage count data (Figure 8). As with its daytime counterpart, this relationship (with a mean adjusted r-square of 0.175) is less robust than the models developed for specific convective modes. The positive correlation between DIV500 and outages counts implies that more outages occurred when stronger mid-level divergence was present. Midlevel divergence stimulates rising motion from below, therefore providing an environmental lifting mechanism that can support and maintain deep convection. First larger divergence supports stronger and wider updrafts, which in turn promotes greater total ice (i.e. ice crystals, graupel and hail) production (McCual et al. 2009). As these ice particles begin to fall, melting/evaporation induced cooling and hydrometeor water loading will play a significant role in the generation of intense downdrafts (Srivastava 1987). Second, stronger and wider updrafts promote appreciable charge separation within a given storm (Blyth et al 2001), and thereby increase the potential for frequent and intense cloud -to-ground lighting capable of damaging energy infrastructure.

ii. MWC Error Analysis

The four error statistics used to evaluate the models are mean absolute error (MAE), root mean square error (RMSE), percent error, and bias, each of which of been computed 500 times using a random 80% of the dataset. Ideally, the distribution of the errors would be narrow, indicating consistent errors that can be easily addressed when using models to forecast outages. In contrast, wide distributions would indicate the errors were not consistent, either due to insufficient sample size that captures the full spectrum of environmental variability or outliers affecting the error statistic. Ideally, the MAE, RMSE, percent errors, and biases, values would be as close to zero as possible. However, in

accordance with Duke Energy's outage repair/ staffing protocol (i.e. practical purposes), errors and biases on the order of 50 are considered acceptable.

When interpreting the MAE (Figure 9a) four of six models displayed acceptable errors [**MWC-HOT-SCAT-WIND-NIGHT (1)**, **MWC-WARM-SQLL-NIGHT (4)**, **MWC-WARM-DAY (5)**, and **MWC-WARM-NIGHT (6)**]. The two models with unacceptable errors were **MWC-HOT-SQLL-WIND-DAY (2)** and **MWC-WARM-SQLL-DAY (3)** as both distributions were wide with means near 120 and 85 outages, respectively. Interestingly, these two models are based on daytime squall line cases and had the largest adjusted r-squares. The RMSE (Figure 9b) showed similar results, however **MWC-WARM-DAY (5)** joined **MWC-HOT-SQLL-WIND-DAY (2)** and **MWC-WARM-SQLL-DAY (3)** in the unacceptable category. All nighttime models had acceptable RMSE distributions. All mean percent errors (Figure 9c) equaled or exceeded 50%, but means were consistently smaller for the nighttime models (ranging from (50-60%)) than daytime models (ranging from 62% to 75%). Lastly, all biases (Figure 9d) were negative, implying a consistent under-prediction, but the mean biases were smaller among the nighttime models (ranging from 5-10 outages) than the daytime models (ranging from 25-90 outages).

Overall, the error analysis for the six MWC models suggests that the nighttime models can predict total outage counts within the acceptable ± 50 outage threshold, while the daytime models provide less reliable under-predictions of total outage count. Sample sizes were similar among all daytime/nighttime model pairs, so the large (unacceptable) daytime errors cannot be attributed to smaller sample sizes. Rather, it is important to recognize that the nighttime outage count distributions were narrow (the majority were less

than 50 and few exceeded 100), while the daytime distributions were much wider (a majority exceeded 50 with some exceeding 500). As a result, the daytime models were trained to predict more outages over a wider range, and thus, are more susceptible to large errors.

b. Midwest Indiana (MWI)

The MWI database comprised 142 event dates, that when stratified, led to twelve categories (MWI-HOT-SCAT-WIND, MWI-HOT-SQLL-WIND, MWI-HOT-SCAT, MWI-HOT-SQLL, MWI-HOT, MWI-WARM-SCAT-WIND, MWI-WARM-SQLL-WIND, MWI-WARM-SCAT-HAIL-TOR, MWI-WARM-SQLL-HAIL-TOR, MWI-WARM-SCAT, MWI-WARM-SQLL, and MWI-WARM) with sufficient events (≥ 10) to construct both day and night multiple-linear regression equations – for a total of *twenty-four* possible regression equations. The number of dates for each category are cataloged in Tables 7a and 7b. The MWI-WARM-SQLL-HAIL-TOR had a sufficient number of events for model development; however no statistically significant estimators could be determined for either the daytime or nighttime summary statistics – lessening the pool of potential regression equations by two. The same shortcoming was experienced during the trials of the MWI-HOT-SCAT-DAY, MWI-HOT-SQLL-DAY, MWI-HOT-DAY, MWI-WARM-SCAT-NIGHT, and MWI-WARM-NIGHT categories.

The following discussion is focused on the remaining *eighteen* scenarios that during regression development, consistently produced statistically significant estimators. However, for the sake of brevity and avoidance of reiteration, detailed discussion will be limited to those models whereby either (1) a plausible physical connection between an

optimal predictor and the total number of outages has *not* been discussed previously, or (2) a different potentially-relevant physical connection exists between an optimal predictor and the outage count for the specific category. Otherwise, the reader should consult Table 5 regarding the optimal summary statistic, optimal predictors, and adjusted r-squared value for a specific model (event category). Likewise, the relative importance among the optimal predictors can be readily determined by comparing respective estimator magnitudes (the largest is the most influential) for the given model.

i. MWI Model Discussion

Power outages that occurred in the **MWI-HOT-SCAT-WIND-DAY** scenario, could be significantly estimated using the MAX-AVG summary statistic of SHR01 (Table 5, Index 7) with a weak mean adjusted r-square of 0.114. Regardless of the faint relationship, a negative dependency ensued between SHR01 and power outages, implying that a larger magnitude of SHR01 led to less outages. The weaker vertical shear aids in the strengthening of a descending downdraft by reducing the downdrafts exposure to drier environmental air and allowing the downdraft to descend moist-adiabatically consequently generating stronger winds at the surface that are capable of producing power outages (Srivastava 1987). These weaker vertical shear settings are quite common for scattered multicells providing some additional insurance for the relationship.

Before attempting to estimate power outages in the **MWI-HOT-SCAT-WIND-NIGHT** setting, a log transformation was performed on the response dataset to reduce skewness (Figure 10). The nocturnal outages were significantly estimated by MAX-MAX summary statistics WNDG and HEL03 (Table 5, Index 8) with a mean adjusted r-square of 0.487. A positive relationship was observed between both the WNDG and HEL03

parameters with power outages, indicating that in the event that there were larger magnitudes of either parameter, more power outages transpired. A WNDG parameter greater than 1 indicates an increased chance of wind damage at the surface so it is not surprising that larger values of WNDG caused more power outages. Larger HEL03 values indicate regions with large amounts of potential streamwise vorticity can be tilted and stretched to develop mid-level rotation (Davies-Jones 1984). Rotating updrafts tend to be more resilient, supporting longer-lived storms that increase the likelihood of strong/frequent downdraft formation through a combination of water-loading and evaporative/melting cooling (Thompson et al. 2007).

The next scenario evaluated was the **MWI-HOT-SQLL-WIND-DAY** events. The power outages in this setting were best estimated using the MAX-MAX summary statistic of LLVVEL and DCAPE with a mean adjusted r-square of 0.301 (Table 5, Index 9). A positive relationship was found between LLVVEL and outage count (recall LLVVEL has units of Pa s^{-1} , such that positive values imply sinking motion and a negative value imply rising motion). Given that the statistical model is based on the MAX-MAX statistics, such a relationship implies that strong mesoscale descent was present somewhere in the service area. When strong ambient descent interacts with convection, the mesoscale descent can become locally enhanced through evaporative cooling, increasing the likelihood of downdrafts reaching the surface and negatively impacting trees and utility infrastructure. As for DCAPE, by definition greater values indicate greater negative buoyancy available to accelerate air down to the surface (Gilmore and Wicker 1998), and thus DCAPE's physical connection to increased outages numbers is straightforward.

MWI-HOT-SQLL-WIND-NIGHT outages underwent a log transformation to reduce skewness prior to model development (Figure 11). This led to statistically significant relationships between power outages and both SHP and HEL01 using MAX-MAX summary statistics (Table 5, Index 10) with a mean adjusted r-square of 0.457. The SHP and HEL01 parameters both expressed positive relationships with power outages. While larger values of SHP indicate a greater chance of large diameter hail, it also indicates an environment supportive of strong updrafts capable of maintaining large amounts of lofted hydrometeor mass, and thus, the formation of strong downdrafts enhanced through water-loading. Proctor (1989) showed that hail-driven microbursts are more intense (upon reaching the surface) than “ordinary” hydrometeor-driven microbursts for two reasons. First, hail has such a large terminal velocity and particle density, thus the negative buoyancy generated by melting occurs over a deeper. Second, because melting occurs more quickly at the warmer low-levels, less depletion of negative buoyancy (due to compressional warming) occurs within the descending microburst. With regard to HEL01, positive influence on power outages was discussed above for Equation 8, and will not be reiterated here.

The power outages that occurred during a **MWI-HOT-SCAT-NIGHT** situation could best be estimated by the MAX-MAX summary statistics of WNDG and LLVVEL, with a mean adjusted r-square of 0.491 (Table 5, Index 11). Both parameters were positively related to power outages numbers. The positive influence of WNDG and LLVVEL on power outages was discussed above for Equations 3 and 9, respectively.

When examining the power outages generated during an **MWI-HOT-SQLL-NIGHT** scenario a log transformation was applied to the outage count dataset to reduce skewness

(Figure 12). After transformation, power outages could be predicted by the MAX-MAX summary statistics of SHP and HEL03 (Table 5, Index 12). Interestingly, similar parameters were identified for MWI-HOT-SQLL-WIND-NIGHT (Index 10, which used SHP and HEL01), however this linear regression model performed slightly better with a mean adjusted r-square of 0.472. The larger sample size may have improved the model fit. The positive relationships exhibited by SHP and HEL03 were explained above for Equations 10 and 8, respectively.

In the broad category of **MWI-HOT-NIGHT** power outages were best identified by the AVG-MAX statistics of LLVVEL and HEL01 with a mean adjusted r-square of 0.418 (Table 5, Index 13). Both parameters were positively related to outages, and physical explanations for such relationships were provided above in discussions of Equations 9 and 8, respectively.

Switching to the warm season events, the **MWI-WARM-SCAT-WIND-DAY** power outages were best predicted by the AVG-MAX of MBURST with a mean adjusted r-square of 0.462 (Table 5, Index 14). The positive relationship between MBURST and power outages demonstrates that MBRUST can perform well (as designed) under certain circumstances. However, it should be noted that MBURST was identified as an optimal predictor for only 7% (4 of 58) of developed regression models among the five service areas. Therefore, the MBURST parameter should be used judiciously by Duke Energy forecasters.

The power outages that resulted on the dates within the **MWI-WARM-SCAT-HAIL-TOR-DAY** category were best predicted by the MAX-MAX statistics of SHP and resulted in a mean adjusted r-square of 0.316 (Table 5, Index 15). The resulting positive relationship

implies that elevated SHP values support a larger number of outages. A full discussion of its physical description can be found above with Equation 10. The fact the SHP performs well for the case dates when large hail was the dominant severe weather type, despite using SHP to forecast power outages, provides further support for the physical explanation.

When evaluating the nocturnal outages for **MWI-WARM-SCAT-HAIL-TOR-NIGHT**, a log transformation was applied to reduce the skewness (Figure 13), and a robust optimal regression equation was identified using the AVG-AVG statistics of the LLVVEL with 0.808 mean adjusted r-square (Table 5, Index 16). In contrast to previous models, a negative relationship between LLVVEL and outages and LLVVEL was identified, implying greater area-averaged ascent supports more power outages. As a result, the physical explanation is rather straightforward and consistent with classic convective theory. Low level rising motion is an important contributor to convection initiation as it allows for warm-moist air in the boundary layer (or just above the nocturnal boundary) to be lifted to saturation and more-readily procure positive buoyancy by reaching the Level of Free Convection (LFC) (Markowski and Richardson 2010). Such environments tend to produce numerous intense storms with strong updrafts, downdrafts, and frequent cloud-to-ground lightning, increasing the likelihood of power infrastructure damage.

The next category examined was **MWI-WARM-SQLL-WIND-DAY**, where the AVG-AVG statistics of MUCIN provided the best prediction of power outages (Table 5, Index 17) after a log transformation was applied to reduce skewness (Figure 14). The negative relationship, whereby CIN corresponded to more outages, exhibited a mean adjusted r-square of 0.320. At first glance, this relationship seems counter-intuitive because greater MUCIN should limit convective development and thus minimize outage numbers.

However, the model is based on the AVG-AVG statistic (i.e. the average of the hourly average over the whole study area) and thus encompasses locations where the severe-wind-producing squall line has already passed. Behind each squall line is a large statically-stable cold pool (i.e. large negative CIN) that has been cultivated by an ensemble of cold convective downdrafts (and microbursts) that both maintain that squall line (Markowski and Richardson 2010) and produce significant damage to power infrastructure.

In the nighttime version of this setting (**MWI-WARM-SQLL-WIND-NIGHT**), a log transformation was applied to reduce the skewness (Figure 15), and outages could be best predicted by the AVG-MAX statistic of the SHP, LI, and HEL01 (Table 5, Index 18) with a mean adjusted r-square of 0.551. The LI and HEL01 both manifested a negative relationship, while SHP expressed a positive relationship, with power outages. As for the positive SHP relationship, a plausible explanation was discussed above with Equation 10. The LI was negatively correlated to outages, meaning more negative LI values were associated with more outages. A negative LI also suggests the presence of midlevel instability that can amplify updrafts and hydrometeor production, which subsequently supports strong downdrafts and microbursts via water-loading and melting/evaporational (Srivastava 1987). Regarding the negative HEL01 relationship (implying smaller HEL01 corresponds to more outages), smaller HEL01 magnitudes often coincides with weaker low-level shear. As noted above, downdraft entrainment is reduced when vertical shear is weak (Proctor 1989), allowing stronger downdrafts to reach the surface.

Power outages for **MWI-WARM-SCAT-DAY** can be best estimated by a linear regression equation relating the MAX-AVG statistics of SHP with a mean adjusted r-

square of 0.301 (Table 5, Index 19). The physical explanation supporting a positive relationship between SHP and power outages was explained above with Equation 10.

An optimal model for the **MWI-WARM-SCAT-NIGHT** category was determined using the MAX-AVG statistics of the LLVVEL (Table 5, Index 20) after a log transformation was applied to the outage dataset to reduce skewness (Figure 16). The model's mean adjusted r-square was 0.342. Discussion on the physical explanation supporting a negative relationship between LLVVEL and power outages can be found with Equation 16.

In the case of **MWI-WARM-SQLL-DAY**, power outages could be best predicted by the AVG-AVG statistics of WSP700 and RHBLML (Table 5, Index 21) with an adjusted r-square of 0.279 for the optimal model. The positive relationship between WSP700 and power outages can be explained through simple downward momentum transfer via convective downdrafts. The relationship between RHBLML is less straightforward. Large RHBLML magnitudes signify relatively moist low-levels (which supports convective development) and dry mid-levels (which supports evaporational cooling and stronger downdrafts). Moreover, a numerical simulation by Proctor (1989) demonstrated that convective environments with dry mid-level often exhibit a more dry-adiabatic layer near the mid-level melting layer (mid-levels), which would enhance mid-level downdraft acceleration and increase the likelihood that downdrafts reach lower levels. Then, upon reaching the moister low-levels, the instability between a downdraft parcel and the ambient environment is enhanced via the virtual temperature effect (Srivastava 1987, Proctor 1989, and Atkins and Wakimoto 1991).

The successful linear regression equation developed for the **MWI-WARM-SQLL-NIGHT** category relied on a log transformation of outage counts to remove skewness (Figure 17). The power outages in this scenario were estimated best by the MAX-AVG summary statistics of MUCIN and MLCAPE, resulting in a mean adjusted r-square of 0.333 (Table 5, Index 22). Both estimators exhibited positive relationships with power outages meaning when MLCAPE was larger and MUCIN was smaller (closer to zero) more outages transpired. MLCAPE represents the positive buoyancy to sustain an updraft needed for convection development. Greater values of MLCAPE lead to stronger updrafts that promote greater hydrometeor production needed for intense downdraft generation (McCaul et al. 2009). Likewise, the smaller value of MUCIN allow deep convection to be more easily achievable (Markowski and Richardson 2010). Bluestein et al. (1987) showed that there was a significant difference between severe and non-severe squall lines, whereby severe squall lines were associated with larger CAPE and smaller CIN.

For the vast category of **MWI-WARM-DAY**, power outages were best estimated by the MAX-AVG statistics of WSP700, SHP, and RHBLML (Table 5, Index 23) with a mean adjusted r-square of 0.323 for the optimal model. All predictor exhibited positive relationships with power outages, and the corresponding physical explanations can be found above with Equations 5, 10, and 21, respectively.

The final scenario investigated for the Midwest Indiana service area was **MWI-WARM-NIGHT**, where power outages were best predicted using the MAX-MAX statistics for THE850, SHR06, and MUCIN (Table 5, Index 24) resulting in mean adjusted r-square of 0.216. All estimators were positively-correlated with power outages. For THE850, Atkins and Wakimoto (1991) found that larger differences between the

equivalent potential temperatures at the surface and the midlevel minimum (generally located between 650-500 mb) would produce the strongest microbursts (assuming the downdraft emanated from the minimum potential temperature level). Such equivalent potential temperature difference is analogous to DCAPE in that it provides a measure of the available negative buoyancy a downdraft parcel would experience upon descent. While, the 850 mb level is often above the surface, large THE850 often coincides with large surface values (and thus large differences from the midlevel minimum) revealing an unstable atmosphere supportive of strong downdrafts. The physical explanations for the positive relationships between SHR06 and MUCIN with power outages has been discussed above with Equations 3 and 22, respectively.

ii. MWI Error Analysis

For the MWI service area, 16 of 18 models exhibited mean MAEs less than the 50-outage threshold and are deemed acceptable (see Figures 18a, 19a, and 20a). Most impressive were the **MWI-HOT-SCAT-WIND-NIGHT (8)**, **MWI-HOT-SCAT-NIGHT (11)**, **MWI-WARM-SAT-HAIL-TOR-DAY (15)**, **MWI-WARM-SCAR-HAIL-TOR-NIGHT (16)**, **MWI-WARM-SQLL-WIND-DAY (17)**, and **MWI-WARM-SCAT-NIGHT (20)** models, with means less than 25 outages and interquartile ranges less than 5 outages. Note that two of the six are daytime models with relatively small sample sizes. The two unacceptable models were **MWI-HOT-SQLL-WIND-DAY (9)** and **MWI-WARM-SQLL-WIND-NIGHT (18)** with mean MAEs near 70 and 90 outages, respectively. Most notably, these two models consisted of case dates when squall line convection and severe winds were dominant, but were developed from opposite

summary statistics (MAX-MAX and AVG-AVG, respectively) using relatively small sample sizes (30 and 10, respectively).

Regarding the RMSE (see Figures 18b, 19b, and 20b), 14 of 18 models exhibited acceptable mean errors less than the 50-outage threshold. As before, the same six models exhibited exceptionally small mean errors (less than 30 outages). The four models that failed to produce acceptable RMSE were the **MWI-HOT-SQLL-WIND-DAY (9)**, **MWI-HOT-NIGHT (13)**, **MWI-WARM-SQLL-WIND-NIGHT (18)**, and **MWI-WARM-SQLL-NIGHT (22)** with means near 90, 75, 125, and 55, respectively. Common characteristics among this unacceptable group were that (a) three are nighttime models and (b) three are squall line models. The only unacceptable model in which the larger RMSE could be attributed to a relatively smaller sample size is **MWI-WARM-SQLL-WIND-NIGHT (18)**, the rest had adequate sample sizes.

Regarding the percent error (see Figures 18c, 19c, and 20c), 15 of 18 models exhibited means less than 60%. Yet again, **MWI-WARM-SCAT-HAIL-TOR-NIGHT (16)** outperformed the other models in this service area with a mean of 23% and an interquartile range less than 5%. Of the three models with percent errors greater than 70%, **MWI-HOT-SQLL-WIND-DAY (9)**, **MWI-HOT-SCAT-NIGHT (11)**, and **MWI-WARM-SQLL-WIND-NIGHT (18)** two exhibited large interquartile ranges exceeding 15% (about means 70-80%), suggesting the models suffer from inconsistency. The **MWI-WARM-SQLL-WIND-NIGHT (18)** had an extremely narrow distribution, which usually is a good sign but not when the mean percent error is 99%. As noted above, the poor error statistics for this model is likely from the small sample size.

Most MWI models (16 of 18) exhibited mean biases smaller than ± 50 outages (see Figures 18d, 19d, and 20d). Of the two models with an unacceptable bias, **MWI-HOT-NIGHT (13)** exhibited a narrow distribution centered on a mean under-prediction of 50 outages, while **MWI-WARM-SQLL-WIND-NIGHT (18)** had a wide asymmetrical distribution with a mean near -95 outages. A bias is not a huge issue because it is easy for a forecaster to account for it by adding or subtracting outages based on the bias but when there is inconsistency on what that bias is, it makes discouraging to implement in an operational setting.

Overall, based on all four error statistics, the best performing daytime and nighttime models were **MWI-WARM-SQLL-WIND-DAY (17)** and **MWI-WARM-SCAT-HAIL-TOR-NIGHT (16)**, respectively. For both models not only were the MAE, RMSE, and percent errors small, but bias distributions were narrow and centered on -10 and zero, respectively. In contrast, the worst performing daytime and nighttime models were **MWI-HOT-SQLL-WIND-DAY (9)** and **MWI-WARM-SQLL-WIND-NIGHT (18)**, and these two models should be used with caution in an operational setting.

c. Florida (FLA)

The entire FLA database had a total of 130 event dates, that when classified, resulted in eleven categories (FLA-HOT-PULSE-WIND, FLA-HOT-SCAT-WIND, FLA-HOT-PULSE, FLA-HOT-SCAT, FLA-HOT, FLA-WARM-SCAT-WIND, FLA-WARM-SQLL-WIND, FLA-WARM-PULSE, FLA-WARM-SCAT, FLA-WARM-SQLL, FLA-WARM) with enough dates to attempt regression development on both day and nighttime summary statistics (Tables 8a and 8b). Of the *twenty-two* regression attempts, only *sixteen* regression models were developed for the FLA region owing to the lack of statistically

significant estimators in the FLA-HOT-PULSE-WIND (DAY and NIGHT), FLA-HOT-PULSE (DAY and NIGHT), FLA-HOT-NIGHT, FLA-WARM-PULSE-NIGHT. For this reason, the remaining discussion focuses on the *sixteen* scenarios that produced statistically significant estimators.

i. FLA Model Discussion

The first successful model was developed based off of the events in **FLA-HOT-SCAT-WIND-DAY** where power outages shared a positive relationship with the MAX-AVG of SHR06 (Table 5, Index 25). This relationship ensued a mean adjusted r-square of 0.493. Larger magnitudes of SHR06 help aid in separating the updraft and the downdraft, consequently increasing the longevity of the deep convection. Due to the separation of the opposing vertical drafts the multicell system can develop a strong, evaporatively-cooled driven gust front (i.e. damaging winds) triggering new cell development and thus the cyclical strengthening of the cold pool occurs (Markowski and Richardson 2010).

The nocturnal power outages of this scenario (**FLA-HOT-SCAT-WIND-NIGHT**) underwent a log transformation prior to regression development to reduce the skewness of the dataset (Figure 21). After the transformation, a linear equation was determined using the AVG-AVG of DCAPE, with a mean adjusted r-square of 0.546 (Table 5, Index 26). Surprisingly, a negative correlation between DCAPE and power outages existed. The likely cause of this negative relationship is moist mid-levels (consistent with the more tropical character of the service area), which would result in smaller DCAPE (a parameter designed to estimate the intensity of an *evaporatively-cooled* downdraft originating from a drier midlevel; Gilmore and Wicker 1998). As a result, the dominant downdraft forcing shifts to water-loading, which is consistent with the greater precipitable water and hydrometeor

concentrations often observed in tropical climates. It should be noted that the proficiency of precipitation drag in forcing strong downdrafts was first noted by Byers and Braham (1948) during the Florida-based Thunderstorm Project.

The **FLA-HOT-SCAT-DAY** events required a log transformation to the power outage dataset to reduce the skewness (Figure 22). The transformed outages were best estimated by the MAX-AVG of SHP and resulted in a mean adjusted r-square of 0.316 (Table 5, Index 27). The positive relationship explanation between power outages and SHP can be found in the explanation for Equation 10.

The following scenario investigated was **FLA-HOT-SCAT-NIGHT** where a log transformation was performed in order to reduce skewness in the power outage dataset (Figure 23). The power outages were then appraised by the MAX-MAX of MUCAPE (Table 5, Index 28). The correlation was summarized by a mean adjusted r-square of 0.303. A negative relationship was established between power outages and MUCAPE, suggesting that more power outages occurred when MUCAPE was smaller. While this seems counter-intuitive, this relationship is most likely a consequence of the nocturnal timeframe when lower CAPE magnitudes are expected (Gropp and Davenport 2018). The outages were likely caused by remnant daytime multicells that had sufficiently mature gust fronts to sustain convection even though MUCAPE values were decreasing due to the nocturnal stabilization.

The all-encompassing category of **FLA-HOT**, was best explained by the MAX-AVG of DIV500 (Table 5, Index 29), after a log transformation was applied to the skewed power-outage count dataset (Figure 24). The DIV500 showed a negative correlation with power outages, implying that strong convergence at 500 mb would result in more power outages.

Multiple observational case studies of microburst-producing storms (Peterson 1984; Caracena and Maier 1987; Wakimoto and Bringi 1988; Roberts and Wilson 1989, Kingsmill and Wakimoto 1991) have noted the presence of strong midlevel convergence. While it's not clear whether the midlevel convergence initiates an ensemble of microbursts via entrainment or is a mass-continuity response to microburst initiation, the presence of midlevel convergence is a tell-tale sign of microburst-producing storms. Our multiyear results are consistent with these case studies.

Moving forward to the warm season, the scenario **FLA-WARM-SCAT-WIND-DAY** led to a linear regression equation that estimated the log transformed power outages (Figure 25) by the MAX-AVG of RHBLML (Table 5, Index 30). This model displayed a mean adjusted r-square of 0.402. A negative correlation was established between RHBLML and power outages, meaning that a small RHBLML resulted in less power outages. While many studies have indicated that moist low-levels and dry mid-levels (large RHBLML) conceive strong, evaporatively-cooled driven microbursts, small RHBLML indicate regions that have moist mid-levels where microbursts are still capable of being produced via waterloading. Such results are broadly consistent with optimal negative relationship between Florida outage and DCAPE discussed above (Equation 26).

The **FLA-WARM-SCAT-WIND-NIGHT** power outages underwent a log transformation to adjust the skewness of the dataset prior to model development (Figure 26). The outages in this case were estimated by the MAX-AVG of MLCIN and MBURST (Table 5, Index 31) with a mean adjusted r-square of 0.715. The negative relationship between MLCIN and power outages, indicates that when MLCIN is larger (further from zero), more power outages transpired. Since the physical effects of MLCIN are virtually as

MUCIN, this relationship can be summarized by the explanation provided for Equation 17. MBURST displayed a positive relationship with power outages, implying that more power outages took place when there were higher values for MBURST. This positive relationship is described with Equation 14.

The power outages that resulted on dates within the **FLA-WARM-SQLL-WIND-DAY** category experienced a log transformation to reduce skewness within the dataset (Figure 27) and then were best estimated by the AVG-MAX of WSP700 and MBURST (Table 5, Index 32). The equation is summarized with a mean adjust r-square of 0.605. Both of the estimators, WSP700 and MBURST exhibited positive relationships with power outages, indicating higher magnitudes of either estimator resulted in more power outages. The corresponding explanations of these relationships can be found with Equations 5 and 14, respectively.

The nocturnal outages in this setting (**FLA-WARM-SQLL-WIND-NIGHT**), also underwent a log transformation to reduce skewness (Figure 28). These outages were predicted best by the MAX-AVG of MLCAPE with an adjusted r-square of 0.392 (Table 5, Index 33). This positive relationship between MLCAPE and power outages, suggests that more outages occurred when MLCAPE was larger. Given that the ultimate effects of MLCAPE on the downdraft are fundamentally the same as MUCAPE, the explanation given with Equation 22 is an adequate representation of this relationship.

An optimal model was developed for the power outages on **FLA-WARM-PULSE-DAY** using log transformed outage counts to reduce skewness (Figure 29) that were best estimated by the MAX-MAX statistics of SHR03, resulting in a mean adjusted r-square of 0.392 (Table 5, Index 34). The positive relationship indicates that when SHR03 was larger,

more power outages arose. Typically, strong SHR03 does not correspond with ordinary, pulse thunderstorms, however strong shear in the lower levels of the atmosphere aids in the separation of the updraft and the downdraft allowing the cell to mature to create a strong downdraft via evaporative cooling and waterloading.

The **FLA-WARM-SCAT-DAY** endured a log transformation and then was best estimated by the MAX-MAX of SOILMS and PW (Table 5, Index 35). The equation resulted in a mean adjusted r-square of 0.393. The two estimators both demonstrated positive relationships with power outages implying that when either estimator was larger, more outages transpired. These positive relationships are explained with Equations 2 and 4, respectively.

The power outages that occurred on dates within the **FLA-WARM-SCAT-NIGHT** tier experienced a log transformation (Figure 30) before being best related to the MAX-AVG of PW with a mean adjusted r-square of 0.303 (Table 5, Index 36). This positive relationship implies larger values of PW resulted in a greater number of power outages. For more information regarding this relationship, refer to the discussion for Equation 4.

FLA-WARM-SQLL-DAY outages were required to undergo a log transformation prior to model development (Figure 31). The outages ended up being most related to the AVG-AVG of SHR01 and MBURST, and resulted in a mean adjusted r-square of 0.599 (Table 5, Index 37). Both of the estimators exhibited positive relationships with power outages indicating large magnitudes of either estimator led to a greater number of outages. A description of these relationships can be found with Equations 2 and 14.

The **FLA-WARM-SQLL-NIGHT** scenario power outages experienced a log transformation and then were best estimated by the AVG-AVG of MLCAPE with an average adjusted r-square of 0.338 (Table 5, Index 38). The relationship between MLCAPE and power outages was positive implying that more outages took place when MLCAPE was larger. This relationship was discussed with Equation 22.

Outages that occurred during the **FLA-WARM-DAY** season were skewed so a log transformation was applied (Figure 32). This led to the development of a model relating power outages to the AVG-MAX of SOILMS and PW with an average adjusted r-square of 0.281 (Table 5, Index 39). In fact, the same summary statistic and estimators were the most reliable at predicting nocturnal power outages (**FLA-WARM-NIGHT**) as well! The nocturnal equation resulted in a mean adjusted r-square of 0.297 (Table 5, Index 40). The estimators in both equations displayed positive relationships with power outages signifying that more power outages resulted from larger values of SOILMS and PW. The discussion of these relationships can be found with Equations 2 and 4, respectively.

ii. **FLA Error Analysis**

For the FLA service area, 11 of 16 models exhibited mean MAEs less than the 50-outage threshold and were considered to be acceptable (see Figures 33a, 34a, and 35a). Multiple exceptional models, **FLA-HOT-WIND-NIGHT (26)**, **FLA-HOT-SCAT-NIGHT (28)**, **FLA-HOT-DAY (29)**, **FLA-WARM-SQLL-WIND-DAY (32)**, **FLA-WARM-PULSE-DAY (34)**, and **FLA-WARM-SCAT-NIGHT (36)**, possessed means less than 35 outages with interquartile ranges less than 7 outages. The 5 unacceptable models that exceeded the 50-outage threshold were **FLA-HOT-SCAT-WIND-DAY (25)**, **FLA-WARM-SCAT-WIND-NIGHT (31)**, **FLA-WARM-SQLL-DAY (37)**, **FLA-**

WARM-DAY (39), and **FLA-WARM-NIGHT (40)** with mean MAEs near 55, 65, 52, 55, and 90 outages, respectively. Among this unacceptable group, (a) four were daytime models, (b) four were warm season models, and (c) two were scattered multicell models. Only **FLA-HOT-SCAT-WIND-DAY (25)**, **FLA-WARM-SCAT-WIND-NIGHT (31)**, and **FLA-WARM-SQLL-DAY (37)** could potentially be attributed to a small sample size, however the other two models were developed from a large sample of 58 case dates.

When using the RMSE error statistic over half the models (9 out of 16) exceeded the 50-outage threshold and qualified as unacceptable (see Figures 33b, 34b, and 35b), however none of the exceptionally acceptable models made the leap into the unacceptable category. The original five unacceptable models discussed above were included in this group, but so were the **FLA-WARM-SCAT-WIND-DAY (30)**, **FLA-WARM-SQLL-WIND-NIGHT (33)**, **FLA-WARM-SCAT-DAY (35)**, and **FLA-WARM-SQLL-NIGHT (38)** models. Interestingly, eight of the nine unacceptable models were for the warm season. Of the three acceptable warm models, both **FLA-WARM-SQLL-WIND-DAY (32)** and **FLA-WARM-SCAT-NIGHT (36)** exhibited wide asymmetrical distributions with interquartile ranges of 10 outages, suggesting inconsistency.

Regarding the percent errors (see Figure 33c, 34c, and 35c) 13 of 16 models displayed means less than 40%. More notably, **FLA-HOT-WIND-NIGHT (26)**, **FLA-HOT-SCAT-DAY (27)**, **FLA-HOT-DAY (29)**, and **FLA-WARM-PULSE-DAY (34)**, had percent error means below 30% and interquartile ranges less than 5%. As for the three models that exhibited percent errors above 40%, **FLA-HOT-SCAT-WIND-DAY (25)**, **FLA-WARM-SCAT-NIGHT (36)**, and **FLA-WARM-NIGHT (40)**, their means were 46%, 45%, and 41%, respectively.

Most models (15 of 16) exhibited mean biases smaller than ± 50 outages (see Figures 33d, 34d, and 35d). The one with an unacceptable bias was the **FLA-WARM-SQLL-WIND-DAY (32)** with a wide asymmetrical distribution with a mean near -60 outages and an interquartile range of 15 outages. An inconsistent bias can be difficult to account for in an operational setting.

In conclusion the four error statistics highlight **FLA-WARM-PULSE-DAY (34)** and **FLA-HOT-WIND-NIGHT (26)** as the most outstanding daytime and nighttime models, respectively. While **FLA-WARM-PULSE-DAY (34)** may not have had the smallest mean MAE and mean RMSE, the model exhibited the narrowest symmetrical error distribution, implying consistency. The worst performing daytime and nighttime models were the **FLA-HOT-SCAT-WIND-DAY (25)**, and **FLA-WARM-NIGHT (40)**, therefore forecasters should be vigilant when using them.

d. Carolina West (DEC)

The DEC event database contained 155 event dates, that when stratified, created thirteen categories (DEC-HOT-PULSE-WIND, DEC-HOT-SCAT-WIND, DEC-HOT-SQLL-WIND, DEC-HOT-PULSE, DEC-HOT-SCAT, DEC-HOT-SQLL, DEC-HOT, DEC-WARM-SCAT-WIND, DEC-WARM-SQLL-WIND, DEC-WARM-PULSE, DEC-WARM-SCAT, DEC-WARM-SQLL, DEC-WARM) with a sufficient number of events (>10) to attempt building both day and night multiple-linear regression equations – for a potential of *twenty-six* equation. Tables 9a and 9b list the number of dates that fell into each classification. No regression equation could be determined for either the daytime or nighttime DEC-HOT-PULSE-WIND, DEC-HOT-PULSE, DEC-HOT-SCAT, or DEC-WARM-PULSE categories due to inconsistent statistically-significant estimators,

lessening the number of equations by eight. This same defect was encountered when attempting to build an equation for DEC-HOT-SCAT-WIND-NIGHT, DEC-HOT-SQLL-WIND-DAY, DEC-HOT-SQLL-DAY, DEC-HOT-NIGHT, DEC-WARM-SCAT-WIND-NIGHT, DEC-WARM-SQLL-WIND-NIGHT, DEC-WARM-SCAT-NIGHT, DEC-WARM-SQLL-NIGHT, and DEC-WARM-NIGHT. Thus, the following discussion will centralize on the remaining *nine* categories that consistently provided statistically significant estimators.

i. DEC Model Discussion

The **DEC-HOT-SCAT-WIND-DAY** event category required a log transformation to the outage dataset prior to model development (Figure 36). The outages were best estimated by the MAX-AVG of LI and DCAPE with an average adjusted r-square of 0.243 (Table 5, Index 41). Both of the estimators were negatively correlated with power outages. The negative relationship between LI and power outages would imply that the more negative (further from zero) LI, would create more power outages. The more negative the LI is, the more unstable atmosphere is and more conducive for strong, deep convection. The negative relationship between DCAPE and power outages was discussed with Equation 26.

The following successful model was created under the **DEC-HOT-SQLL-WIND-NIGHT** category where a log transformation was performed on the outage dataset to reduce skewness (Figure 37). This led to a regression equation that estimates the number of power outages using the MAX-MAX of the SHP with a mean adjusted r-square of 0.481 (Table 5, Index 42). A description regarding the positive relationship between power outages and SHP can be found with Equation 10.

When the dominant severe weather type is not considered, the category of **DEC-HOT-SQLL-NIGHT** was able to be estimated by the MAX-MAX of DCAPE (Table 5, Index 43) with a mean adjusted r-square of 0.361, after a log transformation was applied to the power outage dataset (Figure 38). The equation exhibited a positive relationship between power outages and DCAPE, which was thoroughly discussed with Equation 9.

The broad **DEC-HOT-DAY** tier underwent a log-transformation prior to model development to reduce the skewness in the power outage dataset (Figure 39). The power outages, in this case, were predicted best by the AVG-AVG of the LLVVEL and DIV500 with a mean adjusted r-square of 0.210 (Table 5, Index 44). Both of the estimators were negatively related to power outages meaning that when the service area was subjected to strong ascending air or the air at 500 was converging (instead of diverging), more outages took place. These negative relationships were discussed with Equations 16 and 29, respectively.

Moving into the DEC warm season categories, the **DEC-WARM-SCAT-WIND-DAY** case dates created a successful model relating power outages to the AVG-AVG of MUCAPE (Table 5, Index 45). The equation coincided with an average adjusted r-square of 0.438 and displayed a positive relationship between power outages and MUCAPE, implying larger values of MUCAPE resulted in more power outages. This positive relationship between MUCAPE and power outages is fundamentally the same as the positive relationship between MLCAPE and power outages explained with Equation 22.

In the case of **DEC-WARM-SQLL-WIND-DAY**, a log transformation was applied to the power outage dataset (Figure 40). The scenario led to a regression equation relating power outages to the AVG-AVG of HEL01 with a mean adjusted r-square of 0.743

(Table 5, Index 46). The positive relationship between HEL01 and power outages indicates that more power outages took place when HEL01 was of a larger magnitude. This positive relationship is discussed with Equation 8.

The next situation evaluated was the **DEC-WARM-SCAT-DAY**, where a log transformation was applied to the power outage dataset to reduce skewness (Figure 41). The linear regression equation estimates power outages by using the AVG-AVG of LLVVEL and LI with a mean adjusted r-square of 0.629 (Table 5, Index 47). This equation showed both estimators negatively correlated to outages implying that strong ascending air (more negative LLVVEL) or more unstable air (more negative LI) led to more power outages. These two estimator's negative relationships with power outages are elaborated with Equations 16 and 18, respectively.

In the case of **DEC-WARM-SQLL-DAY**, the power outages required a log transformation to reduce skewness in the dataset (Figure 42). The outages were then best predicted by MAX-AVG of WSP700 and MUCIN with a mean adjusted r-square of 0.439 (Table 5, Index 48). Both estimators resulted in positive relationships with power outages indicating that when WSP700 was a large magnitude and/or when MUCIN was small (close to zero), more outages transpired. The positive relationships between WSP700 and MUCIN with power outages is evaluated with Equations 5 and 22, respectively.

The final equation for the DEC service area, was the broad **DEC-WARM-DAY**, where the power outage dataset was subjected to a log transformation prior to model development (Figure 43). This equation related power outages to the MAX-AVG of the WSPSFC and LLVVEL with an adjusted r-square of 0.401 (Table 5, Index 49). The WSPSFC exhibited a positive relationship with power outages, indicating that when winds

were stronger at the surface, more outages occurred. This relationship is consistent with the theory that strong surface winds cause of trees and utility poles to be uprooted. The LLVVEL displayed a negative relationship with power outages, which is discussed in detail with Equation 16.

ii. DEC Error Analysis

The DEC service area had 2 of 9 models demonstrate acceptable MAE means; the remaining 7 models produced MAE means greater than the 50-outage threshold (see Figures 44a and 45a). The acceptable models were **DEC-WARM-SCAT-WIND-DAY (45)** and **DEC-WARM-NIGHT (49)** with means near 35 and 45 outages, respectively. The only commonality between those models is that they are both warm season models. The unacceptable models could be viewed as two sub-categories: slightly unacceptable (<100 outages) and extremely unacceptable (>100 outages). The slightly unacceptable models include **DEC-HOT-SCAT-WIND-DAY (41)**, **DEC-HOT-SQLL-WIND-NIGHT (42)**, **DEC-HOT-DAY (44)**, and **DEC-WARM-NIGHT (49)**. Most notably, three of these four models are from the hot season and only two [**DEC-HOT-SCAT-WIND-DAY (41)**, and **DEC-HOT-SQLL-WIND-NIGHT (42)**] may have larger MAE errors due to their relatively small sample size. Likewise, all three extremely unacceptable models [**DEC-HOT-SQLL-NIGHT (43)**, **DEC-WARM-SQLL-WIND-DAY (46)**, and **DEC-WARM-SQLL-DAY (48)**] had sample sizes (<20).

The RMSE distributions (see Figures 44b and, 45b) suggest that all of models failed to produce acceptable errors. However, three models [**DEC-HOT-SQLL-WIND-NIGHT (42)**, **DEC-WARM-SCAT-WIND (45)**, and **DEC-WARM-SCAT-DAY (47)**] exhibited narrow distributions with means of 75, 55, and 65, respectively. In contrast, the **DEC-**

HOT-SQLL-NIGHT (43) and **DEC-HOT-DAY (44)** models demonstrated extremely large mean RMSEs of 450 and 200, respectively.

Regarding the percent error (see Figures 44c and 45c), 7 of 9 models exhibited means less than 50%. Not only were the means small for those seven models [**DEC-HOT-SCAT-WIND-DAY (41)**, **DEC-HOT-DAY (44)**, **DEC-WARM-SCAT-WIND-DAY (45)**, **DEC-WARM-SQLL-WIND-DAY (46)**, **DEC-WARM-SCAT-DAY (47)**, **DEC-WARM-SQLL-DAY (48)**, and **DEC-WARM-NIGHT (49)**], but the distributions were narrow with interquartile ranges less than 5%. Of the two models with large percent error, one [**DEC-HOT-SQLL-WIND-NIGHT (42)**] exhibited a mean of 87% and an interquartile range exceeding 12%, indicating an inconsistent model. The second model with a large percent error [**DEC-HOT-SQLL-NIGHT (43)**] exhibited a mean near 75%, but a narrow distribution with an interquartile range less than 5%.

Most DEC models (7 of 9) displayed mean biases smaller than the ± 50 outages (see Figures 44d and 45d). However, two of the seven models [**DEC-WARM-SQLL-WIND-DAY (46)** and **DEC-WARM-SQLL-DAY (48)**] exhibited wide asymmetrical distributions indicating an inconsistent bias, which is arguable more difficult to account for than having a large consistent bias. The **DEC-HOT-SQLL-NIGHT (43)** model also exhibited a wide asymmetrical distribution, but with a large mean bias near -275 outages.

Overall, these four error statistics highlighted **DEC-WARM-SCAT-WIND-DAY (45)** and **DEC-WARM-NIGHT (49)** as the best performing daytime and nighttime model, respectively. In contrast, the error statistics identified **DEC-WARM-SQLL-DAY (48)** and **DEC-HOT-SQLL-NIGHT (43)** model as the least skillful.

e. Carolina East (DEP)

The DEP service area incorporated 127 event dates within its database, that when classified, introduced eleven subcategories (DEP-HOT-PULSE-WIND, DEP-HOT-SCAT-WIND, DEP-HOT-SQLL-WIND, DEP-HOT-SCAT, DEP-HOT-SQLL, DEP-HOT, DEP-WARM-SCAT-WIND, DEP-WARM-SQLL-WIND, DEP-WARM-SCAT, DEP-WARM-SQLL, DEP-WARM) with enough dates (≥ 10) to construct both day and night multiple-linear regression equations – for a total of *twenty-two* potential regression equations (Tables 10a and 10b). Of those attempts, several were unable to produce statistically significant equations for the daytime or nighttime (DEP-HOT-SCAT, DEP-WARM-SCAT-WIND, and DEP-WARM-SCAT), which reduced the equation pool by six. Other scenarios unable to generate a consistent statistically stable equation included DEP-HOT-SQLL-WIND-NIGHT, DEP-HOT-SQLL-NIGHT, DEP-WARM-SQLL-WIND-NIGHT, DEP-WARM-SQLL-DAY, and DEP-WARM-DAY. Nevertheless, the *nine* successful equations will be reviewed in this section.

i. DEP Model Discussion

Power outages for the **DEP-HOT-SCAT-WIND-DAY** were best estimated by the MAX-MAX of SHR01 and RHBLML with a mean adjusted r-square of 0.275 (Table 5, Index 50) after a log transformation was applied (Figure 46). The relationships for these estimators with power outages were both positive, implying that when SHR01 was larger and/or RHBLML was larger, more outages transpired. The positive relationships between SHR01 and RHBLML with power outages is thoroughly justified with Equations 2 and 21, respectively.

The nocturnal scenario (**DEP-HOT-SCAT-WIND-NIGHT**) also required a log transformation to the power outages to reduce for skewness (Figure 47). The resulting linear equation predicted power outages utilizing the MAX-AVG summary statistic of LI with an average adjusted r-square of 0.318 (Table 5, Index 51). The equation suggests a negative relationship between power outages and LI, which is analyzed with Equation 18.

The following category was based off events that occurred in a **DEP-HOT-SQLL-WIND-DAY** environment. The power outages in this case were corrected by a log transformation (Figure 48) and then best predicted in a linear regression equation by the AVG-AVG summary statistic of LLVVEL with an adjusted r-square of 0.505 (Table 5, Index 52). The relationship between the LLVVEL and power outages was negative and was explained with Equation 16.

When neglecting the dominant severe weather type, the category **DEP-HOT-SQLL-DAY** results in an equation that related log transformed power outages (Figure 49) to the AVG-AVG summary statistic of SHP, MLCIN, and LLVVEL with an adjusted r-square of 0.708 (Table 5, Index 53). The SHP displayed a positive relationship with power outages, while the other two estimators, MLCIN and LLVVEL, exhibited negative relationships with power outages. Discussions about these correlations can be found with Equations 10, 17, and 16, respectively.

Zooming outward to the broad category of **DEP-HOT-DAY**, an equation was created by relating the log transformed power outages (Figure 50) to the AVG-AVG of SHP and LLVVEL (Table 5, Index 54). Interestingly, a negative relationship between LLVVEL and power outages formed in the last three equations all within the DEP-HOT category implying that broad-scale rising motion was consistently proving to be statistically

significant in predicting the number of power outages. As noted above, a discussion on how this estimator effects power outages can be found with Equation 16.

As for the nocturnal outages in the **DEP-HOT-NIGHT** category, a log transformation was required to correct the skewness in the power outage dataset (Figure 51). The power outages were best estimated by the MAX-MAX of SHP and PW with an average adjusted r-square of 0.263 (Table 5, Index 55). Both of the estimators demonstrated positive relationships with power outages, implying that when SHP and/or PW was larger, more outages occurred. These relationships are explained with Equations 10 and 4, respectively.

The first successful warm season equation resided in the **DEP-WARM-SQLL-WIND-DAY** category where a log transformation was applied to the outage dataset to reduce skewness (Figure 52). The resulting equation predicted power outages by the MAX-MAX of MLCIN and HGTFRZ with an average adjusted r-square of 0.490 (Table 5, Index 56). The MLCIN showed a positive relationship with power outages (discussed with Equation 22), while the HGTFRZ displayed a negative relationship with power outages (explained with Equation 4).

A nighttime equation was created for the **DEP-WARM-SQLL-NIGHT** category where a log transformation was applied to the outage dataset to decrease skewness (Figure 53). The resulting linear regression equation related power outages to PW and MUCIN with a mean adjusted r-square of 0.538 (Table 5, Index 57). Both of the estimators positively influenced power outages, meaning when either of the estimators were of a larger magnitude, more outages transpired. These relationships were discussed with Equations 4 and 22, respectively.

The final linear regression equation was created for the broad **DEP-WARM-NIGHT** category where the power outage dataset was subjected to a log transformation to reduce the skewness (Figure 54). Power outages in this case were best estimated by the AVG-AVG of LLVVEL and HEL01 with an average adjusted r-square of 0.368 (Table 5, Index 58). Both of the estimators displayed negative relationships with power outages, which were discussed in detail with Equations 16 and 8, respectively.

ii. **DEP Error Analysis**

Only 2 of 9 models [**DEP-WARM-SQLL-NIGHT (57)** and **DEP-WARM-NIGHT (58)**] in the DEP service area displayed acceptable MAE means below the 50-outage threshold (see Figures 55a and 56a). Both were built upon the AVG-AVG summary statistics with sample sizes of 19 and 58, respectively. Since a majority of the models (7 of 9) produced unacceptable mean MAEs, the unacceptable category was viewed as two sub-categories (as with the DEC service area): slightly unacceptable [<100 outages] and extremely unacceptable [>100 outages]. Four of the seven unacceptable models were slightly unacceptable [**DEP-HOT-SCAT-WIND-DAY (50)**, **DEP-HOT-SCAT-WIND-NIGHT (51)**, **DEP-HOT-SQLL-DAY (53)**, and **DEP-HOT-DAY (54)**] exhibiting means of 55-70 outages and narrow symmetrical error distributions with interquartile ranges < 5 outages. Such narrow distribution imply consistency. Moreover, all slightly unacceptable models were for the hot season and three were daytime models. In contrast, the extremely unacceptable models [**DEP-HOT-SQLL-WIND-DAY (52)**, **DEP-HOT-NIGHT (55)**, and **DEP-WARM-SQLL-WIND-DAY (56)**] exhibited mean MAEs of 160-165 outages and interquartile ranges greater than 20 outages.

The RMSE showed all models as unacceptable (see Figures 55b and 56b)! Any model that was acceptable according to MAEs, moved into the slightly unacceptable category for RMSE, and the **DEC-HOT-DAY (54)** model became extremely unacceptable.

Regarding percent error, 4 of 9 models in the DEP service area [**DEP-HOT-SQLL-WIND-DAY (52)**, **DEP-HOT-SQLL-DAY (53)**, **DEP-HOT-DAY (54)**, and **DEP-WARM-SQLL-NIGHT (57)**] had mean percent errors below 50% (see Figures 55c and 56c). Of the five models with mean percent errors above 50%, four [**DEP-HOT-SCAT-WIND-DAY (50)**, **DEP-HOT-SCAT-WIND-NIGHT (51)**, **DEP-WARM-SQLL-WIND-DAY (56)**, and **DEP-WARM-NIGHT (58)**] had relatively wide distributions with interquartile ranges > 8%. The **DEP-HOT-NIGHT (55)** model exhibited a consistently large mean percent error mean near 83%.

As for bias, most models (6 of 9) had narrow symmetrical distributions, with interquartile ranges less than 7 outages (see Figures 55d and 56d). Of those six models, only one [**DEP-HOT-DAY (54)**] had a mean bias greater than the acceptable 50-outage threshold. All three models with unacceptable biases [**DEP-HOT-SQLL-WIND-DAY (52)**, **DEP-HOT-NIGHT (55)**, and **DEP-WARM-SQLL-WIND-DAY (56)**] under predicted by more than 150 outages on average, and exhibited asymmetrical bias distributions.

Overall, the best performing daytime and nighttime models for the DEP service area were **DEP-HOT-SQLL-DAY (53)** and **DEP-WARM-SQLL-NIGHT (57)**, respectively. The worst performing daytime and nighttime models, which should be used with caution, were **DEP-HOT-SQLL-WIND-DAY (52)** and **DEP-HOT-NIGHT (55)**, respectively.

CHAPTER 6: CASE STUDIES

A detailed error analysis for a single case date was performed for each service area, Midwest (MWC, MWI), Florida (FLA), and Carolinas (DEC, DEP) to show the functionality of the models and how the forecasters may wish to use the statistical forecasts. Specifically, we envision the forecaster using multiple applicable models to provide an *ensemble prediction* for a given scenario. Therefore, for each case date discussed below, all applicable models for that service area and time of day were analyzed as an ensemble (i.e. regardless of season, anticipated dominant convective mode, or anticipated severe weather type). This approach will provide the forecaster with a range of potential outages expectations within a given region. For example, when forecasting for the MWC area, all daytime and nighttime model predictions for the Midwest (MWC and MWI) will be examined. Moreover, since MWC and MWI are adjacent to one another and share similar climates, Duke forecasters would benefit from including the individual model forecasts for the adjacent service area into the ensemble.

Such approach has multiple advantages. First, much like ensemble prediction via numerical modeling systems, we believe that an ensemble approach using multiple individual statistical models will improve the final forecast while providing forecasters a measure of confidence through the ensemble variance. Second, the case date categorization process was somewhat subjective and at time non-physical, such that considerable overlap exists between categories. For example, our database contains numerous dates in both late May (warm season) and early June (hot season) that experienced numerous power outages due to a combination of convective modes (both squall lines and scattered multicells) and severe weather reports (both wind and hail). Third, the low computational expense of

running GLM models based on metrics derived from numerical forecast fields make the ensemble approach a feasible option.

Shown below for each analyzed case date are the relevant forecast ensemble separated by day and night (Figures 57-59). In each figure, the observed outage counts are denoted by black cross hairs, individual statistical model forecast are denoted by colored symbols, and the acceptable range of ± 50 outages is marked by red lines (relative to the observed outage count). Recall, that from an operational stand point, Duke's outage mitigation protocols do not change drastically if the outage count is off by ± 50 , therefore model outputs within that range are considered acceptable.

a. Midwest (MWC, MWI)

On June 18th, 2013 disorderly multicells developed in central Indiana and Ohio around 1930-2030 UTC and propagated south/ southeast. The cells became more organized and even developed a slight bowing region before reaching the heavily populated Cincinnati region around 2100 UTC. The storms continued south-southeastward into the few counties in northern Kentucky that are part of Duke Energy's service territory and then the system completely exited their service region by 2330 UTC. The event was classified as a **MWC-HOT-SCAT-NO** event that generated 94 daytime and 11 nocturnal outages. The statistical model forecasts are summarized in Figure 57.

Of the eleven daytime models, seven models within the acceptable ± 50 range (44 - 144) from the observed outage counts (94) and one was **MWI-HOT-SCAT-WIND-DAY (7)**, the most applicable model to this situation. The models closest to the observed outage count were **MWI-WARM-SQLL-WIND-DAY (9)** with 96 predicted outages and **MWI-**

WARM-SQLL-WIND-DAY (17) with 88 predicted outages. The scattered convection did not transform into a well-organized squall line; however, it was organized enough to develop a slight bowing region where most of the outages were concentrated.

In the evening, all thirteen models provided prediction within the ± 50 outage range (0-61; the lower bound was set to zero since only 11 outages were reported) from the observed outage counts. The **MWI-WARM-SCAT-HAIL-TOR-NIGHT (16)** predicted exactly 11 outages and **MWC-HOT-SCAT-WIND-NIGHT** (the most relevant model to this scenario) predicted 61 outages.

b. Florida (FLA)

June 30th, 2013 was a very busy convective day and evening within Duke Energy's Florida service territory. Storms began as pulse convection around 1200 UTC and then quickly transitioned into scattered multicells that persisted through 1200 UTC the next day. Major metropolitan regions such as Orlando, Tallahassee, and Tampa were all impacted during this event, amounting to 152 daytime outages and 102 nighttime outages. This event was classified as **FLA-HOT-SCAT-WIND** event. The statistical model forecasts are summarized in Figure 58.

The nine daytime models predicted outage counts between 111 and 237, with five predictions falling within the acceptable ± 50 outage range (102-202) from the observed outage count (152). Two models designed for multicell events [**FLA-HOT-SCAT-DAY (27)** and **FLA-WARM-SCAT-WIND-DAY (30)**] provided excellent forecasts with 149 and 152 predicted outages, respectively. In contrast, the predictions from two other models also developed for multicell events [**FLA-HOT-SCAT-WIND-DAY (25)** and **FLA-**

WARM-SCAT-DAY (37)] exceeded the upper limit of the acceptable range. However, as noted above, the **FLA-HOT-SCAT-WIND-DAY (25)** equation has an inherent bias for over-prediction (see Figure 33d) and errors of 50 or greater are typical for the **FLA-WARM-SCAT-DAY (37)** (see Figure 35a).

As for the seven nighttime models, predictions ranged from 6 to 108 with five falling within the acceptable ± 50 outage range (52-152). The most accurate model with the largest prediction (108 outages) was from the **FLA-WARM-NIGHT (40)**, which relies on PW and SOILMS. Considering that there had been consistent convection throughout the day and into the evening, SOILMS was likely elevated across the service area, thereby increasing the outage count prediction. The second most accurate model was **FLA-WARM-SCAT-NIGHT (36)**, which also relies on PW, reinforcing the importance of the PW parameter to outage forecasts in Florida.

c. Carolinas (DEC, DEP)

On August 4th, 2017 unorganized convection developed over the western Carolina Mountains around 2030 UTC and became more linear as it descended into the Piedmont, forming a bowing squall line that affected major populated areas across the Carolinas (i.e. Asheville, Shelby, Gastonia, Charlotte, Salisbury, and Greenville). The event was classified as a **DEC-HOT/WARM-SQLL-WIND** event (recall that August was used to build both HOT and WARM models in the Carolinas). Since convective dissipation did not occur until roughly 0230 UTC a large number of outages occurred in both daytime (139) and nighttime (141). The statistical model results are summarized in Figure 59.

The eleven daytime model predictions ranged from 58 – 272 with six falling within ± 50 outages (89-189) of the observed outage count (139). The **DEC-WARM-SQLL-WIND-DAY (46)** provided a perfect forecast despite the model's large MAE and RMSE (see Figures 44a and 44b). Two other models that were highly applicable to this situation, **DEC-WARM-SQLL-DAY (48)** and **DEP-WARM-SQLL-DAY (53)**, did not perform well and provided opposite out-of-acceptable-range forecasts (272 and 58, respectively). More surprisingly was the large **DEC-WARM-SQLL-DAY (48)** over-prediction that contradicted the strong negative bias found during repeated error analysis trials (see Figure 45d). Likewise, the **DEP-WARM-SQLL-DAY (53)** under-prediction was inconsistent with its mean bias (see Figure 55d). In this case, under-estimation can most likely be attributed to the unusual AVG-AVG statistics of SHP and LLVVEL on this day; the SHP was particularly low (~ 0.129 ; resulting in a low outage prediction) and the LLVVEL was positive (resulting in a subsequent reduction in the predicted outage count).

The seven nighttime model predictions ranged between 25 and 142 with four falling within the ± 50 outages (91-191) from the observed outage count (141). As expected, the most accurate models were the **DEC-HOT-SQLL-WIND-NIGHT (42)** and **DEP-WARM-SQLL-NIGHT (57)** with predicted outages of 130 and 142, respectively. The **DEC-HOT-SQLL-NIGHT (43)** under-predicted on this date even though an exceptionally high MAX-MAX of DCAPE ($\sim 1300 \text{ J kg}^{-1}$) was present. However, as previously discussed in the error analysis, this model exhibits a large negative mean bias of -275 outages (see Figure 44d). In practice, an experienced forecaster will place more confidence in the models forecasting large outage counts if an intense, bowing squall line is expected to pass over heavily populated portions of a given service area.

CHAPTER 7: CONCLUSION

This study was designed to help alleviate forecasting errors between power outage causing thunderstorms and ordinary thunderstorms during the meteorological warm season (March 1st – October 31st for this study). Duke Energy has struggled with identifying (1) “short-fuse events” where strong power outage producing storms are not well-forecasted resulting in an understaffing of repair crews, and (2) “non-events” where storms are well forecasted but do not produce the expected outages, leading to an overstaffing of repairs crews. Neither scenario is cost-effective, so a forensic analysis of five years (2013-2017) of thunderstorm-induced power outage events was conducted to improve the outage prediction during such events. This study focused on wet microbursts (a common phenomenon in Duke Energy’s service territories) known to generate divergent strong surface winds capable of knocking down trees and utility poles. Thirty-three specific meteorological diagnostic/forecast parameters, known to identify microburst-conducive environments, were evaluated for use in multiple-regression equations that predict the total number of power outages in a given service area.

The case dates used to build the metric database were identified by reviewing the SPC convective outlook archive and the NWS severe storm report database. The hourly RAP initialization files (i.e. the analysis fields or 0-hr forecast) were then downloaded for all relevant hours during the chosen case date. The outage data provided by Duke Energy was used as the response variable within a series of GLM equations developed using the meteorological parameters as predictors. A 10-km grid covering the five Duke Energy service territories was employed and all 33 meteorological parameters derived from RAP analyses were interpolated onto this grid. This was completed for a 24-h period during each

identified case date, beginning at 1200 UTC and running through 1200 UTC on following day. Next, regional day and night summary statistics were computed for each case date, by finding the (1) average of hourly maximum within the service area, (2) average of the hourly average within the service area, (3) maximum of hourly average within the service area, and (4) maximum of the hourly maximum within the service area. The case dates were then stratified into categories based on the season, the dominant convective mode, and dominant severe weather type, with the potential to build 360 different GLMs (one for each stratification category). However, only 102 scenarios had a sufficient number of case dates (≥ 10 events) to attempt model development, and optimal GLM equations (where p-values for all estimators consistently remained below 0.05 in repeated boot-strapping trials) were successfully developed for only 58 scenarios.

For the MWC service area, a total of 6 optimal models (of 16 attempted) were successfully developed. The only predictor identified for multiple models in this service area was WNDG, a parameter designed to detect damaging winds if there were storms to initiate in that environment. However, WNDG displayed a positive relationship with power outages in one equation and a negative relationship in another. In the MWI service area 18 optimal models were successfully developed (of the 24 attempted). The most common predictor was the SHP (with six appearances), and it exhibited a positive relationship with outage counts in all cases. The LLVVEL was a close second with five appearances, three of which displayed positive correlations with power outages and the other two were negatively related. In the FLA service area, 16 optimal models were successfully developed (of the 24 attempted). The most common predictors in FLA were MBRUST and PW, both occurring in three equations and always exhibiting a positive relationship to power outage

counts. In the DEC service area, 9 optimal models were successfully developed (of 26 attempted), and the most frequent predictor was LLVVEL with three appearances. Finally, in the DEP service area, 9 optimal models were successfully developed (of the 22 attempted), and the most common predictor, again, was LLVVEL (with four appearances). Overall, the 58 successfully developed optimal models utilized 24 of the 33 evaluated predictors, but the two most common predictors were LLVVEL and SHP. Such differences reinforce the idea that outage-producing thunderstorms come in a variety of “flavors”, and that accurate forecasts of all such flavors requires an ensemble approach.

To demonstrate the many advantages of a GLM ensemble approach, three case dates were analyzed in detail. Due to climatological similarities and the low computational requirement to implement multiple GLM equations, the two Midwest (MWC and MWI) and two Carolina (DEC and DEP) service areas were combined. The statistical model predictions, in a manner akin to numerical ensemble prediction, were presented such that the outage forecast spectrum could be easily visualized. In each case, many models provided predictions within the acceptable range of ± 50 outages from the observed outage count; several models provided predictions within five outages or a perfect forecast!

The statistical models developed in this study are envisioned to merely serve as “another tool in a forecaster’s toolbox.” In practice, selection of the best model(s) for a given scenario will remain up to the discretion of the forecaster. However, with (a) practice, (b) daily knowledge of the current atmospheric conditions, and (c) broad expectations as to when and where within a given service area the most outage-producing convection will pass, forecasters will undoubtedly learn to easily identify which optimal models provide the most reliable predictions for a given scenario.

Finally, in line with the “perfect-prognosis” approach (Cerruti and Decker 2012) to forecasting, whereby statistical models are developed from observations (or 0-h model analyses) and then applied to numerical model forecast field, our statistical models should be readily transferable to different numerical forecast systems. For example, our optimal models were developed using RAP analysis fields, but current plans at Duke Energy are to apply these statistical models to the North American Model (NAM) forecast fields to take advantage of the NAM’s multiday forecast period. Such approach will provide Duke Energy with the desired 3-day guidance regarding potential weekend storms, outages, and repair crews placed on standby. The multiday predictions will also enable tracking how the outage forecasts trend from run-to-run as potential outage-producing-events approach a given service area.

CHAPTER 8: FUTURE WORK

Future work should more carefully consider the effects of high-density vs. low-density infrastructure, by sub-dividing each service area based on an appropriate infrastructure metric (e.g. pole or transformer count per unit area). It is possible that the same broad atmospheric conditions could be present on days with few outages and many outages; - the primary difference in total outage counts would be related to where the intense convection occurred. Such differences may have affected some of the correlations between outages and the metrics investigated in this study.

Lastly, it would be wise to reassess the spatiotemporal aspect of the project. One approach would be to only investigate the atmospheric conditions at grid points where power outages and/or deep convection were experienced on that day. Another approach would be to reduce the hours investigated, to only those when power outages were reported (in addition to a few hours prior because often there is a time lag with reporting outages) and/or when deep convection was present. By focusing on the specific hours and grid points where power outages were reported and/or deep convection was present more commonality may be found between which meteorological parameters are most influential on power outages.

TABLES

Table 1. The number of event types and total number of events that occurred in each service over the five-year study period (2013- 2017). Please note that this is the initial event count and does not account for the dates where data was unavailable.

Service Area	Number of Event Types per Service Area			Total
	SF-Events	NON-Events	HIT-Events	
MWC	12	71	38	121
MWI	18	81	70	169
FLA	112	13	29	154
DEC	107	21	44	172
DEP	61	34	43	138

Table 2. The 33 metrics investigated in this study along with their short-hand ID, long name, unit, and computational method.

Metrics			
Short-hand ID	Long-name	Unit	Computational Method
DIV500	Divergence at 500 mb	s^{-1}	Custom Software
HGTFRZ	Height of the 0°C Isotherm	m	Custom Software
HEL03	Helicity 0-3 km	$m^2 s^{-2}$	Custom Software
HEL01	Helicity 0-1 km	$m^2 s^{-2}$	Custom Software
LI	Lifted Index	K	Custom Software
PW	Precipitable Water of the Troposphere	$kg m^{-2}$	Custom Software
RHBLML	The Difference of Relative Humidity in the Boundary Layer and the Average Mid-level (850 – 500 mb)	%	Custom Software
TMP700	700 mb Temperature	K	Custom Software
THE700	700 mb Theta-e	K	Custom Software
THE850	850 mb Theta-e	K	Custom Software
LLVVEL	Low Level Vertical Velocity	$Pa s^{-1}$	Custom Software
WSPSFC	Surface Winds	$m s^{-1}$	Custom Software
WSP700	700 mb Winds	$m s^{-1}$	Custom Software
WSP850	850 mb Winds	$m s^{-1}$	Custom Software
SOILMS	Mean Soil Moisture	Fraction	Native Grid Custom Software
BRN	Bulk Richardson Number	Non-dimensional	SHARPy
DCAPE	Downdraft Convective Available Potential Energy	$J kg^{-1}$	SHARPy
EFFDEPTH	Effective Inflow Layer Depth	m	SHARPy
EFFBASE	Effective Inflow Layer Base Height	m	SHARPy
EFFTOP	Effective Inflow Layer Top Height	m	SHARPy
MBURST	Microburst Composite	Non-Dimensional	SHARPy

MLCAPE	Mixed Layer Convective Available Potential Energy	$J\ kg^{-1}$	SHARPy
MLCIN	Mixed Layer Convective Inhibition	$J\ kg^{-1}$	SHARPy
MUCAPE	Most Unstable Convective Available Potential Energy	$J\ kg^{-1}$	SHARPy
MUCIN	Most Unstable Convective Inhibition	$J\ kg^{-1}$	SHARPy
SCP	Supercell Composite Parameter	Non-dimensional	SHARPy
SHERBE	SHERBE	Non-dimensional	SHARPy
SHP	Significant Hail Parameter	Non-dimensional	SHARPy
STP	Significant Tornado Parameter	Non-dimensional	SHARPy
SHEAR1km	Shear 0-1 km	cts	SHARPy
SHEAR3km	Shear 0-3 km	cts	SHARPy
SHEAR6km	Shear 0-6 km	cts	SHARPy
WNDG	Wind Damage Parameter	Non-dimensional	SHARPy

Table 2. (continued) The 33 metrics investigated in this study along with their short-hand ID, long name, unit, and computational method.

Table 3. The number of dominant severe weather type days in each service area for the case dates selected for this study.

Number of Severe Weather Type Events per Service Area					
Service Area	Wind	Hail	Tornado	Hail/ Tor	No Type
MWC	52	10	2	12	40
MWI	79	25	3	28	35
FLA	95	10	2	12	23
DEC	112	24	1	25	18
DEP	95	13	2	15	17

Table 4. Broad metric categories used for check for multi-collinearity within models. If two predictors within the same category had $r > 0.30$, the predictor, least correlated with outages was removed from the equation.

Positive Buoyancy	Negative Buoyancy	Convective Inhibition
DIV500	THE850	MUCIN
LI	THE700	MLCIN
LLVVVEL	DCAPE	TMP700
MUCAPE	HGTFRZ	
MLCAPE		
Shear	Moisture	Rotation
SHR01	PW	HEL03
SHR03	RHBLML	HEL01
SHR06		
WSPSFC		
WSP850		
WSP700		
Inflow Layer	Storm Type	Other
EFFBASE	BRN	SOILMS
EFFTOP		
EFFDEPTH		
Composite		
WNDG	: MLCAPE, SHR03, MLCIN	
MBURST	: SBCAPE, SBLI, DCAPE, PW	
SCP	: MUCAPE, HEL03, BRN	
STP	: MLCAPE, SHR06, HEL01	
SHERBE	: EFFDEPTH	
SHP	: MUCAPE, SHR06	

Table 5. Table lists the scenario the equation is built for, time of day, summary statistic used, equation, adjusted r-square, and number of event dates used to build the equation.

IDX	Model	Time	Sum. Stat	Equation with Average Estimators	Average Adjusted r-square	n
1	MWC-HOT-SCAT-WIND	N	MAX-AVG	$\text{LOG(OUTS)} = -0.03825*\text{WSP850} + 2.057886$	0.510	17
2	MWC-HOT-SQLL-WIND	D	MAX-MAX	$\text{LOG(OUTS)} = -0.30126*\text{WNDG} + 0.033943*\text{SOILMS} + 0.107044*\text{SHR01}$	0.709	17
3	MWC-WARM-SQLL	D	AVG-MAX	$\text{LOG(OUTS)} = 0.758301*\text{WNDG} + 0.040951*\text{SHR06}$	0.701	17
4	MWC-WARM-SQLL	N	MAX-MAX	$\text{LOG(OUTS)} = 0.04945*\text{PW} - 0.00076*\text{HGTFRZ} + 2.357075$	0.425	17
5	MWC-WARM	D	AVG-MAX	$\text{LOG(OUTS)} = 0.026525*\text{WSP700} + 1.065718$	0.264	42
6	MWC-WARM	N	MAX-MAX	$\text{LOG(OUTS)} = 3478.186*\text{DIV500} + 0.838094$	0.175	42
7	MWI-HOT-SCAT-WIND	D	MAX-AVG	$\text{OUTS} = -5.24034*\text{SHR01} + 164.994$	0.114	15
8	MWI-HOT-SCAT-WIND	N	MAX-MAX	$\text{LOG(OUTS)} = 0.251973*\text{WNDG} + 0.001211*\text{HEL03} + 0.996782$	0.487	15
9	MWI-HOT-SQLL-WIND	D	MAX-MAX	$\text{OUTS} = 80.23204*\text{LLVVEL} + 0.186336*\text{DCAPE} - 177.163$	0.301	30
10	MWI-HOT-SQLL-WIND	N	MAX-MAX	$\text{LOG(OUTS)} = 0.206209*\text{SHP} + 0.002017*\text{HEL01} + 1.08054$	0.457	30
11	MWI-HOT-SCAT	N	MAX-MAX	$\text{OUTS} = 27.9664*\text{WNDG} + 60.64036*\text{LLVVEL} - 24.7924$	0.491	29

Table 5. (continued) Table lists the scenario the equation is built for, time of day, summary statistic used, equation, adjusted r-square, and number of event dates used to build the equation.

12	MWI-HOT-SQLL	N	MAX-MAX	LOG(OUTS) = 0.190731*SHP + 0.001412*HEL03 + 1.019466	0.472	40
13	MWI-HOT	N	AVG-MAX	OUTS = 0.902639*LLVVEL + 0.094496*HEL01 + 0.882346	0.418	75
14	MWI-WARM-SCAT-WIND	D	AVG-MAX	OUTS = 48.03844*MBURST + 56.49236	0.462	10
15	MWI-WARM-SCAT-HAIL-TOR	D	MAX-MAX	OUTS = 39.08919*SHP + 48.94842	0.316	10
16	MWI-WARM-SCAT-HAIL-TOR	N	AVG-AVG	LOG(OUTS) = - 1.10144*LLVVEL +1.1205272	0.808	10
17	MWI-WARM-SQLL-WIND	D	AVG-AVG	LOG(OUTS) = - 0.01181*MUCIN +1.650919	0.320	11
18	MWI-WARM-SQLL-WIND	N	AVG-MAX	LOG(OUTS) = 0.713145*SHP - 0.07388*LI - 0.00223*HEL01	0.551	11
19	MWI-WARM-SCAT	D	MAX-AVG	OUTS = 83.97244*SHP +62.54173	0.301	27
20	MWI-WARM-SCAT	N	MAX-AVG	LOG(OUTS) = - 1.0464*LLVVEL + 1.415195	0.342	27
21	MWI-WARM-SQLL	D	AVG-AVG	OUTS = 4.046051*WSP700 + 1.090225*RHBLML	0.279	31

Table 5. (continued) Table lists the scenario the equation is built for, time of day, summary statistic used, equation, adjusted r-square, and number of event dates used to build the equation.

22	MWI- WARM -SPLL	N	MAX- AVG	LOG(OUTS) = 0.0034*MUCIN + 0.000535*MLCAPE + 1.552794	0.333	31
23	MWI- WARM	D	MAX- AVG	OUTS = 2.629044*WSP700 + 50.19245*SHP + 0.527404*RHBLML	0.323	67
24	MWI- WARM	N	MAX- MAX	OUTS = 0.023305*THE850 + 0.013583*SHR06 + 0.000694*MUCIN - 6.55384	0.216	67
25	FLA- HOT- SCAT- WIND	D	MAX- AVG	OUTS = 9.18441*SHR06 +147.4114	0.493	21
26	FLA- HOT- SCAT- WIND	N	AVG- AVG	LOG(OUTS) = - 0.00089*DCAPE +2.413616	0.546	21
27	FLA- HOT- SCAT	D	MAX- AVG	LOG(OUTS) = 0.878152*SHP +1.964533	0.316	23
28	FLA- HOT- SCAT	N	MAX- MAX	LOG(OUTS) = - 0.00013*MUCAPE +2.330389	0.303	23
29	FLA- HOT	D	MAX- AVG	LOG(OUTS) = - 13118.8*DIV500 + 2.295628	0.216	72
30	FLA- WARM -SCAT- WIND	D	MAX- AVG	LOG(OUTS) = - 0.0051*RHBLML +2.261963	0.402	13
31	FLA- WARM -SCAT- WIND	N	MAX- AVG	LOG(OUTS) = - 0.00301*MLCIN + 0.134266*MBURST + 1.331647	0.715	13
32	FLA- WARM -SPLL- WIND	D	AVG- MAX	LOG(OUTS) = 0.024254*WSP700 + 0.9972*MBURST + 1.156948	0.605	16

Table 5. (continued) Table lists the scenario the equation is built for, time of day, summary statistic used, equation, adjusted r-square, and number of event dates used to build the equation.

33	FLA- WARM -SQLL- WIND	N	MAX- AVG	LOG(OUTS) = 0.000657*MLCAPE + 1.52899	0.392	16
34	FLA- WARM - PULSE	D	MAX- MAX	LOG(OUTS) = 0.046738*SHR03+1.467692	0.396	11
35	FLA- WARM -SCAT	D	MAX- MAX	LOG(OUTS) = 0.218635*SOILMS + 0.019963*PW + 0.858849	0.393	27
36	FLA- WARM -SCAT	N	MAX- AVG	LOG(OUTS) = 0.016364*PW + 0.995989	0.303	27
37	FLA- WARM -SQLL	D	AVG- AVG	LOG(OUTS) = 0.060189*SHR01 + 0.403154*MBURST + 1.618636	0.599	20
38	FLA- WARM -SQLL	N	AVG- AVG	LOG(OUTS) = 0.000527*MLCAPE + 1.6315584	0.338	20
39	FLA- WARM	D	AVG- MAX	LOG(OUTS) = 0.174307*SOILMS + 0.016032*PW +1.200298	0.281	58
40	FLA- WARM	N	AVG- MAX	LOG(OUTS) = 0.213832*SOILMS +0.016257*PW + 0.792062	0.297	58
41	DEC- HOT- SCAT- WIND	D	MAX- AVG	LOG(OUTS) = -0.05364*LI - 0.00031*DCAPE + 2.174527	0.243	34
42	DEC- HOT- SQLL- WIND	N	MAX- MAX	LOG(OUTS) = 0.583582*SHP + 1.722954	0.481	18
43	DEC- HOT- SQLL	N	MAX- MAX	LOG(OUTS) = 0.001013*DCAPE	0.361	19
44	DEC- HOT	D	AVG- AVG	LOG(OUTS) = - 0.81483*LLVVEL - 19973.3*DIV500 + 2.3137	0.210	89

Table 5. (continued) Table lists the scenario the equation is built for, time of day, summary statistic used, equation, adjusted r-square, and number of event dates used to build the equation.

45	DEC- WARM -SCAT- WIND	D	AVG- AVG	OUTS = 0.055698*MUCAPE + 117.346	0.438	13
46	DEC- WARM -SQLL- WIND	D	AVG- AVG	LOG(OUTS) = 0.004562*HEL01 + 2.064235	0.743	13
47	DEC- WARM -SCAT	D	AVG- AVG	LOG(OUTS) = - 0.75148*LLVVEL - 0.01163*LI + 2.09674	0.629	30
48	DEC- WARM -SQLL	D	MAX- AVG	LOG(OUTS) = 0.015447*WSP700 + 0.002546*MUCIN + 2.201393	0.439	20
49	DEC- WARM	N	MAX- AVG	LOG(OUTS) = 0.02008*WSPSFC - 1.14214*LLVVEL + 1.74478	0.401	66
50	DEP- HOT- SCAT- WIND	D	MAX- MAX	LOG(OUTS) = 0.033379*SHR01 + 0.008007*RHBLML + 1.392739	0.275	24
51	DEP- HOT- SCAT- WIND	N	MAX- AVG	LOG(OUTS) = -0.16055*LI + 1.453959	0.318	24
52	DEP- HOT- SQLL- WIND	D	AVG- AVG	LOG(OUTS) = - 1.225*LLVVEL + 1.847398	0.505	28
53	DEP- HOT- SQLL	D	AVG- AVG	LOG(OUTS) = 1.044543*SHP - 0.0059* MLCIN - 1.74688*LLVVEL + 1.530157	0.708	29
54	DEP- HOT	D	AVG- AVG	LOG(OUTS) = 0.720987*SHP - 0.94203*LLVVEL + 1.814984	0.246	69

Table 5. (continued) Table lists the scenario the equation is built for, time of day, summary statistic used, equation, adjusted r-square, and number of event dates used to build the equation.

55	DEP- HOT	N	MAX- MAX	LOG(OUTS) = 0.544709*SHP + 0.019916*PW	0.263	69
56	DEP- WARM -SQLL- WIND	D	MAX- MAX	LOG(OUTS) = 0.001108*MLCIN – 0.00056*HGTFRZ + 5.053452	0.490	10
57	DEP- WARM -SQLL	N	AVG- AVG	LOG(OUTS) = 0.015849*PW + 0.011852*MUCIN + 1.909377	0.538	19
58	DEP- WARM	N	AVG- AVG	LOG(OUTS) = - 1.28543*LLVVEL – 0.00238*HEL01 + 1.808599	0.368	58

Table 6a. Event date stratification for MWC service area for the hot season.

MWC - HOT							
	PULSE	FRNT	SCAT	SQLL	SUPER	NONE	TOTAL
WIND	4	0	17	17	0	0	38
HAIL & TOR	0	0	1	2	0	0	3
NO TYPE	3	0	9	9	0	0	21
TOTAL	7	0	27	28	0	0	62

Table 6b. Event date stratification for MWC service area for the warm season.

MWC - WARM							
	PULSE	FRNT	SCAT	SQLL	SUPER	NONE	TOTAL
WIND	0	1	5	8	0	0	14
HAIL & TOR	0	0	8	1	0	0	9
NO TYPE	1	1	9	8	0	0	19
TOTAL	1	2	22	17	0	0	42

Table 7a. Event date stratification for MWI service area for the hot season.

MWI - HOT							
	PULSE	FRNT	SCAT	SQLL	SUPER	NONE	TOTAL
WIND	6	0	15	30	0	0	51
HAIL & TOR	0	0	5	1	0	0	6
NO TYPE	0	0	9	9	0	0	18
TOTAL	6	0	29	40	0	0	75

Table 7b. Event date stratification for MWI service area for the warm season.

MWI - WARM							
	PULSE	FRNT	SCAT	SQLL	SUPER	NONE	TOTAL
WIND	2	5	10	11	0	0	28
HAIL & TOR	0	0	10	12	0	0	22
NO TYPE	0	2	7	8	0	0	17
TOTAL	2	7	27	31	0	0	67

Table 8a. Event date stratification for FLA service area for the hot season.

FLA-HOT							
	PULSE	FRNT	SCAT	SQLL	SUPER	NONE	TOTAL
WIND	36	0	21	3	0	0	60
HAIL & TOR	1	0	1	0	0	0	2
NO TYPE	9	0	1	0	0	0	10
TOTAL	46	0	23	3	0	0	72

Table 8b. Event date stratification for FLA service area for the warm season.

FLA-WARM							
	PULSE	FRNT	SCAT	SQLL	SUPER	NONE	TOTAL
WIND	6	0	13	16	0	0	35
HAIL & TOR	4	0	5	1	0	0	10
NO TYPE	1	0	9	3	0	0	13
TOTAL	11	0	27	20	0	0	58

Table 9a. Event date stratification for DEC service area for the hot season.

DEC – HOT							
	PULSE	FRNT	SCAT	SQLL	SUPER	NONE	TOTAL
WIND	25	0	34	18	0	0	77
HAIL & TOR	2	0	4	1	0	0	7
NO TYPE	2	0	3	0	0	0	5
TOTAL	29	0	41	19	0	0	89

Table 9b. Event date stratification for DEC service area for the warm season.

DEC - WARM							
	PULSE	FRNT	SCAT	SQLL	SUPER	NONE	TOTAL
WIND	9	0	13	13	0	0	35
HAIL & TOR	2	1	11	4	0	0	18
NO TYPE	1	3	6	3	0	0	13
TOTAL	12	4	30	20	0	0	66

Table 10a. Event date stratification for DEP service area for the hot season.

DEP - HOT							
	PULSE	FRNT	SCAT	SQLL	SUPER	NONE	TOTAL
WIND	10	0	24	28	0	0	62
HAIL & TOR	0	0	2	0	0	0	2
NO TYPE	0	0	4	1	0	0	5
TOTAL	10	0	30	29	0	0	69

Table 10b. Event date stratification for DEP service area for the warm season.

DEP - WARM							
	PULSE	FRNT	SCAT	SQLL	SUPER	NONE	TOTAL
WIND	6	1	16	10	0	0	33
HAIL & TOR	0	1	7	5	0	0	13
NO TYPE	0	0	8	4	0	0	12
TOTAL	6	2	31	19	0	0	58

FIGURES

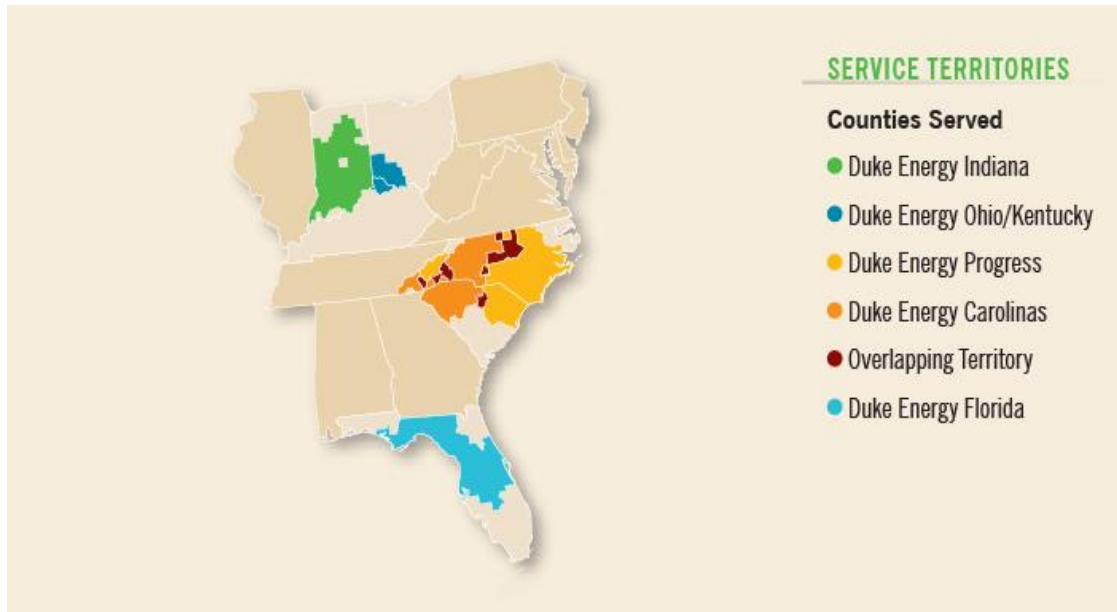


Figure 1. Duke Energy five different service territories. This study will combine Duke Energy Ohio with Duke Energy Indiana and will combine Duke Energy Carolinas with Duke Energy Progress due to the climatological similarities in the regions. (<http://sustainabilityreport.duke-energy.com/2013/images/charts/map-service-territories.png>)

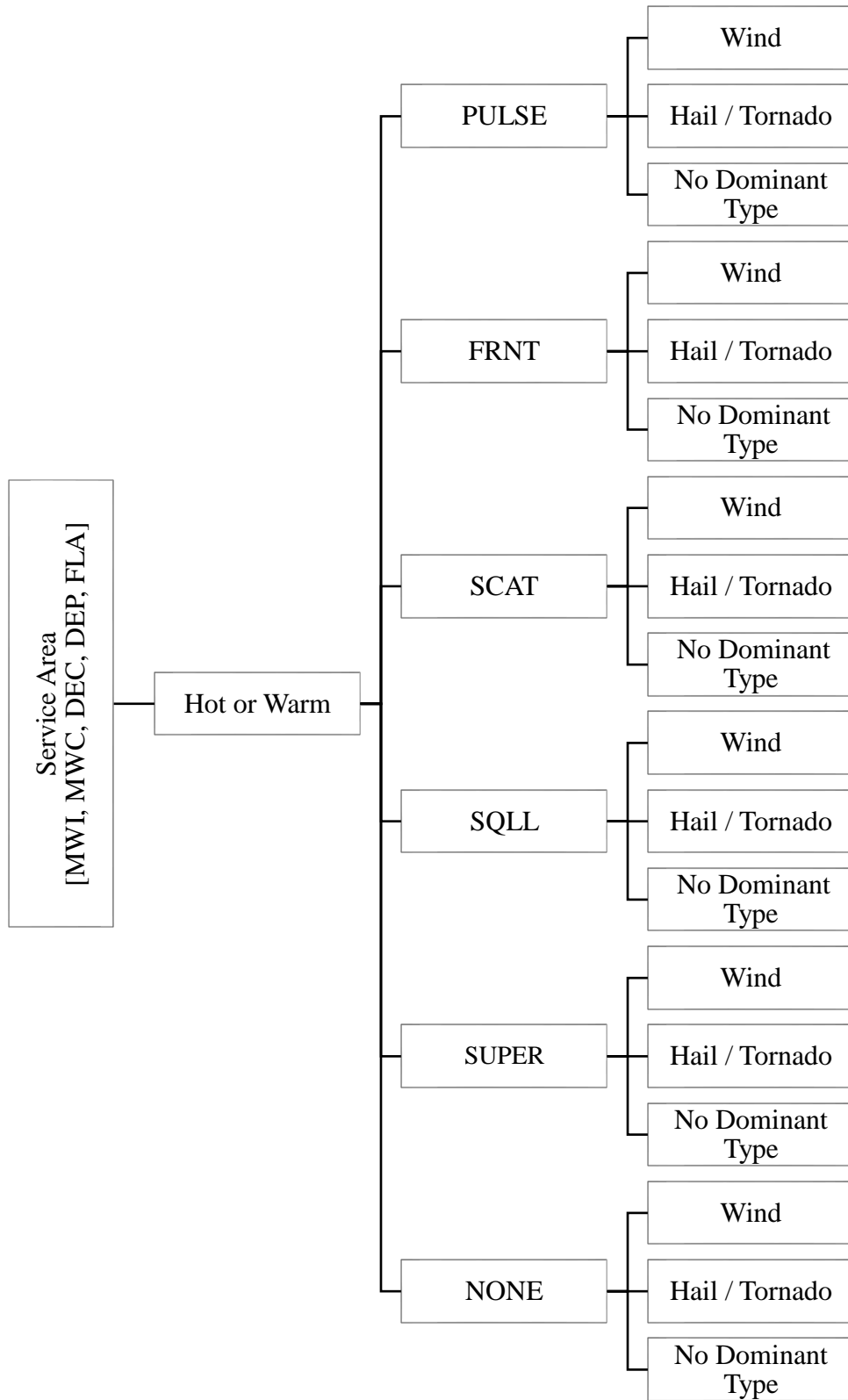


Figure 2. A flow chart indicating how the event pool was stratified by service area, season, dominant convective mode, and dominant severe weather type.

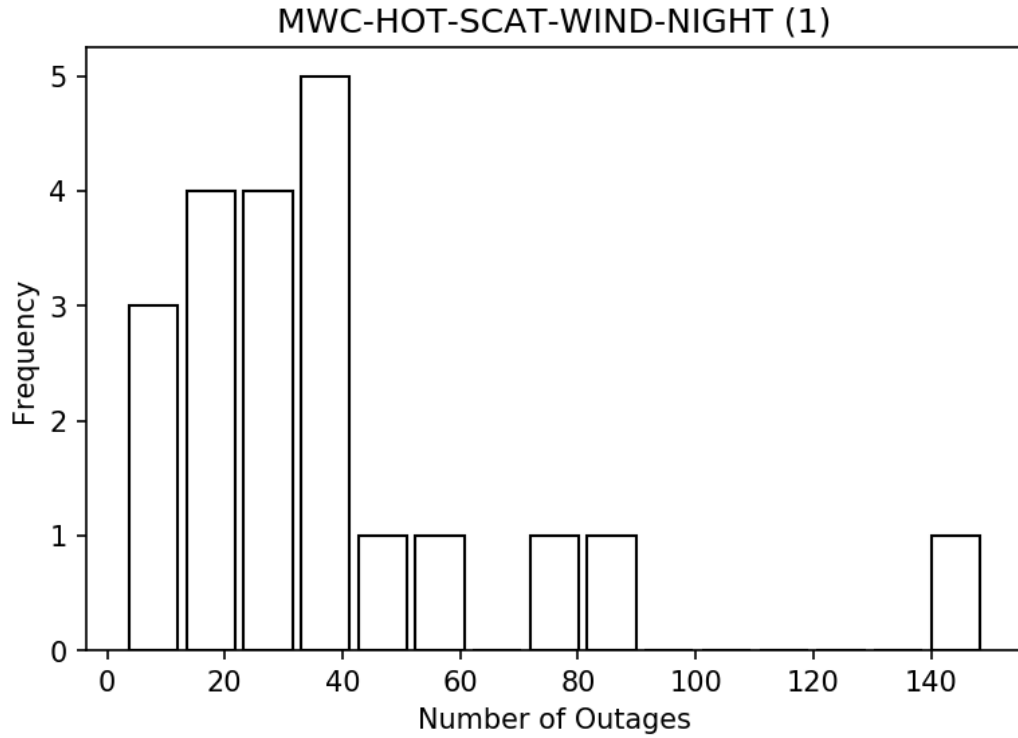


Figure 3. Histogram of observed outage counts on MWC-HOT-SCAT-WIND nights.

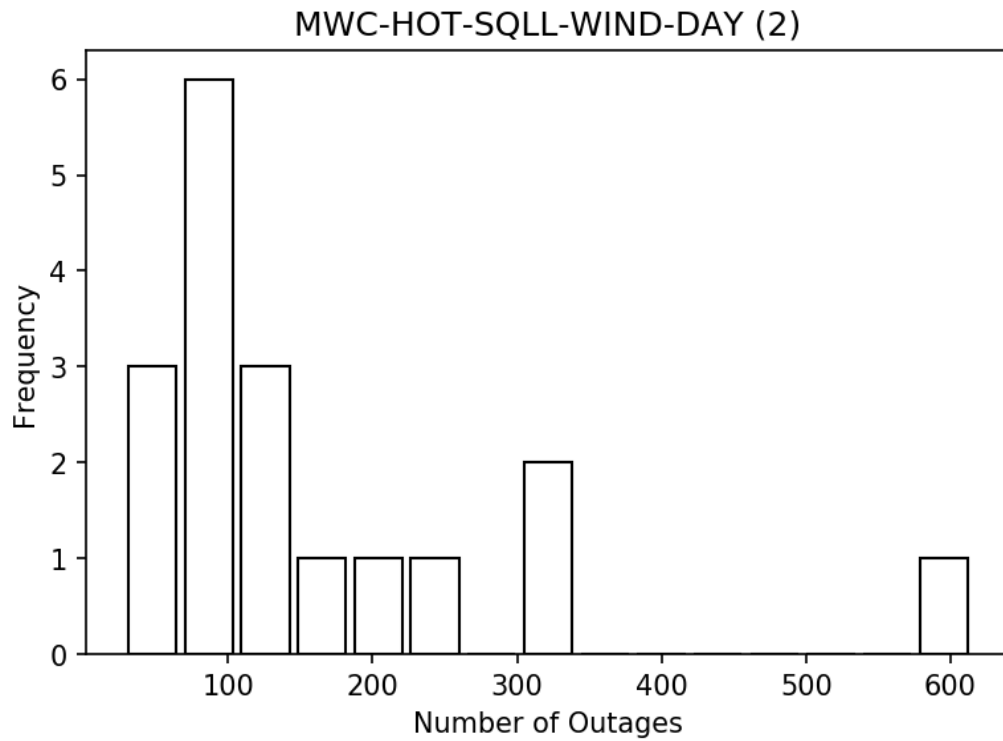


Figure 4. Histogram of observed outage counts on MWC-HOT-SQLL-WIND days.

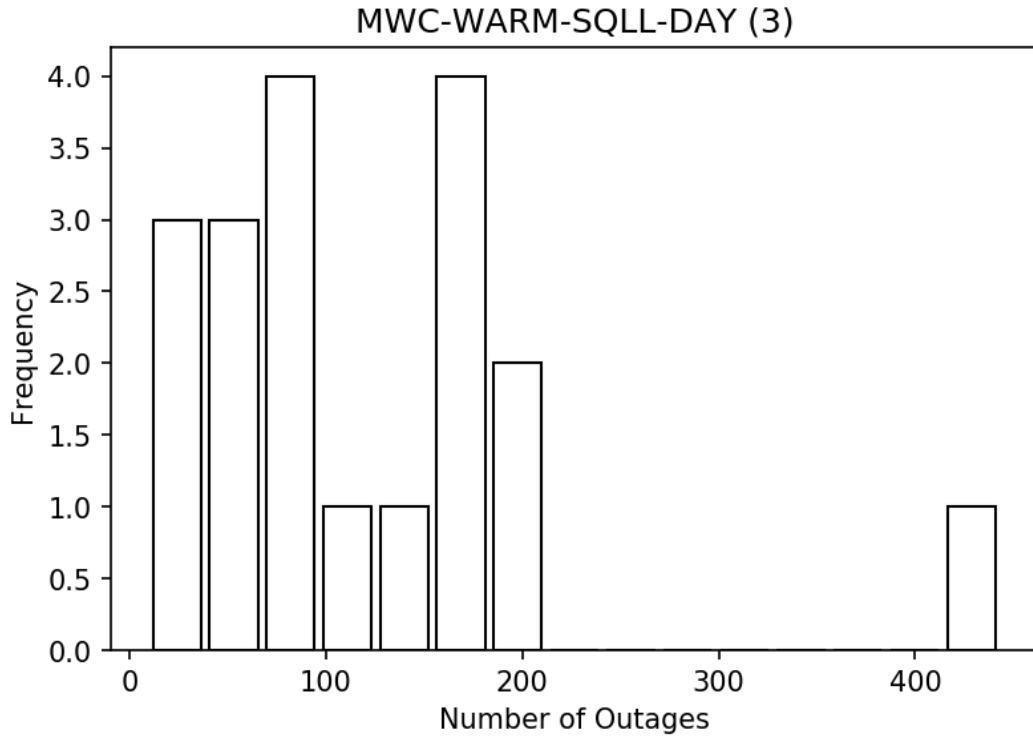


Figure 5. Histogram of observed outage counts on MWC-WARM-SQLL days.

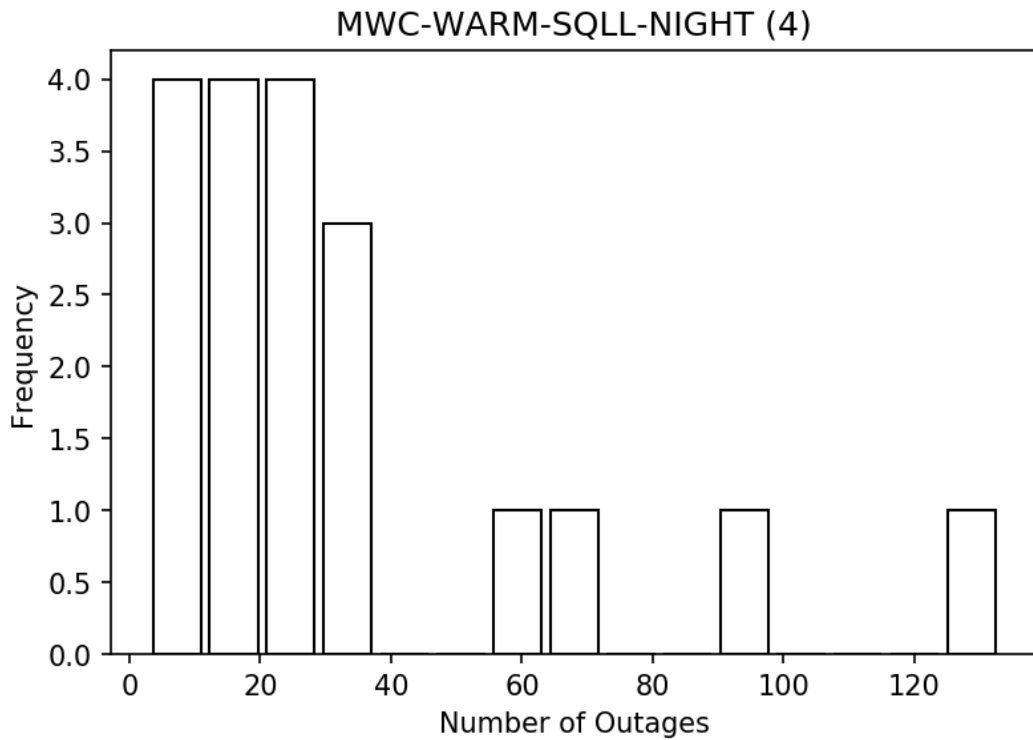


Figure 6. Histogram of observed outage counts on MWC-WARM-SQLL nights.

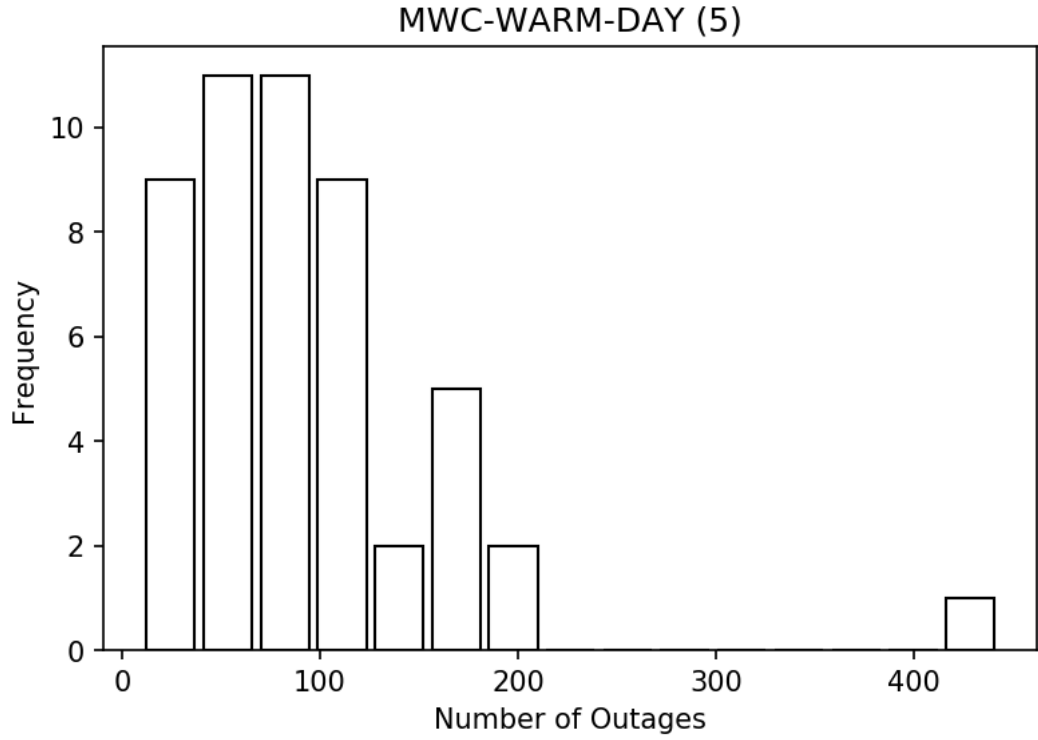


Figure 7. Histogram of observed outage counts on MWC-WARM days.

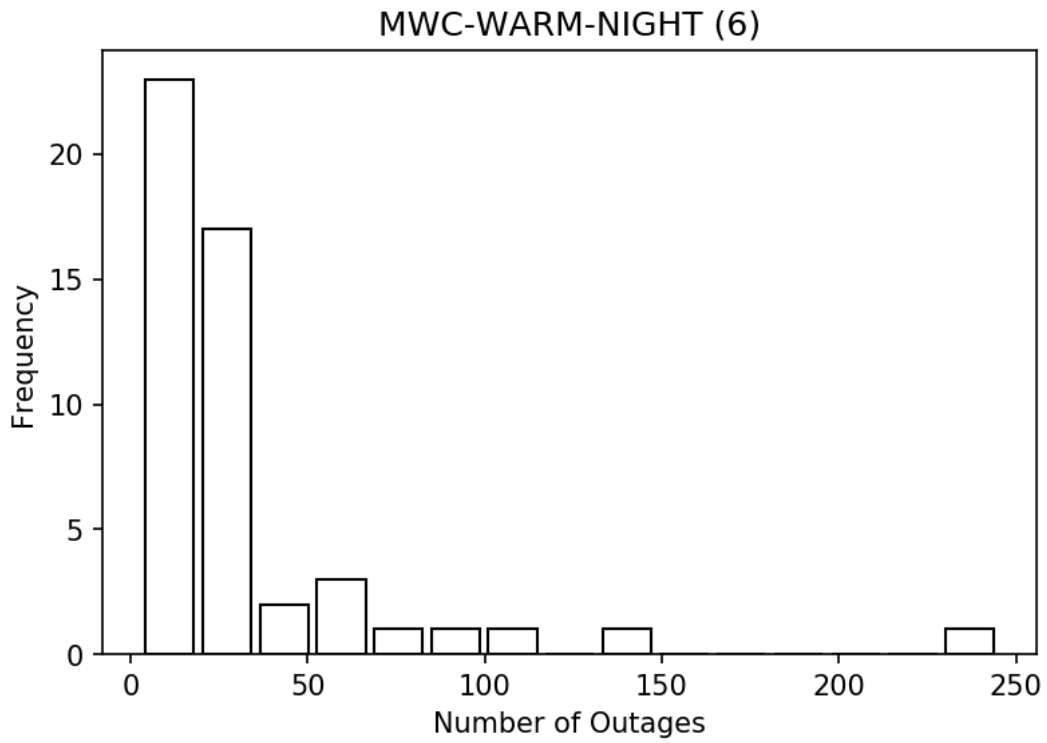


Figure 8. Histogram of observed outage counts on MWC-WARM nights.

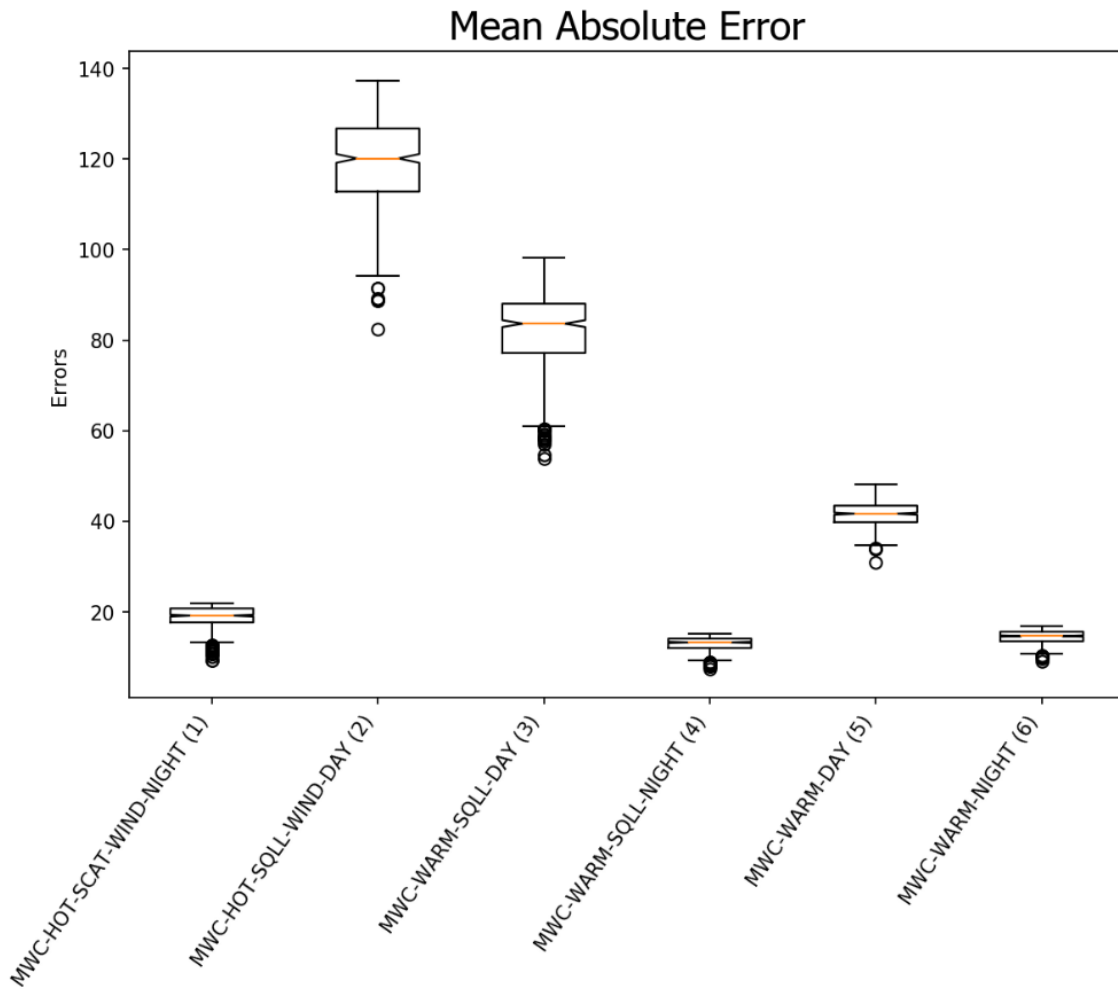


Figure 9a. The mean absolute error distributions of models 1-6. The box marks the 25th percentile (bottom of the box), 50th percentile (centerline), and 75th percentile (top of the box). The lines extending from the boxes mark the 10th percentile (bottom) and 90th percentile (top). The notches signify the 95% confidence intervals of the mean.

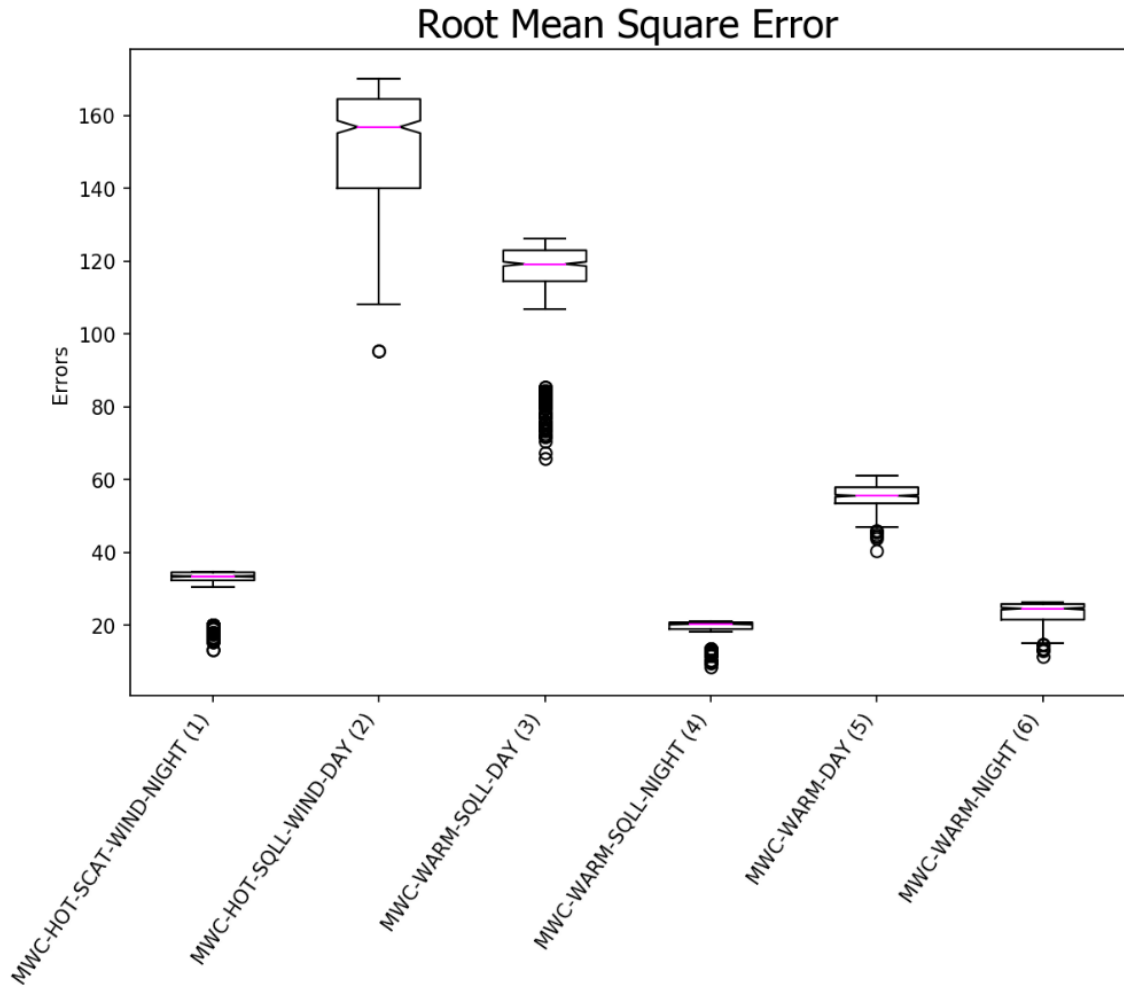


Figure 9b. The root mean square error distributions of models 1-6. The box marks the 25th percentile (bottom of the box), 50th percentile (centerline), and 75th percentile (top of the box). The lines extending from the boxes mark the 10th percentile (bottom) and 90th percentile (top). The notches signify the 95% confidence intervals of the mean.

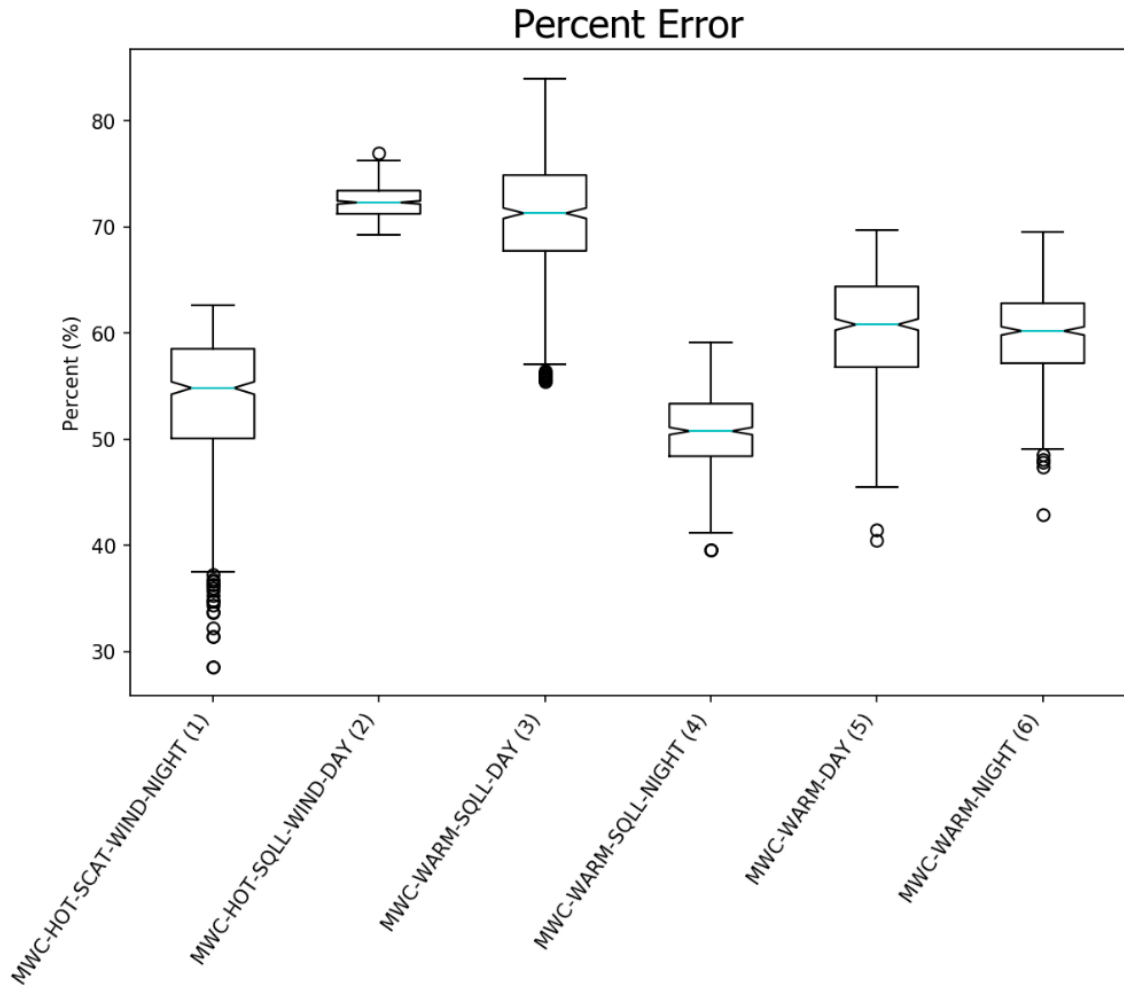


Figure 9c. The percent error distributions of models 1-6. The box marks the 25th percentile (bottom of the box), 50th percentile (centerline), and 75th percentile (top of the box). The lines extending from the boxes mark the 10th percentile (bottom) and 90th percentile (top). The notches signify the 95% confidence intervals of the mean.

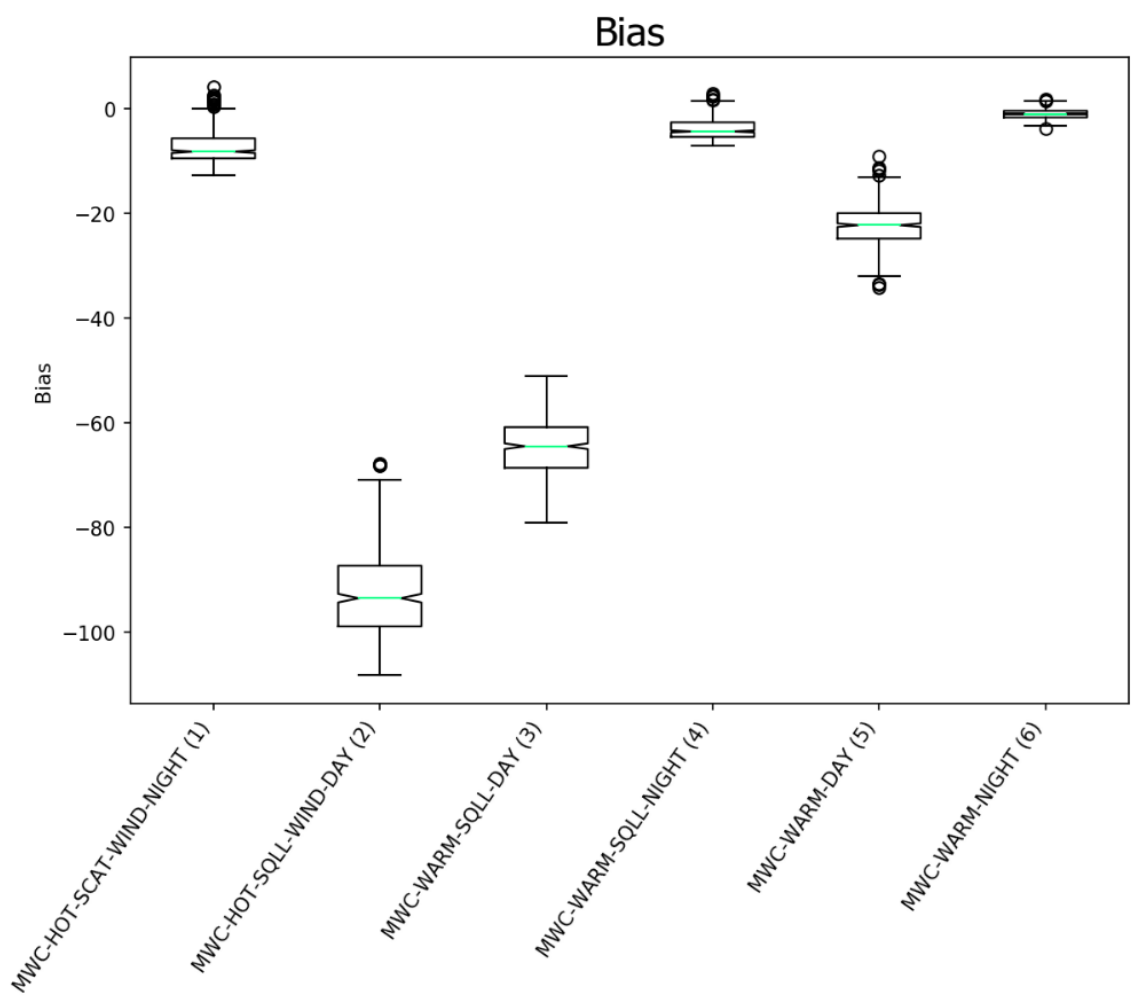


Figure 9d. The bias distributions of models 1-6. The box marks the 25th percentile (bottom of the box), 50th percentile (centerline), and 75th percentile (top of the box). The lines extending from the boxes mark the 10th percentile (bottom) and 90th percentile (top). The notches signify the 95% confidence intervals of the mean.

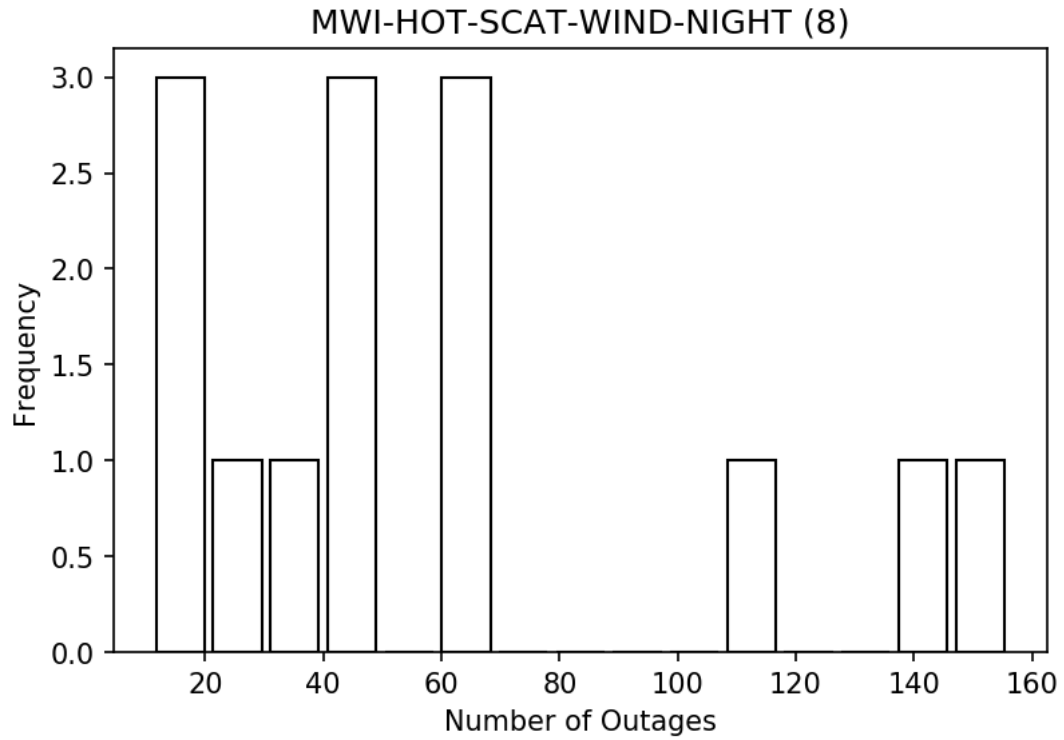


Figure 10. Histogram of observed outage counts on MWI-HOT-SCAT-WIND nights.

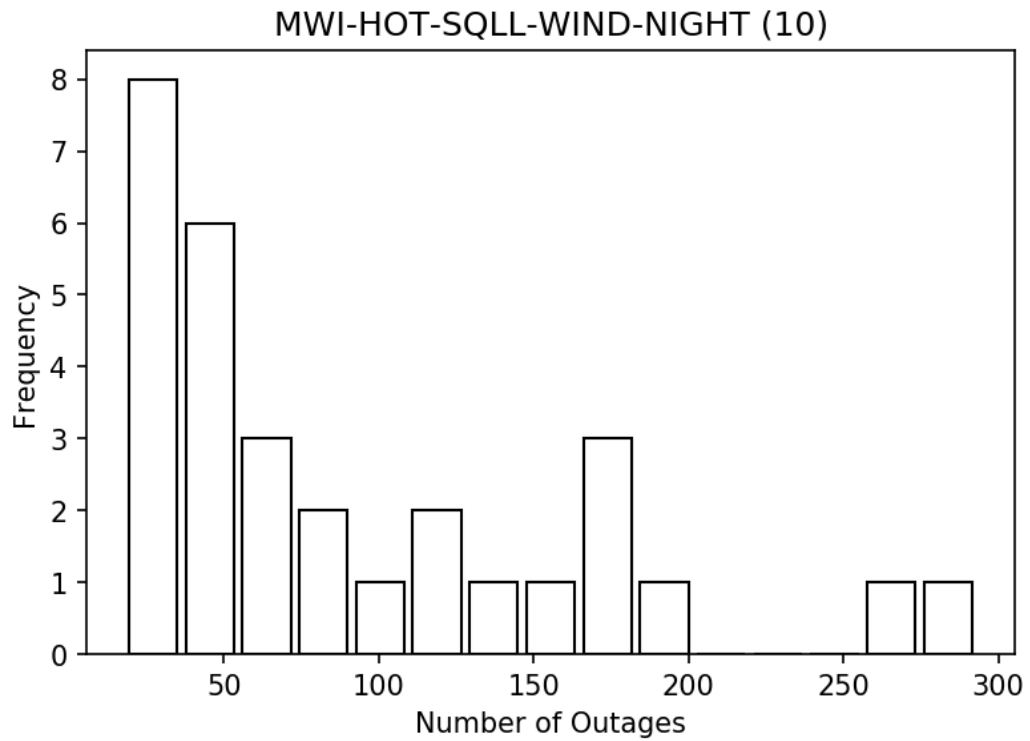


Figure 11. Histogram of observed outage counts on MWI-HOT-SQLL-WIND nights.

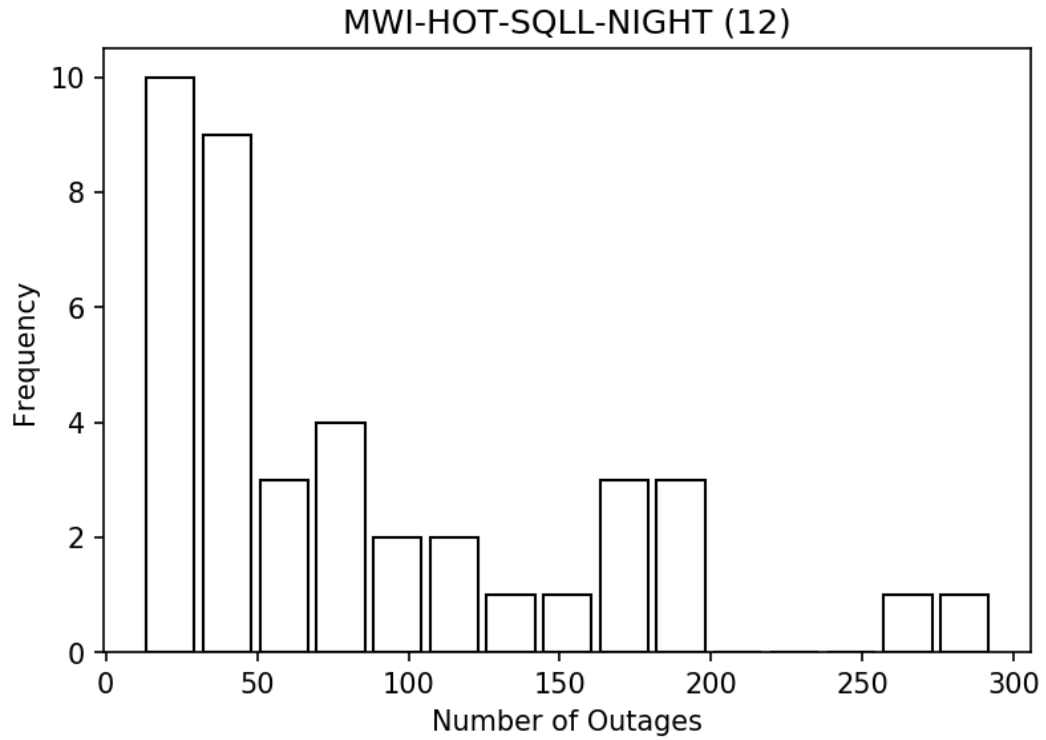


Figure 12. Histogram of observed outage counts on MWI-HOT-SQLL nights.

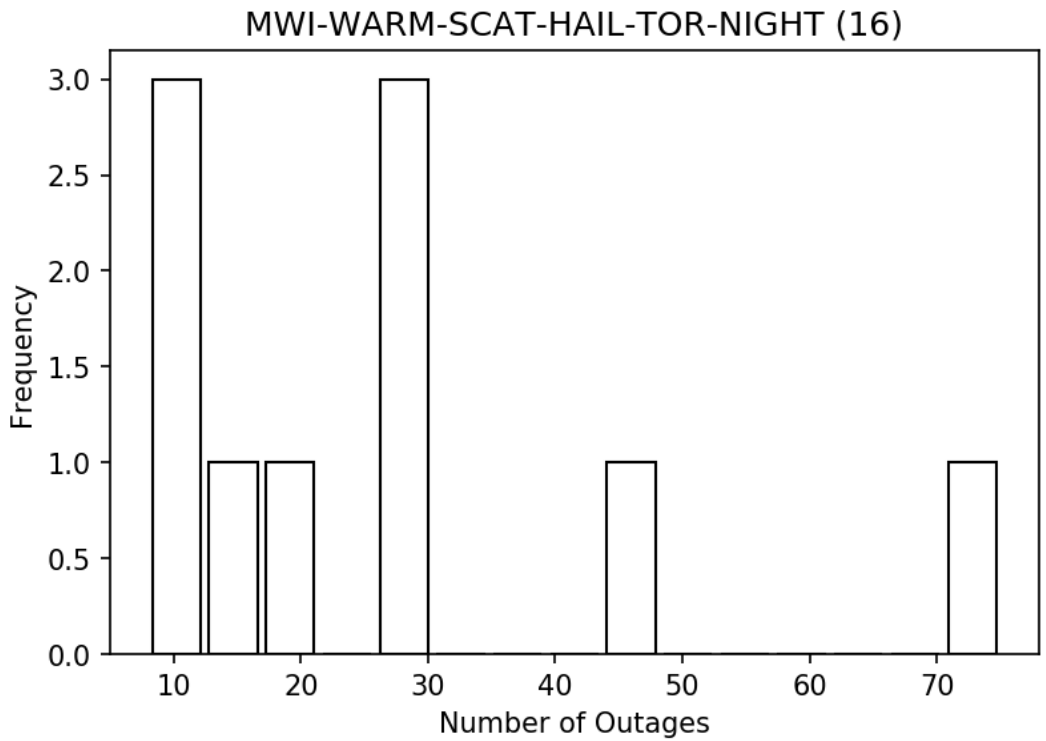


Figure 13. Histogram of observed outage counts on MWI-WARM-SCAT-HAIL-TOR nights.

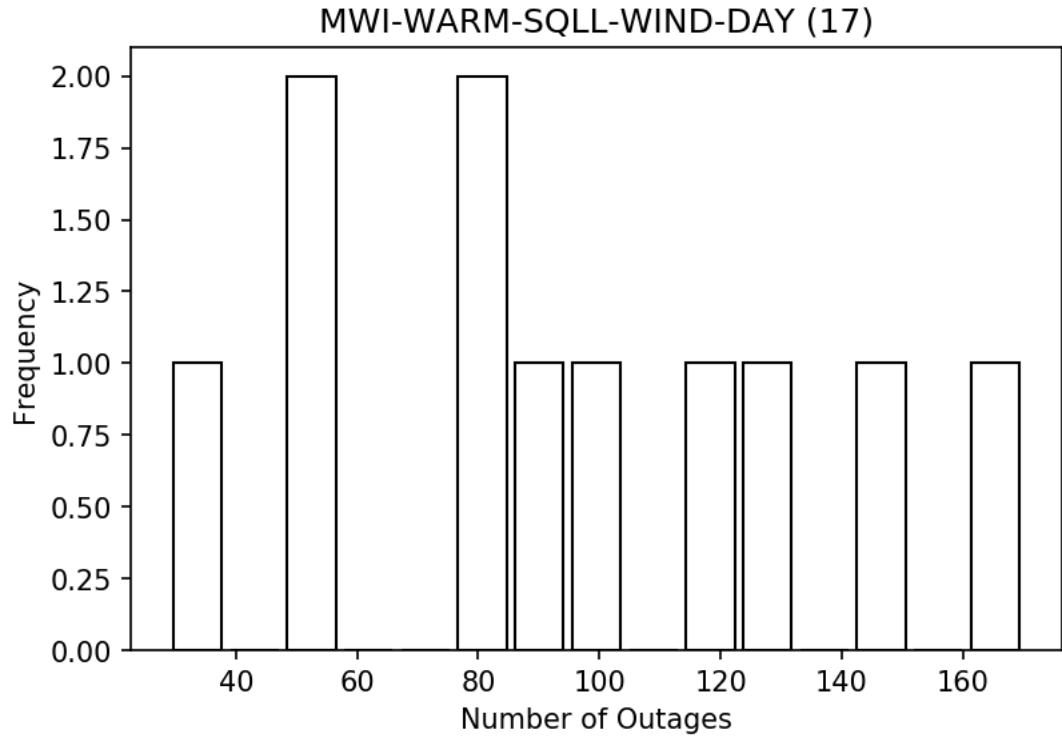


Figure 14. Histogram of observed outage counts on MWI-WARM-SQLL-WIND days.

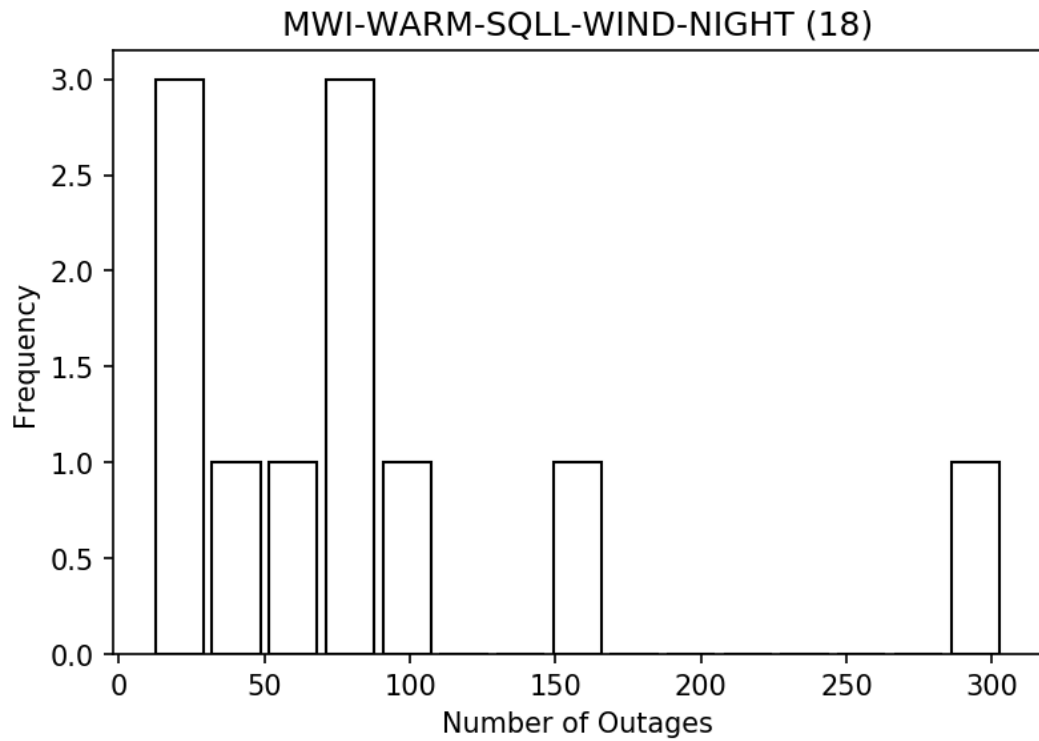


Figure 15. Histogram of observed outage counts on MWI-WARM-SQLL-WIND nights.

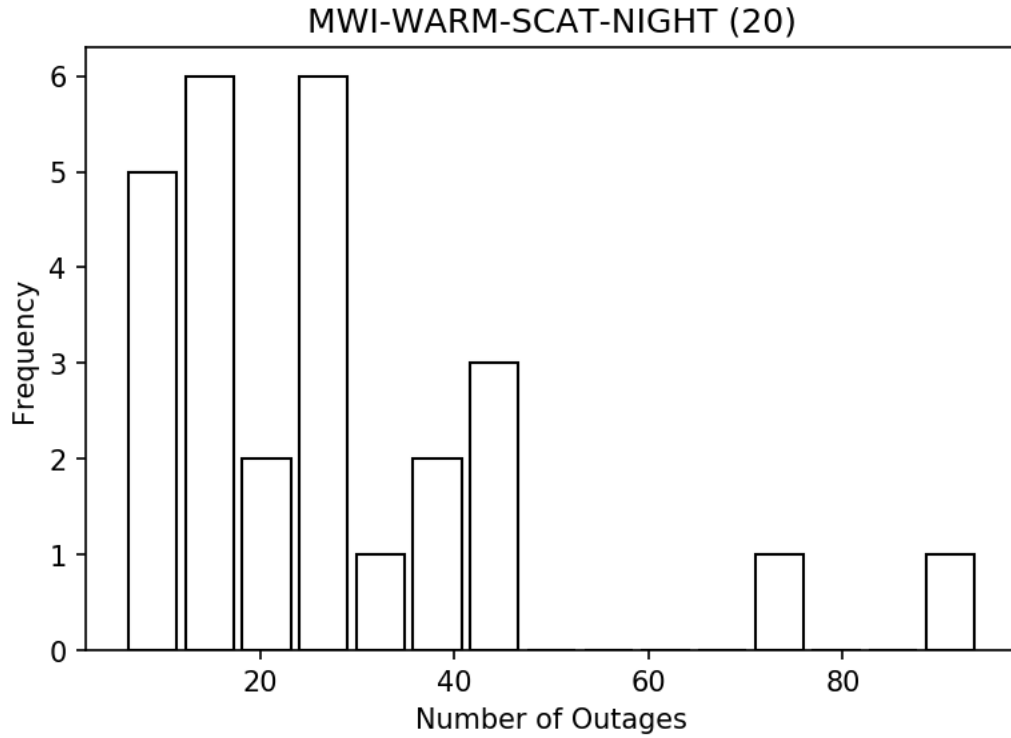


Figure 16. Histogram of observed outage counts on MWI-WARM-SCAT nights.

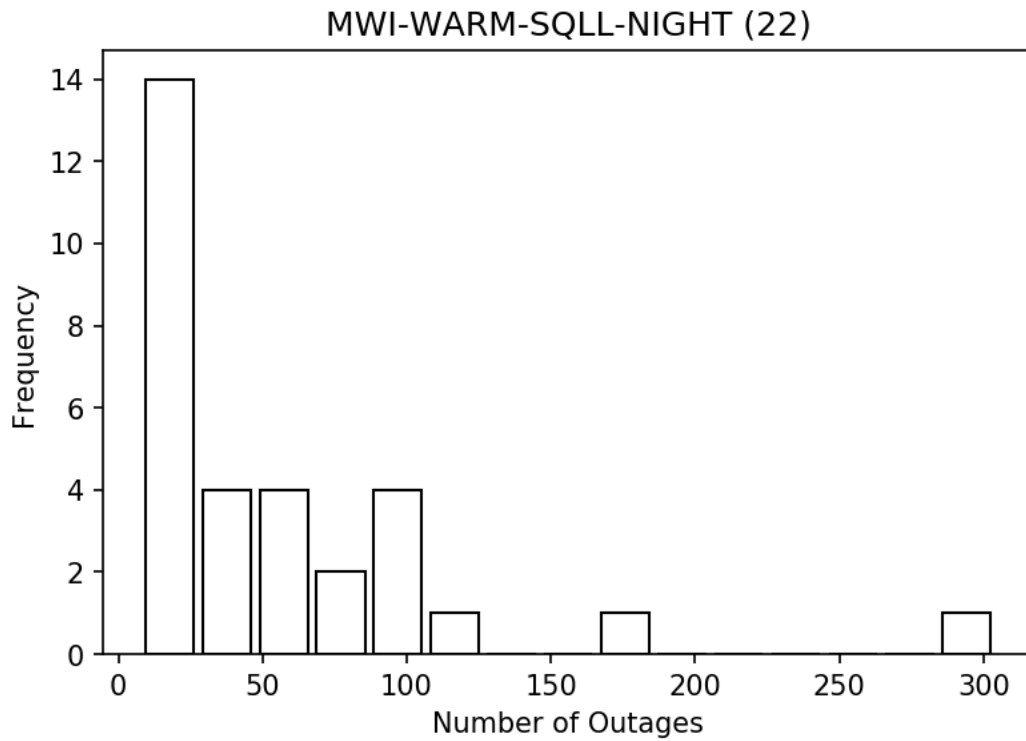


Figure 17. Histogram of observed outage counts on MWI-WARM-SQLL nights.

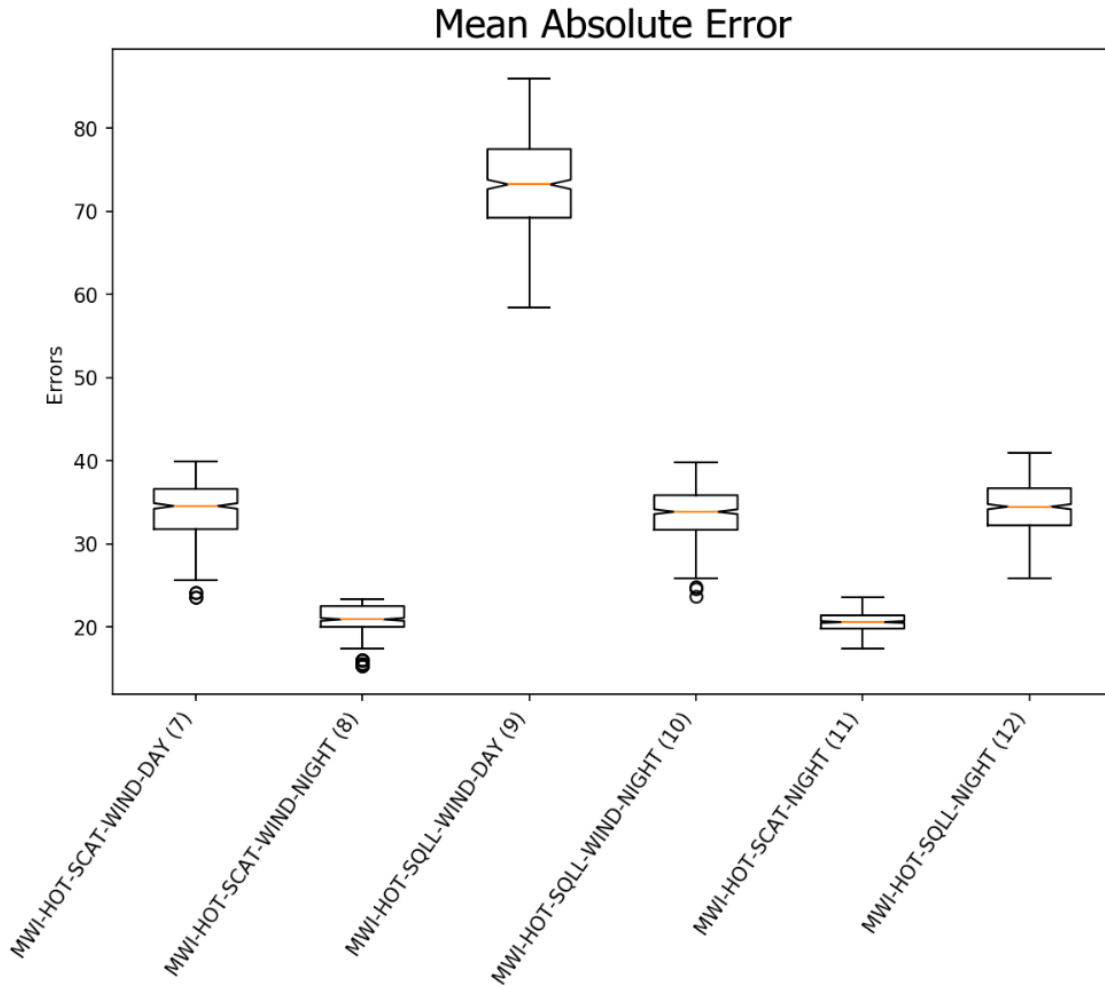


Figure 18a. The mean absolute error distributions of models 7-12. The box marks the 25th percentile (bottom of the box), 50th percentile (centerline), and 75th percentile (top of the box). The lines extending from the boxes mark the 10th percentile (bottom) and 90th percentile (top). The notches signify the 95% confidence intervals of the mean.

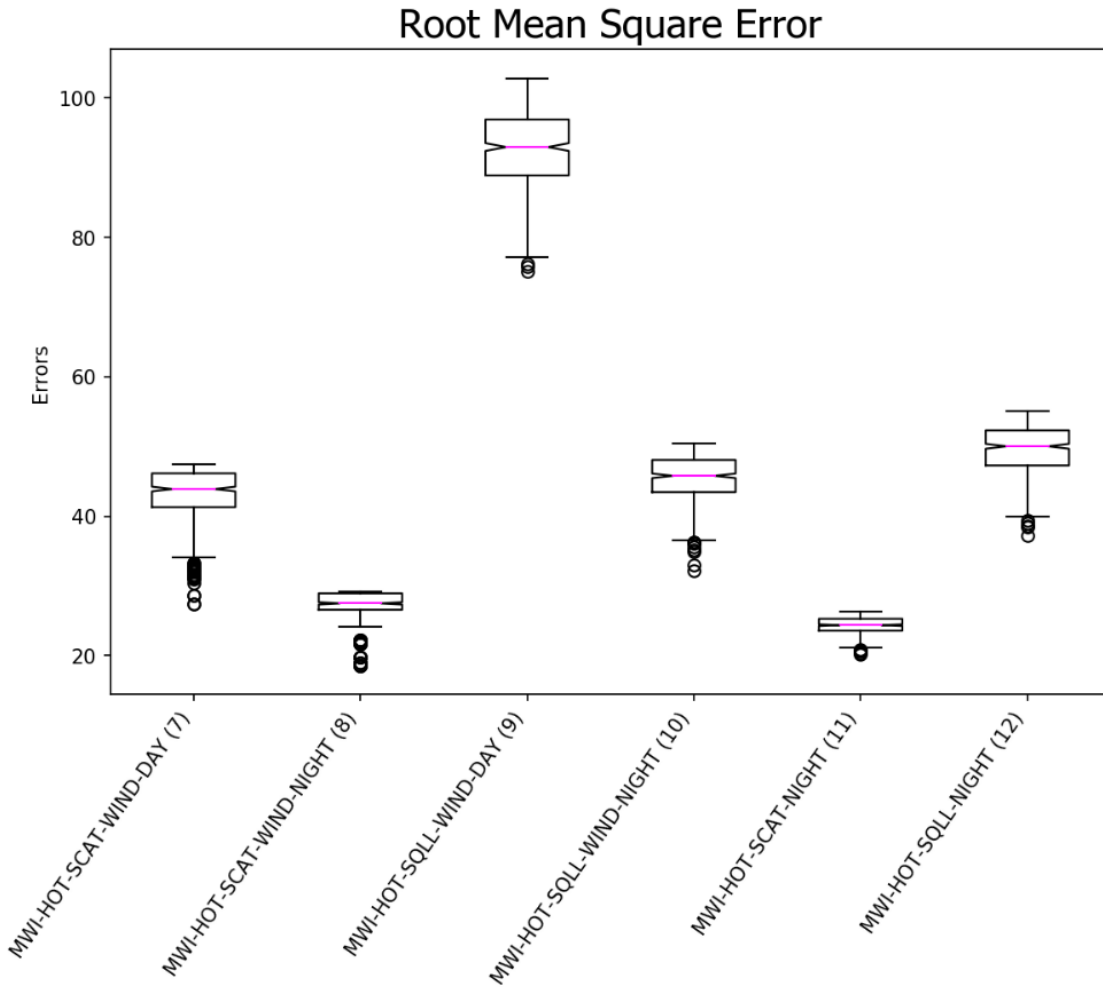


Figure 18b. The root mean square error distributions of models 7-12. The box marks the 25th percentile (bottom of the box), 50th percentile (centerline), and 75th percentile (top of the box). The lines extending from the boxes mark the 10th percentile (bottom) and 90th percentile (top). The notches signify the 95% confidence intervals of the mean.

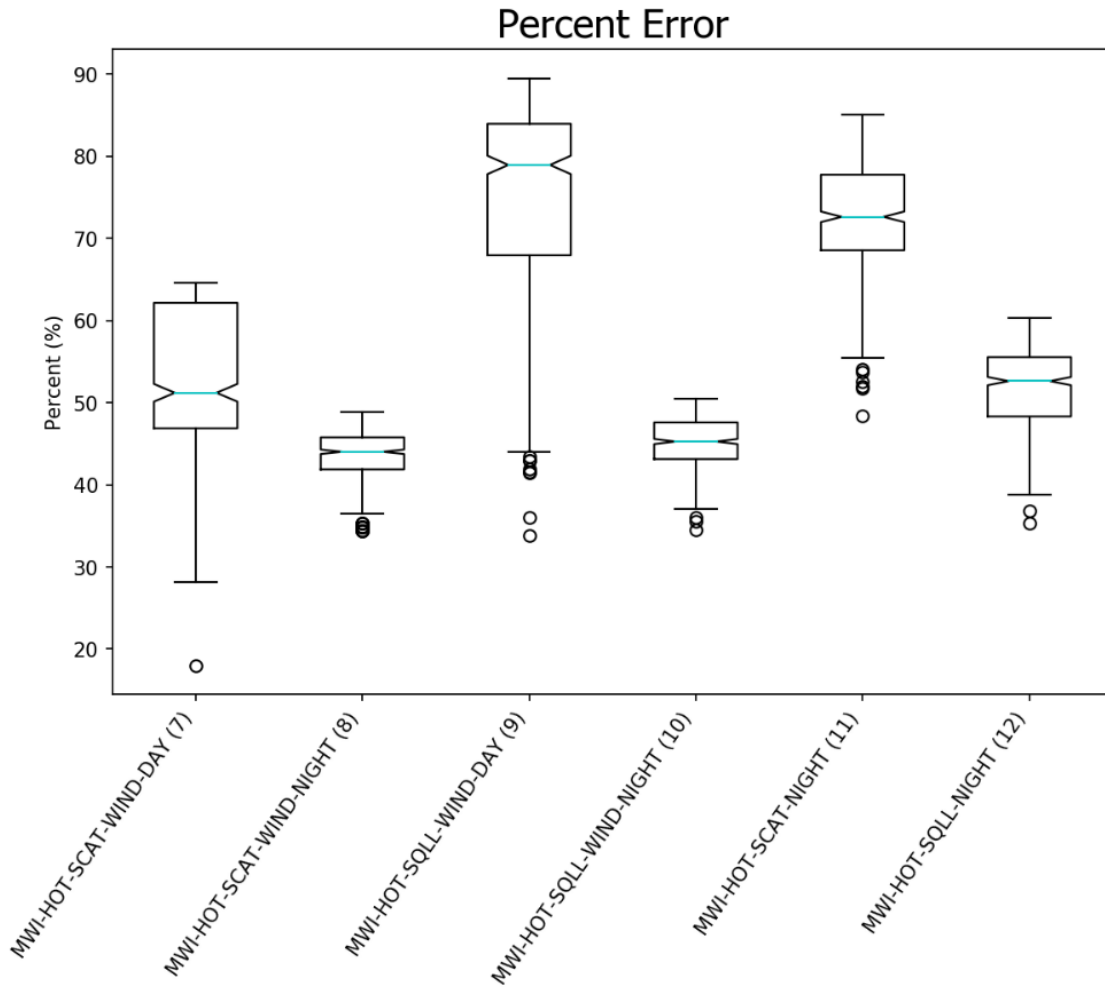


Figure 18c. The percent error distributions of models 7-12. The box marks the 25th percentile (bottom of the box), 50th percentile (centerline), and 75th percentile (top of the box). The lines extending from the boxes mark the 10th percentile (bottom) and 90th percentile (top). The notches signify the 95% confidence intervals of the mean.

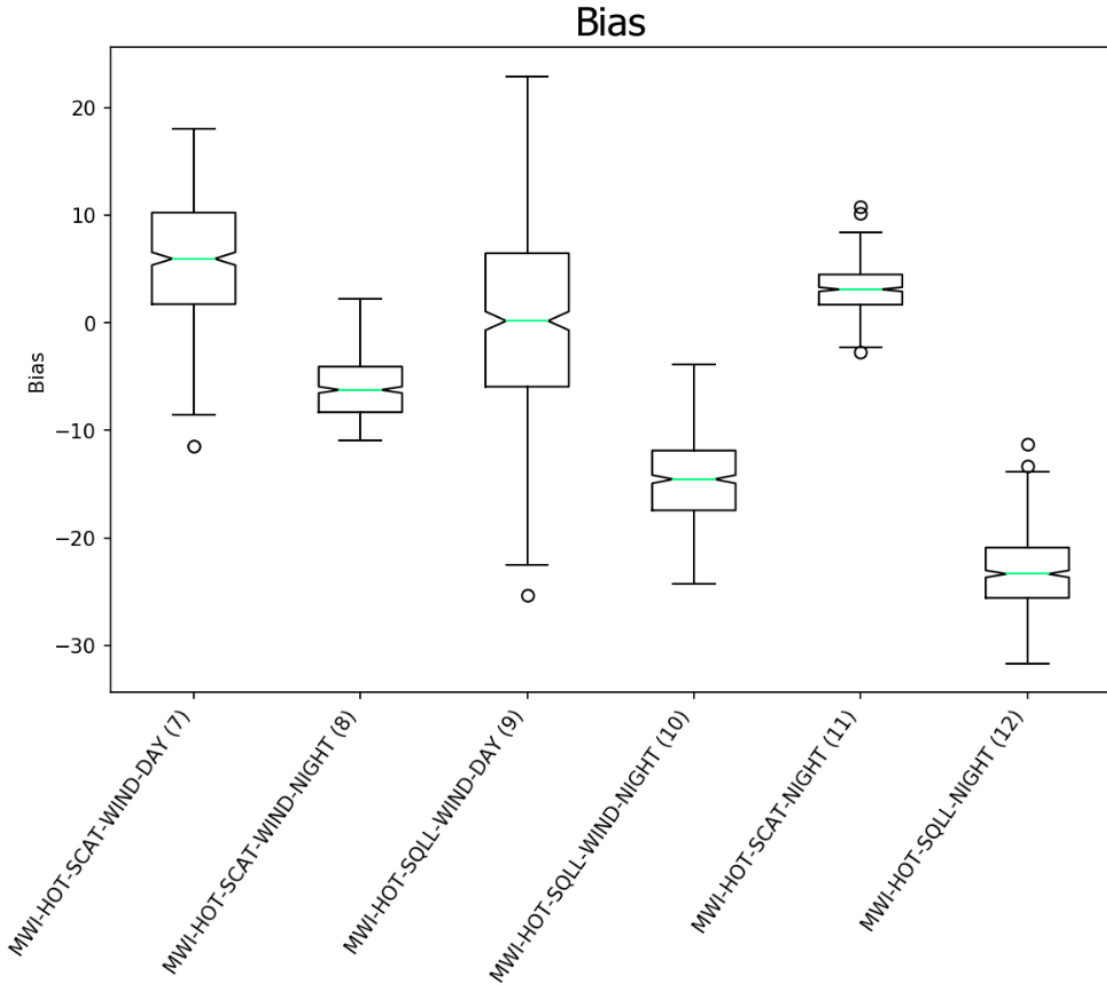


Figure 18d. The bias distributions of models 7-12. The box marks the 25th percentile (bottom of the box), 50th percentile (centerline), and 75th percentile (top of the box). The lines extending from the boxes mark the 10th percentile (bottom) and 90th percentile (top). The notches signify the 95% confidence intervals of the mean.

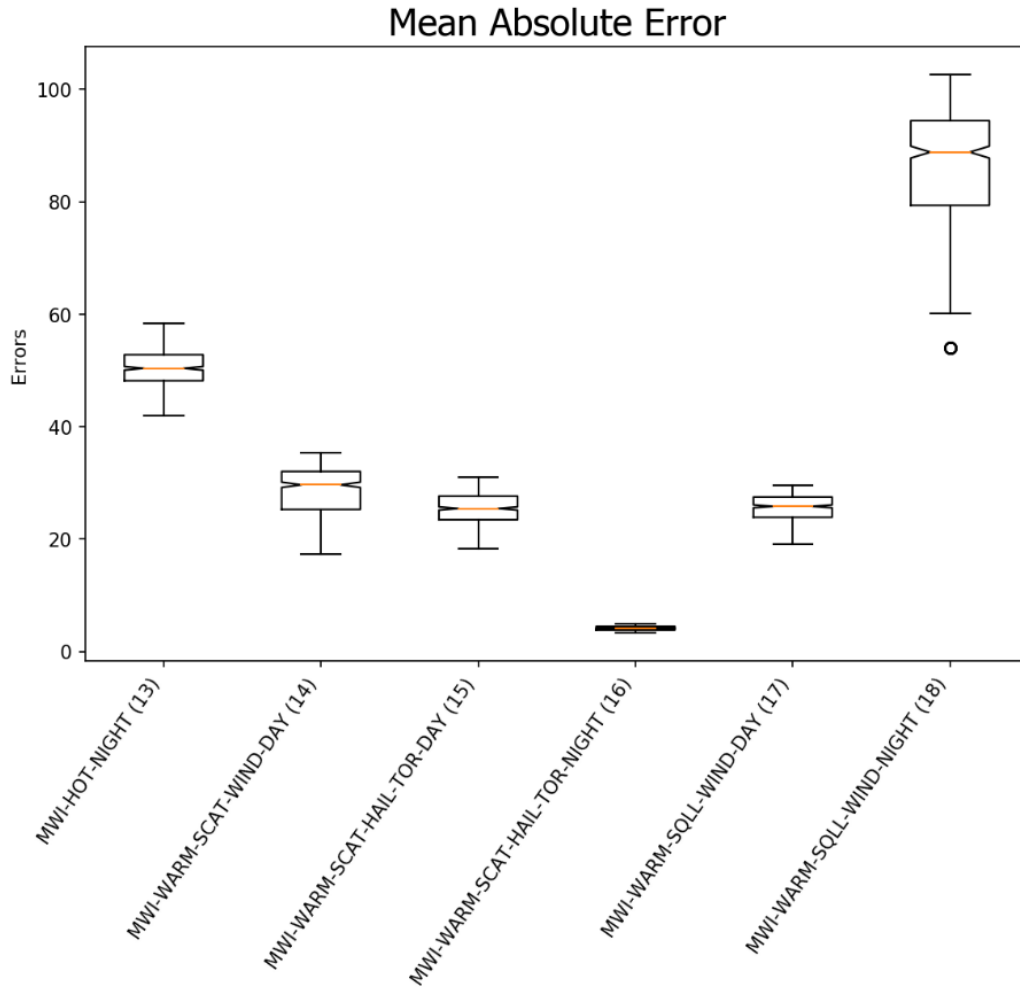


Figure 19a. The mean absolute error distributions of models 13-18. The box marks the 25th percentile (bottom of the box), 50th percentile (centerline), and 75th percentile (top of the box). The lines extending from the boxes mark the 10th percentile (bottom) and 90th percentile (top). The notches signify the 95% confidence intervals of the mean.

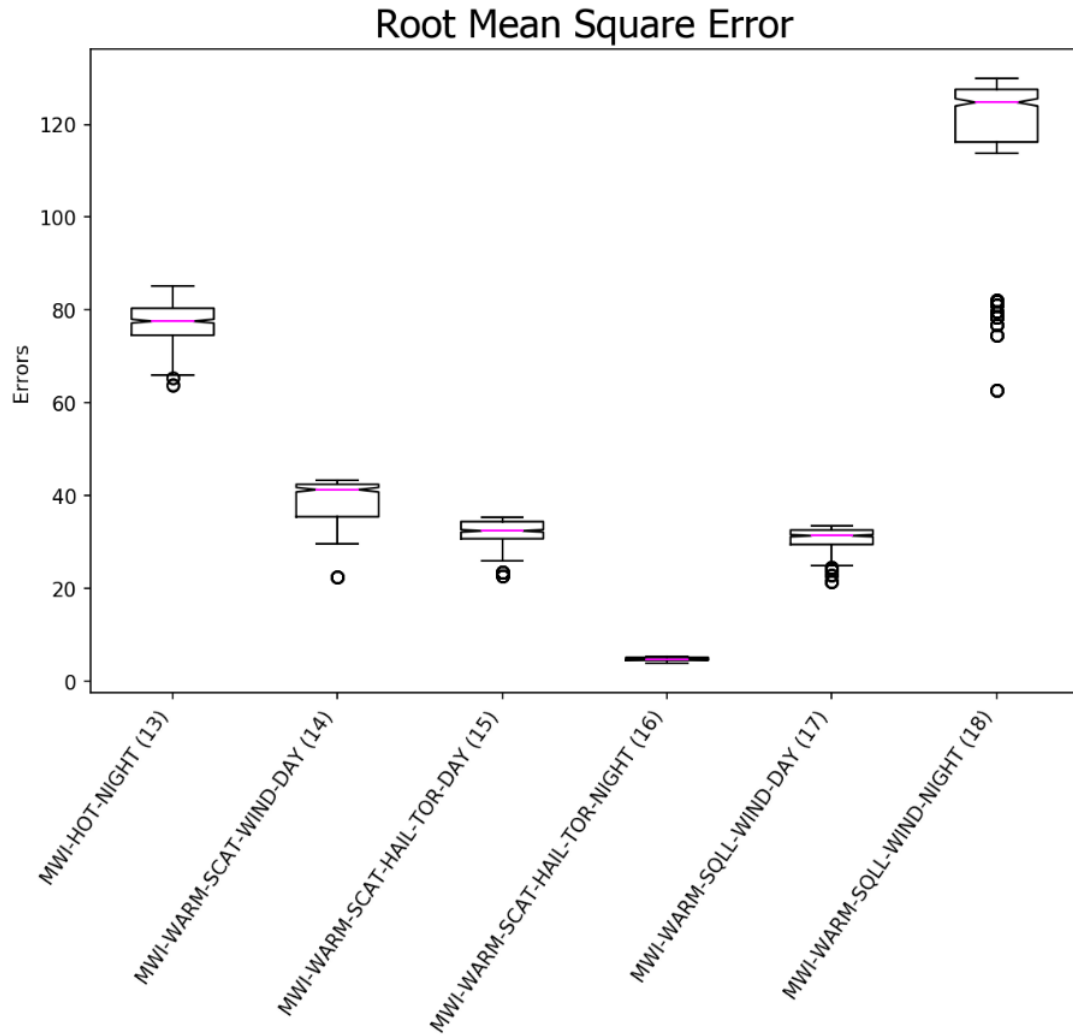


Figure 19b. The root mean square error distributions of models 13-18. The box marks the 25th percentile (bottom of the box), 50th percentile (centerline), and 75th percentile (top of the box). The lines extending from the boxes mark the 10th percentile (bottom) and 90th percentile (top). The notches signify the 95% confidence intervals of the mean.

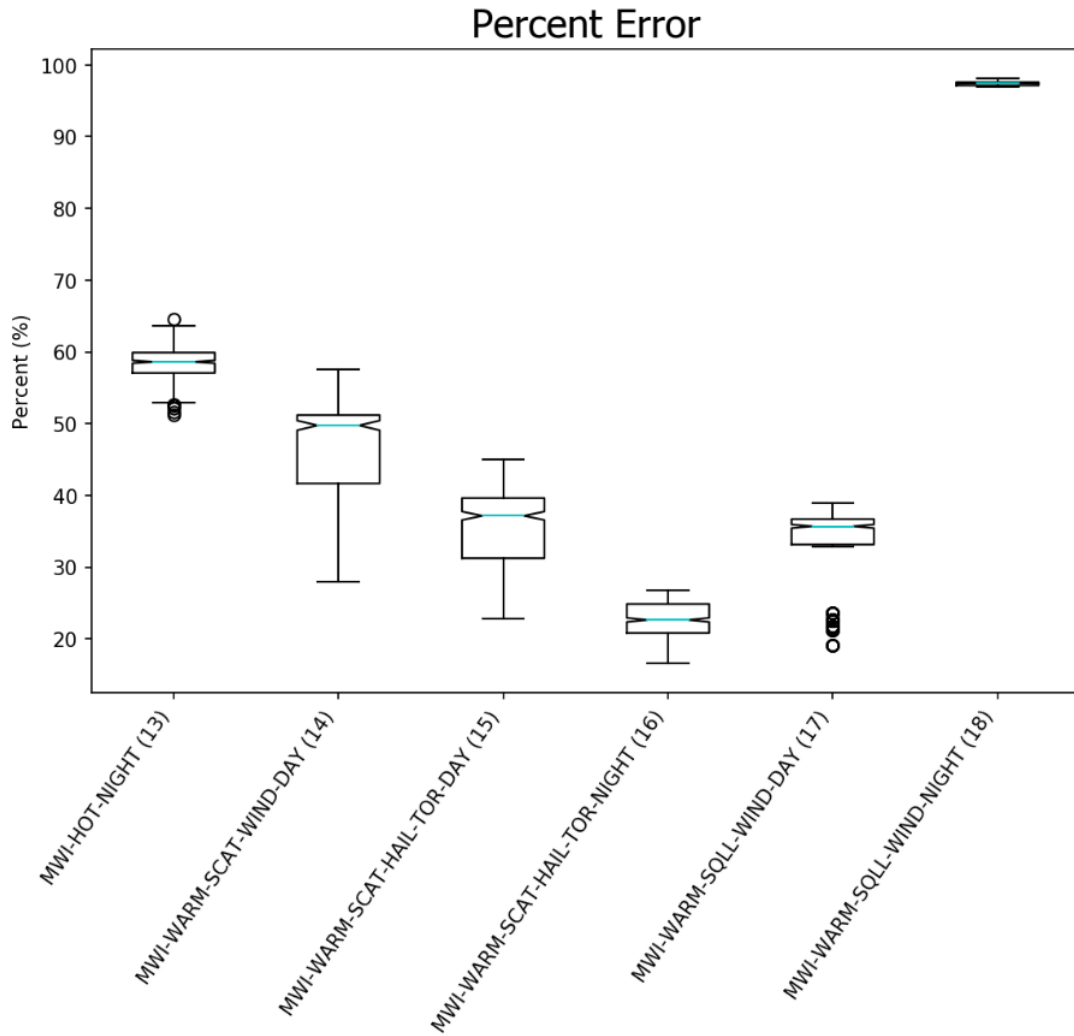


Figure 19c. The percent error distributions of models 13-18. The box marks the 25th percentile (bottom of the box), 50th percentile (centerline), and 75th percentile (top of the box). The lines extending from the boxes mark the 10th percentile (bottom) and 90th percentile (top). The notches signify the 95% confidence intervals of the mean.

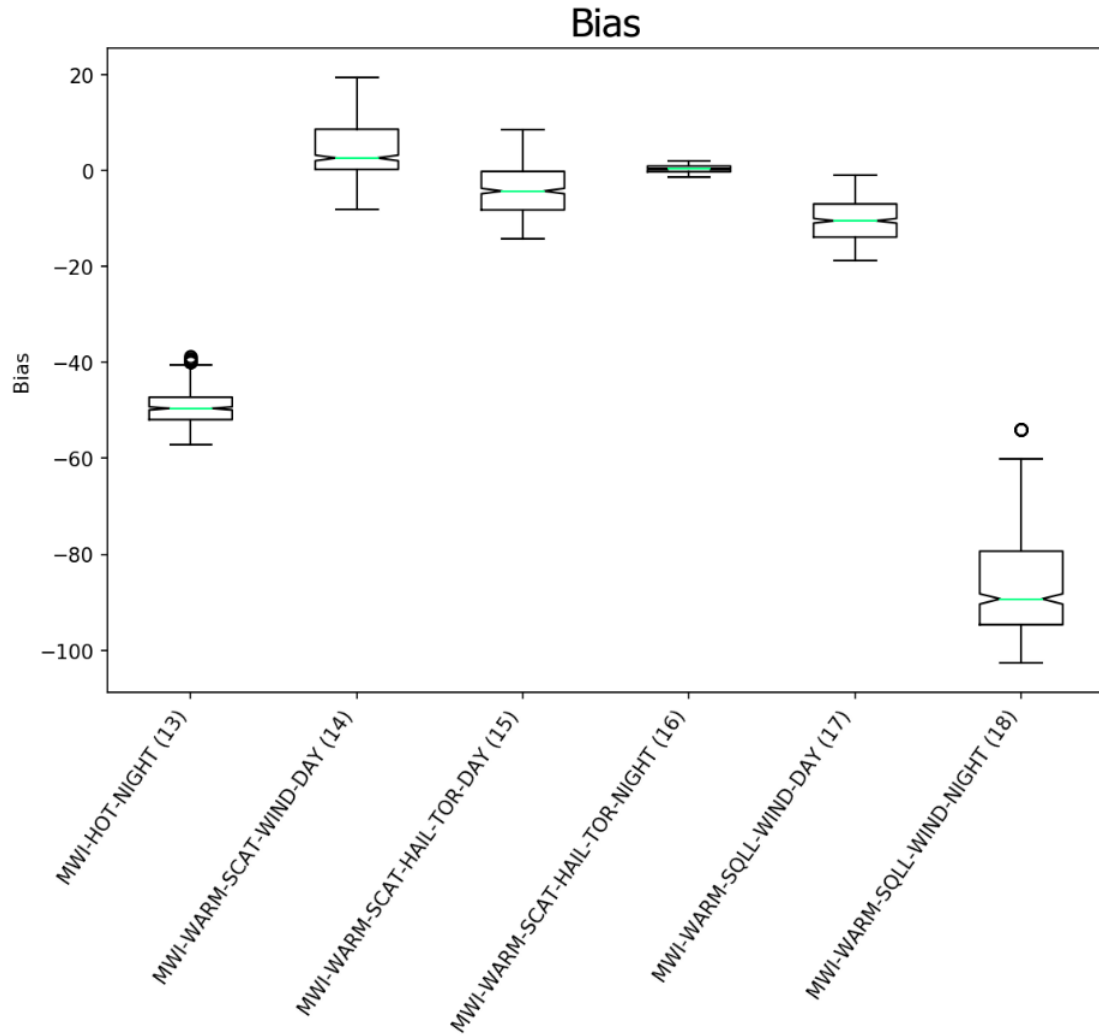


Figure 19d. The bias distributions of models 13-18. The box marks the 25th percentile (bottom of the box), 50th percentile (centerline), and 75th percentile (top of the box). The lines extending from the boxes mark the 10th percentile (bottom) and 90th percentile (top). The notches signify the 95% confidence intervals of the mean.

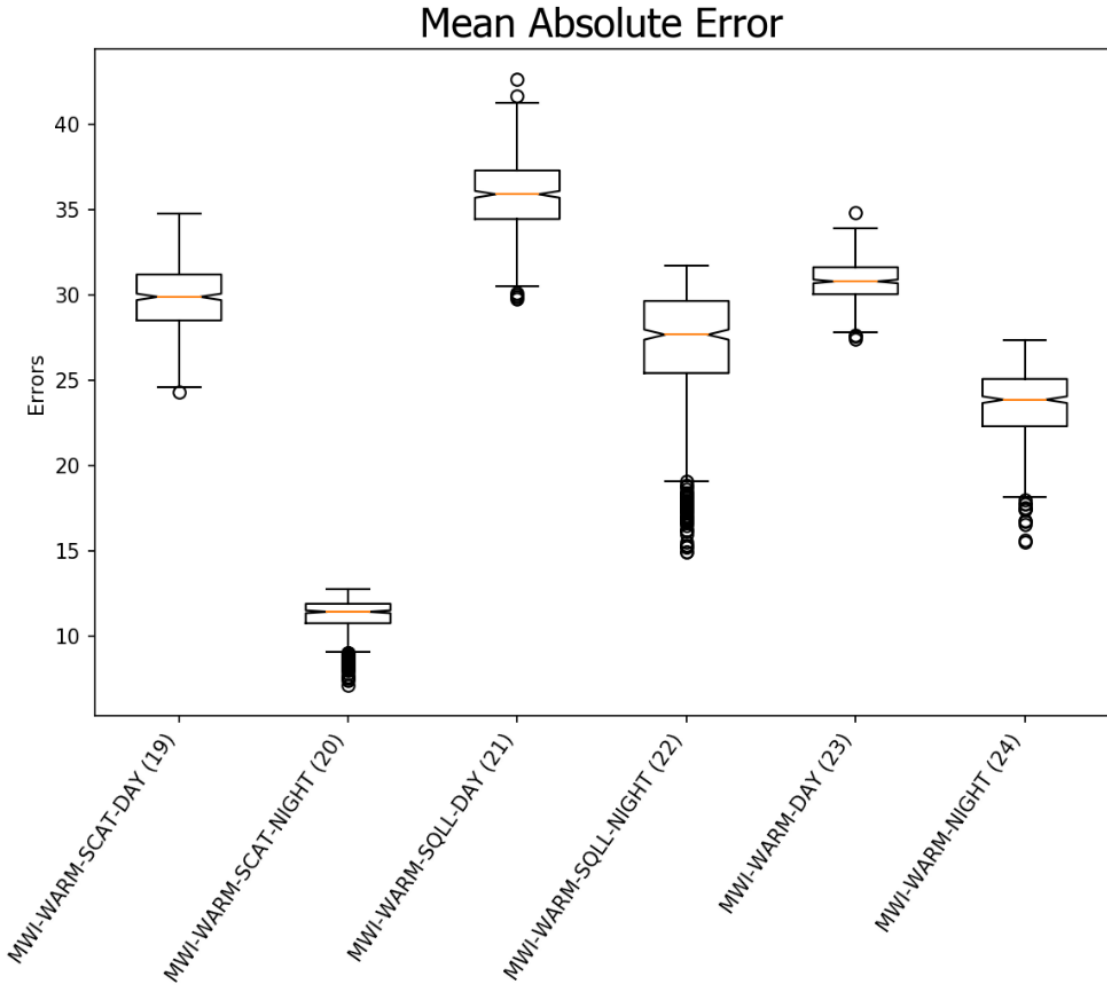


Figure 20a. The mean absolute error distributions of models 19-24. The box marks the 25th percentile (bottom of the box), 50th percentile (centerline), and 75th percentile (top of the box). The lines extending from the boxes mark the 10th percentile (bottom) and 90th percentile (top). The notches signify the 95% confidence intervals of the mean.

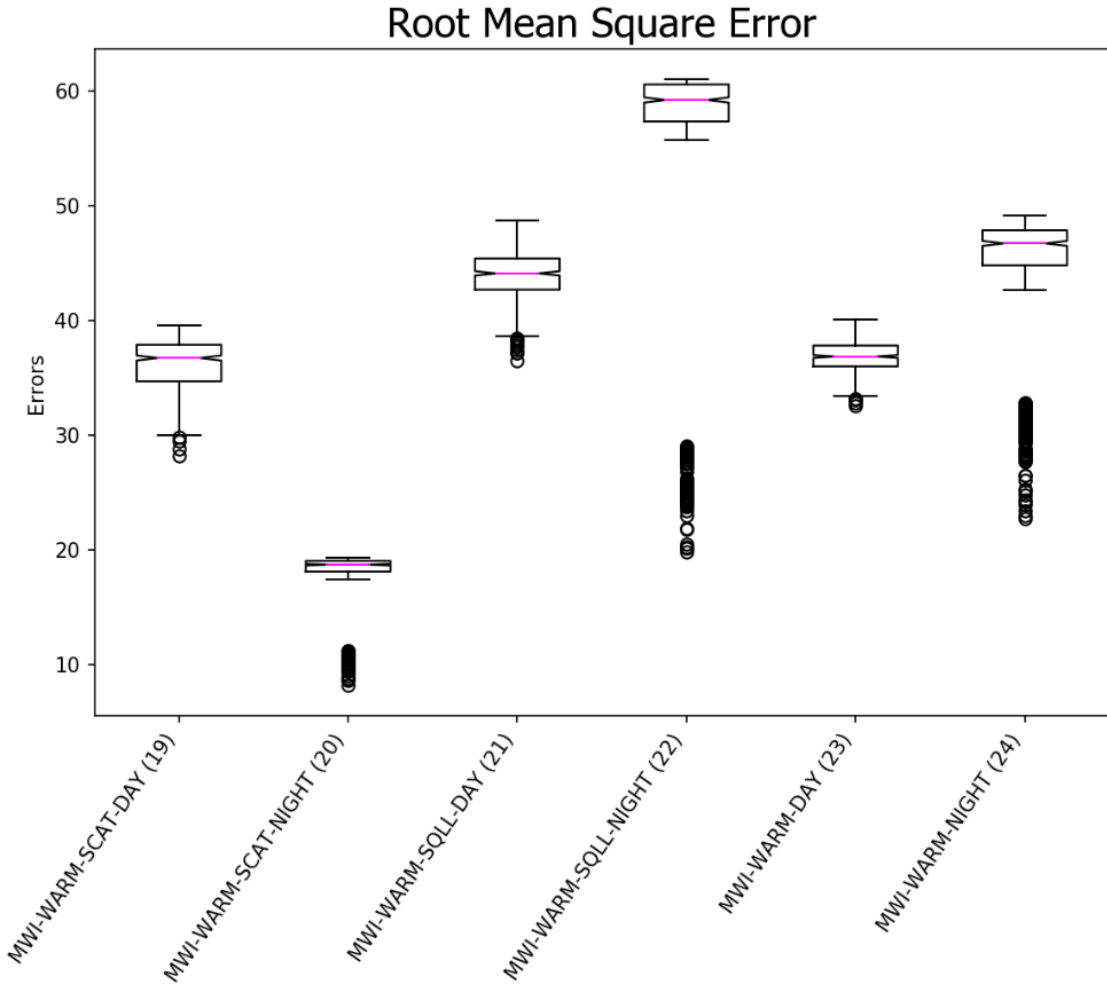


Figure 20b. The root mean square error distributions of models 19-24. The box marks the 25th percentile (bottom of the box), 50th percentile (centerline), and 75th percentile (top of the box). The lines extending from the boxes mark the 10th percentile (bottom) and 90th percentile (top). The notches signify the 95% confidence intervals of the mean.

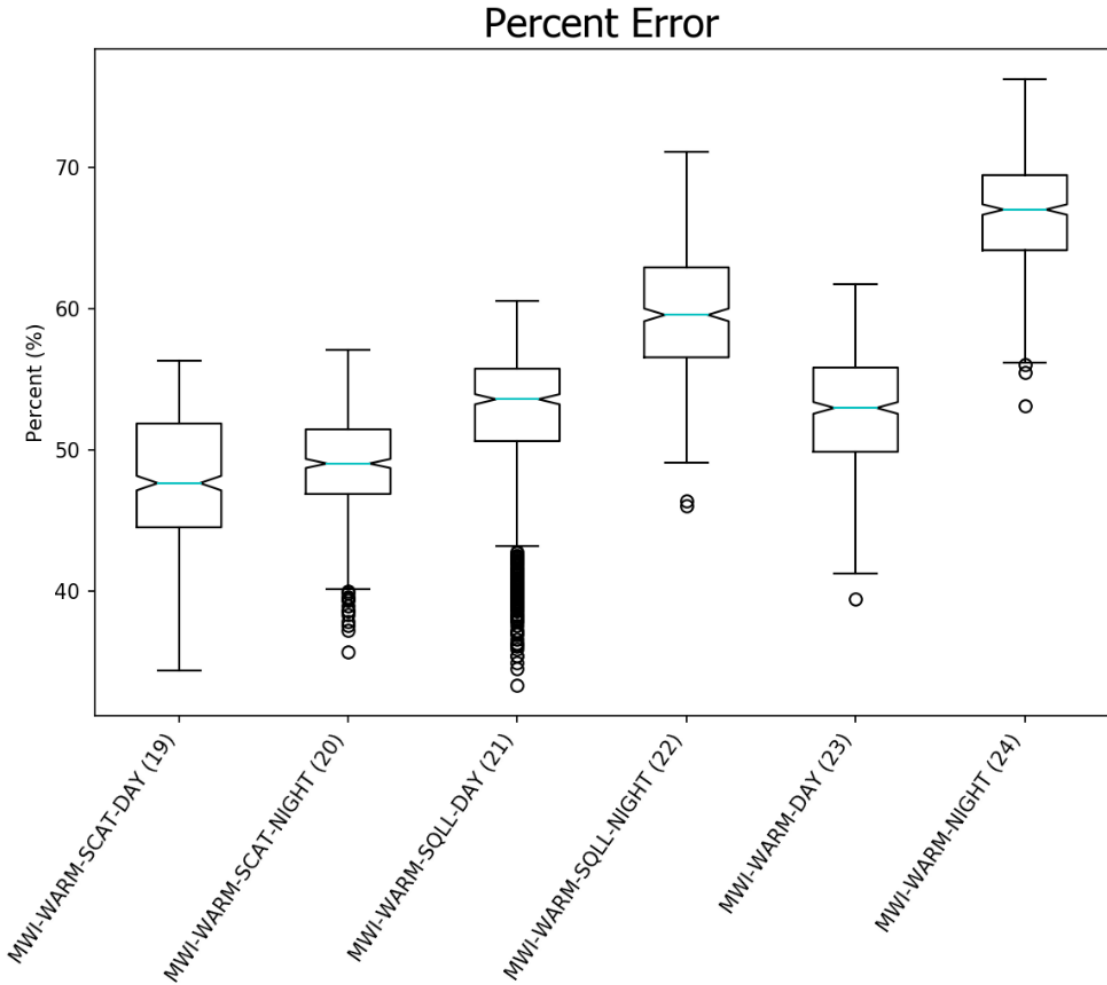


Figure 20c. The percent error distributions of models 19-24. The box marks the 25th percentile (bottom of the box), 50th percentile (centerline), and 75th percentile (top of the box). The lines extending from the boxes mark the 10th percentile (bottom) and 90th percentile (top). The notches signify the 95% confidence intervals of the mean.

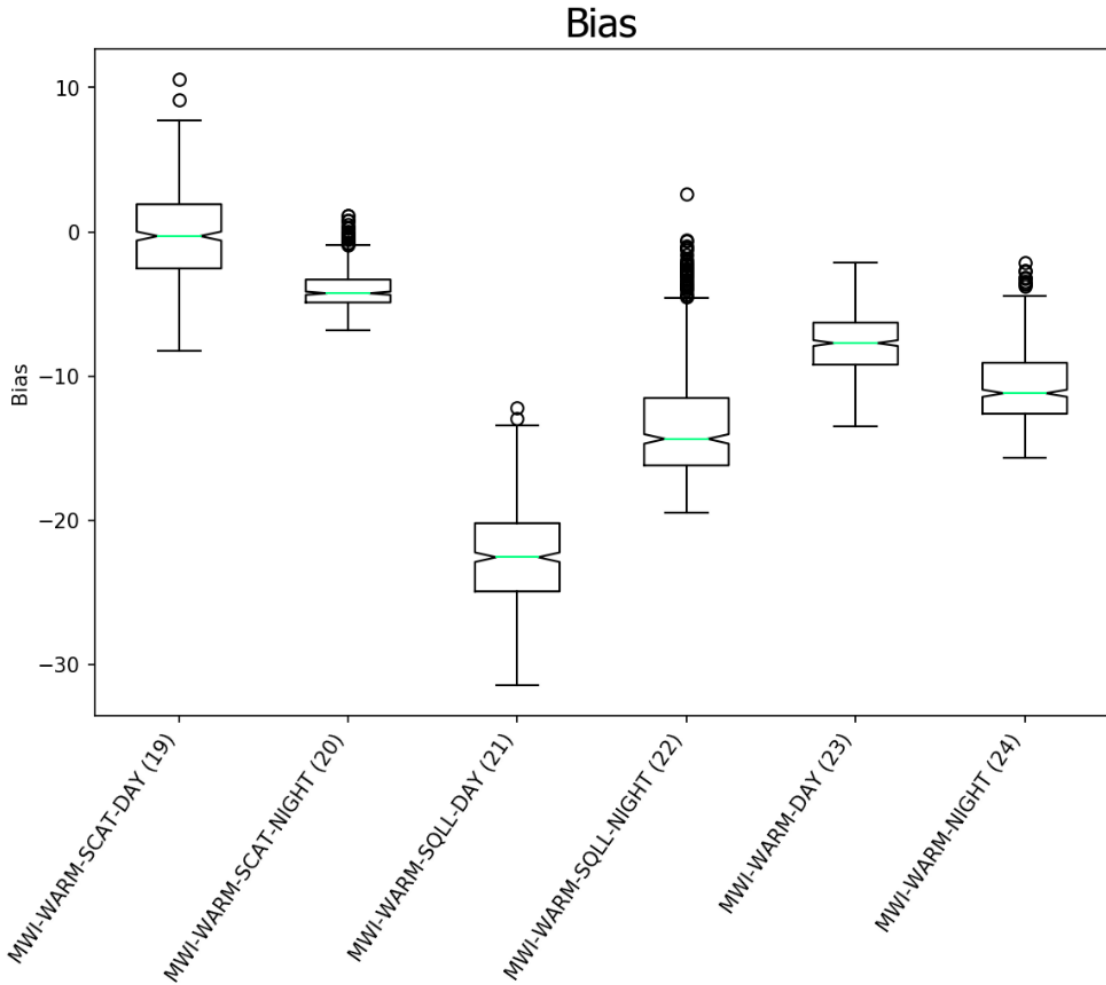


Figure 20d. The bias distributions of models 19-24. The box marks the 25th percentile (bottom of the box), 50th percentile (centerline), and 75th percentile (top of the box). The lines extending from the boxes mark the 10th percentile (bottom) and 90th percentile (top). The notches signify the 95% confidence intervals of the mean.

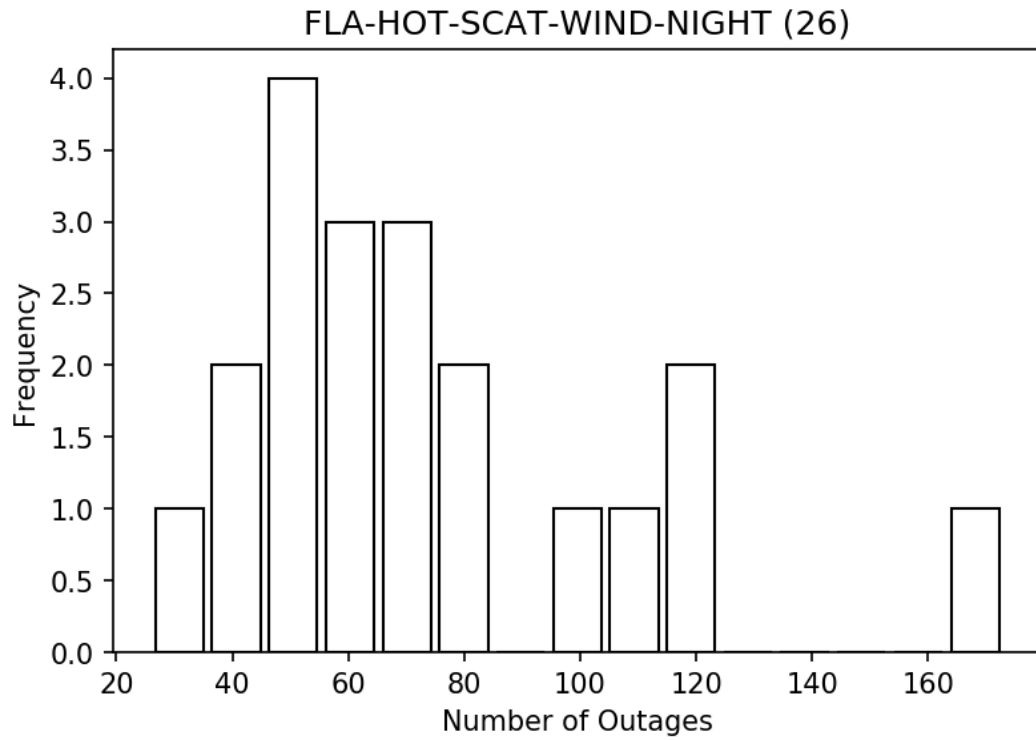


Figure 21. Histogram of observed outage counts on FLA-HOT-SCAT-WIND nights.

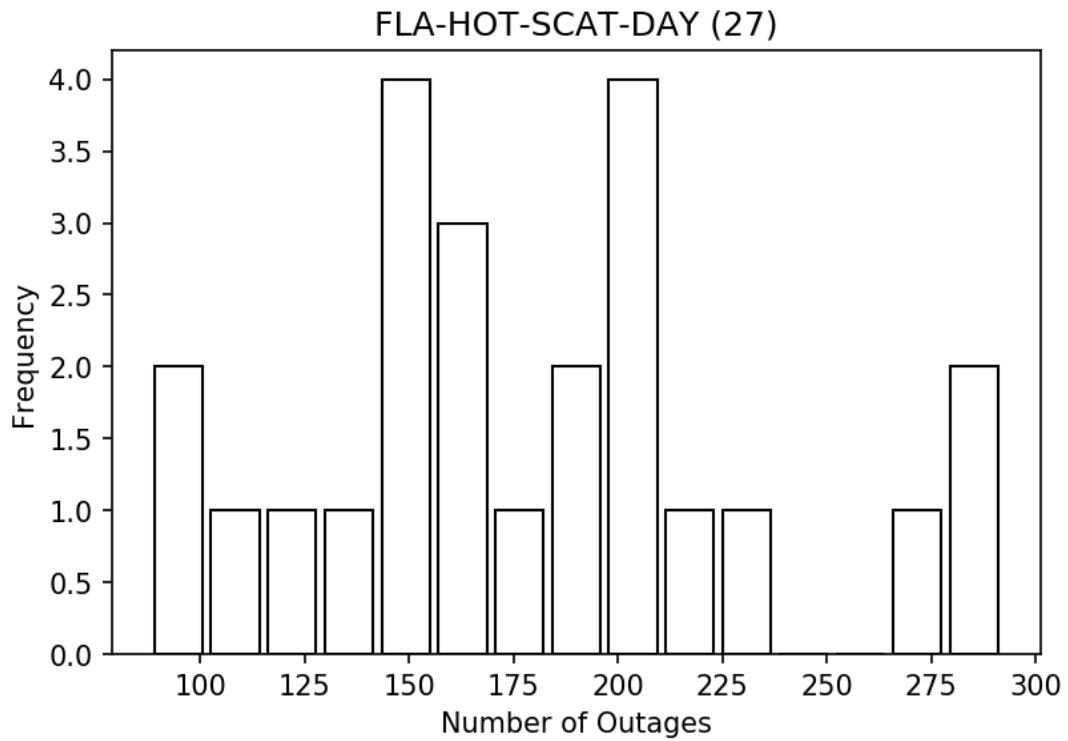


Figure 22. Histogram of observed outage counts on FLA-HOT-SCAT days.

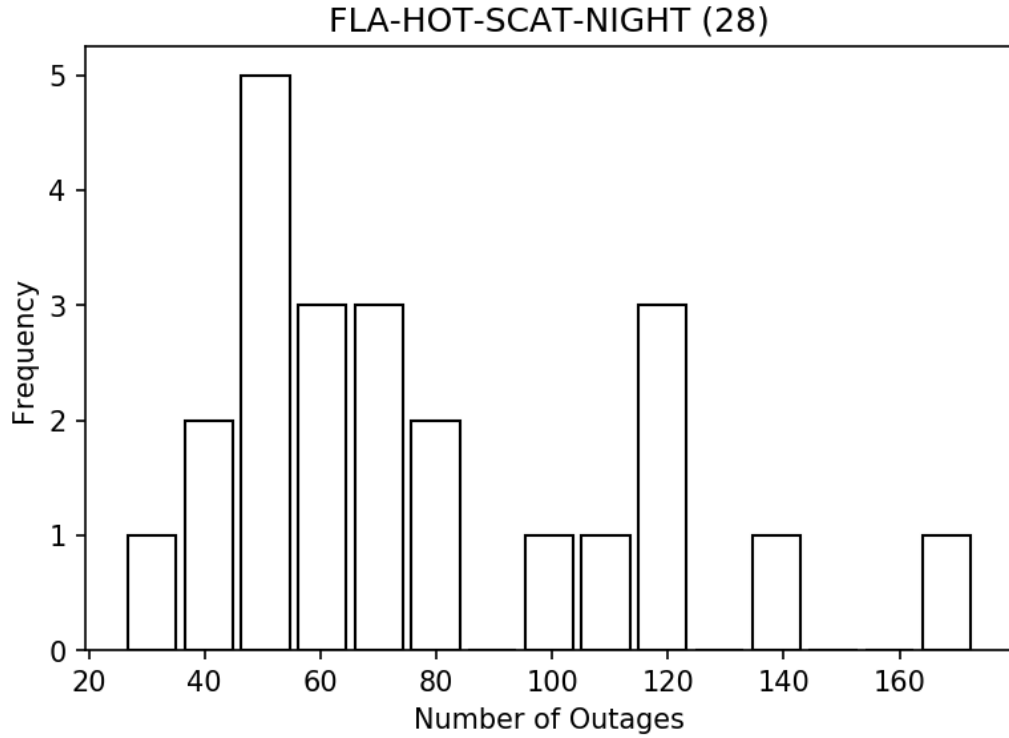


Figure 23. Histogram of observed outage counts on FLA-HOT-SCAT nights.

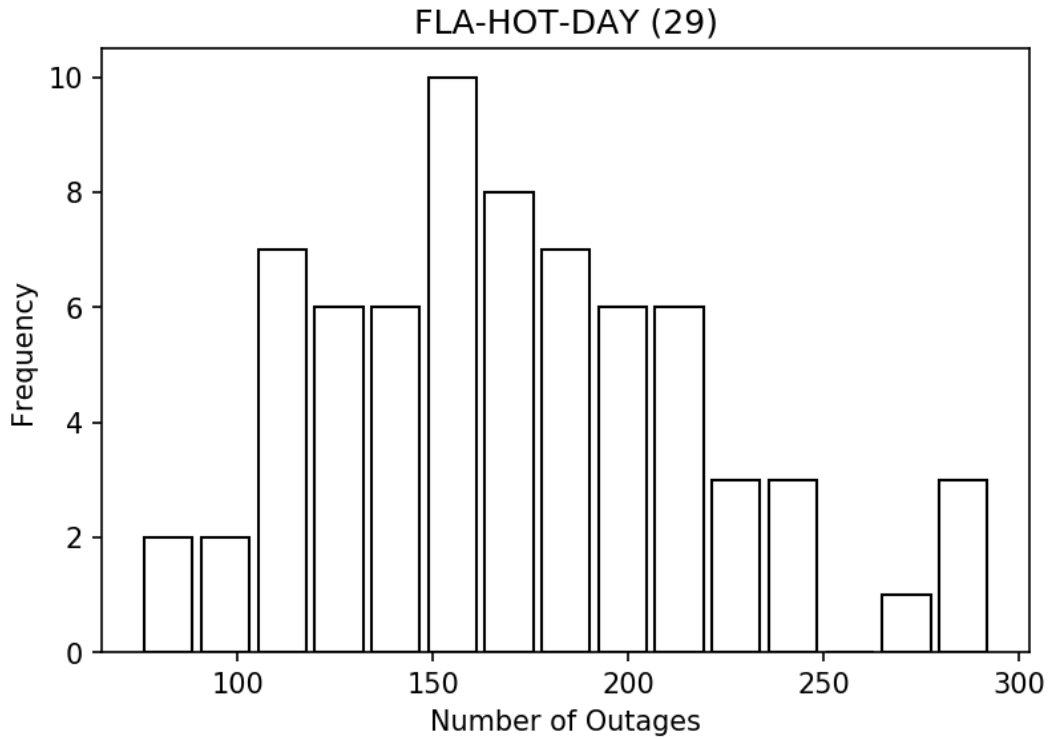


Figure 24. Histogram of observed outage counts on FLA-HOT days.

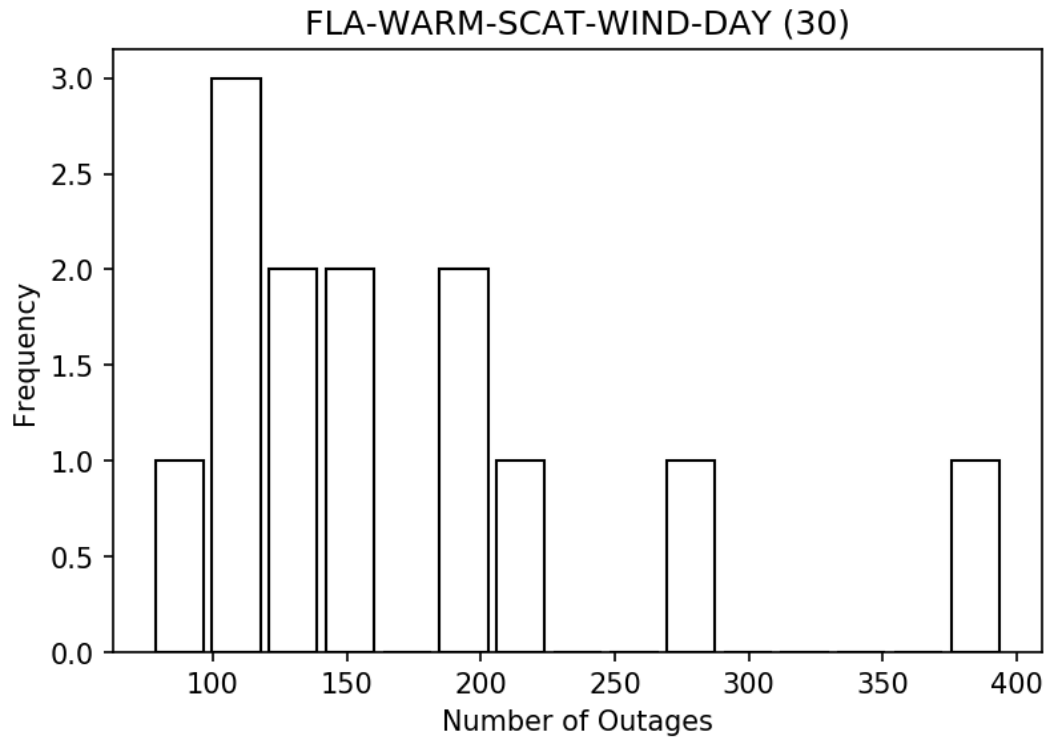


Figure 25. Histogram of observed outage counts on FLA-WARM-SCAT-WIND days.

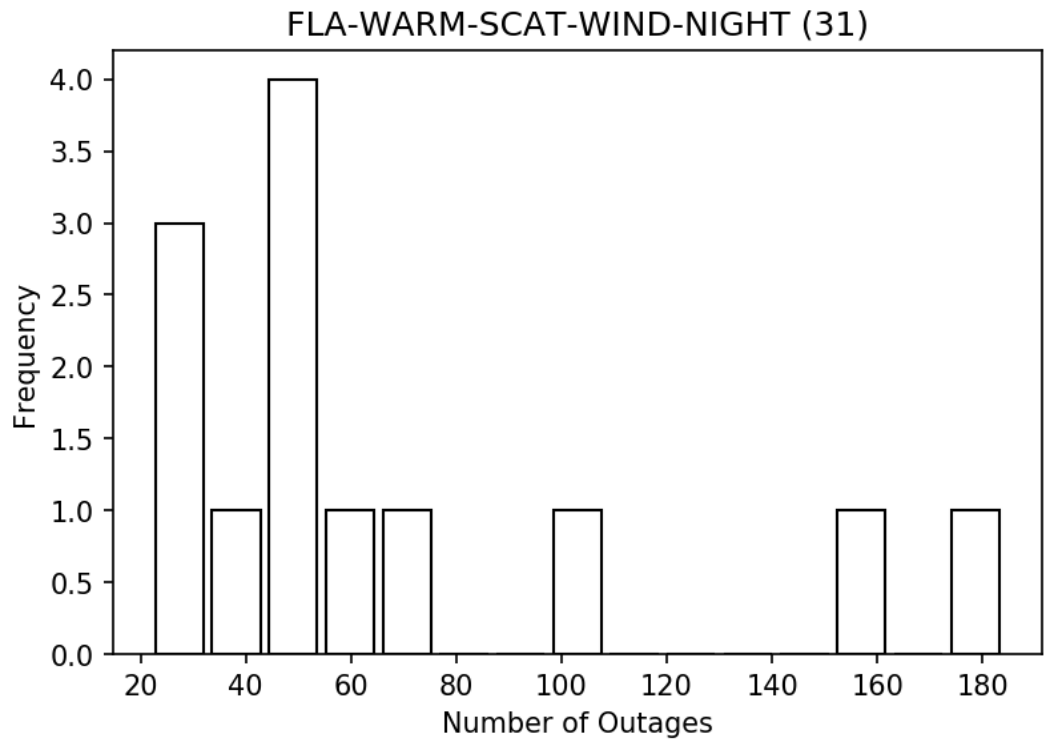


Figure 26. Histogram of observed outage counts on FLA-WARM-SCAT-WIND nights.

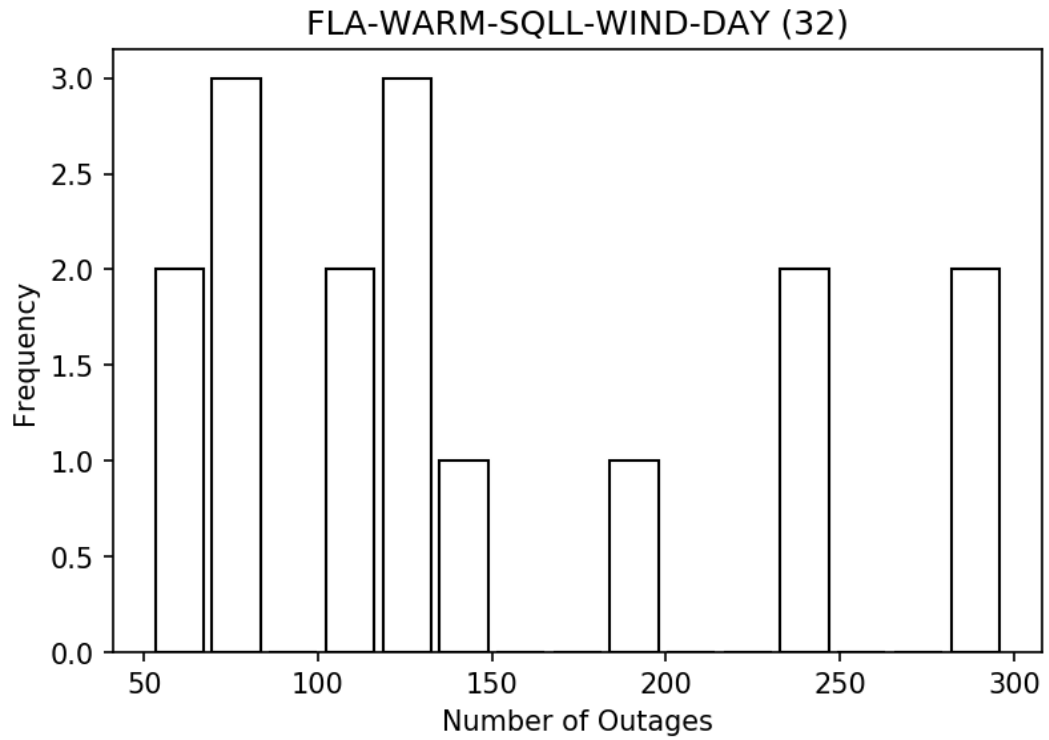


Figure 27. Histogram of observed outage counts on FLA-HOT-SQLL-WIND days.

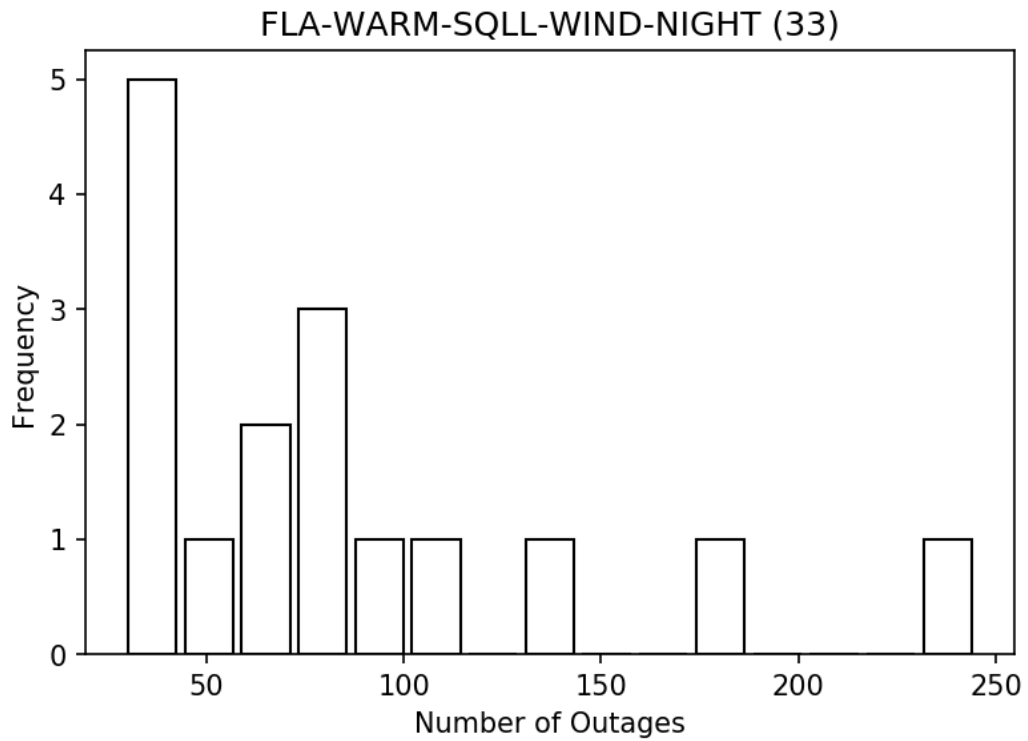


Figure 28. Histogram of observed outage counts on FLA-WARM-SQLL-WIND nights.

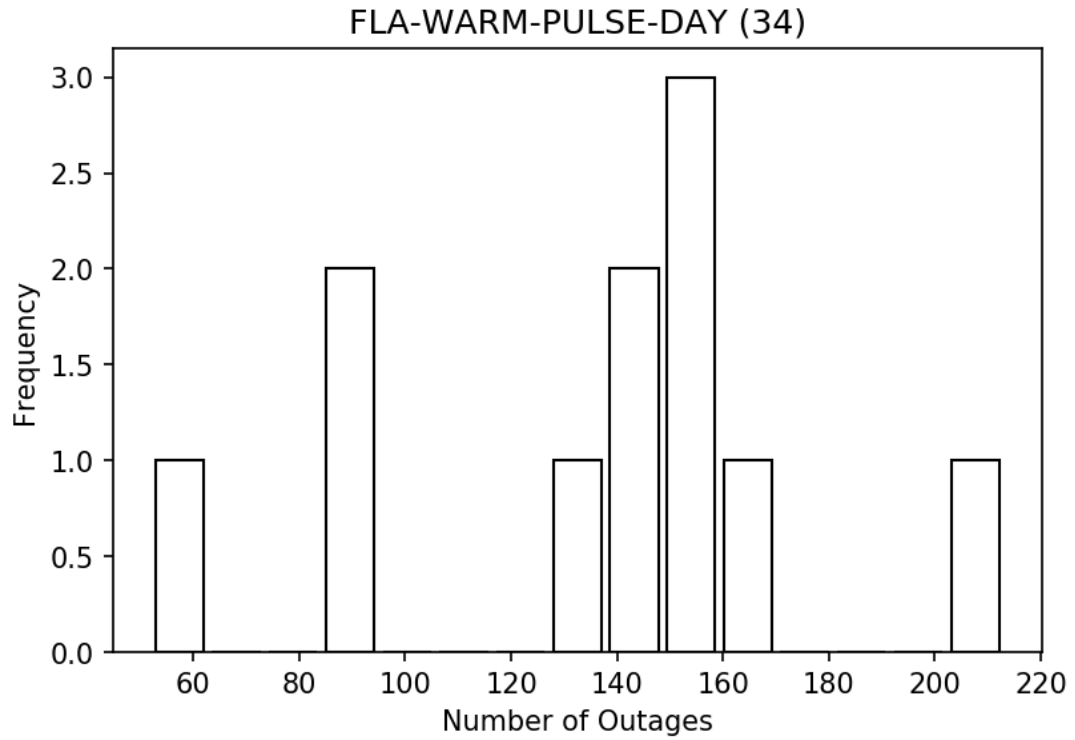


Figure 29. Histogram of observed outage counts on FLA-WARM-PULSE days.

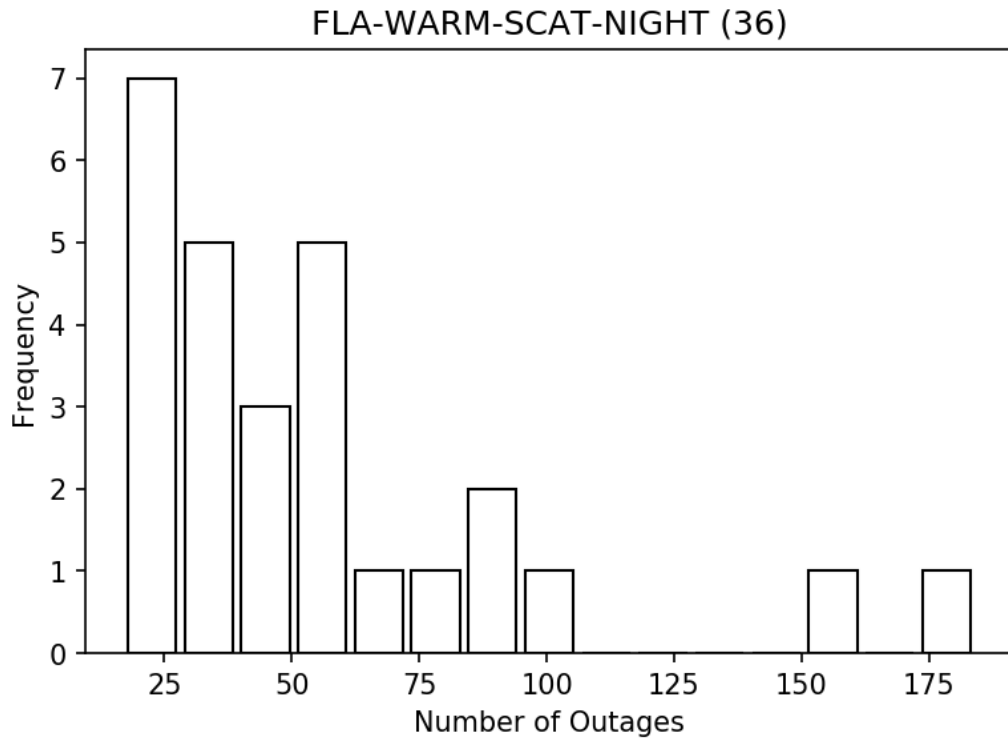


Figure 30. Histogram of observed outage counts on FLA-WARM-SCAT nights.

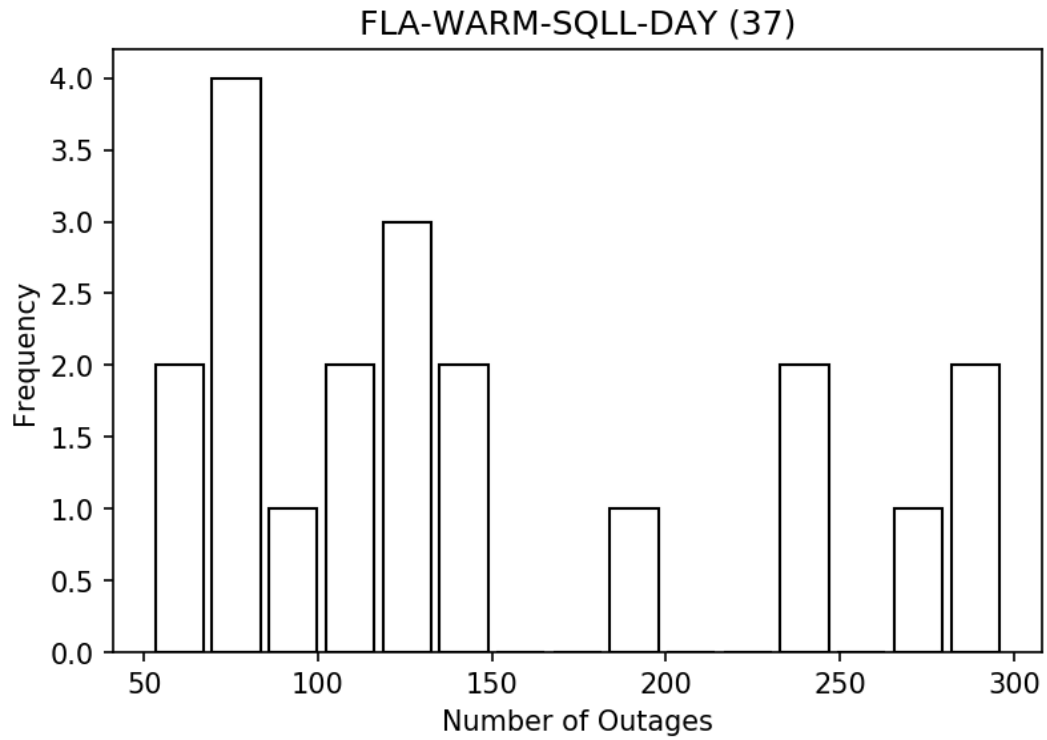


Figure 31. Histogram of observed outage counts on FLA-HOT-SQLL days.

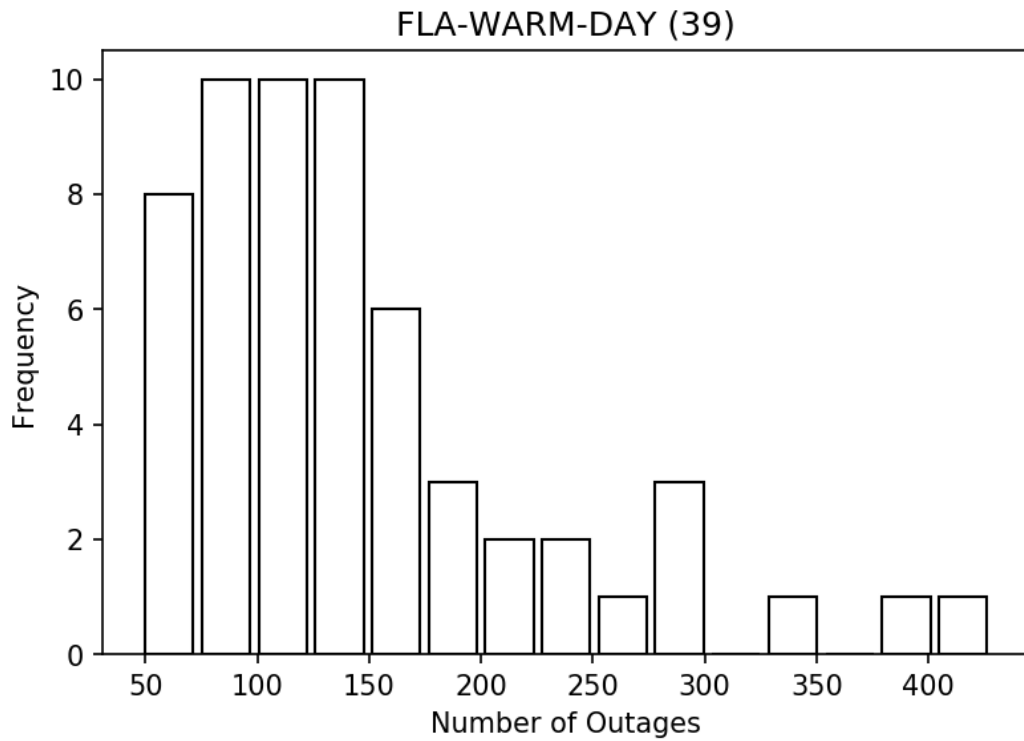


Figure 32. Histogram of observed outage counts on FLA-WARM nights.

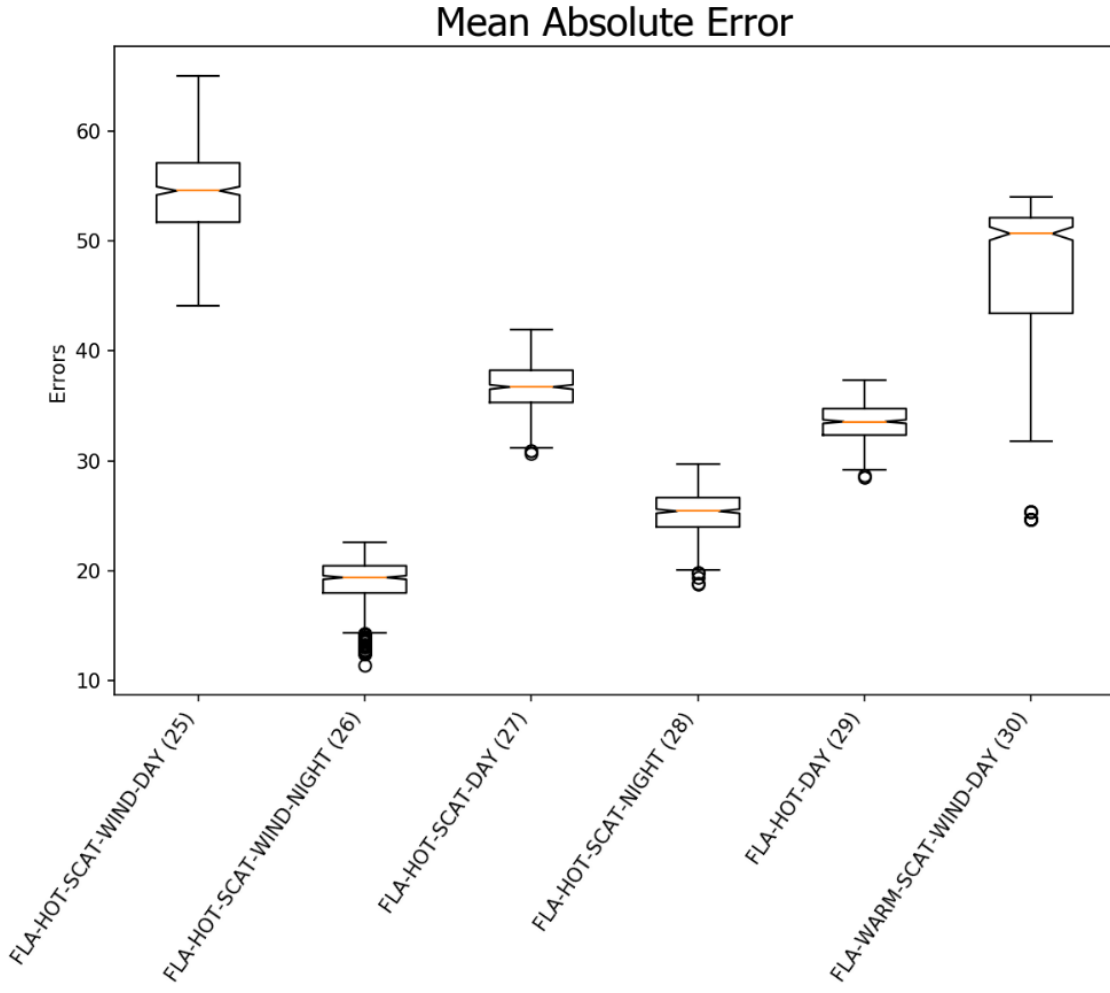


Figure 33a. The mean absolute error distributions of models 25-30. The box marks the 25th percentile (bottom of the box), 50th percentile (centerline), and 75th percentile (top of the box). The lines extending from the boxes mark the 10th percentile (bottom) and 90th percentile (top). The notches signify the 95% confidence intervals of the mean.

Root Mean Square Error

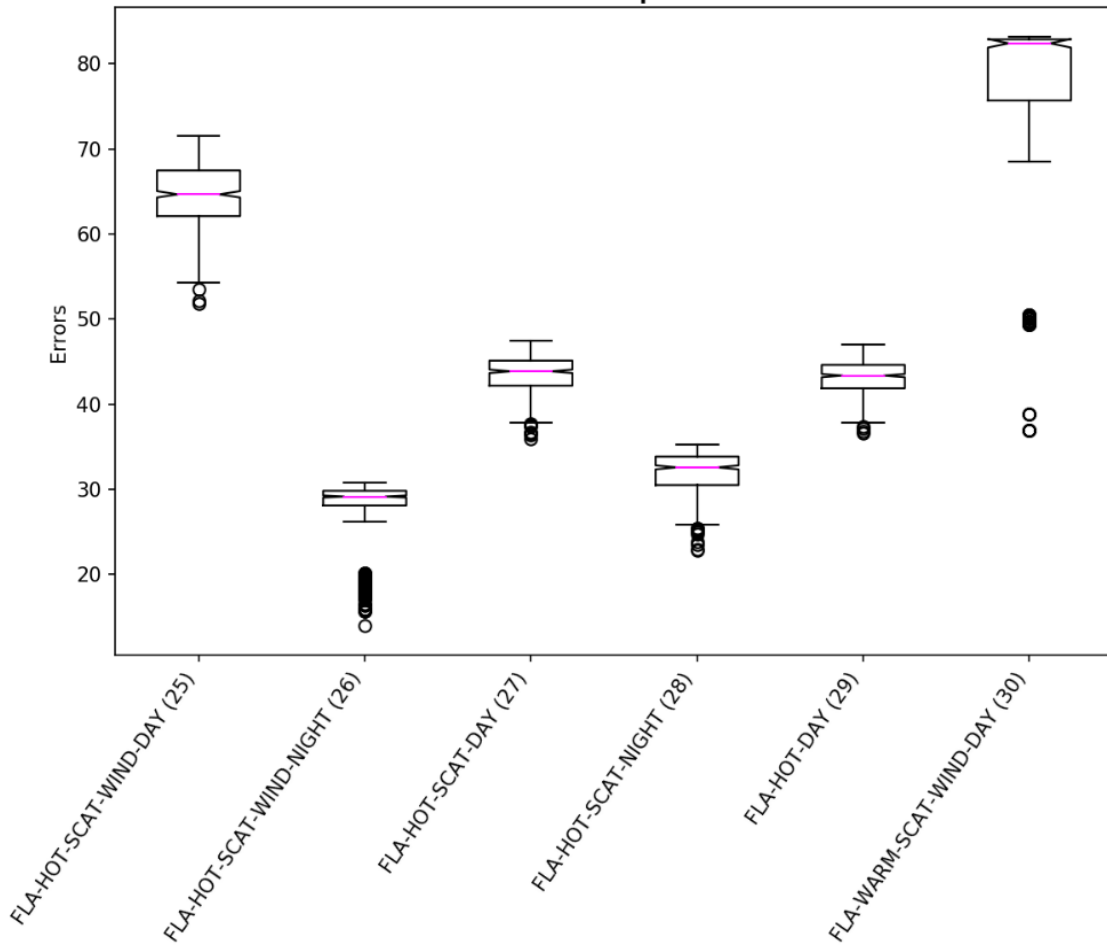


Figure 33b. The root mean square error distributions of models 25-30. The box marks the 25th percentile (bottom of the box), 50th percentile (centerline), and 75th percentile (top of the box). The lines extending from the boxes mark the 10th percentile (bottom) and 90th percentile (top). The notches signify the 95% confidence intervals of the mean.

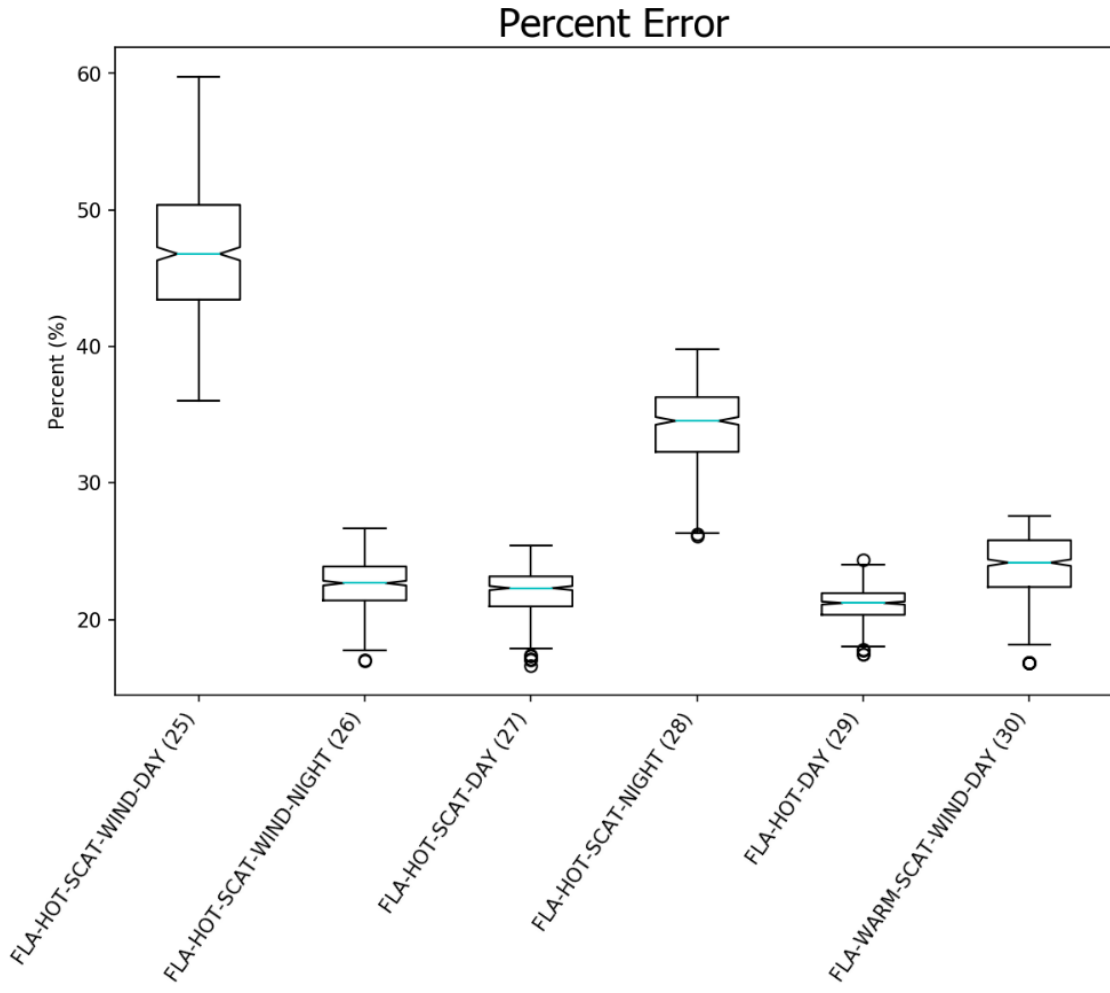


Figure 33c. The percent error distributions of models 25-30. The box marks the 25th percentile (bottom of the box), 50th percentile (centerline), and 75th percentile (top of the box). The lines extending from the boxes mark the 10th percentile (bottom) and 90th percentile (top). The notches signify the 95% confidence intervals of the mean.

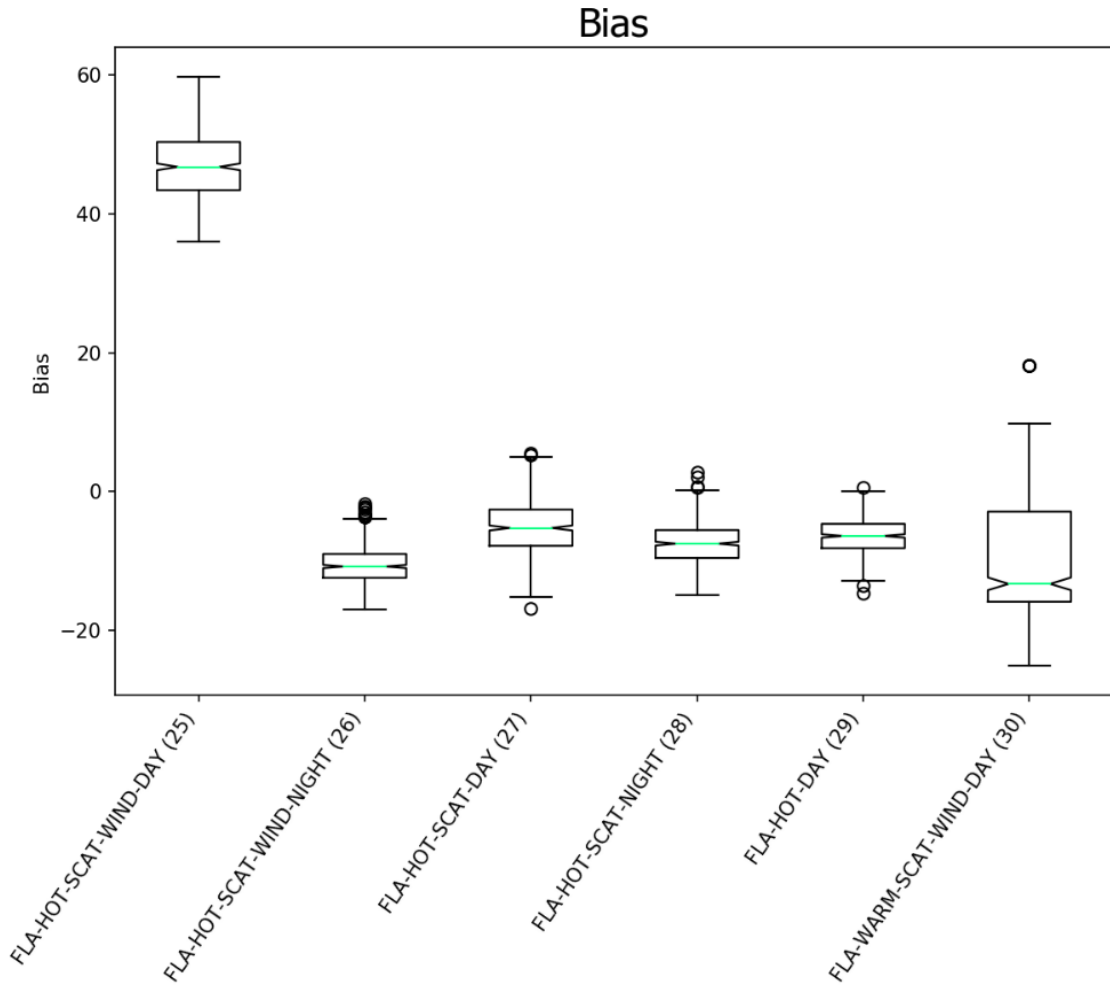


Figure 33d. The bias distributions of models 25-30. The box marks the 25th percentile (bottom of the box), 50th percentile (centerline), and 75th percentile (top of the box). The lines extending from the boxes mark the 10th percentile (bottom) and 90th percentile (top). The notches signify the 95% confidence intervals of the mean.

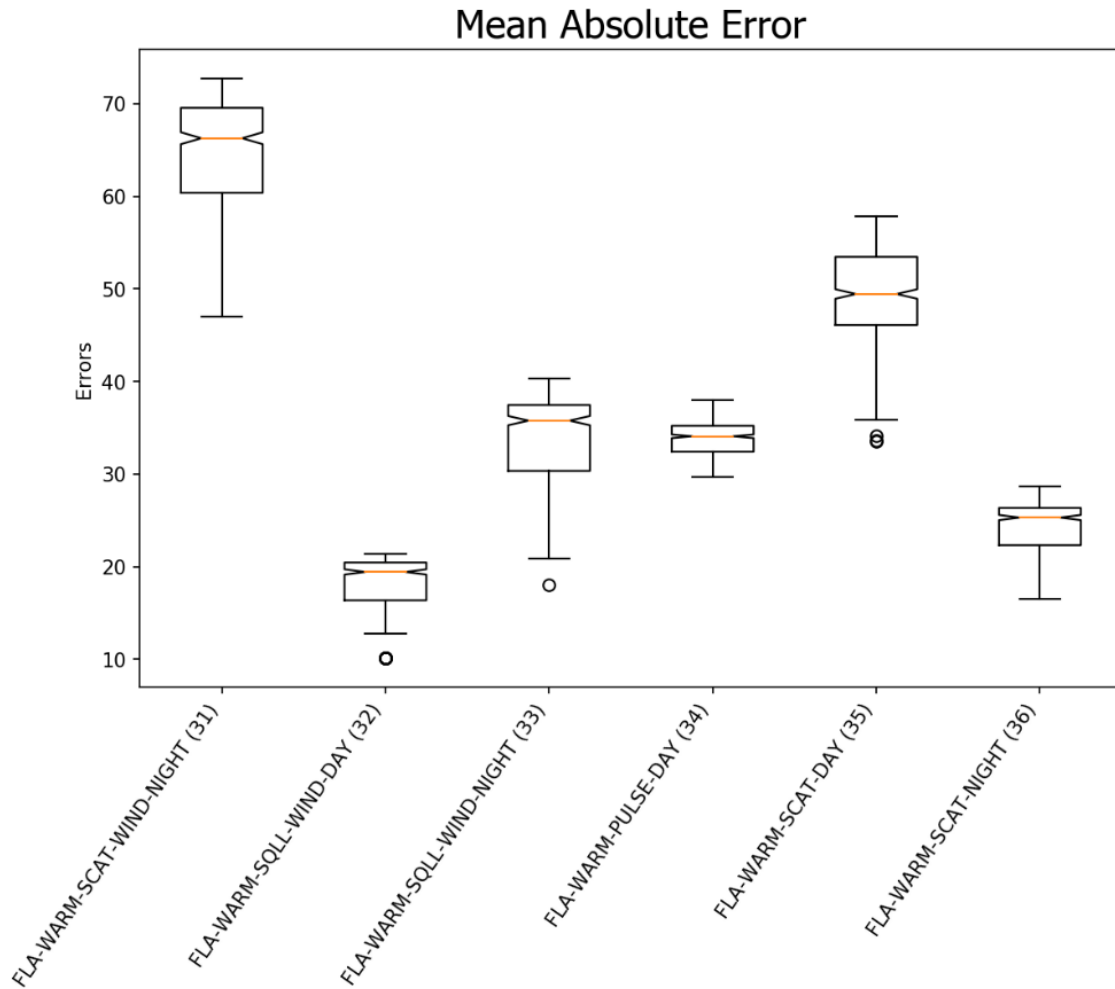


Figure 34a. The mean absolute error distributions of models 31-36. The box marks the 25th percentile (bottom of the box), 50th percentile (centerline), and 75th percentile (top of the box). The lines extending from the boxes mark the 10th percentile (bottom) and 90th percentile (top). The notches signify the 95% confidence intervals of the mean.

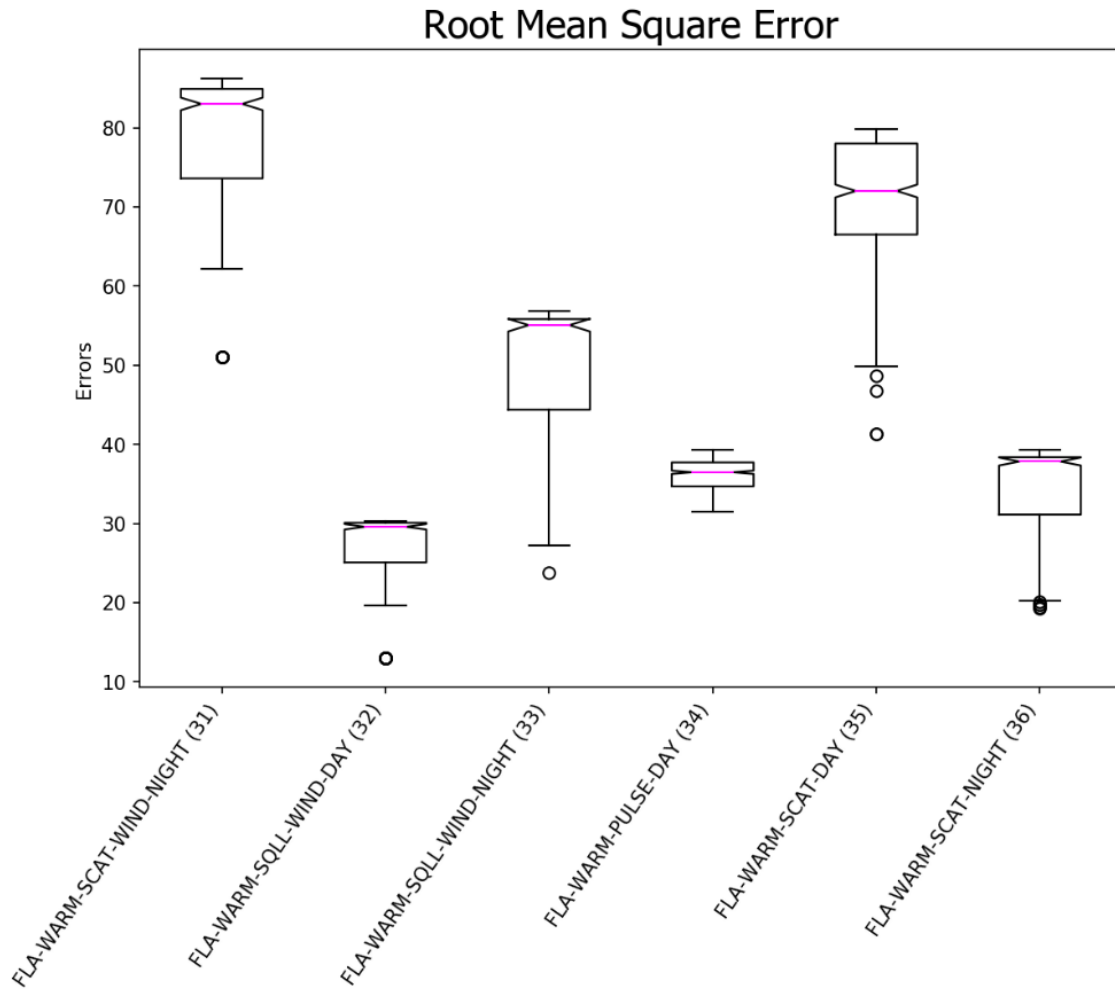


Figure 34b. The root mean square error distributions of models 31-36. The box marks the 25th percentile (bottom of the box), 50th percentile (centerline), and 75th percentile (top of the box). The lines extending from the boxes mark the 10th percentile (bottom) and 90th percentile (top). The notches signify the 95% confidence intervals of the mean.

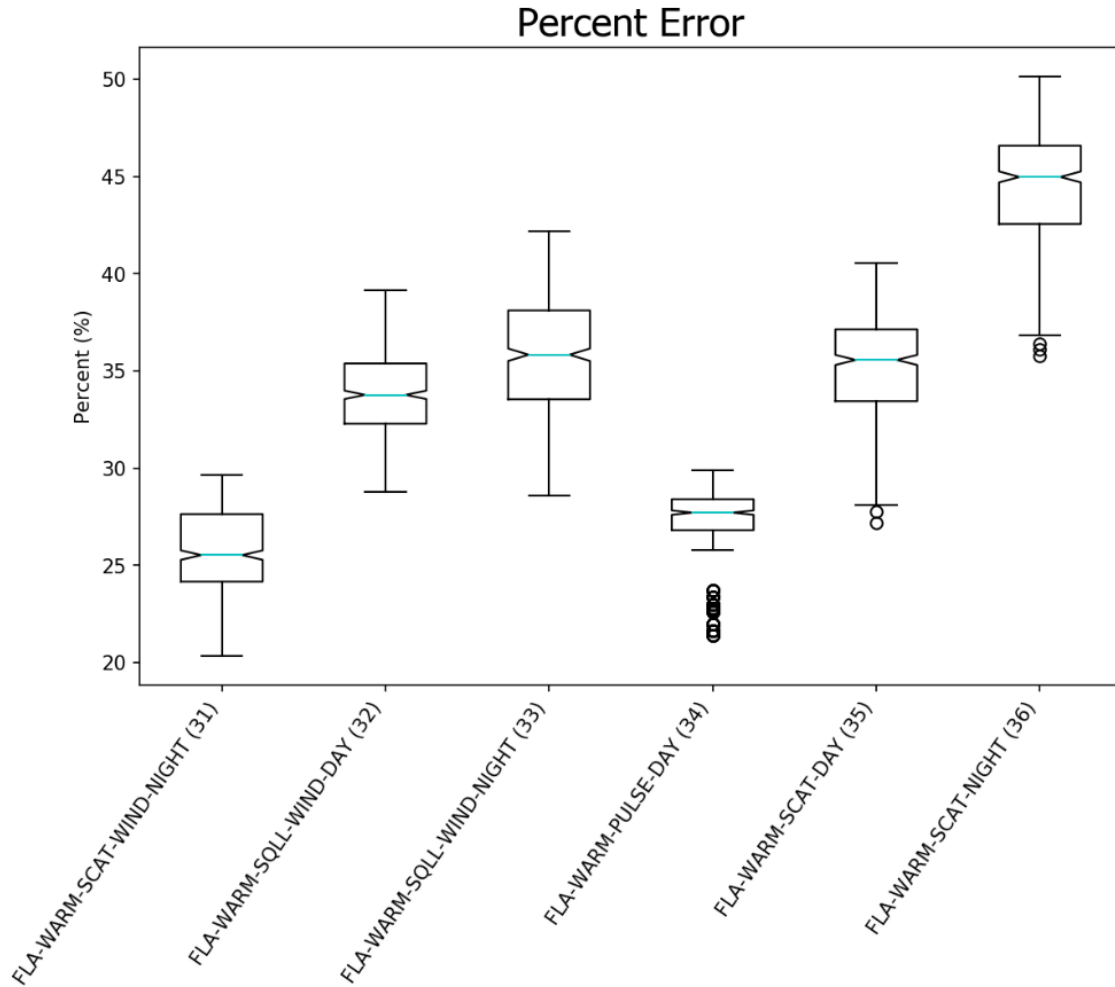


Figure 34c. The percent error distributions of models 31-36. The box marks the 25th percentile (bottom of the box), 50th percentile (centerline), and 75th percentile (top of the box). The lines extending from the boxes mark the 10th percentile (bottom) and 90th percentile (top). The notches signify the 95% confidence intervals of the mean.

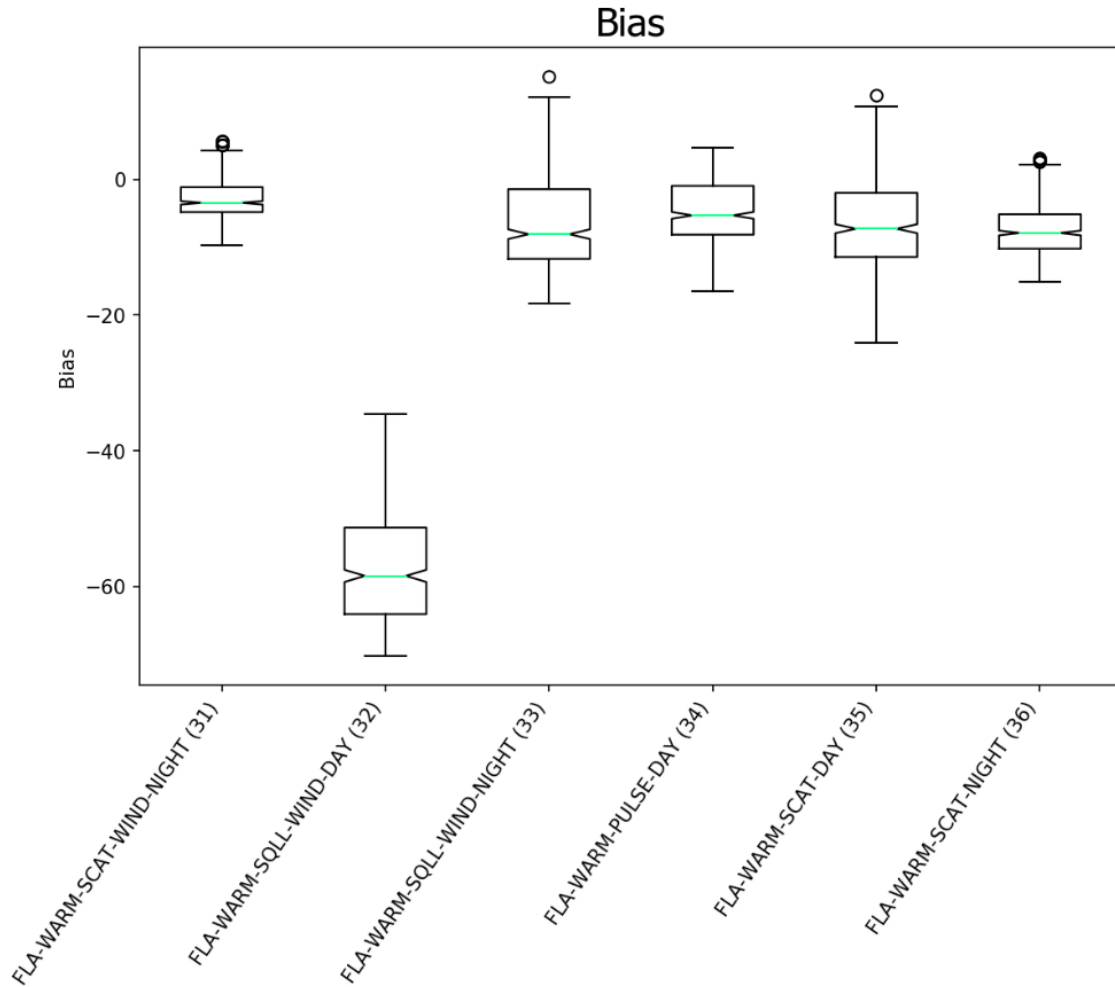


Figure 34d. The bias distributions of models 31-36. The box marks the 25th percentile (bottom of the box), 50th percentile (centerline), and 75th percentile (top of the box). The lines extending from the boxes mark the 10th percentile (bottom) and 90th percentile (top). The notches signify the 95% confidence intervals of the mean.

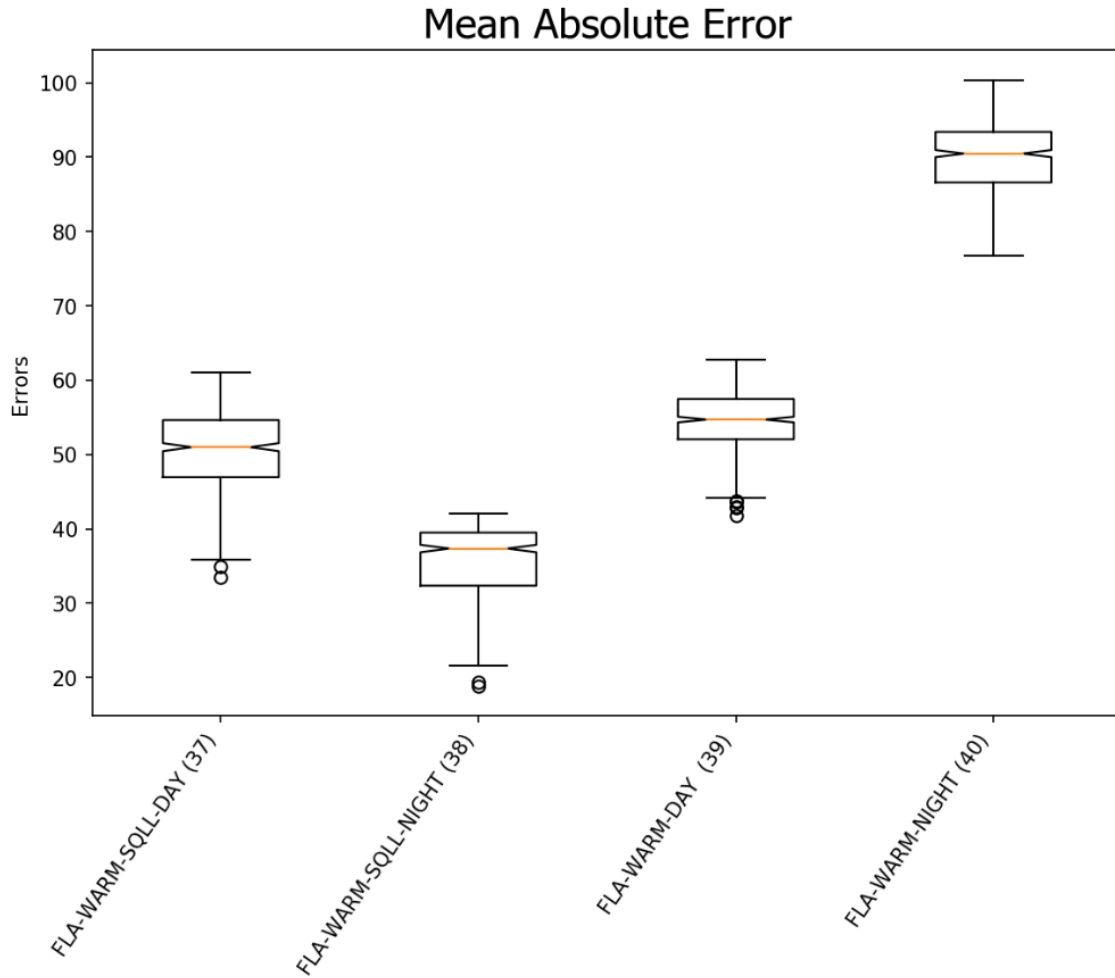


Figure 35a. The mean absolute error distributions of models 37-40. The box marks the 25th percentile (bottom of the box), 50th percentile (centerline), and 75th percentile (top of the box). The lines extending from the boxes mark the 10th percentile (bottom) and 90th percentile (top). The notches signify the 95% confidence intervals of the mean.

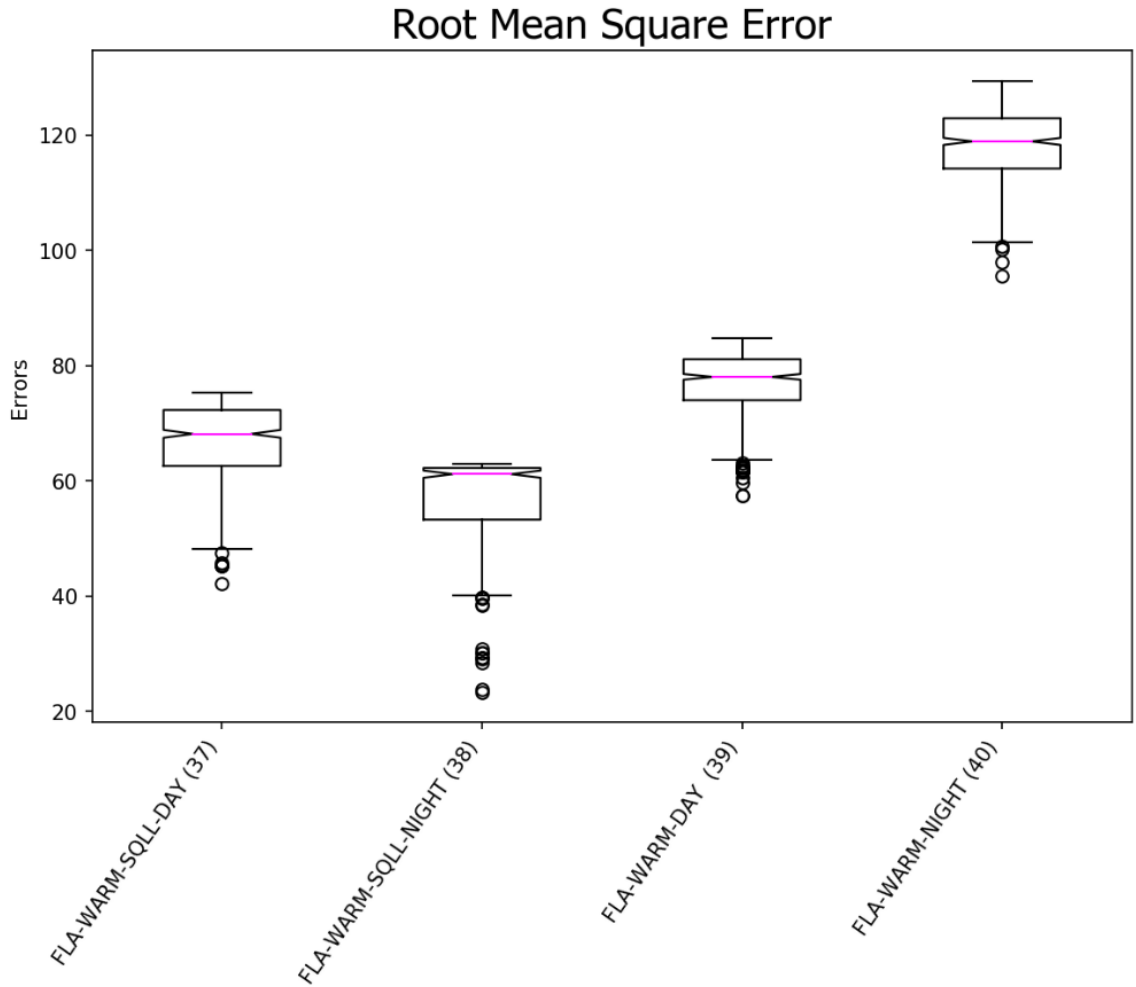


Figure 35b. The root mean square error distributions of models 37-40. The box marks the 25th percentile (bottom of the box), 50th percentile (centerline), and 75th percentile (top of the box). The lines extending from the boxes mark the 10th percentile (bottom) and 90th percentile (top). The notches signify the 95% confidence intervals of the mean.

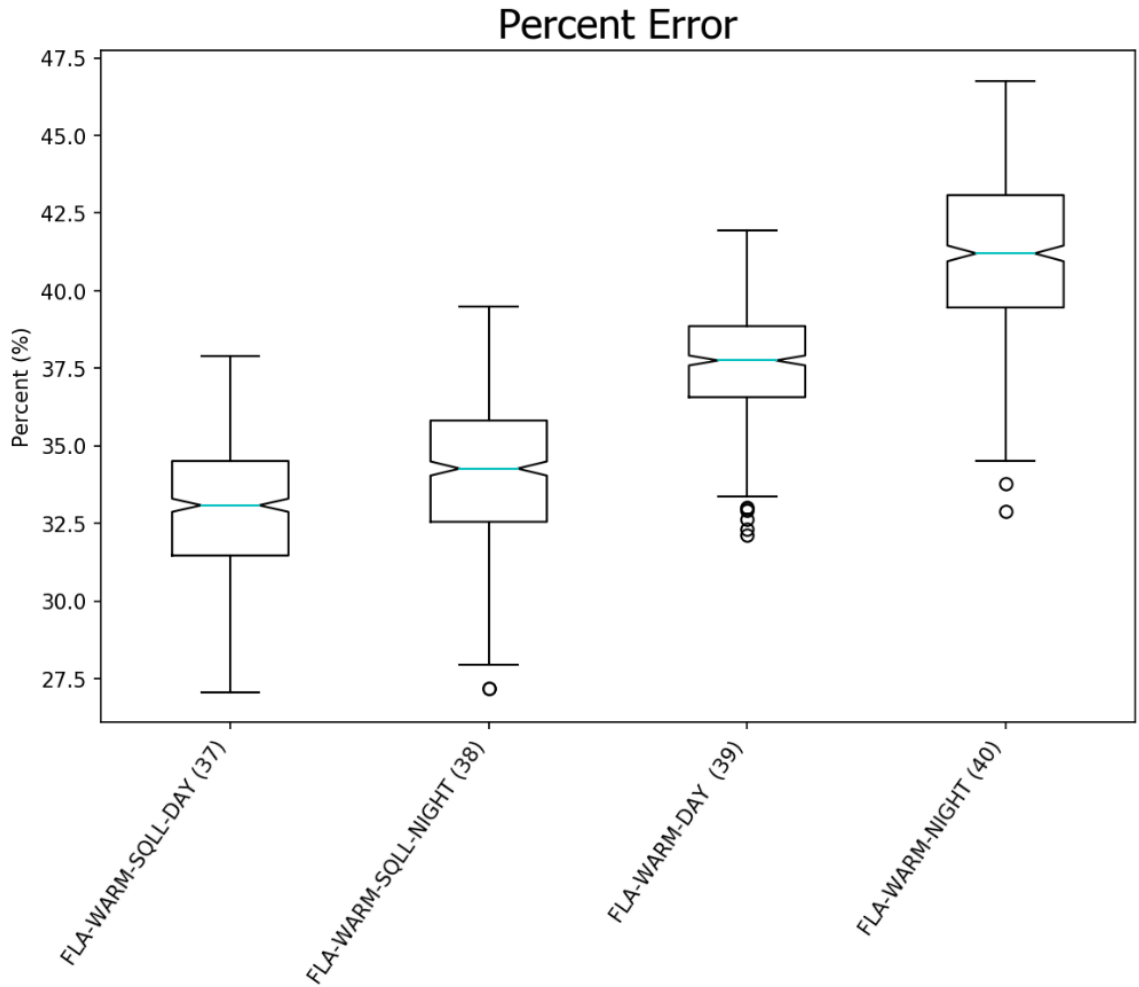


Figure 35c. The percent error distributions of models 37-40. The box marks the 25th percentile (bottom of the box), 50th percentile (centerline), and 75th percentile (top of the box). The lines extending from the boxes mark the 10th percentile (bottom) and 90th percentile (top). The notches signify the 95% confidence intervals of the mean.

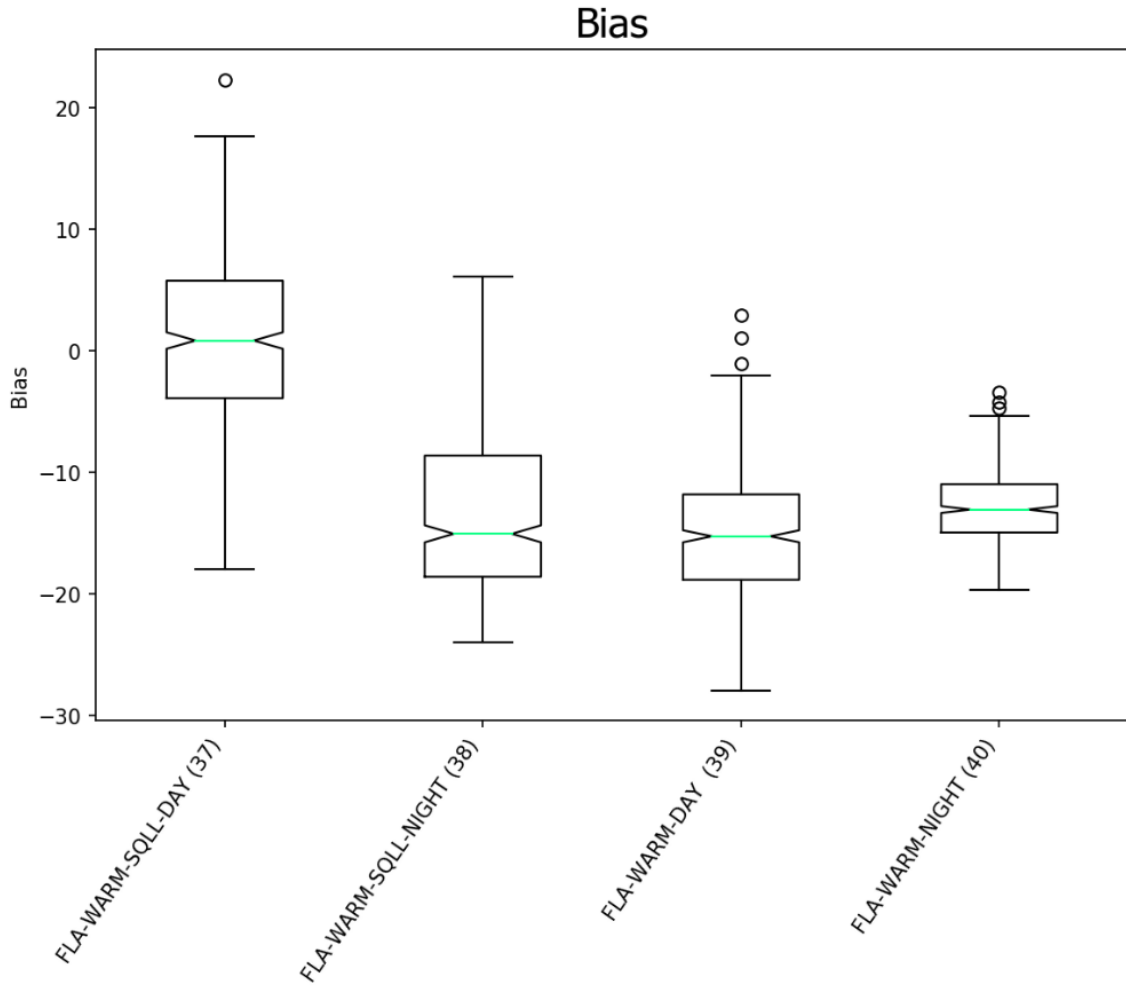


Figure 35d. The bias distributions of models 37-40. The box marks the 25th percentile (bottom of the box), 50th percentile (centerline), and 75th percentile (top of the box). The lines extending from the boxes mark the 10th percentile (bottom) and 90th percentile (top). The notches signify the 95% confidence intervals of the mean.

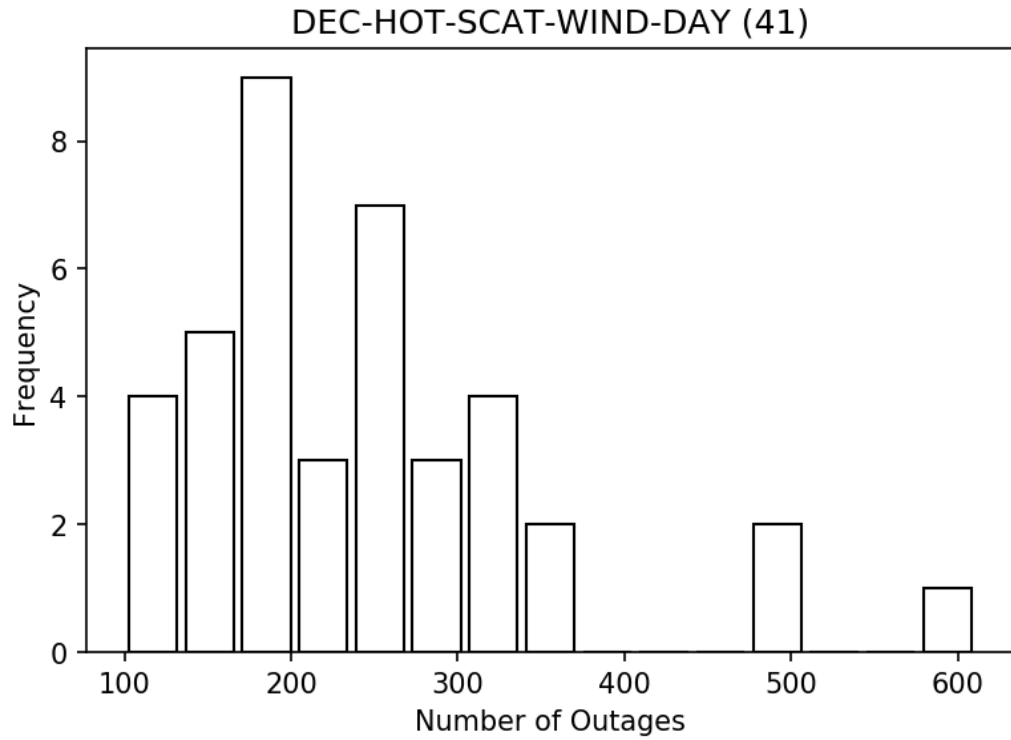


Figure 36. Histogram of observed outage counts on DEC-HOT-SCAT-WIND days.

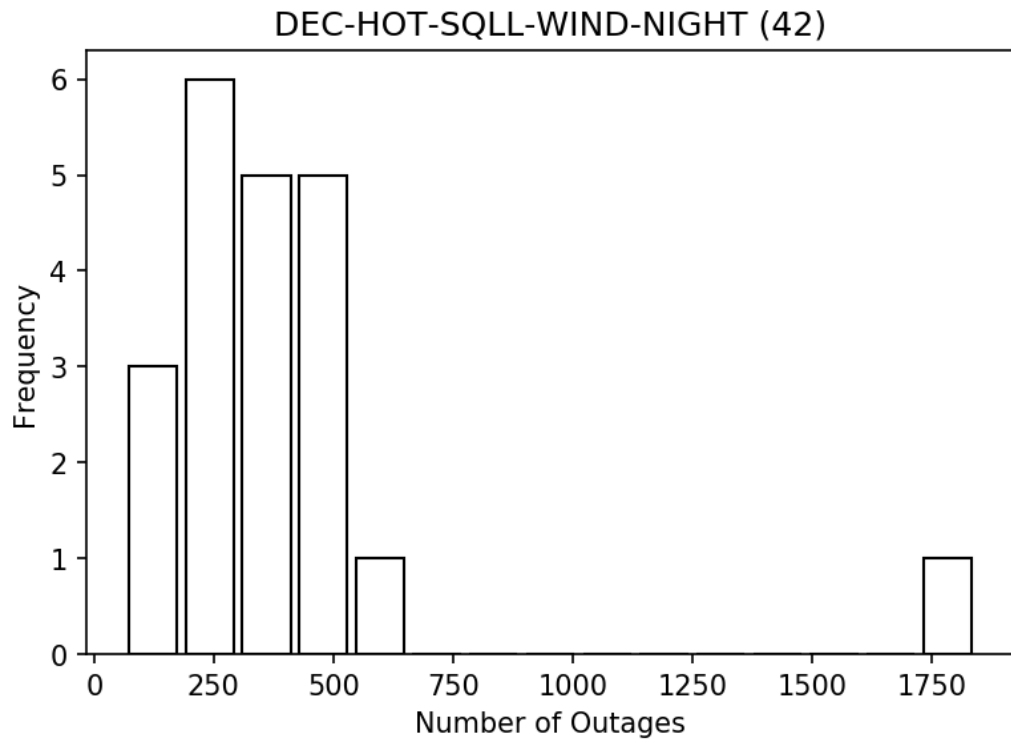


Figure 37. Histogram of observed outage counts on DEC-HOT-SQLL-WIND nights.

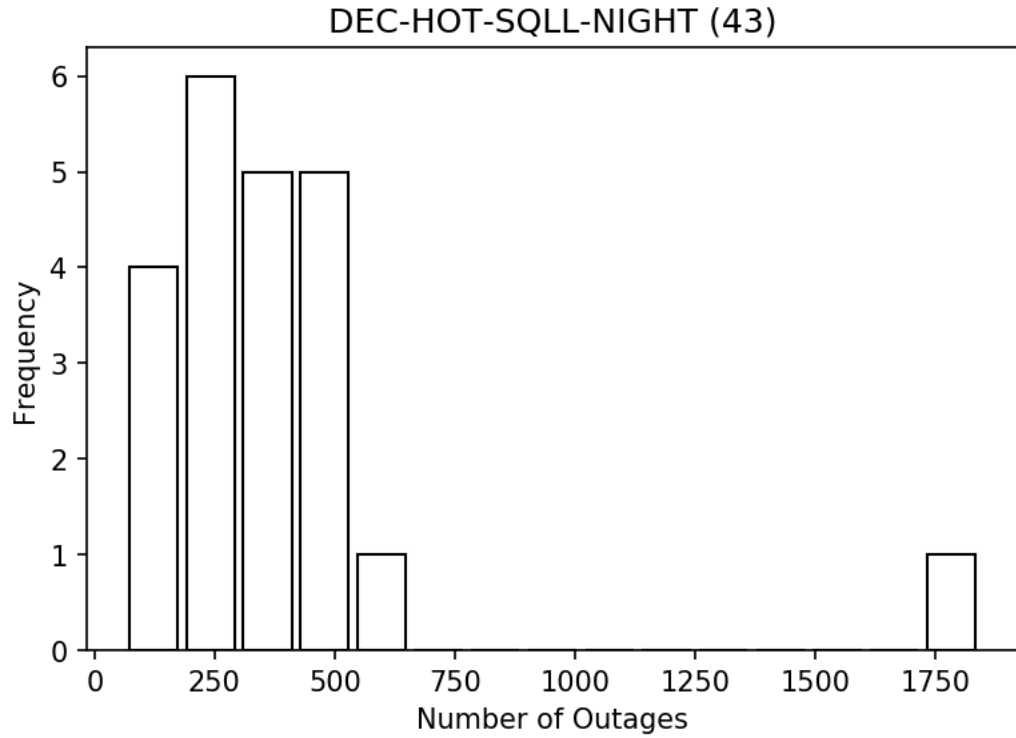


Figure 38. Histogram of observed outage counts on DEC-HOT-SQLL nights.

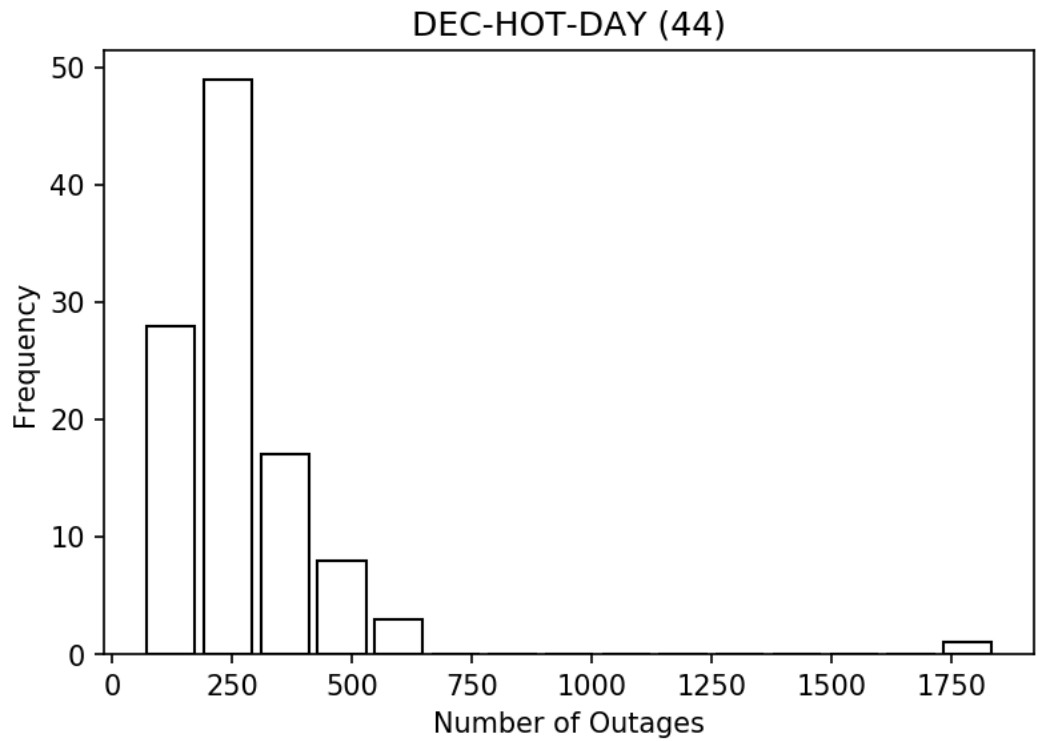


Figure 39. Histogram of observed outage counts on DEC-HOT days.

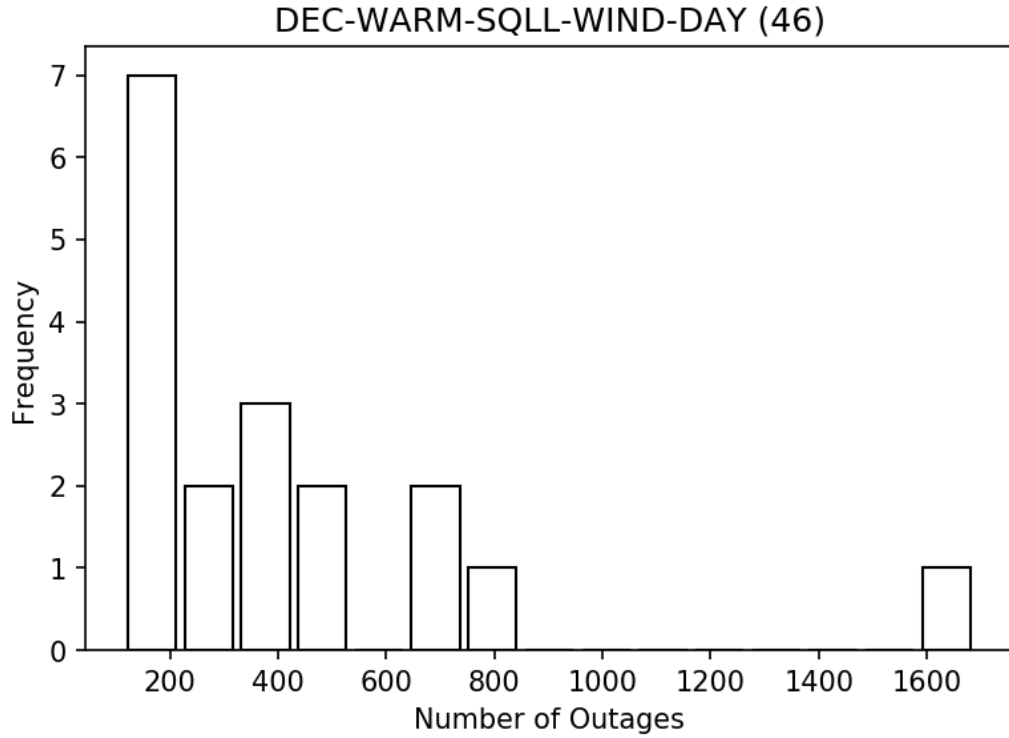


Figure 40. Histogram of observed outage counts on DEC-WARM-SQLL-WIND days.

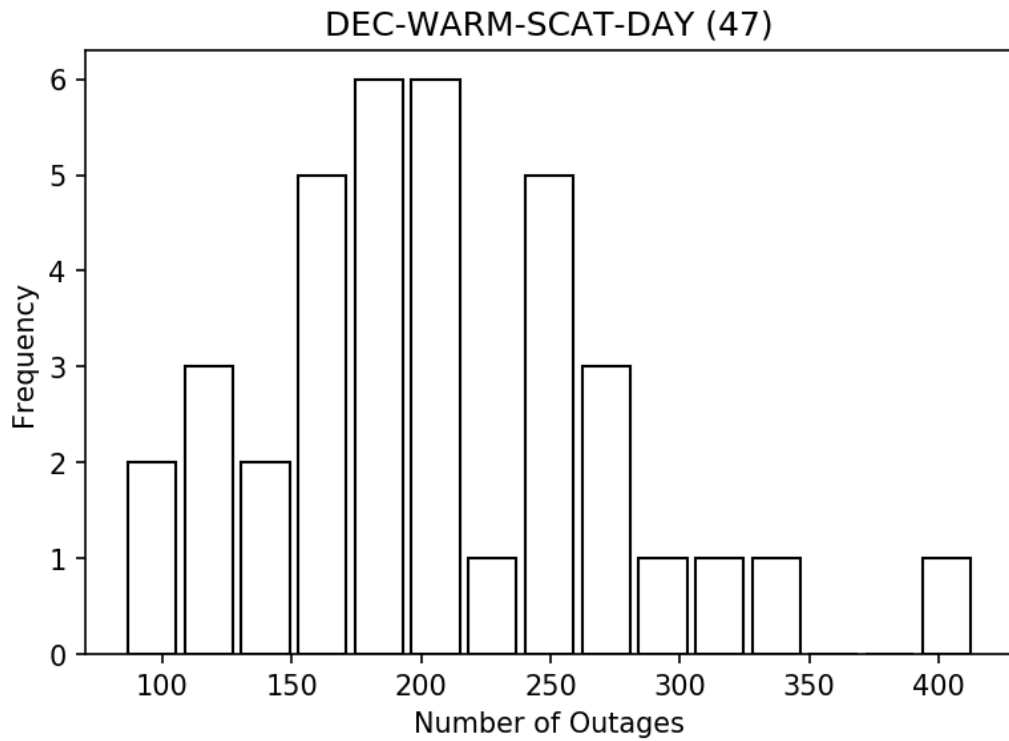


Figure 41. Histogram of observed outage counts on DEC-WARM-SCAT days.

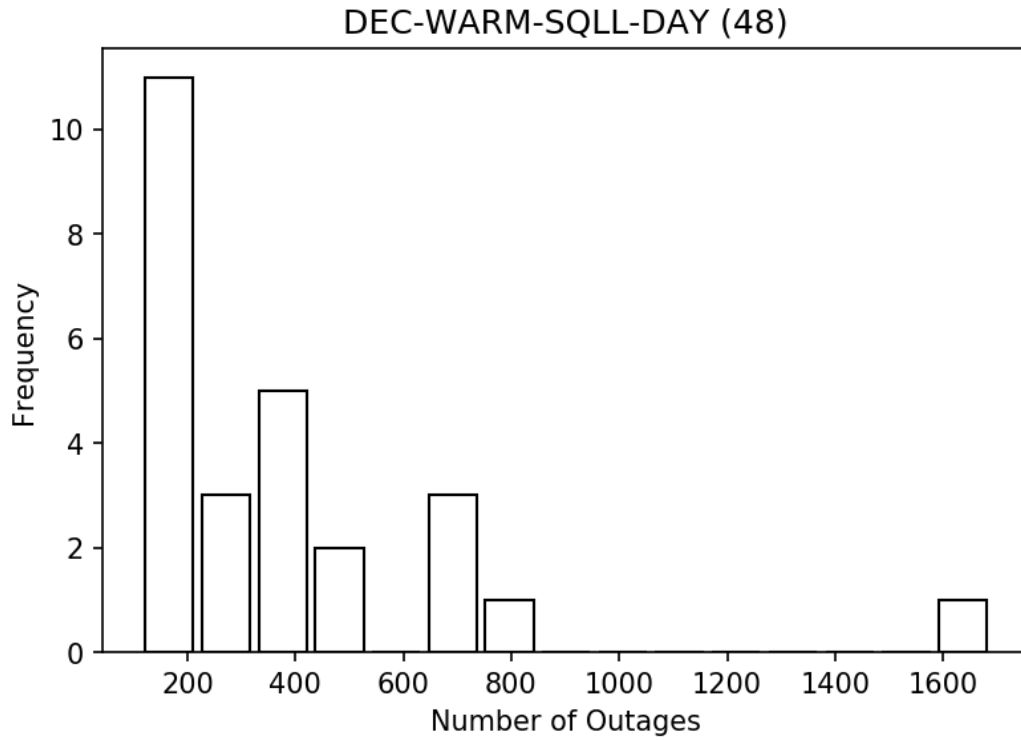


Figure 42. Histogram of observed outage counts on DEC-WARM-SQLL days.

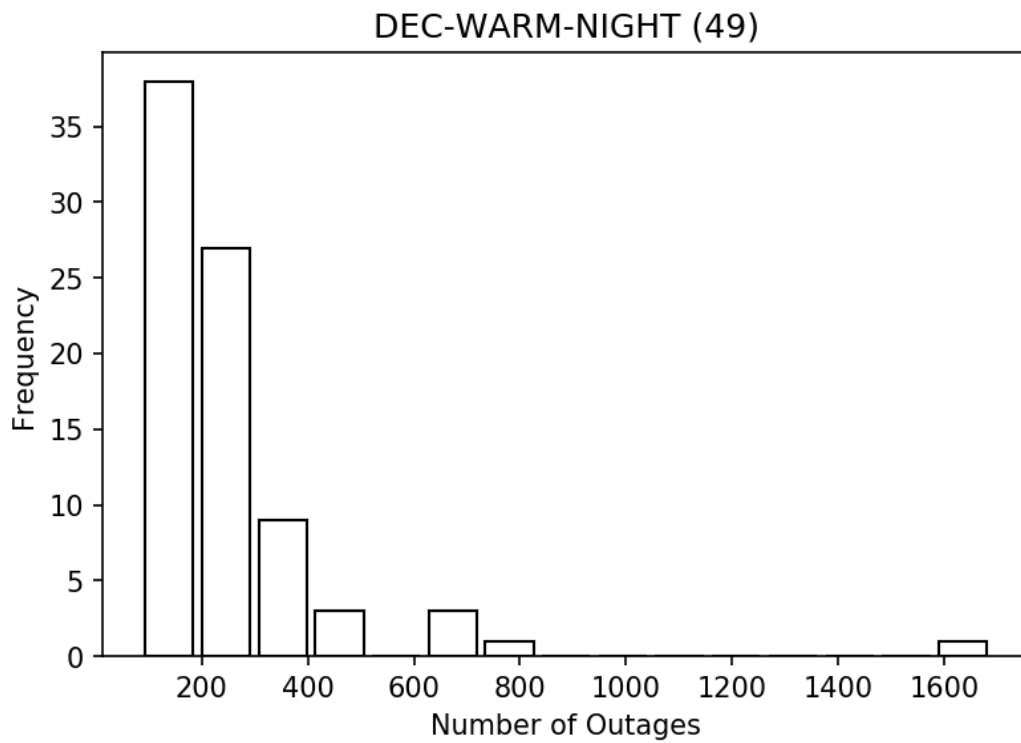


Figure 43. Histogram of observed outage counts on DEC-WARM nights.

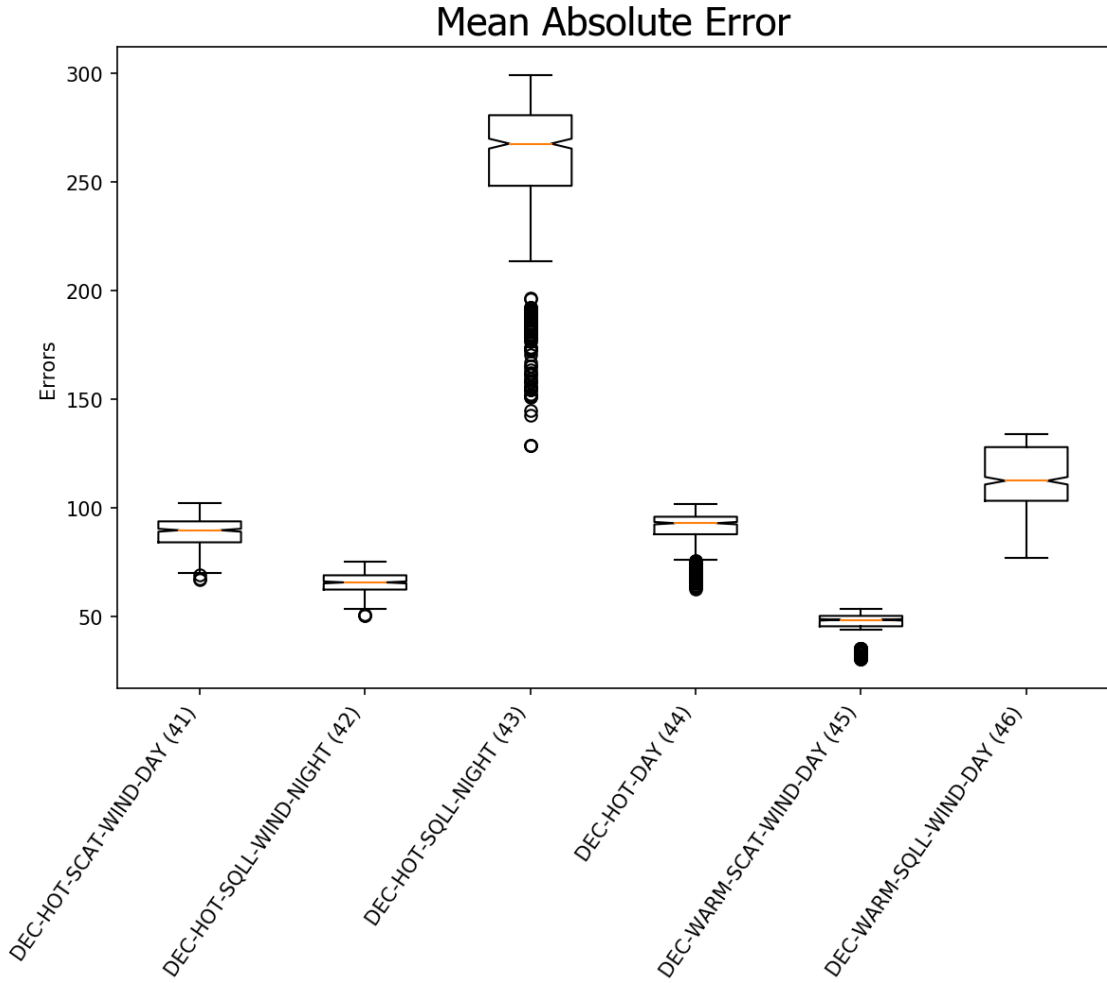


Figure 44a. The mean absolute error distributions of models 41-46. The box marks the 25th percentile (bottom of the box), 50th percentile (centerline), and 75th percentile (top of the box). The lines extending from the boxes mark the 10th percentile (bottom) and 90th percentile (top). The notches signify the 95% confidence intervals of the mean.

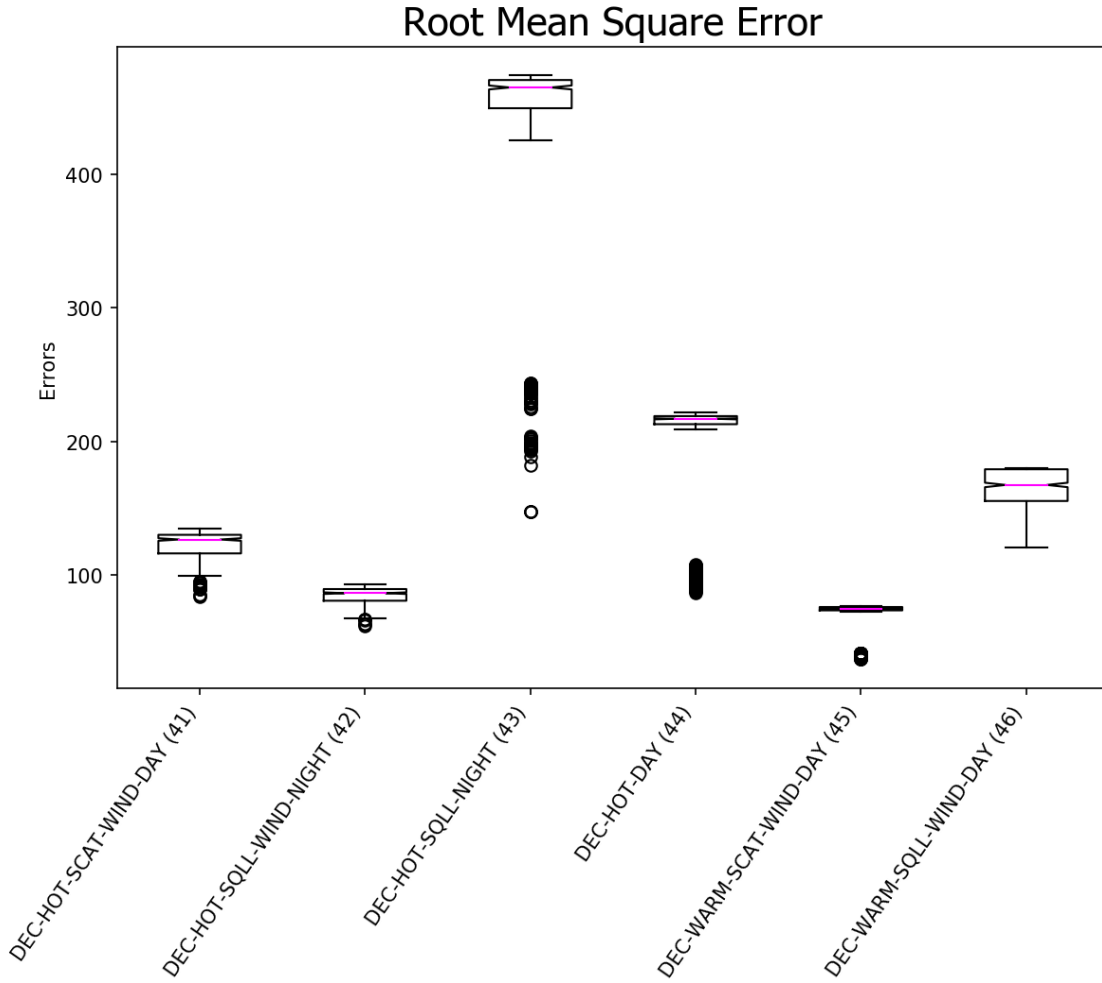


Figure 44b. The root mean square error distributions of models 41-46. The box marks the 25th percentile (bottom of the box), 50th percentile (centerline), and 75th percentile (top of the box). The lines extending from the boxes mark the 10th percentile (bottom) and 90th percentile (top). The notches signify the 95% confidence intervals of the mean.

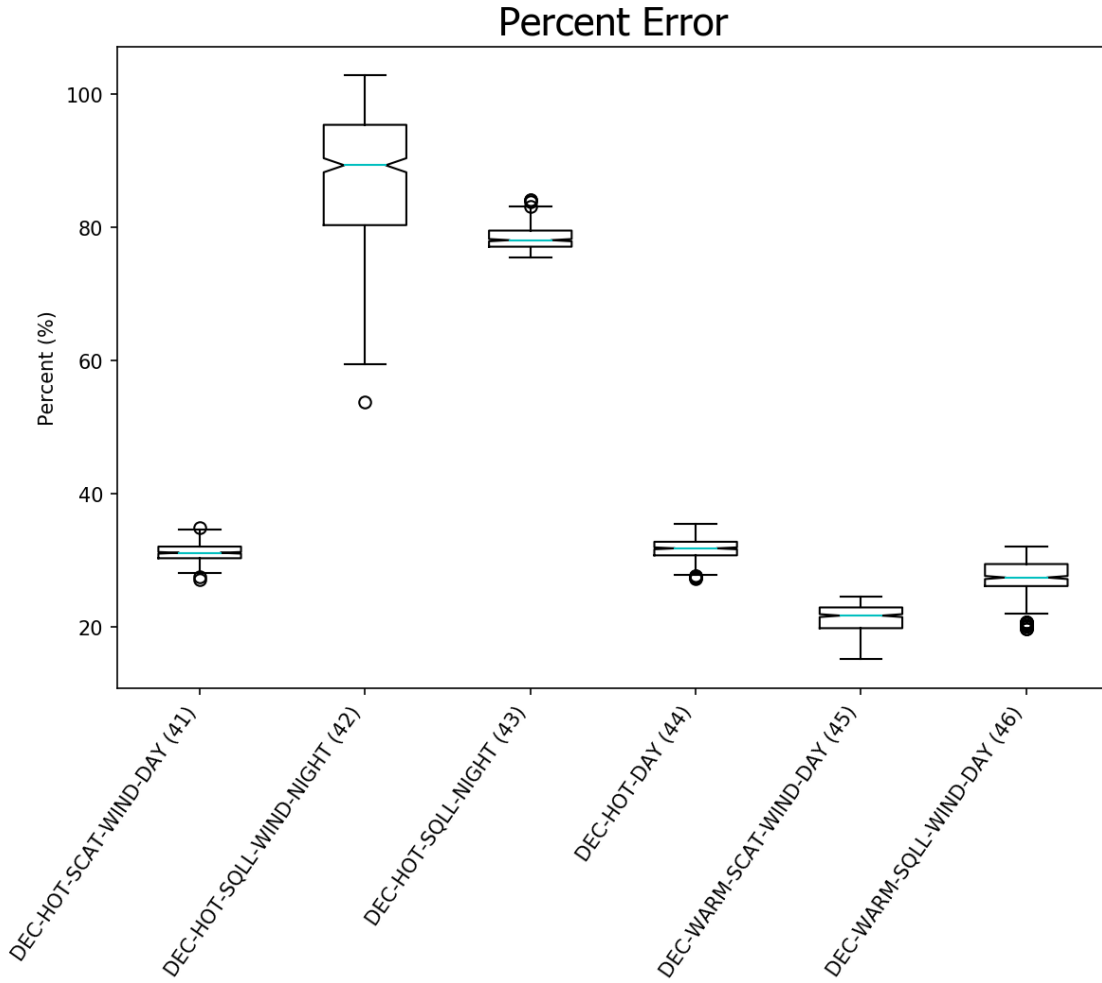


Figure 44c. The percent error distributions of models 41-46. The box marks the 25th percentile (bottom of the box), 50th percentile (centerline), and 75th percentile (top of the box). The lines extending from the boxes mark the 10th percentile (bottom) and 90th percentile (top). The notches signify the 95% confidence intervals of the mean.

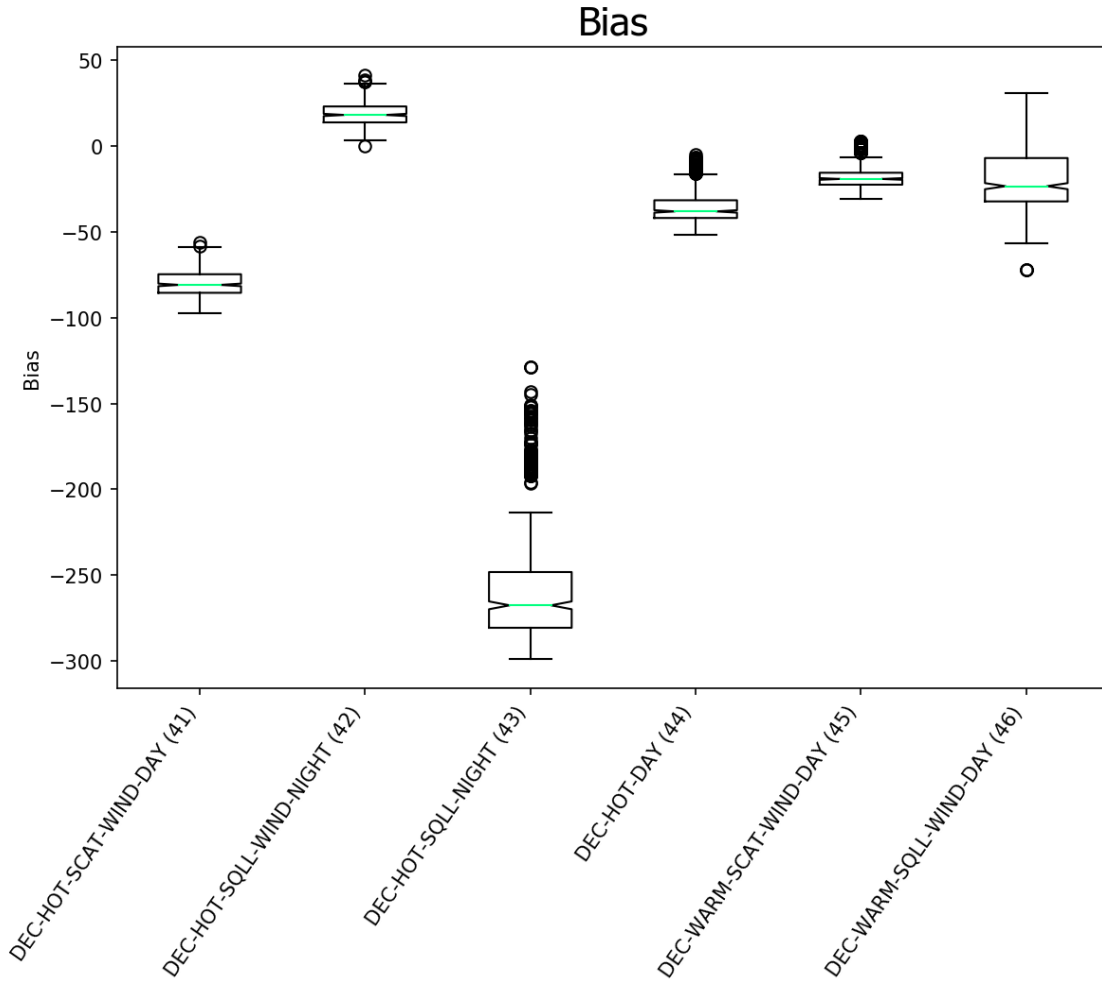


Figure 44d. The bias distributions of models 41-46. The box marks the 25th percentile (bottom of the box), 50th percentile (centerline), and 75th percentile (top of the box). The lines extending from the boxes mark the 10th percentile (bottom) and 90th percentile (top). The notches signify the 95% confidence intervals of the mean.

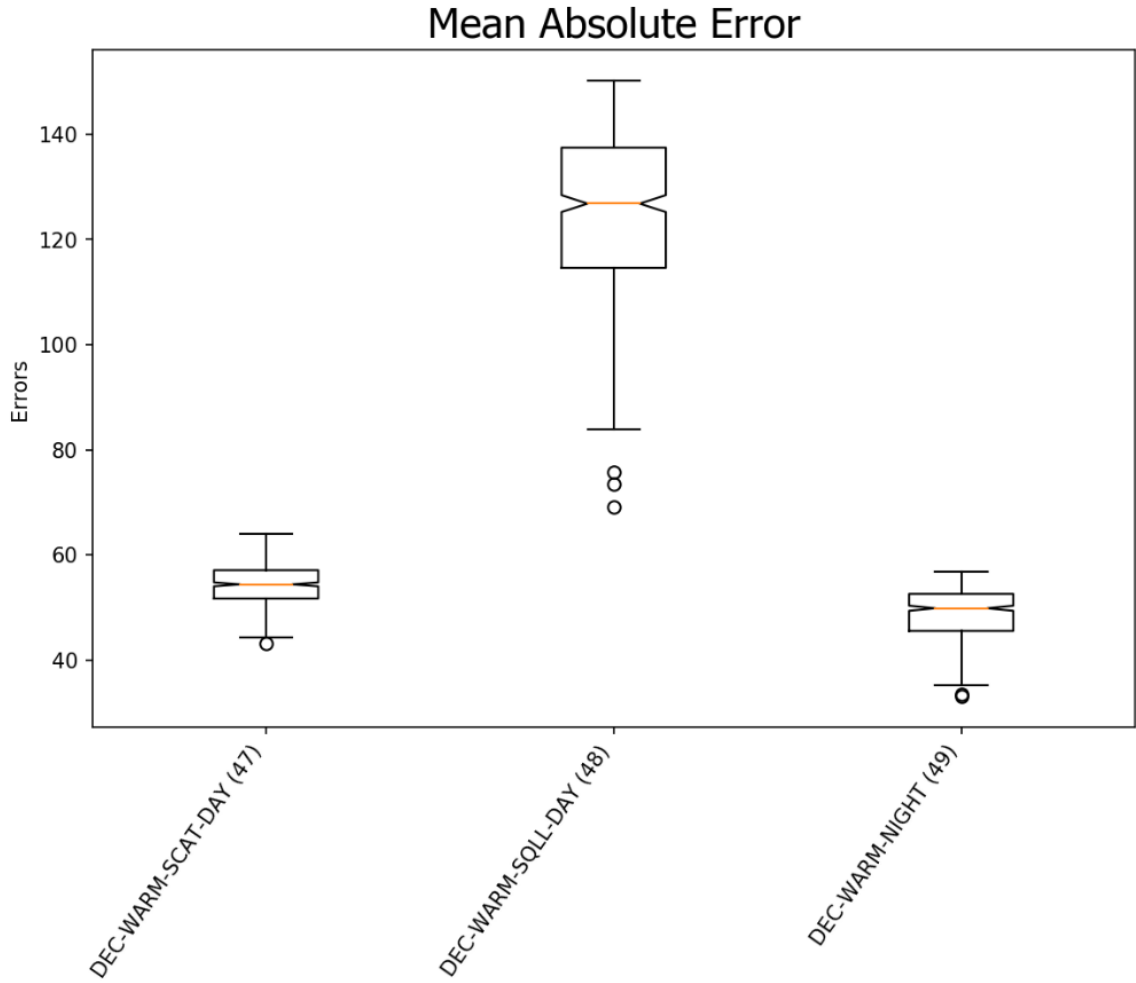


Figure 45a. The mean absolute error distributions of models 47-49. The box marks the 25th percentile (bottom of the box), 50th percentile (centerline), and 75th percentile (top of the box). The lines extending from the boxes mark the 10th percentile (bottom) and 90th percentile (top). The notches signify the 95% confidence intervals of the mean.

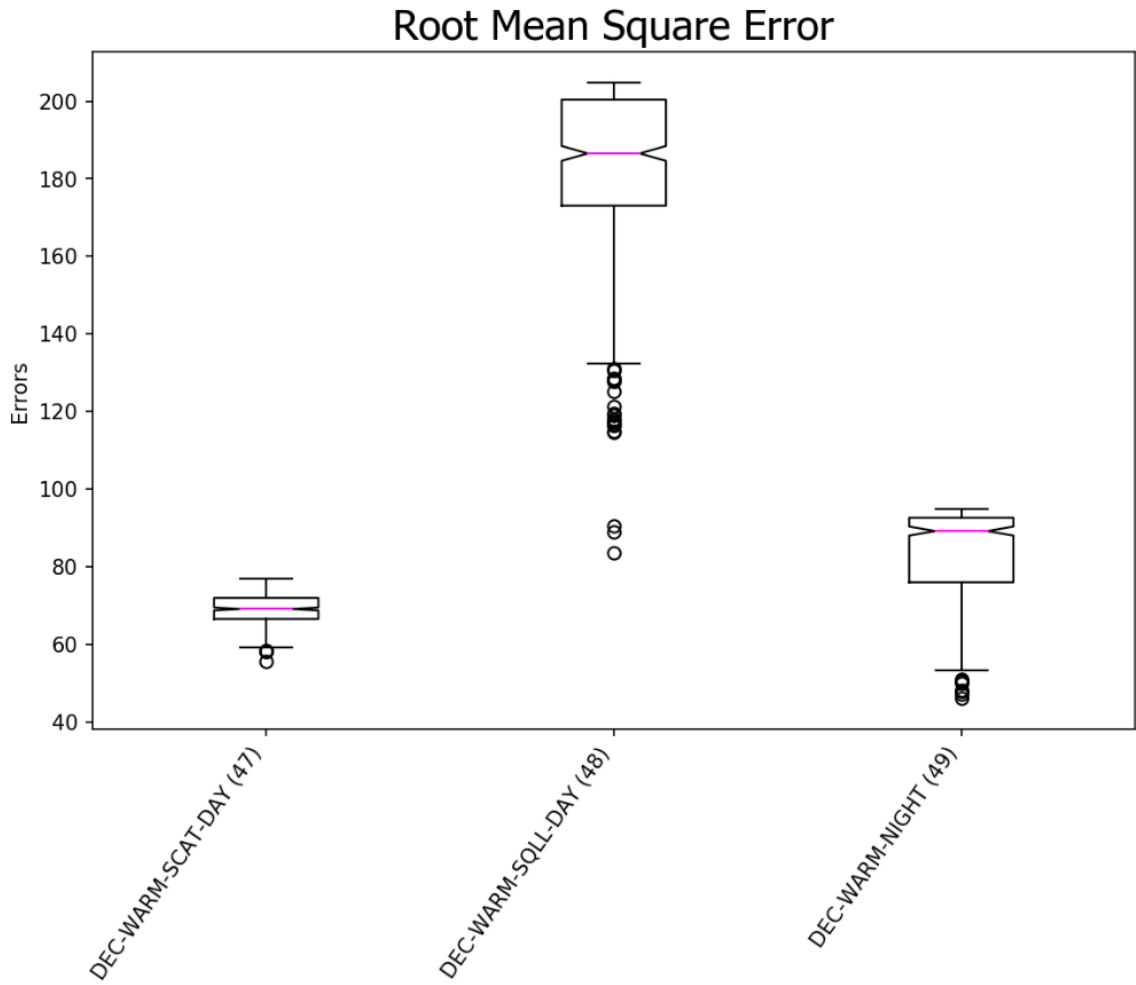


Figure 45b. The root mean square error distributions of models 47-49. The box marks the 25th percentile (bottom of the box), 50th percentile (centerline), and 75th percentile (top of the box). The lines extending from the boxes mark the 10th percentile (bottom) and 90th percentile (top). The notches signify the 95% confidence intervals of the mean.

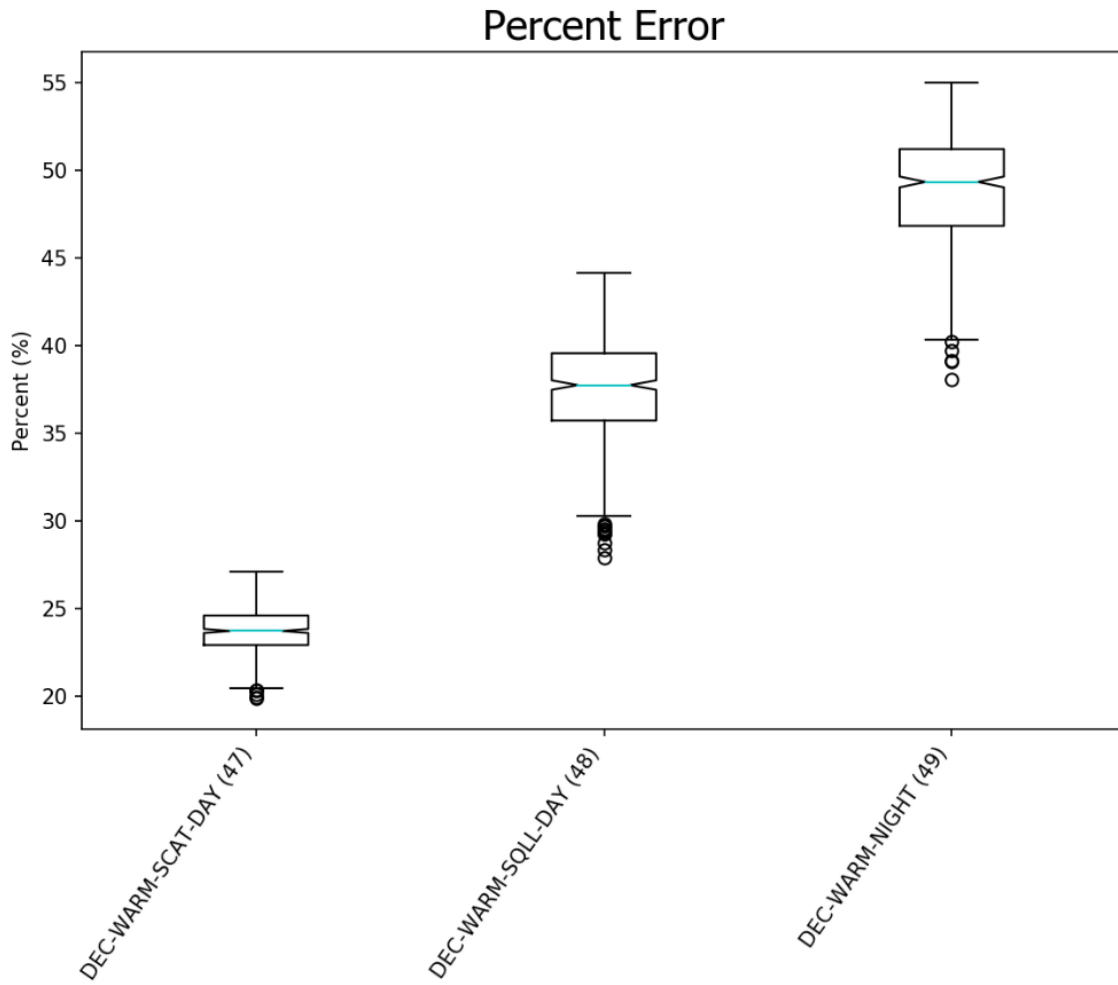


Figure 45c. The percent error distributions of models 47-49. The box marks the 25th percentile (bottom of the box), 50th percentile (centerline), and 75th percentile (top of the box). The lines extending from the boxes mark the 10th percentile (bottom) and 90th percentile (top). The notches signify the 95% confidence intervals of the mean.

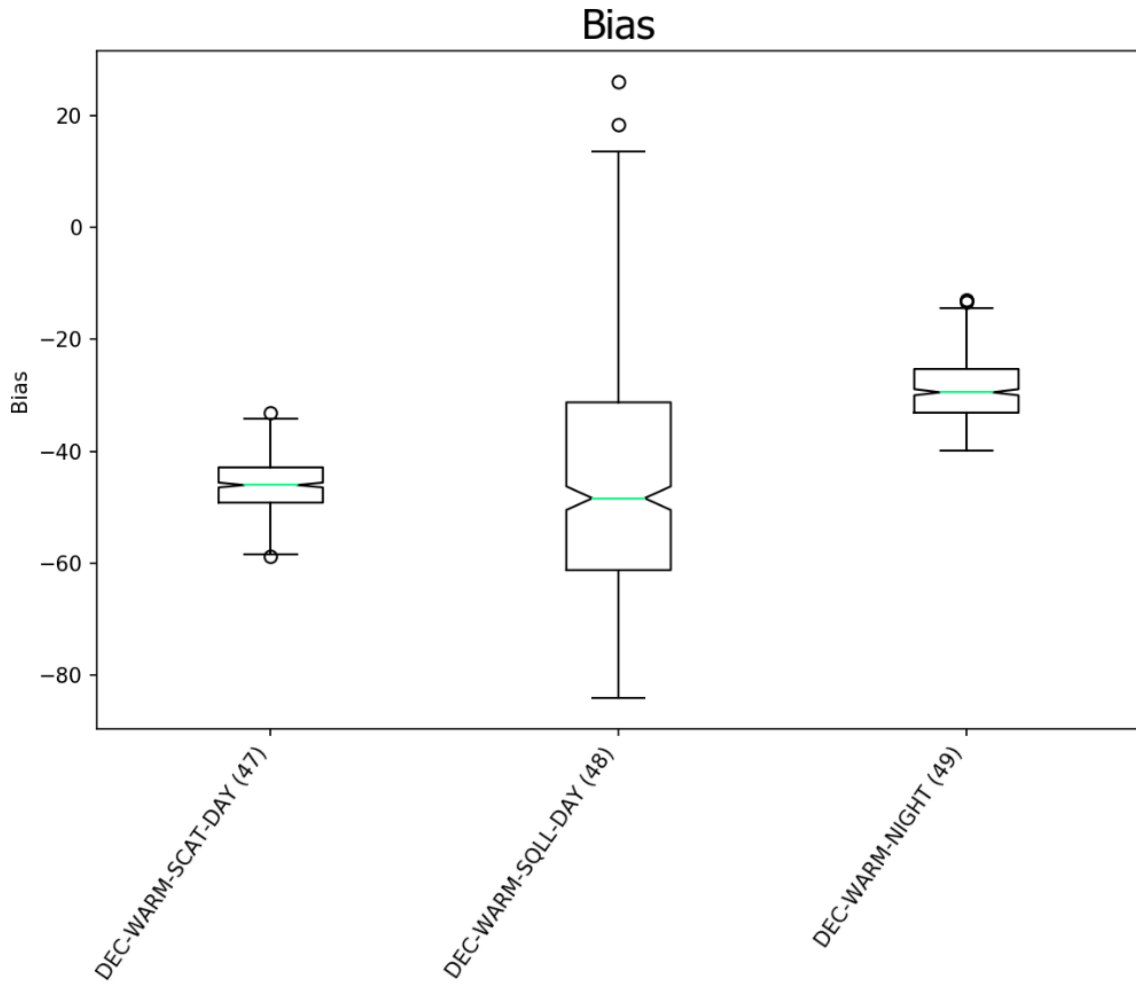


Figure 45d. The bias distributions of models 47-49. The box marks the 25th percentile (bottom of the box), 50th percentile (centerline), and 75th percentile (top of the box). The lines extending from the boxes mark the 10th percentile (bottom) and 90th percentile (top). The notches signify the 95% confidence intervals of the mean.

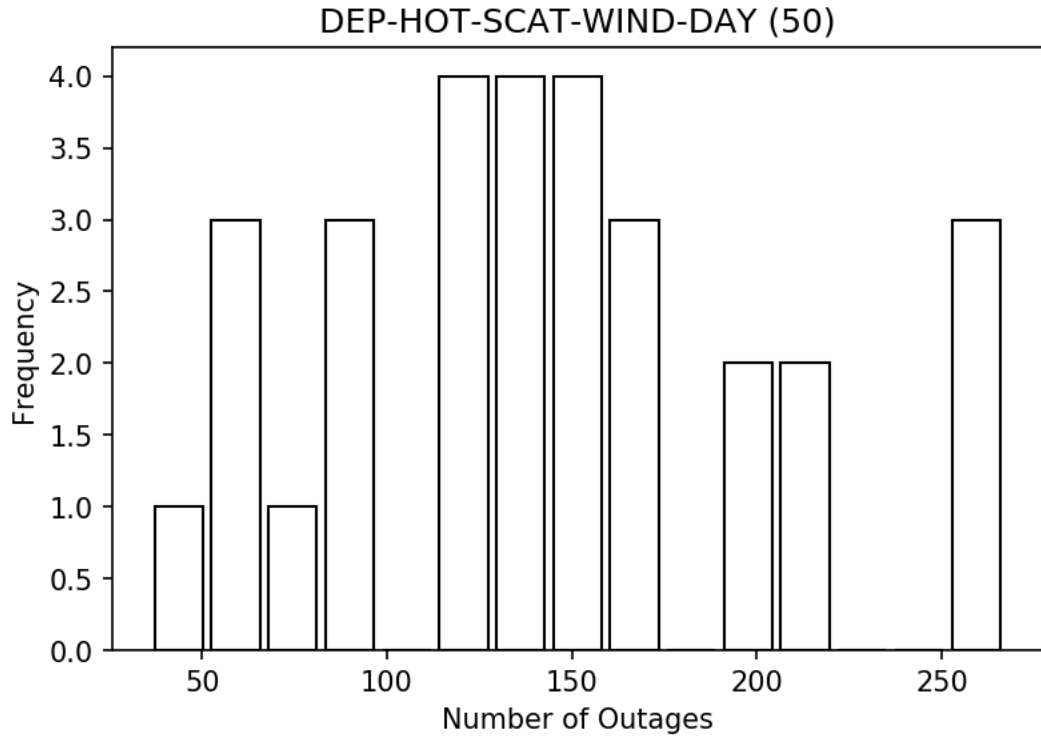


Figure 46. Histogram of outage counts on DEP-HOT-SCAT-WIND days.

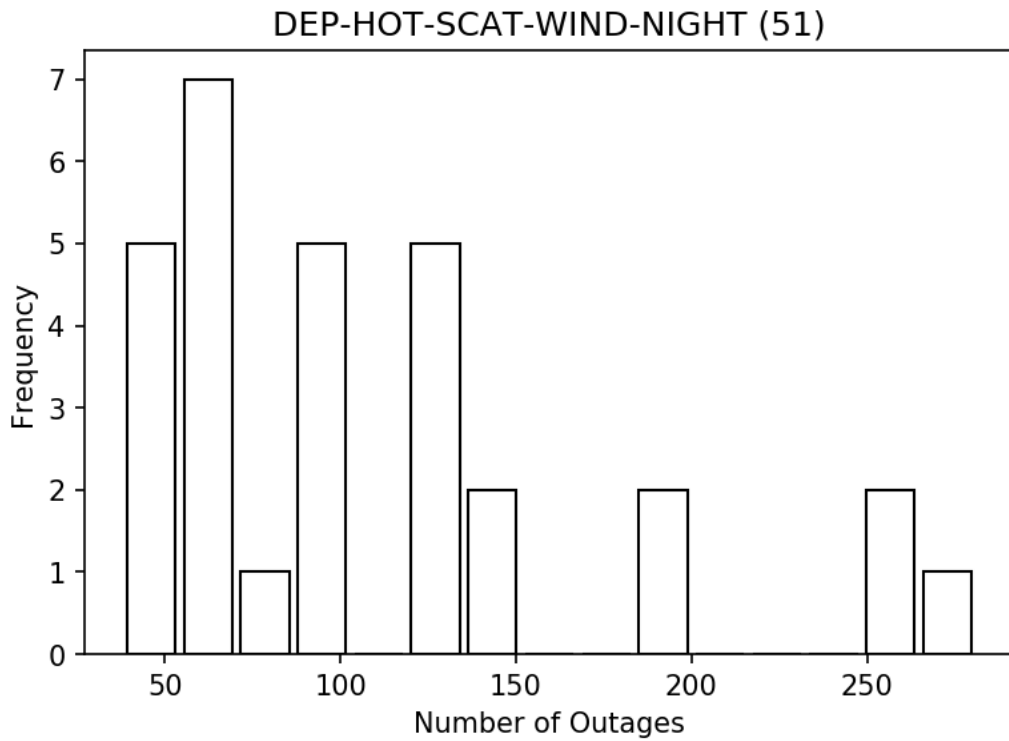


Figure 47. Histogram of outage counts on DEP-HOT-SCAT-WIND nights.

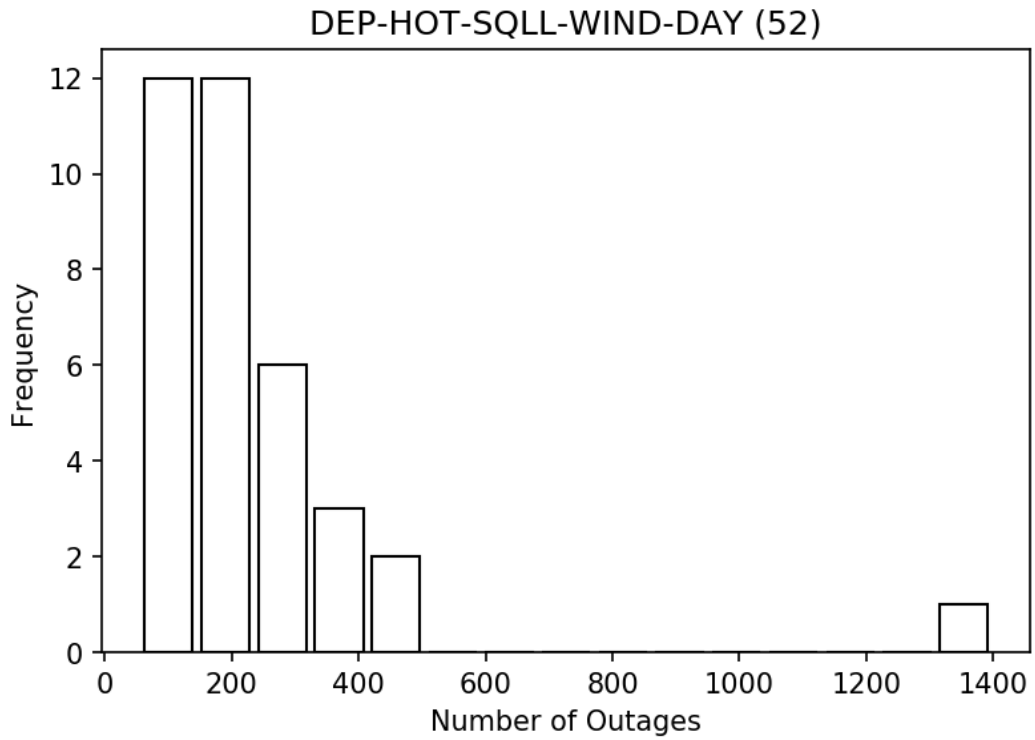


Figure 48. Histogram of outage counts on DEP-HOT-SQLL-WIND days.

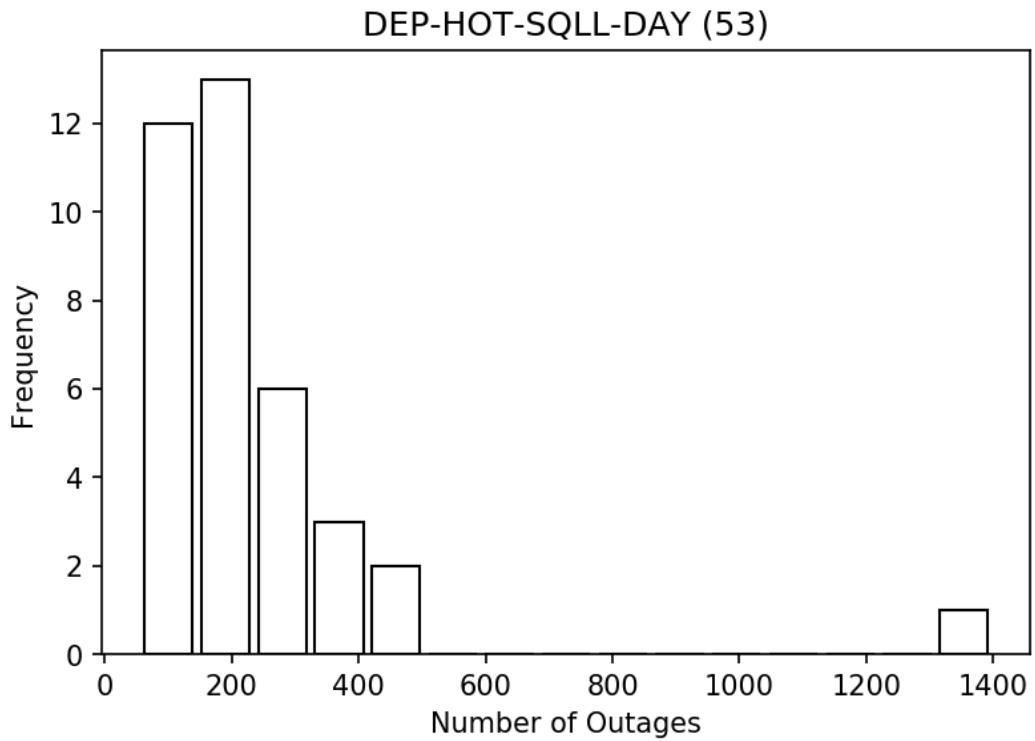


Figure 49. Histogram of outage counts on DEP-HOT-SQLL days.

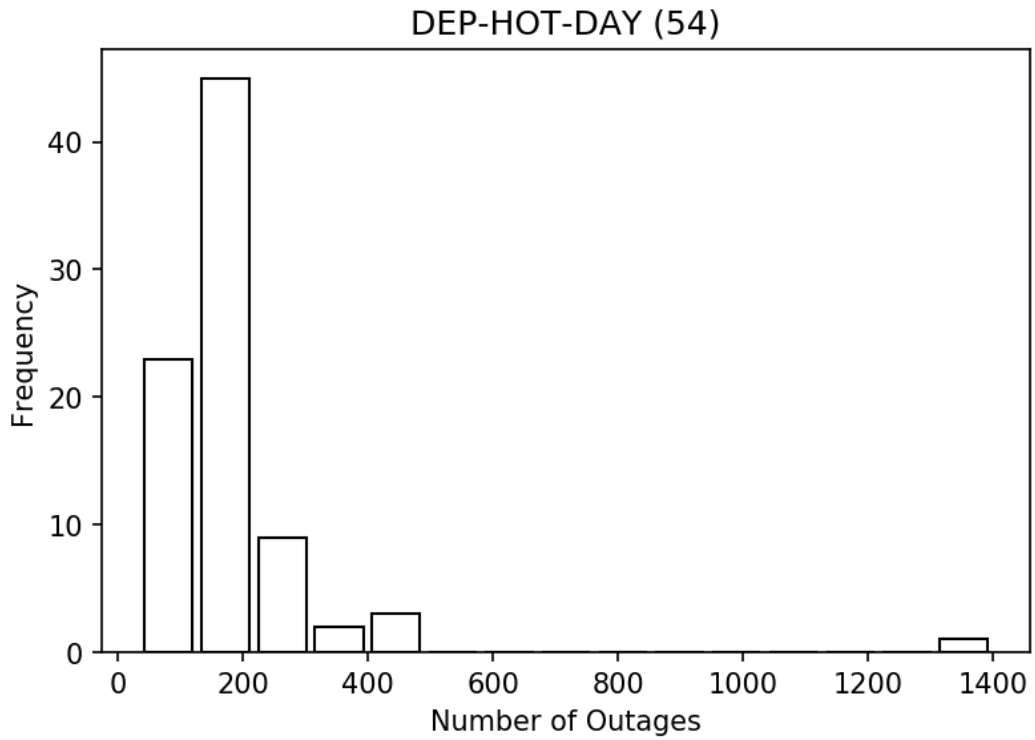


Figure 50. Histogram of outage counts on DEP-HOT days.

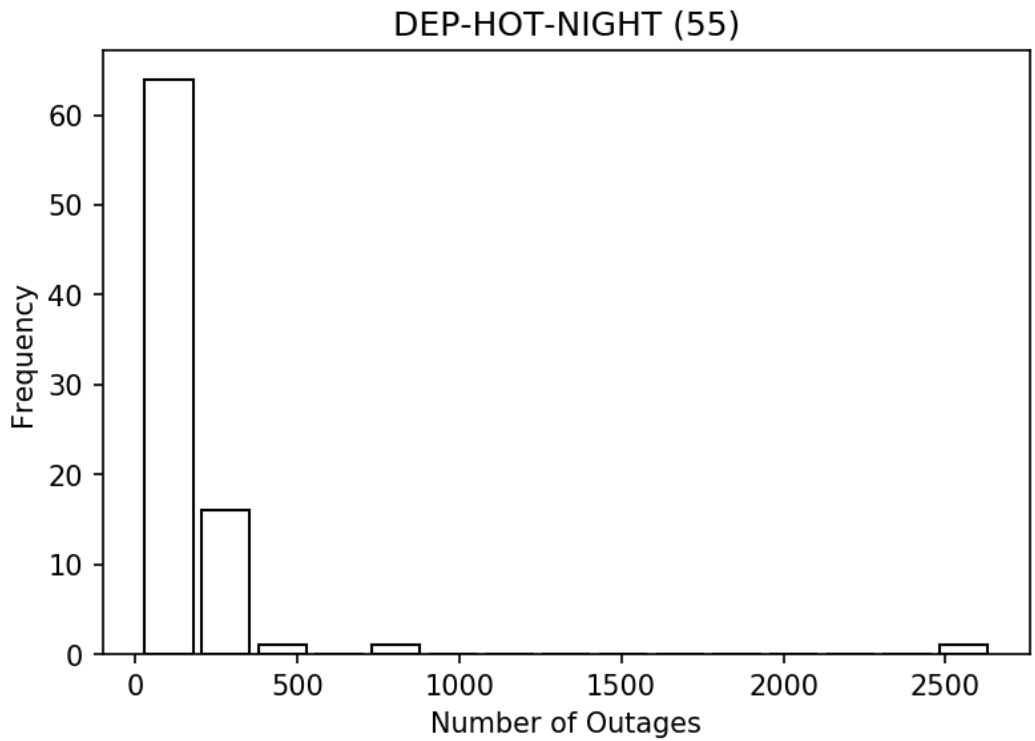


Figure 51. Histogram of outage counts on DEP-HOT nights.

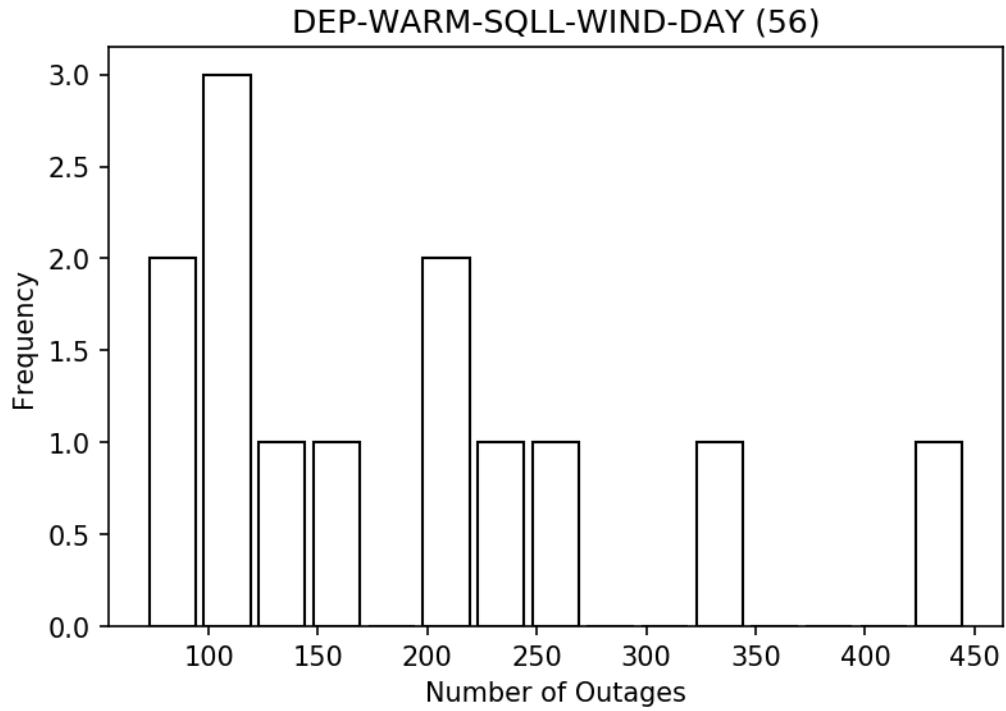


Figure 52 Histogram of outage counts on DEP-WARM-SQLL-WIND days.

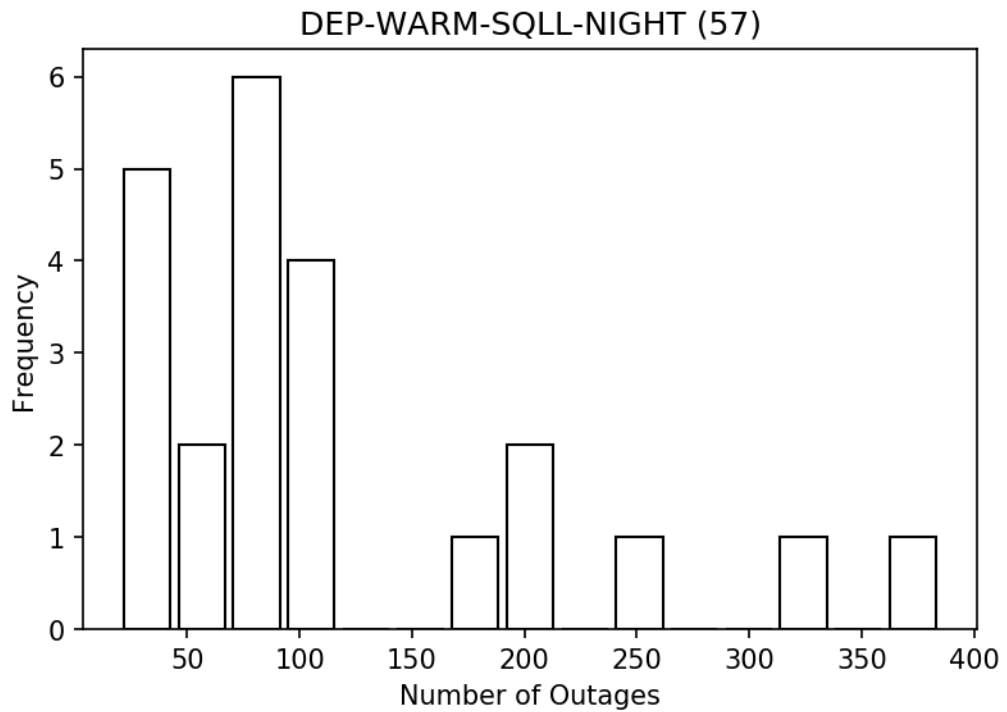


Figure 53. Histogram of outage counts on DEP-WARM-SQLL nights.

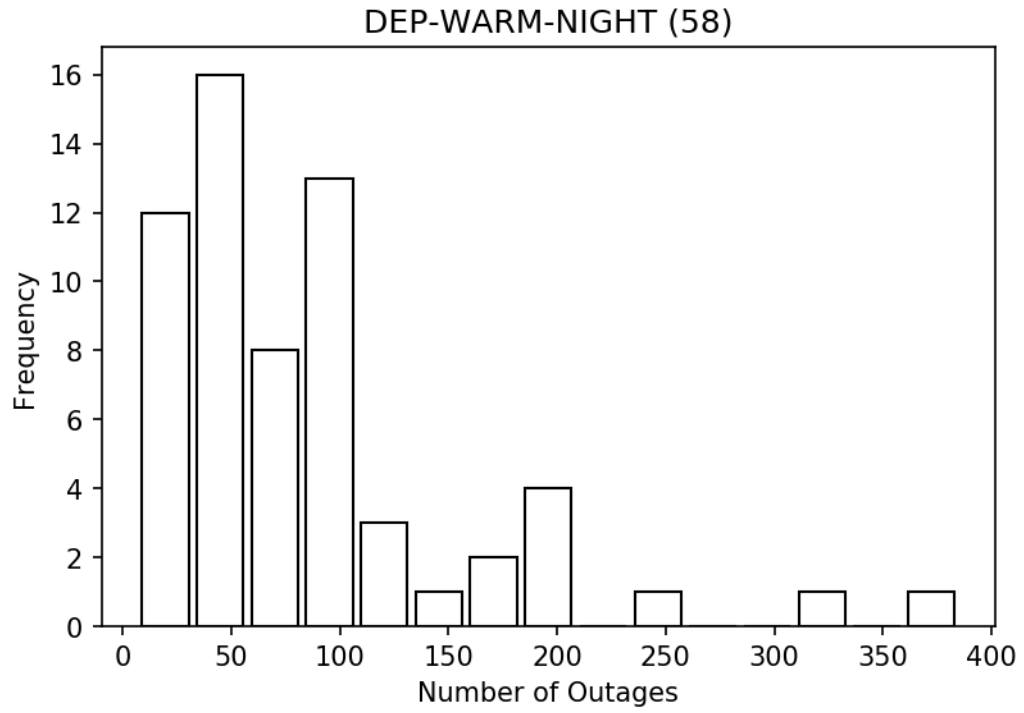


Figure 54. Histogram of outage counts on DEP-WARM nights.

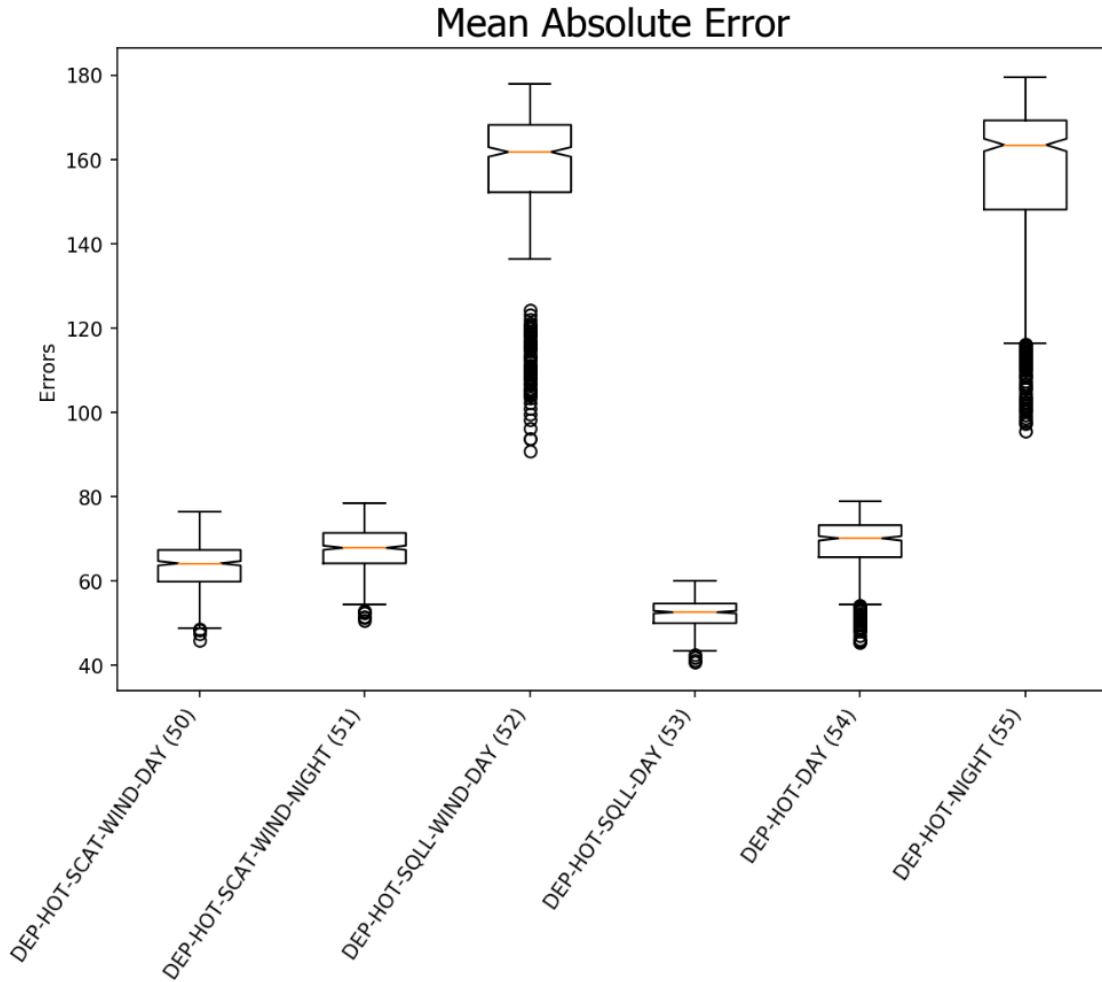


Figure 55a. The mean absolute error distributions of models 50-55. The box marks the 25th percentile (bottom of the box), 50th percentile (centerline), and 75th percentile (top of the box). The lines extending from the boxes mark the 10th percentile (bottom) and 90th percentile (top). The notches signify the 95% confidence intervals of the mean.

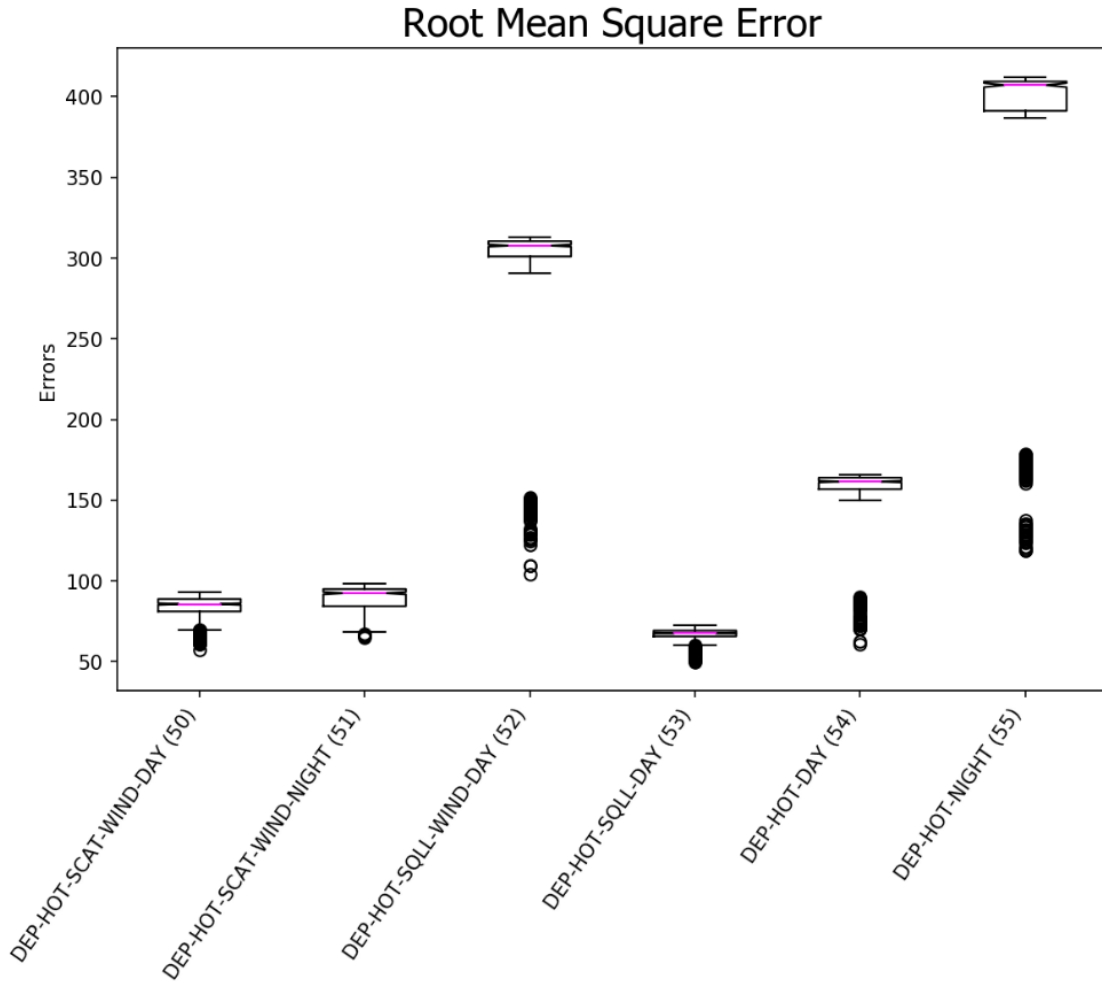


Figure 55b. The root mean square error distributions of models 50-55. The box marks the 25th percentile (bottom of the box), 50th percentile (centerline), and 75th percentile top of the box). The lines extending from the boxes mark the 10th percentile (bottom) and 90th percentile (top). The notches signify the 95% confidence intervals of the mean.

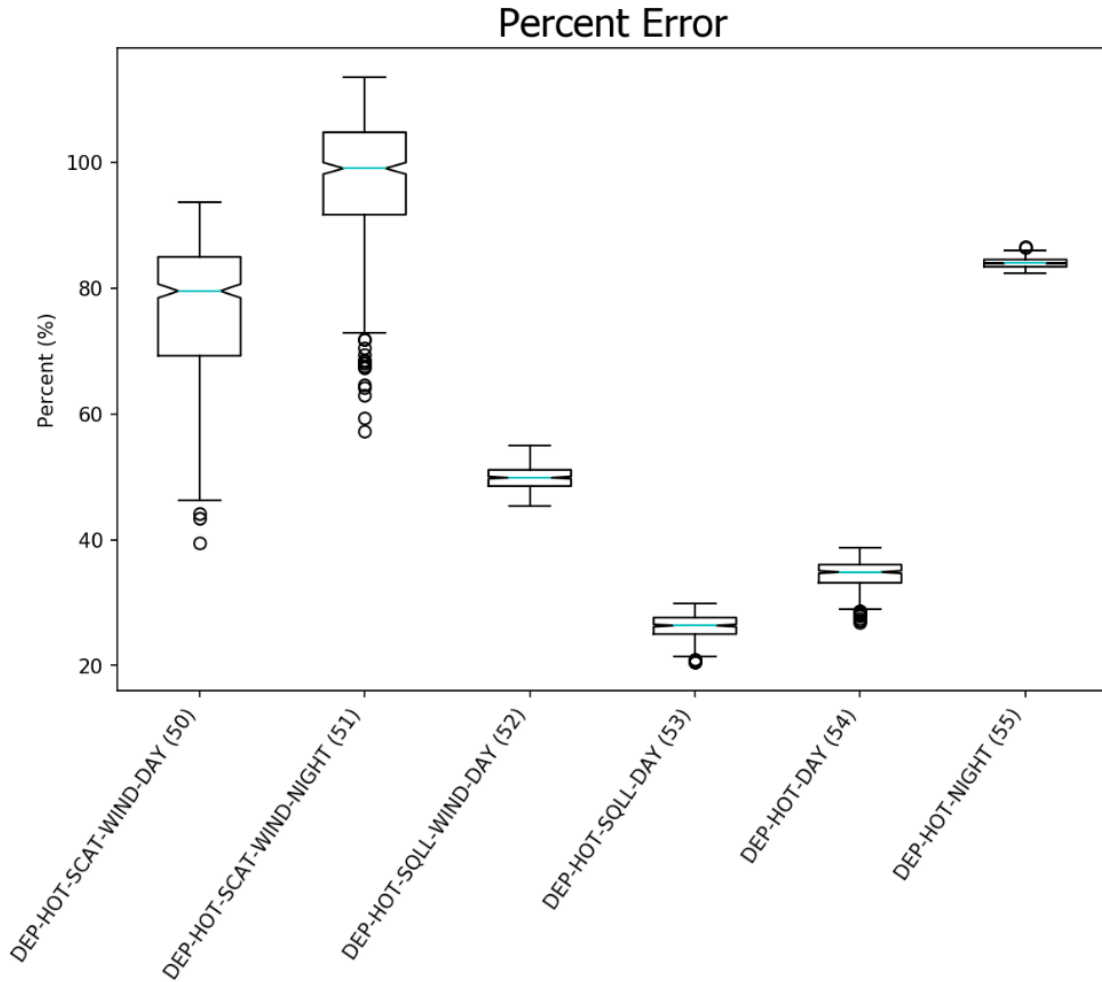


Figure 55c. The percent error distributions of models 50-55. The box marks the 25th percentile (bottom of the box), 50th percentile (centerline), and 75th percentile (top of the box). The lines extending from the boxes mark the 10th percentile (bottom) and 90th percentile (top). The notches signify the 95% confidence intervals of the mean.

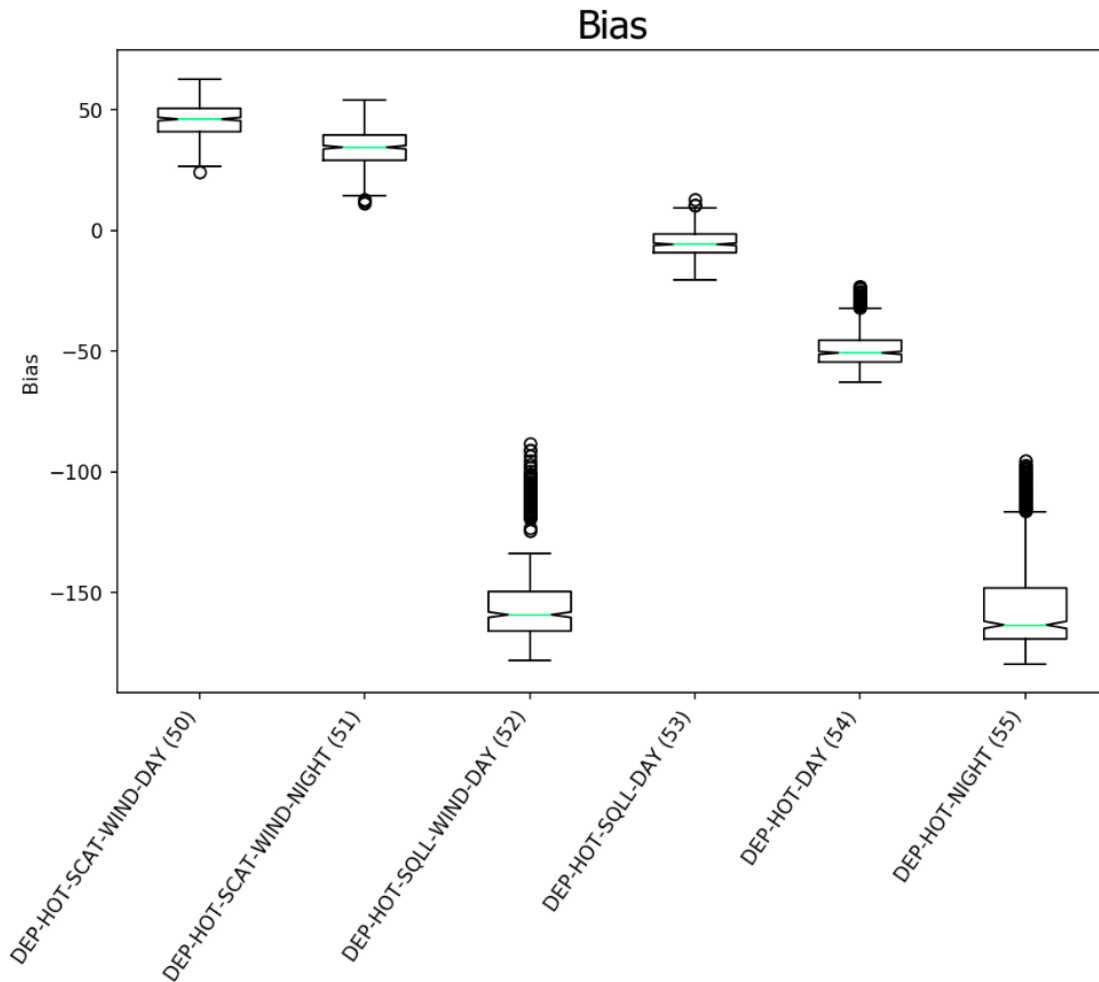


Figure 55d. The bias distributions of models 50-55. The box marks the 25th percentile (bottom of the box), 50th percentile (centerline), and 75th percentile (top of the box). The lines extending from the boxes mark the 10th percentile (bottom) and 90th percentile (top). The notches signify the 95% confidence intervals of the mean.

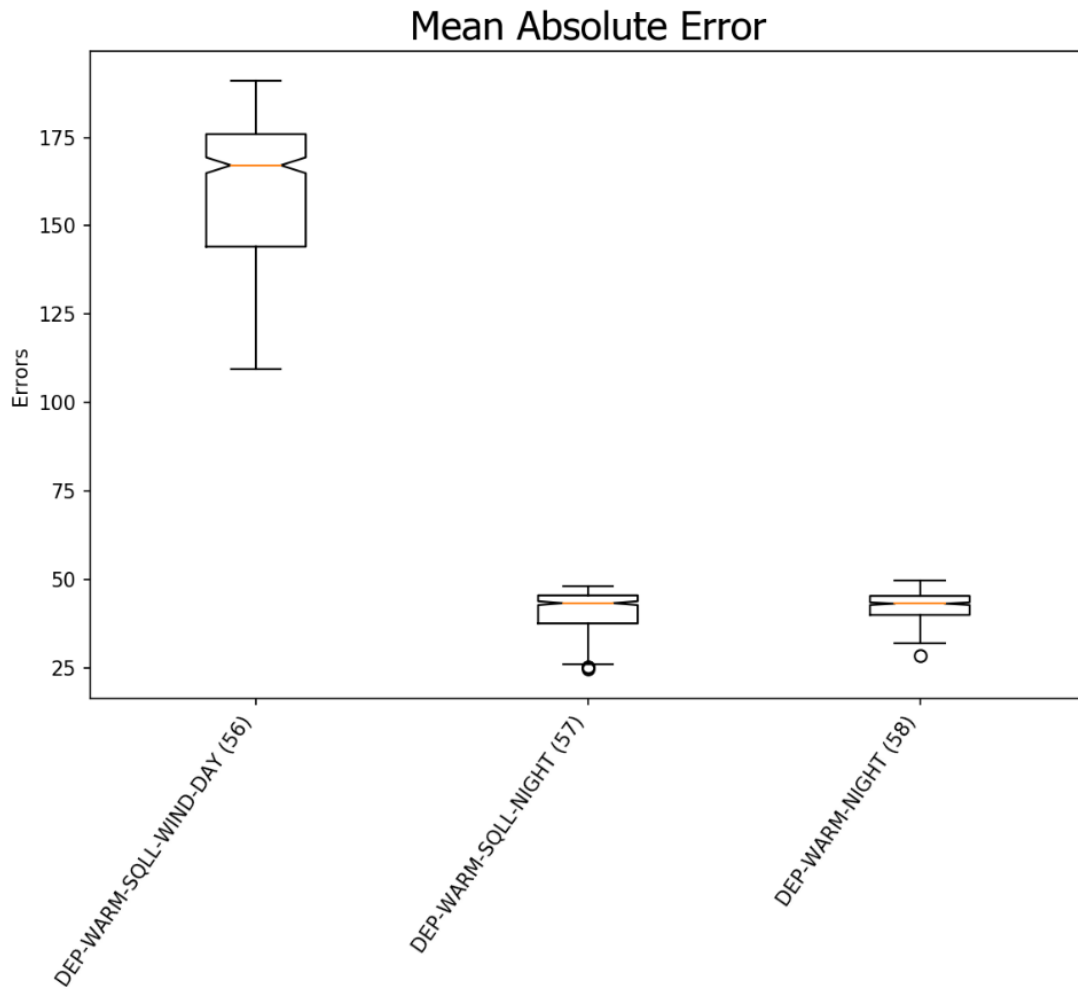


Figure 56a. The mean absolute error distributions of models 56-58. The box marks the 25th percentile (bottom of the box), 50th percentile (centerline), and 75th percentile (top of the box). The lines extending from the boxes mark the 10th percentile (bottom) and 90th percentile (top). The notches signify the 95% confidence intervals of the mean.

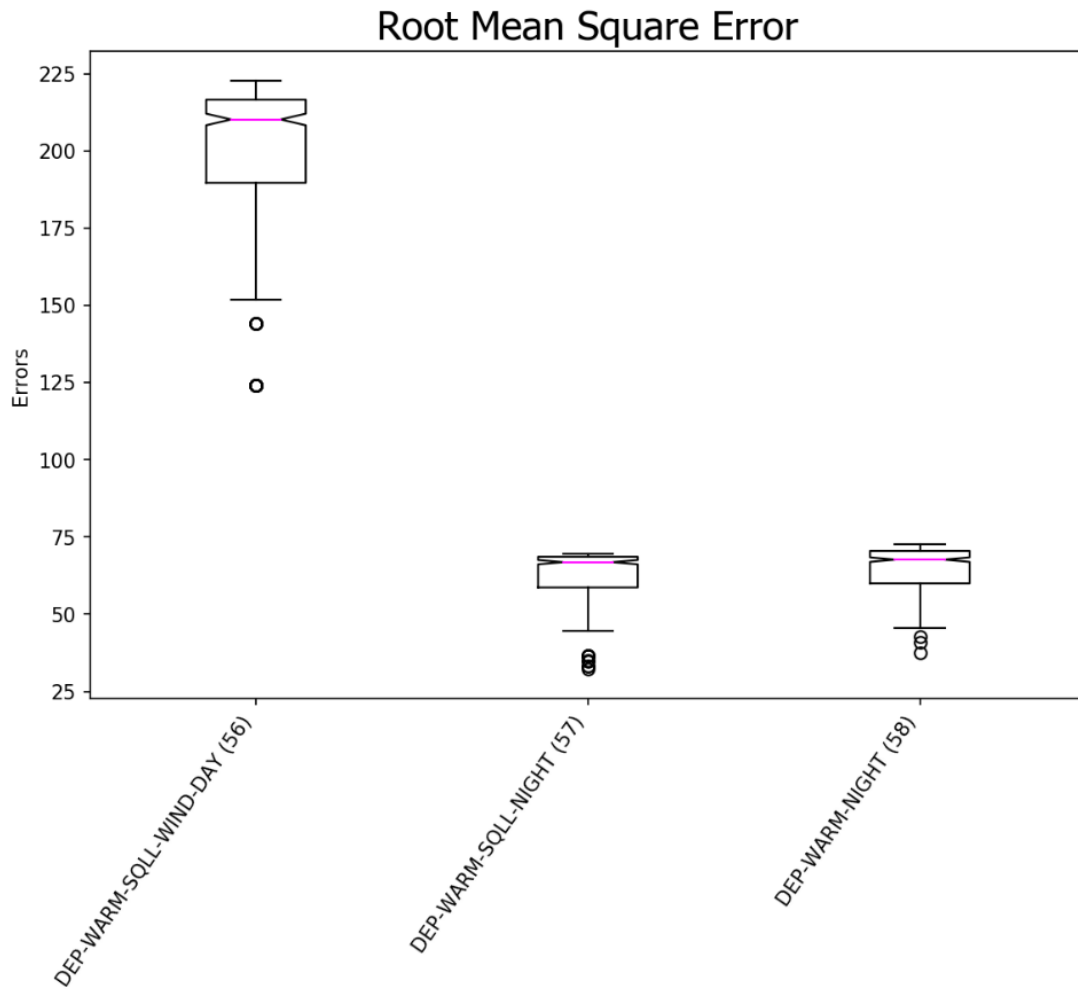


Figure 56b. The root mean square error distributions of models 56-58. The box marks the 25th percentile (bottom of the box), 50th percentile (centerline), and 75th percentile (top of the box). The lines extending from the boxes mark the 10th percentile (bottom) and 90th percentile (top). The notches signify the 95% confidence intervals of the mean.

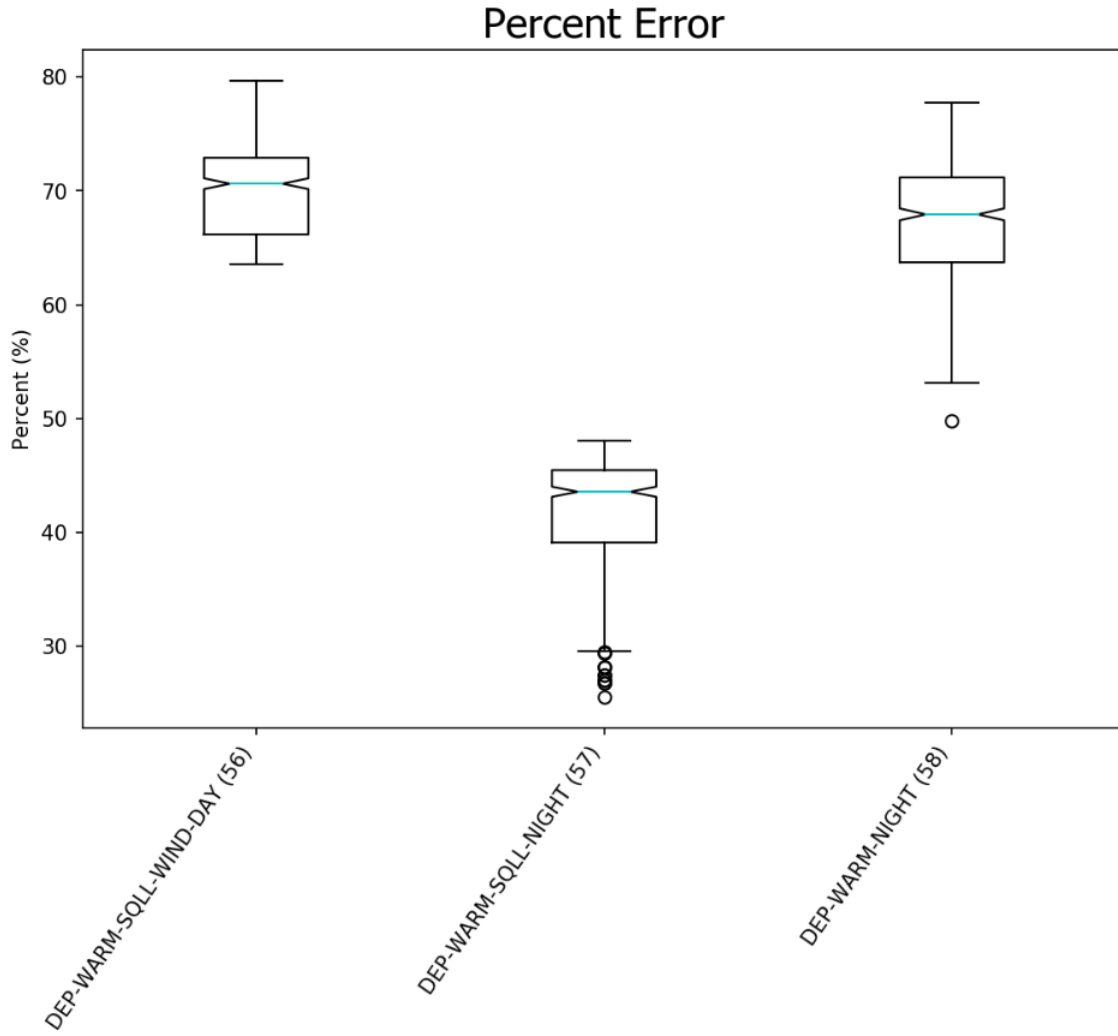


Figure 56c. The percent error distributions of models 56-58. The box marks the 25th percentile (bottom of the box), 50th percentile (centerline), and 75th percentile (top of the box). The lines extending from the boxes mark the 10th percentile (bottom) and 90th percentile (top). The notches signify the 95% confidence intervals of the mean.

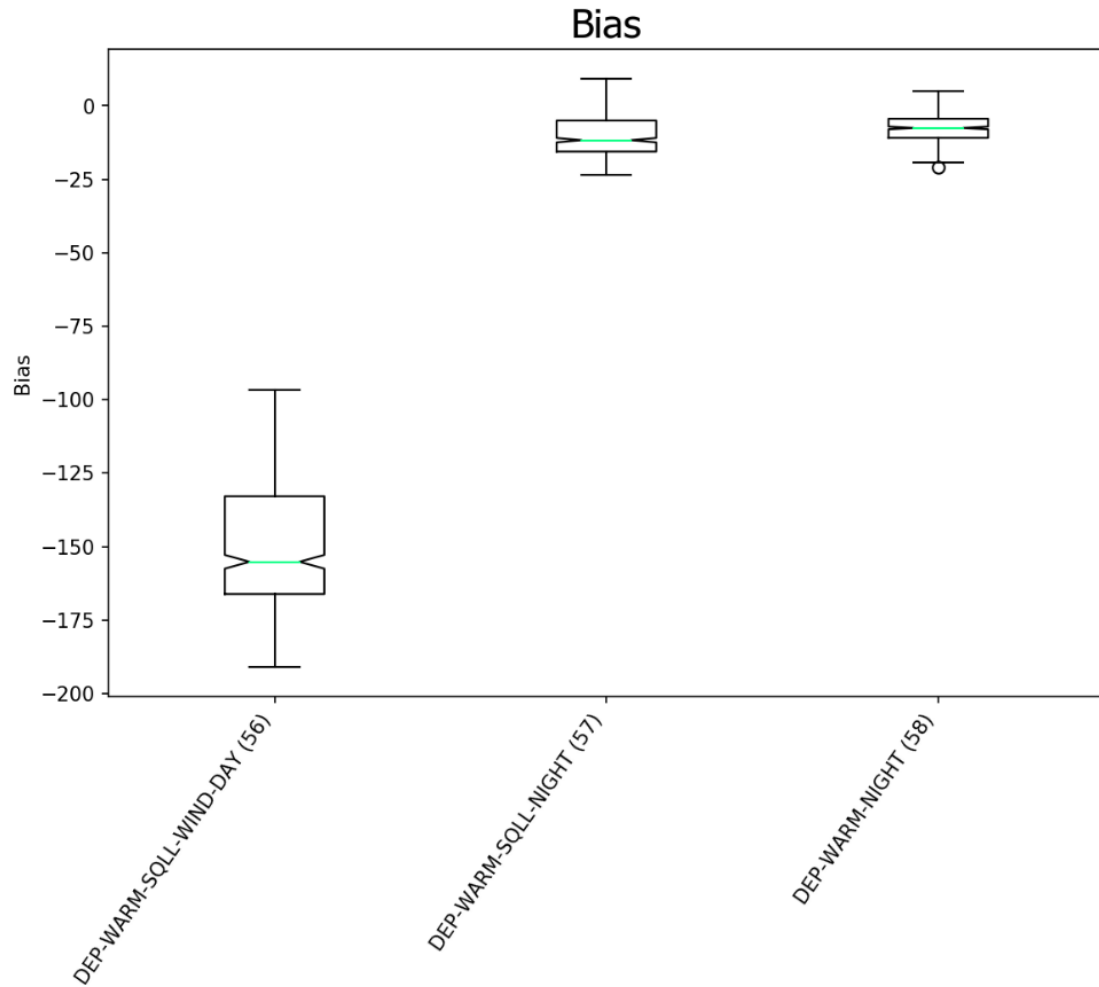


Figure 56d. The bias distributions of models 56-58. The box marks the 25th percentile (bottom of the box), 50th percentile (centerline), and 75th percentile (top of the box). The lines extending from the boxes mark the 10th percentile (bottom) and 90th percentile (top). The notches signify the 95% confidence intervals of the mean.

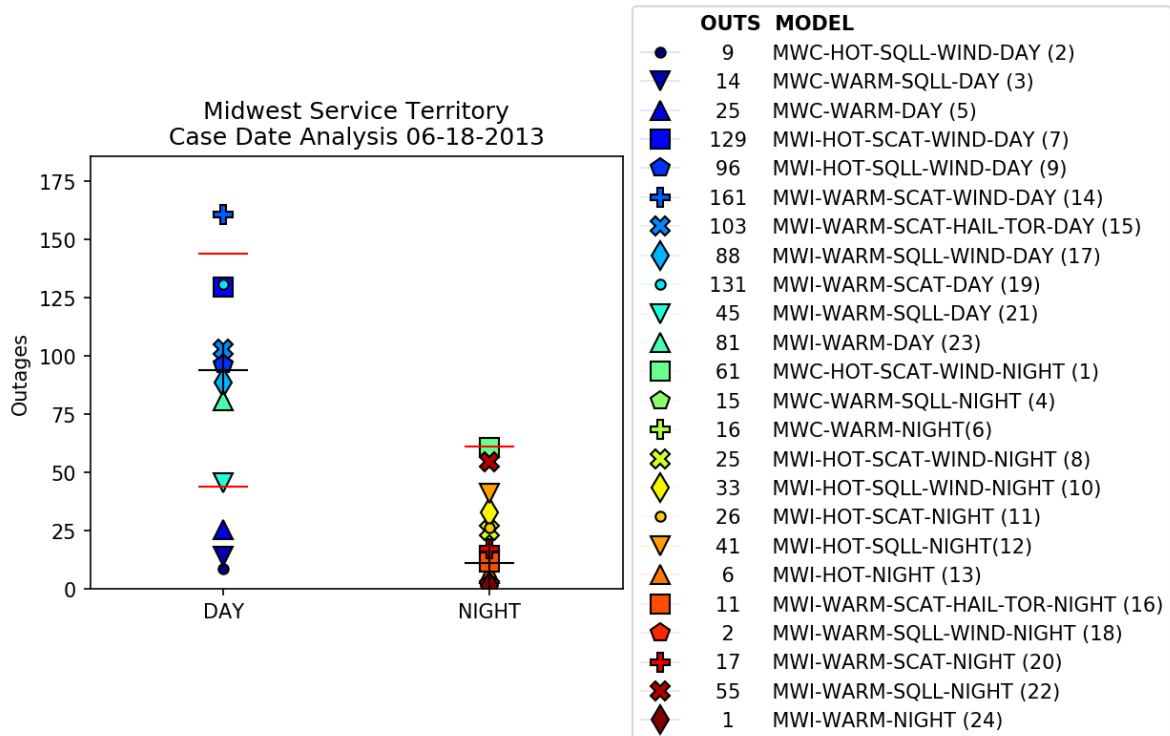


Figure 57. An ensemble forecast for the Midwest service area on 06-18-2013. The observed outage counts are denoted by black cross hairs, individual statistical model forecast are denoted by colored symbols, and the acceptable range of ± 50 outages is marked by red lines (relative to the observed outage count).

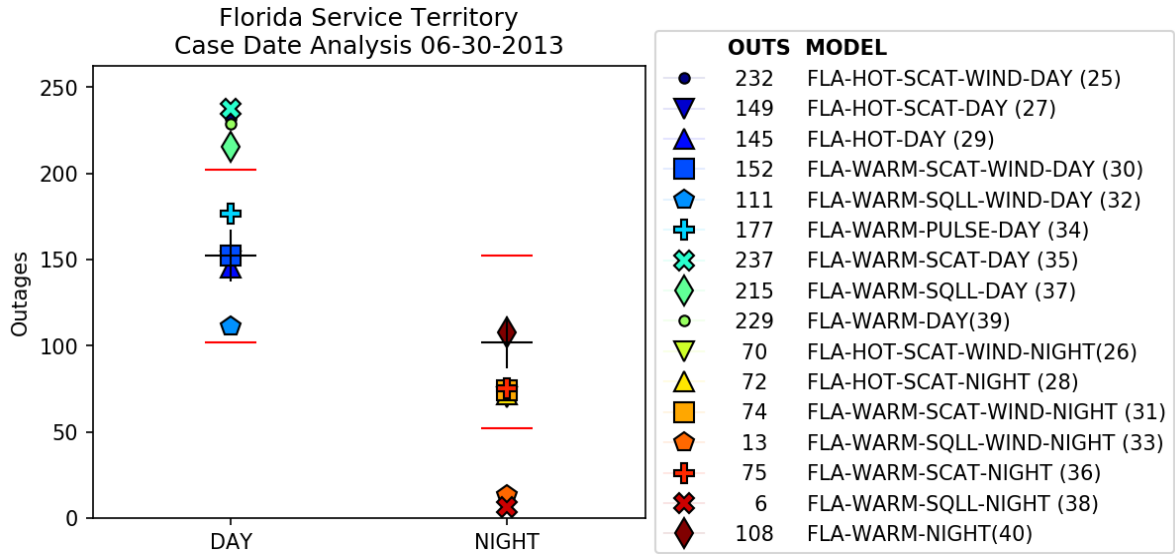


Figure 58. An ensemble forecast for the Florida service area on 06-30-2013. The observed outage counts are denoted by black cross hairs, individual statistical model forecast are denoted by colored symbols, and the acceptable range of ± 50 outages is marked by red lines (relative to the observed outage count).

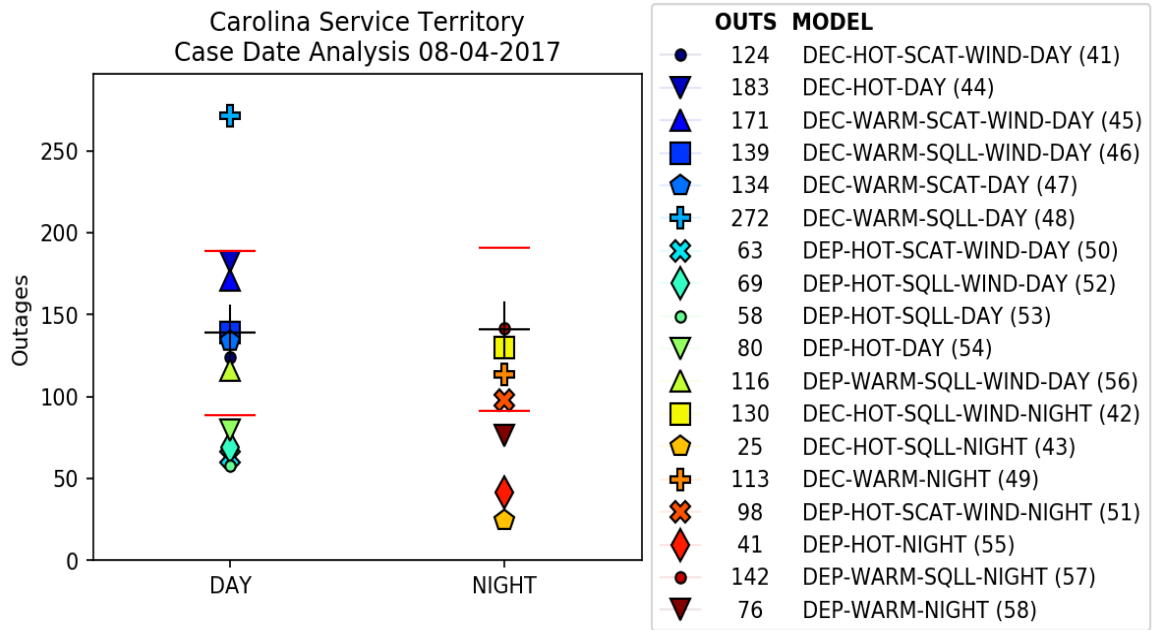


Figure 59. An ensemble forecast for the Carolina service area on 08-04-2017. The observed outage counts are denoted by black cross hairs, individual statistical model forecast are denoted by colored symbols, and the acceptable range of ± 50 outages is marked by red lines (relative to the observed outage count).

REFERENCES

- Atkins, N. T., & Wakimoto, R. M. (1991). Wet Microburst Activity over the Southeastern United States: Implications for Forecasting. *Weather and Forecasting*, 6(4), 470-482. doi:10.1175/1520-0434(1991)006<0470:wmaots>2.0.co;2
- Benjamin, S.G., D. Dévényi, S.S. Weygandt, K.J. Brundage, J.M. Brown, G.A. Grell, D. Kim, B.E. Schwartz, T.G. Smirnova, T.L. Smith, and G.S. Manikin, (2004). An Hourly Assimilation–Forecast Cycle: The RUC. *Mon. Wea. Rev.*, 132, 495–518, [https://doi.org/10.1175/1520-0493\(2004\)132<0495:AHACTR>2.0.CO;2](https://doi.org/10.1175/1520-0493(2004)132<0495:AHACTR>2.0.CO;2)
- Benjamin, S.G., S.S. Weygandt, J.M. Brown, M. Hu, C.R. Alexander, T.G. Smirnova, J.B. Olson, E.P. James, D.C. Dowell, G.A. Grell, H. Lin, S.E. Peckham, T.L. Smith, W.R. Moninger, J.S. Kenyon, and G.S. Manikin, (2016). A North American Hourly Assimilation and Model Forecast Cycle: The Rapid Refresh. *Mon. Wea. Rev.*, 144, 1669–1694, <https://doi.org/10.1175/MWR-D-15-0242.1>
- Bluestein, H.B., G.T. Marx, and M.H. Jain, (1987). Formation of Mesoscale Lines of Precipitation: Nonsevere Squall Lines in Oklahoma during the Spring. *Mon. Wea. Rev.*, 115, 2719–2727, [https://doi.org/10.1175/1520-0493\(1987\)115<2719:FOMLOP>2.0.CO;2](https://doi.org/10.1175/1520-0493(1987)115<2719:FOMLOP>2.0.CO;2)
- Blumberg, W.G., K.T. Halbert, T.A. Supinie, P.T. Marsh, R.L. Thompson, and J.A. Hart, (2017). SHARPPy: An Open-Source Sounding Analysis Toolkit for the Atmospheric Sciences. *Bull. Amer. Meteor. Soc.*, 98, 1625–1636, <https://doi.org/10.1175/BAMS-D-15-00309.1>
- Blyth, A., Christian, H., Driscoll, K., Gadian, A., & Latham, J. (2001). Determination of ice precipitation rates and thunderstorm anvil ice contents from satellite observations of lightning. *Atmospheric Research*, 59-60, 217-229. doi:10.1016/s0169-8095(01)00117-x
- Brimelow, J.C., G.W. Reuter, and E.R. Poolman, (2002). Modeling Maximum Hail Size in Alberta Thunderstorms. *Wea. Forecasting*, 17, 1048–1062, [https://doi.org/10.1175/1520-0434\(2002\)017<1048:MMHSIA>2.0.CO;2](https://doi.org/10.1175/1520-0434(2002)017<1048:MMHSIA>2.0.CO;2)
- Bunkers, M.J., J.R. Wetenkamp, J.J. Schild, and A. Fischer, (2010). Observations of the Relationship between 700-mb Temperatures and Severe Weather Reports across the Contiguous United States. *Wea. Forecasting*, 25, 799–814, <https://doi.org/10.1175/2009WAF2222333.1>
- Byers, H.R. and R.R. Braham, (1948). THUNDERSTORM STRUCTURE AND CIRCULATION. *J. Meteor.*, 5, 71–86, [https://doi.org/10.1175/1520-0469\(1948\)005<0071:TSAC>2.0.CO;2](https://doi.org/10.1175/1520-0469(1948)005<0071:TSAC>2.0.CO;2)
- Caracena, F. and M.W. Maier, (1987). Analysis of a Microburst in the FACE Meteorological Mesonet in Southern Florida. *Mon. Wea. Rev.*, 115, 969–985, [https://doi.org/10.1175/1520-0493\(1987\)115<0969:AOAMIT>2.0.CO;2](https://doi.org/10.1175/1520-0493(1987)115<0969:AOAMIT>2.0.CO;2)

Cerruti, B. J., & Decker, S. G. (2012). A Statistical Forecast Model of Weather-Related Damage to a Major Electric Utility. *Journal of Applied Meteorology and Climatology*, 51(2), 191-204. doi:10.1175/jamc-d-11-09.1

Coniglio, M. C., Corfidi, S. F., Kain, J. S. (2011). Environment and Early Evolution of the 8 May 2009 Derecho-Producing Convective System. *Mon. Wea. Rev.*, 139, 1083–1102, <https://doi.org/10.1175/2010MWR3413.1>

Davies-Jones, R.P., D.W. Burgess, and M. Foster, (1990). Test of helicity as a tornado forecast parameter. *16th conf. On Severe Local Storms*, Kananaskies Park, AB, Canada, Amer. Meteor. Soc., 588-592

Duke, J.W., and J.A. Rogash, (1992). Multiscale Review of the Development and Early Evolution of the 9 April 1991 Derecho. *Wea. Forecasting*, 7, 623–635, [https://doi.org/10.1175/1520-0434\(1992\)007<0623:MROTDA>2.0.CO;2](https://doi.org/10.1175/1520-0434(1992)007<0623:MROTDA>2.0.CO;2)

[Digital image]. (n.d.). Retrieved from <http://sustainabilityreport.duke-energy.com/2013/images/charts/map-service-territories.png>

Evans, J. S., & Doswell, C. A. (2001). Examination of Derecho Environments Using Proximity Soundings. *Weather and Forecasting*, 16(3), 329-342. doi:10.1175/1520-0434(2001)016<0329:eodeup>2.0.co;2

Forbes, G. S., & Wakimoto, R. M. (1983). A Concentrated Outbreak of Tornadoes, Downbursts and Microbursts, and Implications Regarding Vortex Classification. *Monthly Weather Review*, 111(1), 220-236. doi:10.1175/1520-0493(1983)111<0220:acootd>2.0.co;2

Fujita, T. T. (1978). *Manual of downburst identification for Project Nimrod*. Chicago: Satellite and Mesometeorology Research Project, Dept. of the Geophysical Sciences, University of Chicago.

Fujita, T. T., & Wakimoto, R. M. (1981). Five Scales of Airflow Associated with a Series of Downbursts on 16 July 1980. *Monthly Weather Review*, 109(7), 1438-1456. doi:10.1175/1520-0493(1981)109<1438:fsoaaw>2.0.co;2

Galway, J. G. (1956). The Lifted Index as a Predictor of Latent Instability. *Bulletin of the American Meteorological Society*, 37(10), 528-529. doi:10.1175/1520-0477-37.10.528

Gilmore, M. S., & Wicker, L. J. (1998). The Influence of Midtropospheric Dryness on Supercell Morphology and Evolution. *Monthly Weather Review*, 126(4), 943-958. doi:10.1175/1520-0493(1998)126<0943:tioindo>2.0.co;2

- Gropp, M.E. and C.E. Davenport, (2018). The Impact of the Nocturnal Transition on the Lifetime and Evolution of Supercell Thunderstorms in the Great Plains. *Wea. Forecasting*, 33, 1045–1061, <https://doi.org/10.1175/WAF-D-17-0150.1>
- Guikema, S., Davidson, R., & Liu, H. (2006). Statistical Models of the Effects of Tree Trimming on Power System Outages. *IEEE Transactions on Power Delivery*, 21(3), 1549-1557. doi:10.1109/tpwr.2005.860238
- Guikema, S., Han, S., & Quiring, S. (2008). Estimating Power Outages during Hurricanes Using Semi-Parametric Statistical Methods. *Structures Congress 2008*. doi:10.1061/41016(314)189
- Guikema, S. D., Quiring, S. M., & Han, S. (2010). Prestorm Estimation of Hurricane Damage to Electric Power Distribution Systems. *Risk Analysis*, 30(12), 1744-1752. doi:10.1111/j.1539-6924.2010.01510.x
- Guikema, S. D., Nateghi, R., Quiring, S. M., Staid, A., Reilly, A. C., & Gao, M. (2014). Predicting Hurricane Power Outages to Support Storm Response Planning. *IEEE Access*, 2, 1364-1373. doi:10.1109/access.2014.2365716
- Han, S., Guikema, S. D., & Quiring, S. M. (2009). Improving the Predictive Accuracy of Hurricane Power Outage Forecasts Using Generalized Additive Models. *Risk Analysis*, 29(10), 1443-1453. doi:10.1111/j.1539-6924.2009.01280.x
- Hales Jr., J.E., (1993). Biases in the severe thunderstorm data base: Ramifications and solutions. Preprints, 13th Conf. on Weather Analysis and Forecasting, Vienna, VA, Amer. Meteor. Soc., 504–507.
- Johns, R. H., & Hirt, W. D. (1987). Derechos: Widespread Convectively Induced Windstorms. *Weather and Forecasting*, 2(1), 32-49. doi:10.1175/1520-0434(1987)002<0032:dwcw>2.0.co;2
- Johns, R.H., (1993). Meteorological Conditions Associated with Bow Echo Development in Convective Storms. *Wea. Forecasting*, 8, 294–299, [https://doi.org/10.1175/1520-0434\(1993\)008<0294:MCAWBE>2.0.CO;2](https://doi.org/10.1175/1520-0434(1993)008<0294:MCAWBE>2.0.CO;2)
- Kingsmill, D.E. and R.M. Wakimoto, (1991). Kinematic, Dynamic, and Thermodynamic Analysis of a Weakly Sheared Severe Thunderstorm over Northern Alabama. *Mon. Wea. Rev.*, 119, 262–297, [https://doi.org/10.1175/1520-0493\(1991\)119<0262:KDATAO>2.0.CO;2](https://doi.org/10.1175/1520-0493(1991)119<0262:KDATAO>2.0.CO;2)
- Knupp, K.R., (1987). Downdrafts within High Plains Cumulonimbi. Part I: General Kinematic Structure. *J. Atmos. Sci.*, 44, 987–1008, doi:10.1175/1520-0469(1987)044<0987:DWHPCP>2.0.CO;2

- Knupp, K.R., (1988). Downdrafts within High Plains Cumulonimbi. Part II: Dynamics and Thermodynamics. *J. Atmos. Sci.*, 45, 3965–3982, doi:10.1175/1520-0469(1988)045<3965:DWHPCP>2.0.CO;2
- Lackmann, G. (2012). *Midlatitude synoptic meteorology: Dynamics, analysis, and forecasting*. Boston, MA: American Meteorological Society.
- Liu, H., Davidson, R. A., Rosowsky, D. V., & Stedinger, J. R. (2005). Negative Binomial Regression of Electric Power Outages in Hurricanes. *Journal of Infrastructure Systems*, 11(4), 258-267. doi:10.1061/(asce)1076-0342(2005)11:4(258)
- Liu, H., Davidson, R. A., & Apanasovich, T. V. (2008). Spatial generalized linear mixed models of electric power outages due to hurricanes and ice storms. *Reliability Engineering & System Safety*, 93(6), 897-912. doi:10.1016/j.res.2007.03.038
- Mahoney, K. M., Lackmann, G. M., & Parker, M. D. (2009). The Role of Momentum Transport in the Motion of a Quasi-Idealized Mesoscale Convective System. *Monthly Weather Review*, 137(10), 3316-3338. doi:10.1175/2009mwr2895.1
- Markowski, P., & Richardson, Y. (2010). *Mesoscale meteorology in midlatitudes*. Oxford: Wiley-Blackwell.
- McCaul, E.W., S.J. Goodman, K.M. LaCasse, and D.J. Cecil, (2009). Forecasting Lightning Threat Using Cloud-Resolving Model Simulations. *Wea. Forecasting*, 24, 709–729, <https://doi.org/10.1175/2008WAF2222152.1>
- McRoberts, D. B., Quiring, S. M., & Guikema, S. D. (2016). Improving Hurricane Power Outage Prediction Models Through the Inclusion of Local Environmental Factors. *Risk Analysis*. doi:10.1111/risa.12728
- Montgomery, D. C., Peck, E. A., & Vining, G. G. (2013). *Introduction to Linear Regression Analysis*. Chichester: Wiley.
- Nateghi, R., Guikema, S. D., & Quiring, S. M. (2011). Comparison and Validation of Statistical Methods for Predicting Power Outage Durations in the Event of Hurricanes. *Risk Analysis*, 31(12), 1897-1906. doi:10.1111/j.1539-6924.2011.01618.x
- Nateghi, R., Guikema, S., & Quiring, S. M. (2014). Power Outage Estimation for Tropical Cyclones: Improved Accuracy with Simpler Models. *Risk Analysis*, 34(6), 1069-1078. doi:10.1111/risa.12131
- Parker, M. D., & Johnson, R. H. (2000). Organizational Modes of Midlatitude Mesoscale Convective Systems. *Monthly Weather Review*, 128(10), 3413-3436. doi:10.1175/1520-0493(2001)129<3413:omommc>2.0.co;2

Peterson, R.E., (1984). A Triple-Doppler Radar Analysis of a Discretely Propagating Multicell Convective Storm. *J. Atmos. Sci.*, 41, 2973–2990, [https://doi.org/10.1175/1520-0469\(1984\)041<2973:ATDRAO>2.0.CO;2](https://doi.org/10.1175/1520-0469(1984)041<2973:ATDRAO>2.0.CO;2)

Proctor, F.H., (1988). Numerical Simulations of an Isolated Microburst. Part I: Dynamics and Structure. *J. Atmos. Sci.*, 45, 3137–3160, [https://doi.org/10.1175/1520-0469\(1988\)045<3137:NSOAIM>2.0.CO;2](https://doi.org/10.1175/1520-0469(1988)045<3137:NSOAIM>2.0.CO;2)

Proctor, F.H., (1989). Numerical Simulations of an Isolated Microburst. Part II: Sensitivity Experiments. *J. Atmos. Sci.*, 46, 2143–2165, [https://doi.org/10.1175/1520-0469\(1989\)046<2143:NSOAIM>2.0.CO;2](https://doi.org/10.1175/1520-0469(1989)046<2143:NSOAIM>2.0.CO;2)

Quiring, S.M., A.B. Schumacher, and S.D. Guikema, (2014). Incorporating Hurricane Forecast Uncertainty into a Decision-Support Application for Power Outage Modeling. *Bull. Amer. Meteor. Soc.*, 95, 47–58, <https://doi.org/10.1175/BAMS-D-12-00012.1>

Rasmussen, E.N., and D.O. Blanchard, (1998). A baseline climatology of sounding-derived supercell and tornado forecast parameters. *Wea. Forecasting*, 13, 1148-1164.

Roberts, R.D. and J.W. Wilson, (1989). A Proposed Microburst Nowcasting Procedure Using Single-Doppler Radar. *J. Appl. Meteor.*, 28, 285–303, [https://doi.org/10.1175/1520-0450\(1989\)028<0285:APMNPU>2.0.CO;2](https://doi.org/10.1175/1520-0450(1989)028<0285:APMNPU>2.0.CO;2)

Rotunno, R., J.B. Klemp, and M.L. Weisman, (1988). A Theory for Strong, Long-Lived Squall Lines. *J. Atmos. Sci.*, 45, 463–485, [https://doi.org/10.1175/1520-0469\(1988\)045<0463:ATFSSL>2.0.CO;2](https://doi.org/10.1175/1520-0469(1988)045<0463:ATFSSL>2.0.CO;2)

Reed, D. A. (2008). Electric utility distribution analysis for extreme winds. *Journal of Wind Engineering and Industrial Aerodynamics*, 96(1), 123-140. doi:10.1016/j.jweia.2007.04.002

Renick, J. H., and J. B. Maxwell, (1977). Forecasting hailfall in Alberta. *Hail: A Review of Hail Science and Hail Suppression, Meteor. Monogr.*, No. 38, Amer. Meteor. Soc., 145–151.

Sherburn, K.D. and M.D. Parker, (2014). Climatology and Ingredients of Significant Severe Convection in High-Shear, Low-CAPE Environments. *Wea. Forecasting*, 29, 854–877, <https://doi.org/10.1175/WAF-D-13-00041.1>

Smirnova, T.G., J.M. Brown, and S.G. Benjamin, (1997). Performance of Different Soil Model Configurations in Simulating Ground Surface Temperature and Surface Fluxes. *Mon. Wea. Rev.*, 125, 1870–1884, [https://doi.org/10.1175/1520-0493\(1997\)125<1870:PODSMC>2.0.CO;2](https://doi.org/10.1175/1520-0493(1997)125<1870:PODSMC>2.0.CO;2)

Storm Prediction Center. (n.d.). Retrieved October 18, 2018, from https://www.spc.noaa.gov/sfctest/help/help_sigh.html

Storm Prediction Center. (n.d.). Retrieved October 18, 2018, from https://www.spc.noaa.gov/exper/mesoanalysis/help/help_mbc.html

Storm Prediction Center. (n.d.). Retrieved October 30, 2018, from https://www.spc.noaa.gov/exper/mesoanalysis/help/help_brn.html

Straka, J.M. and J.R. Anderson, (1993). Numerical Simulations of Microburst-producing Storms: Some Results from Storms Observed during COHMEX. *J. Atmos. Sci.*, 50, 1329–1348, [https://doi.org/10.1175/1520-0469\(1993\)050<1329:NSOMPS>2.0.CO;2](https://doi.org/10.1175/1520-0469(1993)050<1329:NSOMPS>2.0.CO;2)

Srivastava, R.C., (1987). A Model of Intense Downdrafts Driven by the Melting and Evaporation of Precipitation. *J. Atmos. Sci.*, 44, 1752–1774, [https://doi.org/10.1175/1520-0469\(1987\)044<1752:AMOIDD>2.0.CO;2](https://doi.org/10.1175/1520-0469(1987)044<1752:AMOIDD>2.0.CO;2)

Tonn, G. L., Guikema, S. D., Ferreira, C. M., & Quiring, S. M. (2016). Hurricane Isaac: A Longitudinal Analysis of Storm Characteristics and Power Outage Risk. *Risk Analysis*, 36(10), 1936-1947. doi:10.1111/risa.12552

Thompson, R.L., R. Edwards, J.A. Hart, K.L. Elmore, and P. Markowski, (2003). Close Proximity Soundings within Supercell Environments Obtained from the Rapid Update Cycle. *Wea. Forecasting*, 18, 1243–1261, [https://doi.org/10.1175/1520-0434\(2003\)018<1243:CPSWSE>2.0.CO;2](https://doi.org/10.1175/1520-0434(2003)018<1243:CPSWSE>2.0.CO;2)

Thompson, R.L., C.M. Mead, and R. Edwards, (2007). Effective Storm-Relative Helicity and Bulk Shear in Supercell Thunderstorm Environments. *Wea. Forecasting*, 22, 102–115, <https://doi.org/10.1175/WAF969.1>

Tuttle, J.D., V.N. Bringi, H.D. Orville, and F.J. Kopp, (1989). Multiparameter Radar Study of a Microburst: Comparison with Model Results. *J. Atmos. Sci.*, 46, 601–620, doi:10.1175/1520-0469(1989)046<0601:MRSOAM>2.0.CO;2

Wanik, D. W., Anagnostou, E. N., Hartman, B. M., Frediani, M. E., & Astitha, M. (2015). Storm outage modeling for an electric distribution network in Northeastern USA. *Natural Hazards*, 79(2), 1359-1384. doi:10.1007/s11069-015-1908-2

Wakimoto, R.M. and V.N. Bringi, (1988). Dual-Polarization observations of Microbursts Associated with Intense Convection: The 20 July Storm during the MIST Project. *Mon. Wea. Rev.*, 116, 1521–1539, [https://doi.org/10.1175/1520-0493\(1988\)116<1521:DPOOMA>2.0.CO;2](https://doi.org/10.1175/1520-0493(1988)116<1521:DPOOMA>2.0.CO;2)

Wakimoto, R.M., H.V. Murphey, A. Nester, D.P. Jorgensen, and N.T. Atkins, (2006). High Winds Generated by Bow Echoes. Part I: Overview of the Omaha Bow Echo 5 July 2003 Storm during BAMEX. *Mon. Wea. Rev.*, 134, 2793–2812, <https://doi.org/10.1175/MWR3215.1>

Watson, A. I., & Blanchard, D. O. (1984). The Relationship between Total Area Divergence and Convective Precipitation in South Florida. *Monthly Weather Review*, 112(4), 673-685. doi:10.1175/1520-0493(1984)112<0673:TDONSC>2.0.CO;2

Weisman, M.L. and J.B. Klemp, (1982). The Dependence of Numerically Simulated Convective Storms on Vertical Wind Shear and Buoyancy. *Mon. Wea. Rev.*, 110, 504–520, [https://doi.org/10.1175/1520-0493\(1982\)110<0504:TDONSC>2.0.CO;2](https://doi.org/10.1175/1520-0493(1982)110<0504:TDONSC>2.0.CO;2)

Williams, E., Boldi, B., Matlin, A., Weber, M., Hodanish, S., Sharp, D., Goodman, S., Raghavan, R., Buechler, D. (1999). The behavior of total lightning activity in severe Florida thunderstorms. *Atmospheric Research*, 51(3-4), 245-265. doi:10.1016/s0169-8095(99)00011-3

Wilks, D. S. (2006). *Statistical methods in the atmospheric sciences: An introduction*. Amsterdam: Academic Press.

Zhu, D., Cheng, D., Broadwater, R. P., & Scirbona, C. (2006). Storm modeling for prediction of power distribution system outages. *Electric Power Systems Research*, 77(8), 973-979. doi:10.1016/j.epsr.2006.08.020